

Methodologies and algorithms for sound propagation in complex environments with application to urban air mobility

A ray acoustics approach

Yunus, F.

DOI

[10.4233/uuid:72d10b7a-6790-41fc-9b15-26f9cccdb77f](https://doi.org/10.4233/uuid:72d10b7a-6790-41fc-9b15-26f9cccdb77f)

Publication date

2023

Document Version

Final published version

Citation (APA)

Yunus, F. (2023). *Methodologies and algorithms for sound propagation in complex environments with application to urban air mobility: A ray acoustics approach*. [Dissertation (TU Delft), Delft University of Technology]. <https://doi.org/10.4233/uuid:72d10b7a-6790-41fc-9b15-26f9cccdb77f>

Important note

To cite this publication, please use the final published version (if applicable). Please check the document version above.

Copyright

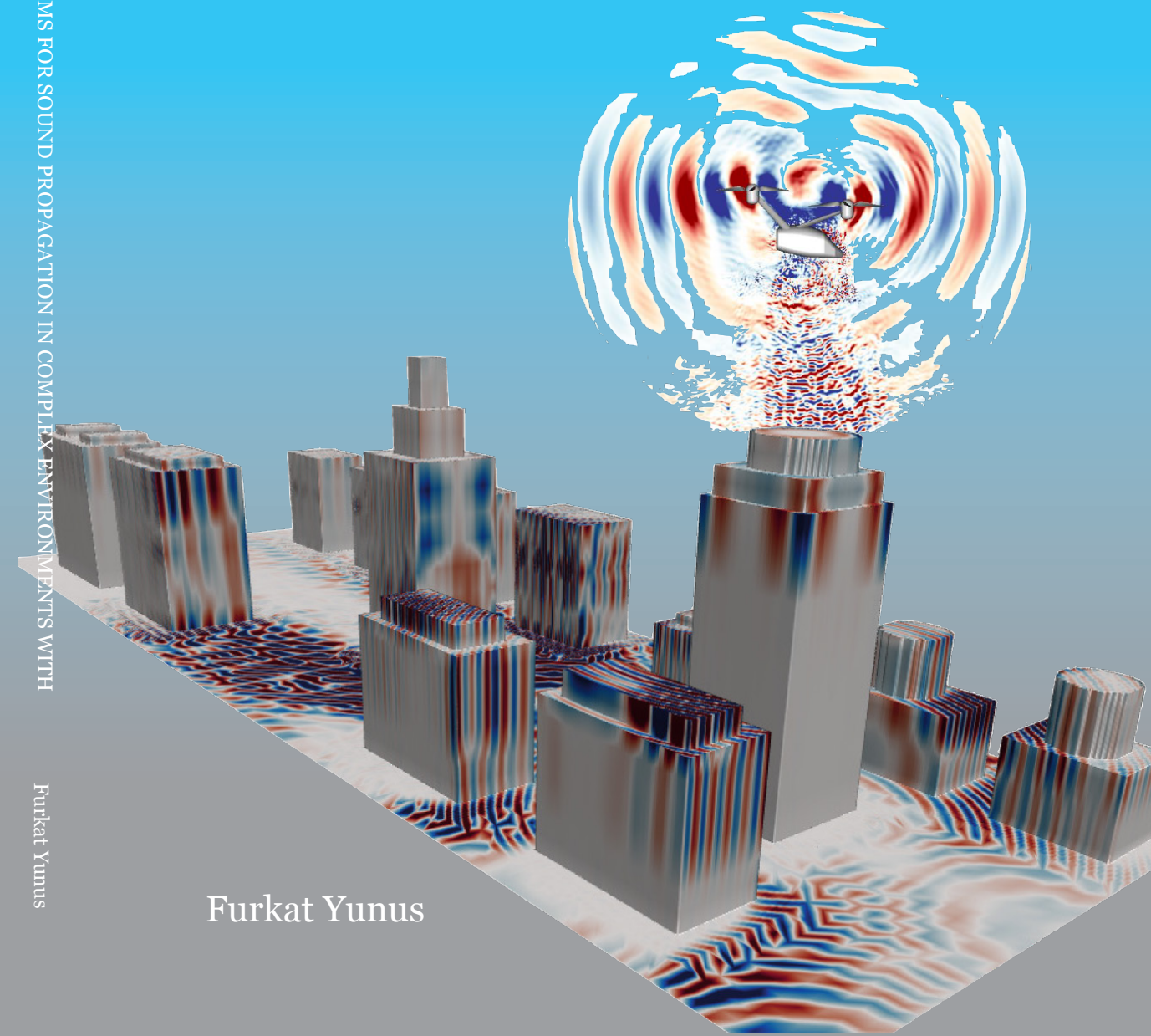
Other than for strictly personal use, it is not permitted to download, forward or distribute the text or part of it, without the consent of the author(s) and/or copyright holder(s), unless the work is under an open content license such as Creative Commons.

Takedown policy

Please contact us and provide details if you believe this document breaches copyrights. We will remove access to the work immediately and investigate your claim.

METHODOLOGIES AND ALGORITHMS FOR SOUND PROPAGATION IN COMPLEX ENVIRONMENTS WITH APPLICATION TO URBAN AIR MOBILITY

A ray acoustics approach



METHODOLOGIES AND ALGORITHMS FOR SOUND PROPAGATION IN COMPLEX ENVIRONMENTS WITH

Furkat Yunus

Furkat Yunus

Propositions

accompanying the dissertation

METHODOLOGIES AND ALGORITHMS FOR SOUND PROPAGATION IN COMPLEX ENVIRONMENT WITH APPLICATION TO URBAN AIR MOBILITY

A RAY ACOUSTICS APPROACH

by

Furkat YUNUS

1. Sound waves tend to refract away from mediums with higher phase velocities and towards those with lower ones, much like how heat naturally flows from hotter areas to cooler ones (Chapter 2).
2. UAM vehicles exhibit a complex directional pattern in sound radiation that causes large variations in noise levels at different receiver locations (Chapter 4 & 7).
3. As sound propagates over flat terrain, the impact of vertical variations in wind and temperature increases proportionally with propagation distance (Chapter 5).
4. In urban areas, wind flow weakens diffraction patterns and primarily impacts high-frequency noise (Chapter 6 & 7).
5. To mitigate aircraft-community-noise, all three factors - noise source, propagation, and community response - must be carefully considered and researched.
6. Mitigation of noise pollution is limited by our incomplete understanding of how the intensity of sound is affected by its interaction with the surrounding environment.
7. Misusing education delays a sustainable future and leads to a totalitarian environment that does not propagate ideas.
8. The severity of climate effects is proportional to the severity of human rights abuse.
9. Thousands of intellectuals who speak truth to power are necessary for sustainable aviation to become a reality.
10. Despite our increasing knowledge of the observable universe, its fundamental behavior remains constant.

These propositions are regarded as opposable and defensible, and have been approved as such by the promotor prof. dr. D. Casalino.

Stellingen

behorende bij het proefschrift

METHODOLOGIES AND ALGORITHMS FOR SOUND PROPAGATION IN COMPLEX ENVIRONMENT WITH APPLICATION TO URBAN AIR MOBILITY A RAY ACOUSTICS APPROACH

door

Furkat YUNUS

1. Soundgolven buigen af van media met hogere fase-snelheden en naar media met lagere snelheden, net als warmte (Hoofdstuk 2).
2. UAM-voertuigen vertonen een complex richtingspatroon in geluidsuitstraling dat grote variaties in geluidsniveaus veroorzaakt op verschillende ontvangstlocaties (Hoofdstuk 4 & 7).
3. Als geluid zich voortplant over vlak terrein, neemt de invloed van verticale variaties in wind en temperatuur proportioneel toe met de voortplantingsafstand (Hoofdstuk 5).
4. In stedelijke gebieden verzwakt de windstroom de diffractiepatronen en heeft het voornamelijk invloed op hoogfrequent geluid (Hoofdstuk 6 & 7).
5. Om vliegtuig-gemeenschapslawaai te verminderen, moeten alle drie de factoren - geluidsbron, propagatie en gemeenschapsreactie - zorgvuldig worden overwogen en onderzocht.
6. Beperking van geluidsoverlast wordt belemmerd door ons onvolledige begrip van hoe de intensiteit van geluid wordt beïnvloed door de interactie met de omgeving.
7. Het misbruiken van onderwijs vertraagt een duurzame toekomst en leidt tot een totale omgeving die geen ideeën voortplant.
8. De ernst van klimaateffecten is evenredig met de ernst van de schendingen van de mensenrechten.
9. Duizenden intellectuelen die de waarheid durven te spreken zijn nodig om duurzame luchtvaart werkelijkheid te laten worden.
10. Ondanks onze groeiende kennis van het waarneembare universum blijft het fundamentele gedrag ervan constant.

Deze stellingen worden oponeerbaar en verdedigbaar geacht en zijn als zodanig goedgekeurd door de promotor prof. dr. D. Casalino.

**METHODOLOGIES AND ALGORITHMS FOR SOUND
PROPAGATION IN COMPLEX ENVIRONMENTS WITH
APPLICATION TO URBAN AIR MOBILITY**

A RAY ACOUSTICS APPROACH

METHODOLOGIES AND ALGORITHMS FOR SOUND PROPAGATION IN COMPLEX ENVIRONMENTS WITH APPLICATION TO URBAN AIR MOBILITY

A RAY ACOUSTICS APPROACH

Proefschrift

ter verkrijging van de graad van doctor
aan de Technische Universiteit Delft,
op gezag van de Rector Magnificus Prof. dr. ir. T. H. J. J. van der Hagen,
voorzitter van het College voor Promoties,
in het openbaar te verdedigen op maandag 18 September 2023 om om 17:30 uur

door

Furkat YUNUS

Master of Science in Electromechanical Engineering
Free University of Brussels, België,
geboren te Xinjiang Uyghur Autonomous Region, China.

Dit proefschrift is goedgekeurd door de

Promotor: Prof. dr. D. Casalino

Copromotor: Dr. D. Ragni

Copromotor: Dr. F. Avallone

Samenstelling promotiecommissie:

Rector Magnificus,	voorzitter
Prof. dr. D. Casalino,	Technische Universiteit Delft, promotor
Dr. D. Ragni,	Technische Universiteit Delft, copromotor
Dr. F. Avallone,	Politecnico di Torino, Italy, copromotor

Onafhankelijke leden:

Prof. dr. ir. M. Snellen,	Technische Universiteit Delft
Dr. V. E. Ostashev,	University of Colorado Boulder, Verenigde Staten
Prof. dr. ir. C. Schram,	von Kármán Institute of Fluid Dynamics, België
Dr. S. Mancini ,	Airbus Defence and Space GmbH, Duitsland
Prof. dr. S. J. Watson,	Technische Universiteit Delft, reservelid



Keywords: Acoustic wave propagation, ray acoustics, aeroacoustics, aircraft community noise, urban air mobility noise

Printed by: Ridderprint

Front & Back: Illustration of eVTOL noise footprint in an urban area. Cover designed by Furkat Yunus.

Copyright © 2023 by F. Yunus

ISBN 000-00-0000-000-0

An electronic version of this dissertation is available at
<http://repository.tudelft.nl/>.

*To my wife, Hanife, and sons, Yusuf and Ilyas, your steadfast support propels my
academic journey.*

*To my parents and fellow Uyghurs living under the CCP regime, your strength and
endurance fuel my determination to strive for progress, even in the absence of knowledge
about your current circumstances.*

CONTENTS

Summary	xi
Samenvatting	xv
List of abbreviations	xix
1 Introduction	1
1.1 Aircraft-community-noise Challenges	2
1.2 Urban Air Mobility Noise	5
1.3 Aircraft-community-noise Prediction	6
1.4 Dissertation Objectives and Thesis Outline	9
References	14
2 Sound Propagation in Outdoor Environments	17
2.1 Sound Propagation in Outdoor Environments	18
2.1.1 long-range propagation around airports.	19
2.1.2 Sound propagation within an urban setting	20
2.2 Existing Numerical Methods	22
2.2.1 Wave-based methods	22
2.2.2 Geometrical Acoustics Methods	25
2.3 Propagation Modelling Using Ray Acoustics	30
2.3.1 Ray path tracing	30
2.3.2 Dynamic ray tracing	33
2.3.3 Gaussian beams and wavefield calculation.	36
References	38
3 Noise Source Prediction	47
3.1 High-fidelity Methods.	48
3.1.1 Computational Fluid Dynamics	48
3.1.2 Aeroacoustic predictions.	52
3.2 low-order Methods	56
3.2.1 Blade element momentum theory	56
3.2.2 Time-domain compact dipole/monopole FW-H formulation	58
3.2.3 Frequency-domain analytical formulation.	60
References	62
4 Low-order Aeroacoustic Permanence Calculation of Propellers	67
4.1 Objectives.	68
4.2 Overview of The Low-Order Approach	68
4.3 Low-Order Approach Validation	70
4.3.1 Case setup	70

4.3.2	Aerodynamic validation	72
4.3.3	Aeroacoustic validation	72
4.4	Acoustic Effects of Varying Advance Ratio and Number of Blades	78
4.4.1	The correlation between J and noise footprint	79
4.4.2	The correlation between NB and noise footprint	80
4.5	Concluding Remarks	83
	References	84
5	Atmospheric Effects in Aircraft-community-noise Predictions	85
5.1	Objectives.	86
5.2	Extension of the NHD to An Inhomogeneous Moving Atmosphere	86
5.3	Case Study	88
5.3.1	Validation	90
5.3.2	Results	92
5.4	Concluding Remarks	96
	References	96
6	Airborne Noise Propagation in A Non-turbulent Urban Environment	99
6.1	Objectives.	100
6.2	An Overview of The Computational Approach	100
6.2.1	Wavefield on the terrain surfaces.	102
6.3	Validation Case Study	104
6.3.1	Reference solution	104
6.3.2	Case setup	105
6.3.3	Validation	107
6.4	Concluding Remarks	109
	References	114
7	Urban Air Mobility Noise in A Vertiport Environment	117
7.1	Objectives.	118
7.2	An Overview of The Computational Approach	118
7.2.1	Noise sphere calculation	119
7.2.2	GBT-based noise footprint prediction	119
7.3	Validation and Verification	121
7.3.1	The spatial resolution of the noise sphere	121
7.3.2	Inclusion of complex source directivity into the acoustic footprint.	123
7.4	Case Study	124
7.4.1	Case setup	124
7.4.2	Results	126
7.5	Concluding Remarks	133
	References	134
8	Aircraft-community-noise Prediction in Outdoor Environments	137
8.1	Objectives.	138
8.2	An Overview of The Computational Approach	138
8.2.1	Broadband noise calculation.	139

8.3	Validation	140
8.4	Case Study	142
8.4.1	Noise source prediction	143
8.4.2	Terrain geometry and wind flow	143
8.4.3	Results	146
8.5	Concluding Remarks	147
	References	148
9	Conclusions and Recommendations	151
9.1	Summary and Conclusions	152
9.2	Recommendations for Future Work	155
A	Frequency domain tonal noise solver input file description	157
A.1	Input File	158
A.1.1	Propeller data	158
A.1.2	Atmosphere data	158
A.1.3	Receiver data	158
A.2	Output Files	159
	References	159
B	3D curved-ray tracer input file description	161
B.1	Atmosphere Model	161
B.1.1	Option 1000	161
B.1.2	Option 2000	161
B.1.3	Option 3000	162
C	UYGUR input file description	163
C.1	Input File	163
C.1.1	Atmosphere section	163
C.1.2	Source section	163
C.1.3	Terrain/Receiver section	165
C.2	Output Files	167
C.2.1	UYGUR.py	167
	List of Publications	169

SUMMARY

The demand for transportation has increased significantly over the years, leading to a rise in community noise pollution, with aircraft being identified as one of the primary sources. The rise of urban air mobility (UAM) vehicles as a new form of transportation has greatly increased noise concerns as they feature different operational characteristics than conventional aircraft and are anticipated to operate within an urban area. Hence, effectively and efficiently evaluating their noise footprint in urban areas, considering various design, operational, and environmental factors, is of paramount interest in further developing noise mitigation strategies. However, existing aircraft-community-noise (ACN) prediction methods often oversimplify or ignore all the factors mentioned above. To address this gap, this thesis proposes novel methodologies and algorithms to improve ACN predictions that incorporate these factors.

The study initially focuses on investigating the correlation between various design and operational parameters and the acoustic footprint over a large square area in a homogeneous propagation environment (Chapter 4). A novel computational framework, which includes a low-fidelity noise source prediction approach and a straight-ray propagator, is employed. Three cases that feature the acoustic effect of varying advance ratio and the number of blades in a steady, forward-flight condition are considered. The results show that the case with a higher advance ratio can alter the source directivity and lead to an increase of up to 30 dBA on the acoustic footprint compared to the one with a lower advance ratio. Additionally, increasing the blade count from 5 to 7 while keeping the advance ratio constant results in a variation of 16 dBA due to the change in the source directivity. Although the latter condition reduces each blade's loading and, consequently, the associated noise, the total noise remains unchanged due to the increasing thickness noise resulting from the lower advance ratio, high blade tip Mach number, and addition of extra blades. The study also finds that adding blades raises the frequencies generated, resulting in a slight increase in metrics such as A-weighted OASPL. The study shows that on-ground noise levels are more sensitive to the variation in the advance ratio than blade count. Specifically, increasing the advance ratio can substantially reduce on-ground noise levels. Alternatively, increasing the blade count can reduce on-ground noise levels if targeting tonal noise at higher harmonics.

The impact of atmospheric conditions on the propagation of aircraft noise over long distances is studied (Chapter 5). A new 3D point-to-point curved-ray tracing algorithm is developed to simulate the noise footprint of a UAM vehicle over flat terrain. The noise footprint is studied for a steady, level flight condition and two different weather conditions typical of summer days: clear day and clear night, each with varying wind velocities. It is shown that when the UAM vehicle is flown upwind, a refractive shadow zone appears. This shadow zone is more pronounced when the vehicle is farther from the receivers and becomes weaker or disappears entirely as the vehicle approaches the receivers. However, when the vehicle is flown downwind, no significant impact is observed

on the noise footprint for any of the weather conditions that are tested. Valuable insight into the ways in which atmospheric conditions can affect the long-range propagation of sound over flat ground is obtained. However, in a realistic urban environment, the ground is rarely flat, and irregular terrain topology can highly distort the weather profiles, hence, could significantly impact noise propagation when the source is closer to the receivers.

The effect of irregular terrain and weather profiles on sound propagation in urban areas is investigated in this study (Chapter 6). An advanced ray-acoustics model is developed using the Gaussian beam tracing technique to account for 3D variations in air temperature and wind velocity distributions, as well as multiple reflections over uneven terrain surfaces. To improve accuracy, a semi-empirical formulation is derived and used to reduce truncation errors that occur when the Gaussian beam summation is applied to calculate wavefields on solid boundaries. The study evaluates the accuracy and efficiency of the developed Gaussian beam tracer by comparing its results against the finite element method (FEM) solutions of the convected wave equation. An airborne monopole source and an urban environment consisting of three building blocks and wind flow data obtained from high-fidelity CFD solutions are considered. It is found that the empirical formulation greatly reduces the truncation error in the beam summation. The presence of mean flow can cause strong refraction above building rooftops. Overall, the Gaussian beam tracer proved to be a reliable and computationally efficient tool for simulating high-frequency noise propagation in urban environments.

The Gaussian beam tracer has been extended to include complex source directivity in the presence of a moving medium to study the noise impact of UAM vehicles in a typical urban environment (Chapter 7). By coupling the Gaussian beam tracer with a low-fidelity noise source prediction approach, the study examines the impact of terrain geometry, source directivity, and wind flow on the noise footprint of an eVTOL hovering in a vertiport environment. The study reveals that building blocks increase on-ground noise levels by 5 dB in the illuminated zone due to multiple reflections, while also shielding the noise by creating shadow zones behind the buildings. Wind flow can significantly affect the acoustic footprint by changing the lobes of the pattern and intensifying the noise levels, with the effect becoming more pronounced at higher frequencies. Compared to the straight-ray propagator, the present approach reduces the prediction error and delivers a fast yet reliable methodology to evaluate eVTOL noise footprint in urban environments, aiding in the development of effective noise mitigation strategies.

Finally, the Gaussian beam tracer is further extended to enable computationally efficient broadband noise calculations. Range dependence of the terrain and weather data on the long-range acoustic propagation is studied by coupling the developed Gaussian beam tracer approach with a high-fidelity noise source prediction approach (Chapter 8). The noise footprint of a helicopter hovering over a mountain is calculated considering the 3D mean flow obtained from high-fidelity CFD simulations and terrain geometry extracted from the available geographic information system (GIS) database. The results show that, in a quiescent atmosphere, noise levels decrease drastically in the terrain shadow zone, while a variation of up to 15 dB in the illuminated zone is observed as a consequence of changes in source directivity. In the presence of mean flow, upward refraction occurs around the terrain shadow zone boundary, resulting in an overall en-

largement of the shadow zone and a variation of up to 35 dB in the noise footprint. This study provides valuable insights that can inform the design and operation of UAM vehicles to minimize noise impacts on communities near airports and other landing zones.

SAMENVATTING

De vraag naar transport is de afgelopen jaren aanzienlijk toegenomen, wat heeft geleid tot een toename van het gemeenschapslawaai. Vooral vliegtuigen worden geïdentificeerd als een van de belangrijkste bronnen van dit geluid. Nu er steeds meer voertuigen voor stedelijke luchtmobiliteit (UAM) op de markt komen, neemt de zorg over geluidsoverlast nog meer toe. Deze voertuigen hebben namelijk andere operationele kenmerken dan conventionele vliegtuigen en worden verwacht binnen een stedelijk gebied te opereren. Daarom is het van groot belang om hun geluidsbelasting effectief en efficiënt te evalueren in stedelijke gebieden, waarbij rekening wordt gehouden met diverse ontwerp-, operationele en milieufactoren. Het ontwikkelen van geluidsmitigatiestrategieën is daarbij cruciaal. Bestaande voorspellingsmethoden voor vliegtuig-gemeenschapslawaai (ACN) zijn echter vaak te simplistisch of negeren alle bovengenoemde factoren. Om deze lacune op te vullen, presenteert dit proefschrift nieuwe methodologieën en algoritmen die de ACN-voorspellingen verbeteren door deze factoren juist wel te incorporeren.

De studie richt zich aanvankelijk op het onderzoeken van de correlatie tussen diverse ontwerp- en operationele parameters en de akoestische voetafdruk over een groot vierkant gebied in een homogene propagatieomgeving (Hoofdstuk 4). Hiervoor wordt een nieuw computationeel raamwerk gebruikt dat bestaat uit een benadering voor geluidsbronvoorspelling met een lage nauwkeurigheid en een straight-ray propagator. Drie gevallen die het akoestische effect van variërende voortgangsverhouding en het aantal bladen onder een gestage, voorwaartse vluchtconditie omvatten, worden overwogen. De resultaten tonen aan dat het geval met een hogere voortgangsverhouding de bron directiviteit kan veranderen en leiden tot een toename van maximaal 30 dBA op de akoestische voetafdruk in vergelijking met het geval met een lagere voortgangsverhouding. Bovendien leidt het verhogen van het aantal bladen van 5 naar 7, terwijl de voortgangsverhouding constant blijft, tot een variatie van 16 dBA als gevolg van de verandering in de bron directiviteit. Hoewel deze laatste conditie de belasting van elke blade vermindert en dus de bijbehorende geluidsproductie, blijft het totale geluid ongewijzigd als gevolg van de toenemende dikte van het geluid als gevolg van de lagere voortgangsverhouding, hoge blade tip Mach-nummer en de toevoeging van extra bladen. De studie toont ook aan dat het toevoegen van bladen de gegenereerde frequenties verhoogt, wat resulteert in een lichte toename van de metriek zoals de A-gewogen OASPL. De studie toont aan dat on-ground geluidsniveaus gevoeliger zijn voor de variatie in voortgangsverhouding dan in het aantal bladen. Het verhogen van de voortgangsverhouding kan specifiek de on-ground geluidsniveaus aanzienlijk verminderen. Alternatief kan het verhogen van het aantal bladen on-ground geluidsniveaus verminderen als het gericht is op toonlawaai bij hogere harmonischen.

De impact van atmosferische omstandigheden op de propagatie van vliegtuigeluid over lange afstanden wordt bestudeerd (Hoofdstuk 5). Een nieuw 3D-punt-naar-

punt curved-ray tracing algoritme wordt ontwikkeld om het geluidsprofiel van een UAM-voertuig over vlak terrein te simuleren. Het geluidsprofiel wordt bestudeerd voor een steady, level flight conditie en twee verschillende weersomstandigheden die typerend zijn voor zomerdagen: heldere dag en heldere nacht, elk met variërende windsnelheden. Er wordt aangetoond dat wanneer het UAM-voertuig tegen de windrichting in vliegt, een refractieve schaduwzone ontstaat. Deze schaduwzone is meer uitgesproken wanneer het voertuig verder van de ontvangers vliegt en zwakker wordt of volledig verdwijnt naarmate het voertuig de ontvangers nadert. Echter, wanneer het voertuig met de windrichting mee vliegt, wordt er geen significante impact waargenomen op het geluidsprofiel voor een van de geteste weersomstandigheden. Waardevol inzicht in de manieren waarop atmosferische omstandigheden de geluidspropagatie over lange afstanden over vlak terrein kunnen beïnvloeden, wordt verkregen. Echter, in een realistische stedelijke omgeving is de grond zelden vlak en kan de onregelmatige terreintopologie de weersomstandigheden sterk verstoren, waardoor de geluidspropagatie aanzienlijk kan worden beïnvloed wanneer de bron dicht bij de ontvangers staat.

In dit onderzoek (Hoofdstuk 6) wordt het effect van onregelmatig terrein en weerprofielen op geluidspropagatie in stedelijke gebieden onderzocht. Hiervoor is een geavanceerd ray-acoustics model ontwikkeld met behulp van de Gaussian beam tracing techniek om 3D variaties in luchttemperatuur, windverdeling en reflecties over ongelijk terrein te verwerken. Om de nauwkeurigheid te verbeteren, is een semi-empirische formule afgeleid om de truncatiefouten te verminderen die optreden bij het berekenen van golfvelden op solide grenzen met behulp van de Gaussian beam sommatie. De nauwkeurigheid en efficiëntie van de ontwikkelde Gaussian beam tracer zijn geëvalueerd door de resultaten te vergelijken met de oplossingen van de convected wave equation met de finite element methode (FEM). Hierbij is gebruik gemaakt van een luchtgedragen monopool bron en een stedelijke omgeving bestaande uit drie gebouwenblokken met windstroomgegevens verkregen uit high-fidelity CFD-oplossingen. Er is vastgesteld dat de empirische formule de truncatiefouten in de beam sommatie aanzienlijk vermindert. De aanwezigheid van mean flow kan sterke refractie veroorzaken boven gebouwen. Over het algemeen bleek de Gaussian beam tracer een betrouwbaar en rekenkundig efficiënt instrument te zijn voor het simuleren van hoogfrequente geluidspropagatie in stedelijke omgevingen.

De Gaussian beam tracer is uitgebreid om complexe bronrichting in een bewegende medium te omvatten om de geluidsimpact van UAM-voertuigen in een typische stedelijke omgeving te bestuderen (Hoofdstuk 7). Door de Gaussian beam tracer te koppelen aan een low-fidelity voorspellingsmethode voor geluidsbronnen, onderzoekt de studie de impact van terreingeometrie, bronrichting en windstroming op de geluidszone van een eVTOL die zweeft in een vertiport omgeving. De studie onthult dat bouwblokken de grondgeluidsniveaus met 5 dB verhogen in de verlichte zone door meerdere reflecties, terwijl ze ook het geluid afschermen door schaduwzones achter de gebouwen te creëren. Windstroming kan de akoestische zone significant beïnvloeden door de lobben van het patroon te veranderen en de geluidsniveaus te intensiveren, waarbij het effect meer uitgesproken wordt bij hogere frequenties. Vergeleken met de straight-ray propagator vermindert de huidige benadering de voorspellingsfout en levert een snelle en betrouwbare methodologie om de eVTOL-geluidszone in stedelijke omgevingen te evalueren,

wat kan bijdragen aan de ontwikkeling van effectieve geluidsmitigatiestrategieën.

Ten slotte is de Gaussian beam tracer verder uitgebreid om computatief efficiënte breedbandgeluidsberekeningen mogelijk te maken. De bereikafhankelijkheid van de terrein- en weergegevens op de langeafstandsakoestische voortplanting wordt bestuurd door de ontwikkelde Gaussian beam tracer te koppelen aan een high-fidelity voor-spellingsmethode voor geluidsbronnen (Hoofdstuk 8). De geluidszone van een helikopter die over een berg zweeft, wordt berekend met behulp van de 3D-gemiddelde stroming verkregen uit high-fidelity CFD-simulaties en terreingeometrie uit het beschikbare geografische informatiesysteem (GIS)-database. De resultaten tonen aan dat in een rustige atmosfeer de geluidsniveaus drastisch afnemen in de terreinschaduwzone, terwijl een variatie tot 15 dB in de verlichte zone wordt waargenomen als gevolg van veranderingen in de bronrichting. In aanwezigheid van gemiddelde stroming treedt er boven de grens van de terreinschaduwzone opwaartse refractie op, wat resulteert in een algehele vergroting van de schaduwzone en een variatie tot 35 dB in de geluidszone. Deze studie biedt waardevolle inzichten die kunnen bijdragen aan het ontwerpen en bedienen van UAM-voertuigen om de geluidsimpact op gemeenschappen in de buurt van luchthavens en andere landing zones te minimaliseren.

LIST OF ABBREVIATIONS

ACN	aircraft community noise
BEM	boundary element method
BEMT	blade element momentum theory
BPF	blade passing frequency
BT	beam tracing
BTE	Boltzmann transport equation
CAA	computational aeroacoustics
CD	controlling dimension
CFD	computational fluid dynamics
CPU	central processing unit
DNC	direct numerical computation
DRT	dynamic ray tracing
eVTOL	electric vertical take-off and landing vehicle
FATO	final approach and take-off area
FTD	finite-difference time-domain
FEM	finite element method
FFP	fast field program
FW-H	Ffocws-Williams & Hawking acoustic analogy
GPU	graphic processing unit
GBT	Gaussian beam tracing
GA	geometrical acoustics
GIS	geographic information system
IS	image source
LBM	lattice-Boltzmann method

NHD	noise hemisphere/sphere database
OASPL	overall sound pressure level
PE	parabolic equation
PBT	paraxial beam tracing
PSTD	pseudo-spectral time domain
RA	ray acoustics
RPT	ray path tracing
RT	ray tracing
SPL	sound pressure level
SRT	straight ray tracing
SRTM	shuttle radar topography mission database
STL	standard triangle language
TLM	transmission line matrix
TLOF	touchdown and lift-off area
UAM	urban air mobility
VR	variable resolution
VLES	very-large eddy simulation

1

INTRODUCTION

*All of physics is either impossible or trivial.
It is impossible until you understand it, and then it becomes trivial.*

Ernest Rutherford

Aircraft noise has long been recognized as a major contributor to community noise pollution. With the advent of urban air mobility (UAM) vehicles, this problem is likely to become more pressing. UAM operations are expected to take place over densely populated residential areas, making it necessary to use low-noise aircraft and flight paths to reduce noise impact. However, existing aircraft-community-noise (ACN) prediction methods often overlook critical factors such as design, operation, weather, and terrain profiles, which can significantly affect the noise footprint. This chapter reviews existing ACN prediction techniques, highlights the motivations behind the research, and outlines the research objectives and dissertation structure.

SINCE the advent of the first airplane, the aviation industry has advanced rapidly, inspired by the need to minimize travel time and maximize travel distances and payload. Airplanes are most likely one of the noisiest machines humans have ever built. Furthermore, compared to other transportation vehicles, for equivalent noise levels, aviation noise is perceived as the most "annoying" [1], as indicated in Fig. 1.1. In addition to annoyance, more serious health-related issues, such as sleep disturbance [2, 3], cardiovascular diseases [4], and altered cognitive performance among children [5], were reported recently. The noise pollution also interferes with communication and outdoor activities, making it difficult for residents to enjoy their homes and communities.

To protect the health of residents around airports and reduce the noise impact on wildlife, the Environmental Noise Guidelines for the European Region (2018) recommended reducing aircraft noise levels to 45 dB L_{den} (day-evening-night-weighted sound pressure level) and 40 dB L_{night} (night-time equivalent continuous sound pressure level). Nevertheless, it has been reported that 47 major European airports have been responsible for exposing more than 2.5 million people to a noise level that is well above the recommended limit from the WHO [6].

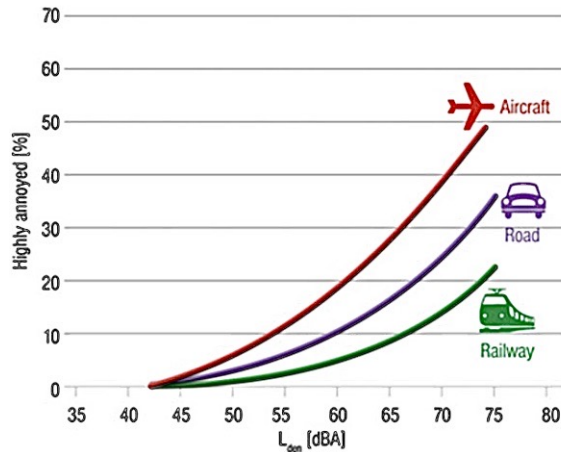


Figure 1.1: Comparison of annoyance due to transportation systems [1].

1.1.1. AIRCRAFT-COMMUNITY-NOISE CHALLENGES

In the aviation industry, aircraft design and manufacturing have long been driven by the need to meet mission requirements and achieve optimal aerodynamic performance. Historically, noise has not been a central consideration in the design and manufacturing of aircraft. However, in recent years, there has been a growing recognition of the impact of aircraft noise on local communities and the environment. Increased expectations for quality of life, along with a growing global focus on environmental protection, have led to a heightened concern about aircraft-community-noise (ACN). This has driven a renewed focus on reducing the impact of aircraft noise on communities and the environment. In response, the aviation industry is exploring new technologies, design concepts,

and operational procedures aimed at minimizing aircraft noise and mitigating its impact on local communities.

Over the years, advances in technology have led to the integration of noise reduction technologies into aircraft design, resulting in a significant reduction of aircraft noise levels (see Fig. 1.2.). In comparison to 60 years ago, communities today are exposed to significantly less noise from individual aircraft flights. At the aircraft noise source level, for instance, significant noise mitigation technologies have been developed. These technologies mainly focused on the reduction of engine noise and have been implemented into aircraft design continuously over the years. The present thesis focuses on methodologies to predict ACN; hence, aircraft noise reduction technology is beyond the scope of the current work.

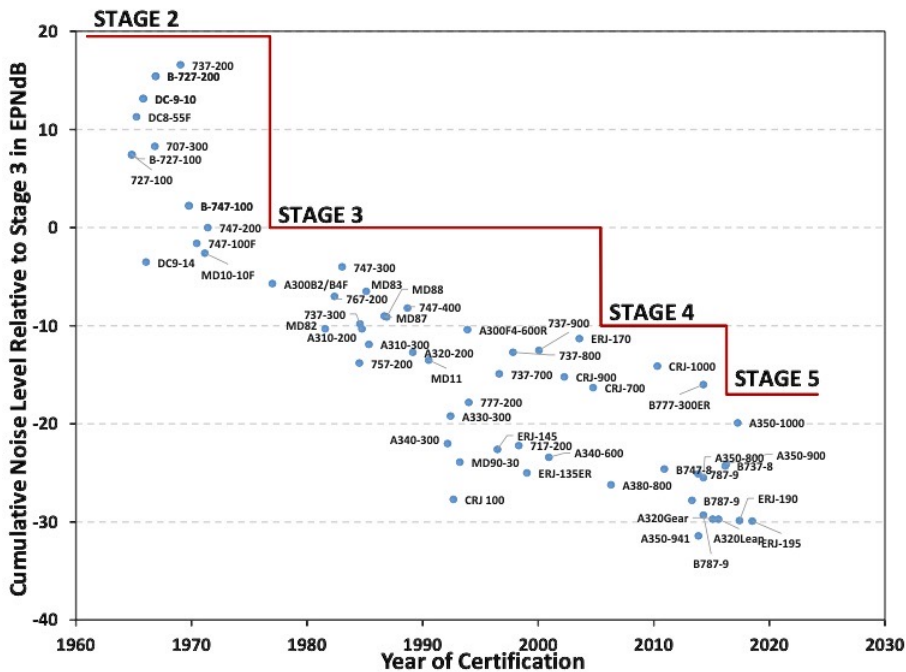


Figure 1.2: Commercial transport noise cumulative noise level reduction relative to stage 3 [7].

Although tremendous efforts have been put into aircraft noise mitigation at the source, communities around airports have still been exposed to aircraft noise. As a matter of fact, aircraft noise turned into a high-profile issue that demands the attention of experts in the aviation industry, airframe and engine manufacturers, airline operators, the general public, and health and occupational services.

Over the last few decades, regulations have been developed by the International Civil Aviation Organisation (ICAO) and other organizations to ensure the environment and public health protection [8, 9]. Those regulations are typically established based on noise contours (see Fig. 1.3) generated either by ACN prediction tools or statistical methods based on postal or online questionnaires [10]. Depending on the level of noise exposure

indicated on the noise contours, different measures can be taken. For example, insulation can be installed in living spaces such as homes, schools, and public buildings, or flight paths for takeoff and landing can be modified to avoid noise-sensitive areas like hospitals and schools. Most airports have implemented sophisticated instrumentation to monitor the noise produced by air traffic.

Despite these measures and regulations, communities around airports sometimes complain about unexpected annoyance. This is attributed to other acoustic and non-acoustic factors whose effects still need to be included in the above-mentioned regulations. For the acoustic factors, among others, temporal and spatial variations in wind velocity and temperature can significantly affect community noise depending on the complexity of the terrain topography, atmospheric inhomogeneities, and propagation distances. Neglecting or oversimplifying these factors in approach and landing trajectory planning can result in unexpected and highly annoying noise levels [11]. The non-acoustic factors are typically related to the cultural, socio-economic, psychological, and physical state of individuals' exposure to noise and may vary from no effect to severe annoyance [12]. Therefore, it is a significant challenge to fully comprehend, predict and characterize the noise exposure and noise impact on the community by dismantling the acoustical and non-acoustical factors. The present thesis focuses on two main acoustic factors that are directly related to the received noise levels: i) aircraft noise emission under varying flight and operational conditions; and ii) environmental factors such as spatial variations in wind velocity, air temperature distributions, and terrain topology in a 3D environment.

Furthermore, recent studies have also shown that community annoyance is strongly

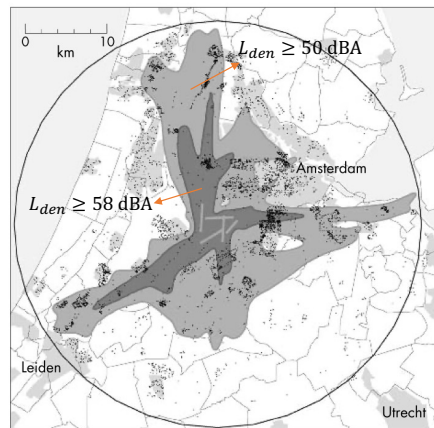


Figure 1.3: L_{den} noise contour for Amsterdam Schiphol airport (1996). The circle represents a distance of 25 kilometers around Schiphol. The dots show the residential locations of the respondents [10].

influenced not only by the maximum sound level but also by the number of flights [13]. It has been demonstrated that a specific level of annoyance can be generated by a low number of noisy aircraft or by a much higher number of flights characterized by a lower noise level [13]. According to the European Aviation Safety Agency (EASA) report, the

number of flights will increase by 42% between 2017 and 2040 under the basic traffic forecast, as shown in Fig. 1.4. This increase in air traffic further underlines the possible challenges in mitigating aircraft noise impact worldwide for the foreseeable and distant future despite major global events such as the COVID-19 pandemic. Any technological advancement in the aviation industry may likely contribute to further increased noise annoyance, especially the introduction of urban air mobility (UAM).

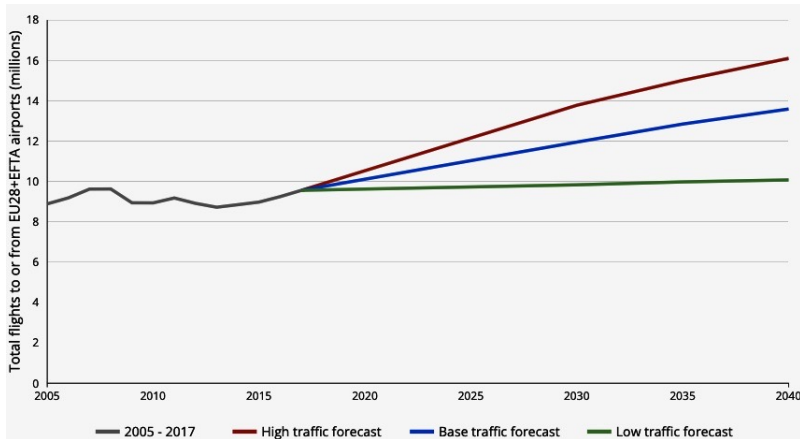


Figure 1.4: Number of flights increases by 42% between 2017 and 2040 under the base traffic forecast [6].

1.2. URBAN AIR MOBILITY NOISE

UAM represents a new opportunity for aviation that could revolutionize the urban transportation system by bringing it into the third dimension. Piloted and autonomously controlled UAM vehicles, such as electric vertical takeoff and landing (eVTOL) aircraft powered by propellers, are envisioned to fly numerous short missions at relatively low altitudes over densely populated residential areas. From noise generation mechanisms to noise footprint, the UAM noise is expected to be different from existing helicopters and general aviation aircraft and poses a unique challenge [7].

In terms of noise generation mechanisms, various interactions between the rotors and the airframe components can be expected. Those interactions include blade-vortex interaction (BVI), blade-airframe interaction (BAI), fuselage-wake interaction (FWI), and steady rotor loading, as illustrated in Fig. 1.5. Other noise sources can also be considered based on the vehicle configuration. For instance, rotor pairs in a coaxial configuration or in a side-by-side helicopter configuration can have rotor-rotor interference, whereas rotors installed in ducts will interfere with the support structures such as the shroud and other components. Due to these interactions and considering low operational altitude, broadband noise will be much more substantial for UAM vehicles than for conventional rotorcraft [7, 14, 15].

The operating environments of UAM aircraft will include vertiports connecting residential locations and airports to city centers, urban canyons, and densely populated areas. In a typical modern city environment, high-rise buildings and urban canyons highly

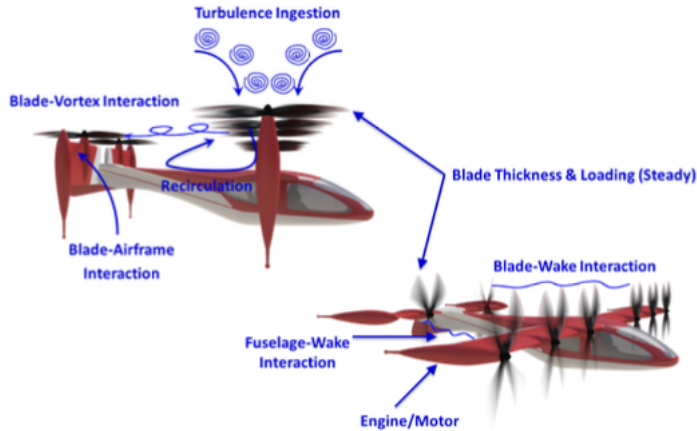


Figure 1.5: Some potential noise sources on a UAM vehicle [7].

affect the local wind and air temperature distribution, therefore, affecting UAM flight performance, sound emissions, and propagation, eventually altering perceived noise levels. Thus, a very complex noise propagation environment can be expected. Various aspects of noise propagation in a generic 3D environment will be outlined in Chapter 2.

1.3. AIRCRAFT-COMMUNITY-NOISE PREDICTION

There are two main approaches to evaluating the ACN. The first one is a direct noise computation (DNC) approach that solves the compressible Navier-Stokes (or Euler in those cases where viscosity is not important) or lattice-Boltzmann equations. Since these equations govern the total flowfield, including the acoustics, solving them in a domain that reaches out to the far field could provide the acoustic emissions, propagation, and the corresponding acoustic footprint at receiver points. In other words, DNC allows one to calculate the flowfield around the aircraft, noise emissions, propagation, and the noise footprint in a single simulation [16]. The DNC approach is, however, restricted to relatively low-frequency and short-range propagation problems as it is computationally demanding and could be unaffordable when the acoustic impact of high-frequency noise or large propagation distances are considered.

The second one adopts a hybrid approach that breaks down the whole computation procedure into the following three steps: source noise calculation, propagation, and noise footprint and metric calculation. In the source noise calculation step, the flow field around the vehicle is obtained by computational fluid dynamics (CFD) simulation and noise sources are sampled over a sphere/hemisphere surrounding the aircraft (see Fig. 1.6) by means of the Ffowcs Williams & Hawkins (FW-H) acoustic analogy¹. In the prop-

¹This step can also be performed by DNC. However, DNC can be computationally expensive and time-consuming. The FW-H acoustic analogy provides a simpler and faster way to estimate aircraft noise by relating it to the aerodynamic forces produced by the aircraft.

agation step, the noise signals are propagated from the noise sphere towards the ground receiver. Sound propagation can be depicted as straight rays in a uniform and stable atmosphere, and straight-ray-tracing can be used to propagate noise signals from the source to the ground receiver [17]. However, in realistic scenarios where sound travels over long distances, atmospheric refraction causes the rays to bend, making the straight-ray model incorrect. In these situations, wave-based methods, curved-ray-tracing, or beam-tracing techniques must be employed [18–24]. In the noise footprint and metric calculation step, noise footprint and corresponding metrics, such as A-weighted sound pressure level, effective perceived noise level (EPNL), etc., are calculated. These steps are illustrated in Fig. 1.6. More details on the first and second steps will be provided in Chapter 3 and Chapter 2, respectively.

The present thesis focuses on the hybrid approach. The hybrid approach has been

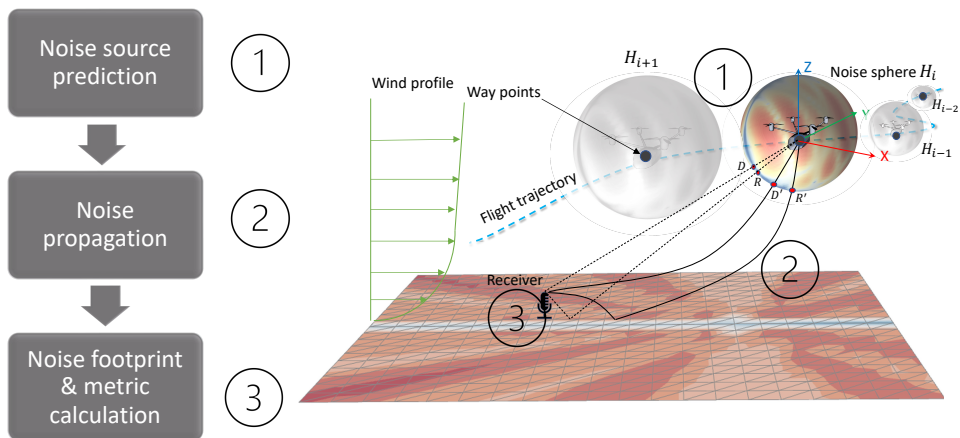


Figure 1.6: Steps of ACN prediction. H_i indicates a precomputed noise sphere corresponding to a specific flight and operating condition.

adopted by well known ACN prediction tools like the FAA Aviation Environmental Design Tool (AEDT) [25], NASA's second-generation Aircraft Noise Prediction Program (ANOPP2) [26] and *OptydB-FOOTPRINT* tool [17]. They typically incorporate all elements of ACN from source to the receiver with varying fidelity, including source noise definition for various flight and operating conditions, propagation, and noise certification metrics calculations at a set of prescribed ground-observer points. The inclusion of aircraft noise due to different flight and operating conditions is achieved by means of the noise-hemisphere/sphere-database (NHD) approach [27, 28, 28]. The approach involves pre-computing noise spheres for each combination of flight and operating parameters that cover the full flight envelope of a given flight mission profile. These precomputed results are then stored in a database, which can be used to quickly estimate noise signatures for specific flight and operating scenarios without the need for time-consuming simula-

tions. The NHD approach is particularly useful when assessing low-noise flight trajectories or when there is a need to quickly estimate on-ground noise levels while accounting for a wide range of flight and operating parameters. However, the accuracy of the results depends on the fidelity of the database and the complexity of the propagation medium. For more details on the NHD approach, readers can refer to Chapters 4 and 5.

In the hybrid approach, the main computational limitation in the noise source prediction comes from the calculation of noise spheres. High-fidelity CFD simulations [16] or experimental measurements [29] are typically used to calculate the noise spheres, but they can be expensive and time-consuming, particularly when designing and evaluating low-noise aircraft and flight mission profiles that involve thousands of noise spheres. Therefore, these methods are not suitable for coupling with a design optimization process that explores the acoustic effects of various environmental and operational parameters on noise footprints in an industrial context.

To minimize computational cost while maintaining a reasonable degree of accuracy, low-order methods such as blade element momentum theory (BEMT) coupled with an acoustic module have been used to estimate both tonal and broadband acoustic radiation [30–35]. Low-order methods are computationally efficient and can provide accurate results under certain conditions. Namely, these methods consider propellers as the primary noise sources and assume only steady loading without accounting for aerodynamic interactions between propellers and airframes. Nevertheless, their application has been limited to stationary sources and short propagation distances of a few times the rotor diameter [33–35]. Despite these limitations, low-order methods can still be applied to moving sources to examine the correlation between different design and operating parameters and their impact on the acoustic footprint over large areas. The present thesis adopts a low-order approach to explore the link between various designs, operating parameters, and noise footprints. More details of this approach will be given in Chapter 4.

After calculating the noise spheres, the next step is to propagate the noise to the ground receivers. The accuracy of this step can vary depending on the complexity of the propagation medium and the available computational resources. While more detailed methods can provide a higher level of accuracy, they require more computational power. For example, the fast field program (FFP) [36] can only account for stationary sources, a layered atmosphere, and a homogeneous ground surface. Methods based on the parabolic equation (PE) [37] are less accurate when considering moving sources, and they can be computationally demanding at high-frequency ranges. In contrast, methods based on the solution of wave equations using discretized versions of partial differential equations, such as finite element or finite difference methods, can include all properties of wave propagation, but they are computationally demanding and become prohibitively expensive when the source frequency or propagation range increases. While wave-based methods can provide highly accurate results, geometric acoustics methods such as ray tracing are often used to strike a balance between accuracy and computational efficiency in certain scenarios.

Straight-ray tracing techniques are often applied to propagate noise signals from the source to the ground receiver if a homogeneous, quiescent atmosphere and simple terrain geometries are considered. Most of the above-mentioned ACN prediction

tools adopt this approach. However, this approach does not account for atmospheric refraction causing sound rays to be curved and multiple reflections over irregular terrain surfaces. To overcome these limitations, curved ray tracers have been developed [21, 38]. However, they are limited to simplified weather profiles such as range-independent linear sound speed profiles, which can only account for refraction due to vertical variations in air temperature distribution. Furthermore, the intrinsic limitations of curved-ray tracings, such as singularities in shadow zones and caustic² regions [39, 40], called for further improvements. To address the singularity issue at the boundary of the shadow zone, a correction model was developed by Arntzen et al. [41]. Whereas, caustics can be neglected if the source-receiver distance is large enough and a weak refracting atmosphere³ is considered such that there are only two contributing rays, i.e., one direct ray and one ground reflected ray, to the pressure field at the receiver location [39]. Therefore, by employing the correction model for shadow zones and assuming only two contributing rays from the source to the receiver, a two-point 3D curved-ray tracing propagation model can be developed to propagate the noise signals properly from the source sphere to a set of receiver points in the presence of varying air temperature and wind velocity. More details of this propagation model will be outlined in Chapters 2 and 5.

As an alternative, Gaussian beam tracing (GBT), which has been widely used in seismology and ocean acoustics, has been adapted for atmospheric acoustic propagation by several authors [21, 23, 24]. The GBT approach can remove the singularities at the shadow boundary and caustic regions. The GBT method is preferred over curved-ray tracing if acoustic footprint over a vast area is considered as eigenrays connecting the source to the receiver are not need to be identified. However, the studies mentioned above are limited to analytical sound speed profiles. Furthermore, existing GBT tools for atmospheric acoustic prediction have been established based on GBT formulations for an inhomogeneous motionless medium⁴; hence, they cannot be employed for sound propagation in an inhomogeneous moving atmosphere. Therefore, there is a need to develop a GBT model that accounts for the acoustic effects of 3D varying terrain topology and atmospheric conditions on acoustic propagation. Terrain geometry can be extracted from an available geographic information system (GIS) database. At the same time, the 3D wind profile can be directly imported from CFD simulation, which could provide more realistic predictions and hence could improve the aircraft noise impact evaluation. More details of the GBT method for sound propagation in urban environment including wind flow will be given in Chapters 2 and 6.

1.4. DISSERTATION OBJECTIVES AND THESIS OUTLINE

Based on the reported studies, developing computationally efficient and robust methodologies to calculate source noise spheres for different flight trajectories and operating

²Caustics in ray acoustics refer to areas of concentrated sound energy that occur when multiple sound rays converge at a single point. Caustics are a result of the refraction of sound waves as they travel through an environment.

³A weak refracting atmosphere refers to an atmospheric environment in which the sound speed profile changes slowly with height. In this type of environment, sound waves experience only small amounts of refraction as they propagate through the atmosphere.

⁴A medium can be inhomogeneous due to 'regular' inhomogeneities, such as those associated with the range-dependent temperature profile.

conditions and including atmospheric and irregular terrain topology in the acoustic propagation are necessary to improve the ACN predictions for both conventional aircraft and UAM noise. The goals of the present research can be summarized in the following:

1. **To study the correlation between various design and operating parameters and acoustic footprint and identify trends to mitigate the noise impact.**
2. **To explore the link between vertical variation in air temperature and wind velocity profiles and noise footprint of a moving source with respect to the propagation range.**
3. **To develop a propagation model based on ray acoustics to be applied to sound propagation in urban areas and study the correlation between variations in terrain geometry, wind flow, and acoustic propagation.**
4. **To evaluate the noise distribution in a vertiport environment by exploring the correlation between variations in source directivity, vertiport geometry, wind flow, and the noise footprint distribution.**
5. **To study the impact of range-dependence of weather and terrain profiles on long-range noise propagation, and investigate the resulting changes in the noise footprint distribution.**

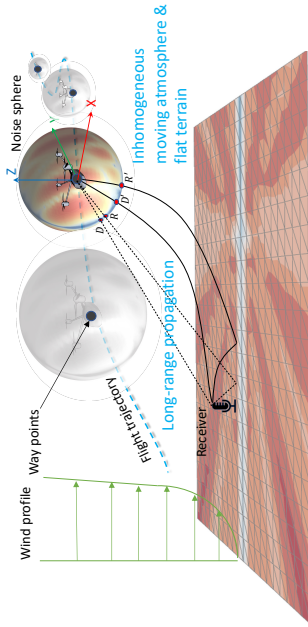
To achieve the aforementioned objectives, this dissertation is divided into chapters as follows, with a graphical outline of the chapters provided in Fig. 1.7.

- **Chapter 2** reports a literature review on the fundamentals of sound propagation in an outdoor environment: short-range propagation within an urban area and long-range propagation around an airport. It includes a review of the state of the art of noise propagation tools and a description of propagation modeling using ray acoustics for an inhomogeneous moving medium, which is necessary to achieve the goals mentioned above.
- **Chapter 3** presents two approaches for calculating the noise sources: a high-fidelity approach using the lattice-Boltzmann method (LBM), and a low-order approach using the BEMT coupled with a time-domain compact monopole/dipole FW-H analogy and a frequency-domain analytical formulation. The LBM is used to predict both the noise source and wind flow distribution in urban and rural environments. The chapter provides an overview of these methods and their limitations.
- **Chapter 4** presents a low-order methodology for evaluating propeller-driven aircraft noise footprint quickly while considering various design and operating parameters. The methodology uses a straight-ray propagator to propagate noise signals from the source sphere towards ground receivers. The results demonstrate that the low-order approach offers a reliable and speedy evaluation of the aircraft noise impact for different design and operational parameters, aiding in identifying trends to minimize noise impact.

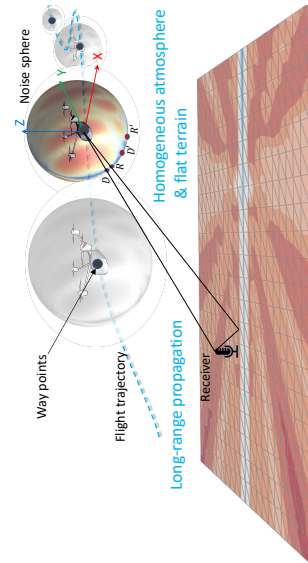
- **Chapter 5** reports the development and application of a two-point 3D curved-ray tracer for ACN prediction under various weather conditions over flat terrain. Through numerical simulations, it is shown that weather conditions have a significant impact on noise propagation if receivers are at a distant location, and weather effects disappear if the source approaches the receiver. Based on the results obtained from flat terrain simulations, it is hypothesized that in an urban environment, the irregularity of the terrain topology could lead to different trends of weather effects on noise propagation than those observed over flat terrain.
- **Chapter 6** describes the development and validation of a noise propagation model using the GBT method, which takes into account the effects of complex 3D terrain and weather conditions in non-turbulent urban environments. The validation studies show that the GBT approach has acceptable accuracy compared to the more computationally expensive full-wave solutions, while providing significant advantages in terms of computational efficiency. The results highlight the significant impact of range-dependent weather and terrain profiles on noise propagation, even when the source is located closer to the receivers. This finding supports the hypothesis proposed in the previous chapter that weather conditions should be considered even if the source is close to the receivers, as long as the terrain is not flat.
- **Chapter 7** builds upon the GBT approach developed in Chapter 6 to predict the noise footprints of an eVTOL vehicle in a realistic urban area. The GBT method is extended to include complex source directivity and coupled with a low-order noise source prediction method for efficient evaluation of noise impact under varying conditions. Results show that the presence of buildings increases on-ground noise levels by 5 dB in the illuminated zone due to multiple reflections, and create shadow zones that shield the incoming sound field. This shielding effect increases with frequency in a quiescent atmosphere. Differences in source directivity between the first and second harmonics of the blade passing frequency result in up to 40 dB differences in the noise footprint. Wind flow contributes to significant variations in the acoustic footprint, intensifying noise levels and changing the lobes of the footprint pattern, with these variations increasing with frequency.
- **Chapter 8** further extends the GBT approach to account for broadband noise calculation and applies it to study the impacts of range-dependence of weather and terrain profiles on long-range noise propagation. A higher-fidelity workflow is proposed, in which high-fidelity CFD simulations predict noise sources and wind flow, while terrain geometry is extracted from a GIS database. The study focuses on the noise footprints of a helicopter hovering over mountainous terrain. The results show that, in a still atmosphere, noise levels decrease significantly in the terrain shadow zone, with up to 15 dB variation in the illuminated zone due to changes in source directivity. In the presence of mean flow, upward refraction occurs at the terrain shadow zone boundary, leading to an overall enlargement of the shadow zone and up to 35 dB variation in the noise footprint. This study provides valuable insights that can inform the design and operation of UAM vehicles and conven-

tional aircraft to reduce noise impacts on communities near airports and landing zones.

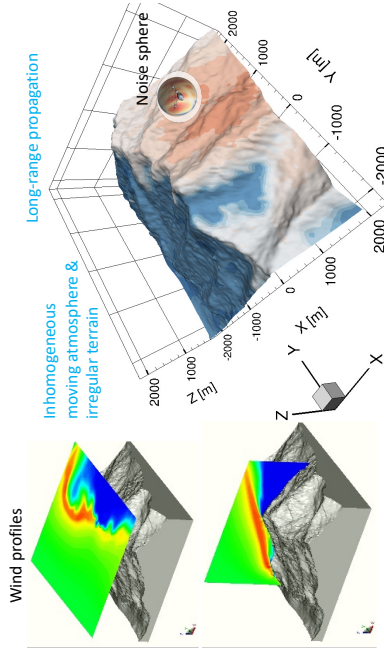
- **Chapter 9** concludes this dissertation by highlighting the key findings from the previous chapters. This is followed by several recommendations that encourage new ideas and plans for future investigation.



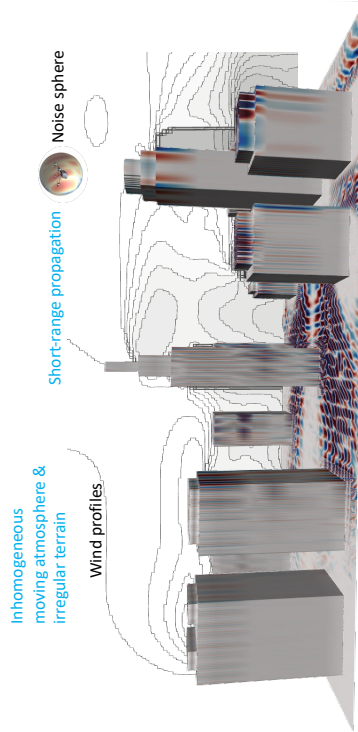
Chapter 5



Chapter 4



Chapter 8



Chapter 6-7

Figure 1.7: Graphical outline of the thesis.

REFERENCES

- [1] D. Gély and F. Márki, *Understanding the basics of aviation noise*, in *Aviation Noise Impact Management* (Springer, Cham, 2022) pp. 1–9.
- [2] M. Basner and S. McGuire, *WHO environmental noise guidelines for the european region: a systematic review on environmental noise and effects on sleep*, *International journal of environmental research and public health* **15**, 519 (2018).
- [3] A.-M. Nassur, M. Lefèvre, B. Laumon, D. Léger, and A.-S. Evrard, *Aircraft noise exposure and subjective sleep quality: the results of the débats study in france*, *Behavioral sleep medicine* **17**, 502 (2019).
- [4] E. Van Kempen, M. Casas, G. Pershagen, and M. Foraster, *WHO environmental noise guidelines for the european region: a systematic review on environmental noise and cardiovascular and metabolic effects: a summary*, *International journal of environmental research and public health* **15**, 379 (2018).
- [5] A.-S. Evrard, L. Bouaoun, P. Champelovier, J. Lambert, and B. Laumon, *Does exposure to aircraft noise increase the mortality from cardiovascular disease in the population living in the vicinity of airports? results of an ecological study in france*, *NOISE HEALTH* **17**, 328 (2015).
- [6] EASA, *European aviation environmental report*, (2019).
- [7] S. A. Rizzi, D. L. Huff, D. D. Boyd, P. Bent, B. S. Henderson, K. A. Pascioni, D. C. Sargent, D. L. Josephson, M. Marsan, H. B. He, *et al.*, *Urban air mobility noise: Current practice, gaps, and recommendations*, Tech. Rep. (2020).
- [8] ICAO, *Annex 16 - environmental protection - volume I - aircraft noise*, (2014).
- [9] ICAO, *Annex 16 — environmental protection volume II — aircraft engine emissions*, (2017).
- [10] E. Franssen, C. Van Wiechen, N. Nagelkerke, and E. Lebret, *Aircraft noise around a large international airport and its impact on general health and medication use*, *J. Occup. Environ.* **61**, 405 (2004).
- [11] M. Basner, C. Clark, A. Hansell, J. I. Hileman, S. Janssen, K. Shepherd, and V. Sparrow, *Aviation noise impacts: state of the science*, *NOISE HEALTH* **19**, 41 (2017).
- [12] O. Zaporozhets, *Balanced approach to aircraft noise management*, in *Aviation Noise Impact Management* (Springer, Cham, 2022) pp. 29–56.
- [13] N. Gualandi and L. Mantecchini, *Aircraft noise pollution: a model of interaction between airports and local communities*, *Int. J. Mech. Sci.* **2**, 137 (2008).
- [14] S. Lee *et al.*, *Prediction of urban air mobility multirotor VTOL broadband noise using ucd-quietfly*, *J. Am. Helicopter Soc.* **66**, 1 (2021).

- [15] Z. H. Jia and S. Lee, *Computational study on noise of urban air mobility quadrotor aircraft*, *J. Am. Helicopter Soc.* **67**, 1 (2022).
- [16] D. Casalino, W. C. van der Velden, G. Romani, and I. Gonzalez-Martino, *Aeroacoustic analysis of urban air operations using the lb/vles method*, in *25th AIAA/CEAS Aeroacoustics Conference* (2019) p. 2662.
- [17] D. Casalino, W. C. van der Velden, and G. Romani, *Community noise of urban air transportation vehicles*, in *AIAA Scitech 2019 Forum* (2019) p. 1834.
- [18] E. M. Salomons, *Computational Atmospheric Acoustics* (Springer Science & Business Media, 2001).
- [19] J. S. Lamancusa and P. A. Daroux, *Ray tracing in a moving medium with two-dimensional sound speed variation and application to sound propagation over terrain discontinuities*. *J. Acoust. Soc. Am.* **93**, 1716 (1993).
- [20] V. E. Ostashev and D. K. Wilson, *Acoustics in moving inhomogeneous media*, 2nd ed. (CRC Press, 2015).
- [21] Q. Mo, H. Yeh, M. Lin, and D. Manocha, *Outdoor sound propagation with analytic ray curve tracer and Gaussian beam*, *J. Acoust. Soc. Am.* **141**, 2289 (2017).
- [22] M. B. Porter and H. P. Bucker, *Gaussian beam tracing for computing ocean acoustic fields*, *J. Acoust. Soc. Am.* **82**, 1349 (1987).
- [23] Y. Gabillet, H. Schroeder, G. A. Daigle, and A. L'Espérance, *Application of the Gaussian beam approach to sound propagation in the atmosphere: Theory and experiments*, *J. Acoust. Soc. Am.* **93**, 3105 (1993).
- [24] H. Bian, R. Fattah, S. Zhong, and X. Zhang, *An efficient rectilinear Gaussian beam tracing method for sound propagation modelling in a non-turbulent medium*, *J. Acoust. Soc. Am.* **148**, 4037 (2020).
- [25] C. Lee, T. Thrasher, E. R. Boeker, R. S. Downs, S. Gorshkov, A. J. Hansen, S. Hwang, J. Koopmann, A. Malwitz, G. J. Noel, *et al.*, *Aviation Environmental Design Tool (AEDT): Technical Manual, Version 3b*, Tech. Rep. (United States. Department of Transportation. Federal Aviation Administration, 2019).
- [26] L. Lopes and C. Burley, *ANOPP2 User's Manual: Version 1.2*, Tech. Rep. (2016).
- [27] M. J. Lucas and M. A. Marcolini, *Rotorcraft noise model*, *J. Acoust. Soc. Am.* **101**, 3188 (1997).
- [28] M. Gennaretti, J. Serafini, G. Bernardini, A. Castorrini, G. De Matteis, and G. Avanzini, *Numerical characterization of helicopter noise hemispheres*, *Aerospace Science and Technology* **52**, 18 (2016).
- [29] E. Greenwood, *Fundamental Rotorcraft Acoustic Modelling From Experiments (FRAME)*, *Ph.D. dissertation*, University of Maryland, Maryland, USA (2011).

- 1
- [30] C. Nana, J.-M. Moschetta, E. Bénard, S. Prothin, and T. Jardin, *Experimental and numerical analysis of quiet mav rotors*, in *50th 3AF international conference on applied aerodynamics* (2015).
 - [31] N. S. Zawodny, D. D. Boyd Jr, and C. L. Burley, *Acoustic characterization and prediction of representative, small-scale rotary-wing unmanned aircraft system components*, in *Proceedings of 72nd American Helicopter Society International Annual Forum* (2016).
 - [32] R. Serré, N. Gourdain, T. Jardin, A. Sabaté López, V. Sujjur Balamraja, S. Belliot, M. C. Jacob, and J.-M. Moschetta, *Aerodynamic and acoustic analysis of an optimized low Reynolds number rotor*, in *International Symposium on Transport Phenomena and Dynamics of Rotating Machinery* (2017).
 - [33] K. Pascioni and S. A. Rizzi, *Tonal noise prediction of a distributed propulsion unmanned aerial vehicle*, in *2018 AIAA/CEAS Aeroacoustics Conference* (2018) p. 2951.
 - [34] M. T. Kotwicz Herniczek, D. Feszty, S.-A. Meslioui, J. Park, and F. Nitzsche, *Evaluation of acoustic frequency methods for the prediction of propeller noise*, *AIAA Journal* **57**, 2465 (2019).
 - [35] D. Casalino, E. Grande, G. Romani, D. Ragni, and F. Avallone, *Definition of a benchmark for low reynolds number propeller aeroacoustics*, *Aerospace Science and Technology* **113**, 106707 (2021).
 - [36] S. J. Franke and S. G. W., *A brief tutorial on the fast field program (ffp) as applied to sound propagation in the air*, *Appl. Acoust.* **27**, 203 (1989).
 - [37] K. E. Gilbert and M. J. White, *Application of the parabolic equation to sound propagation in a refracting atmosphere*, *J. Acoust. Soc. Am.* **85**, 630 (1989).
 - [38] Q. Mo, H. Yeh, and D. Manocha, *Tracing analytic ray curves for light and sound propagation in non-linear media*, *IEEE transactions on visualization and computer graphics* **22**, 2493 (2015).
 - [39] E. M. Salomons, *Computational atmospheric acoustics* (Springer Science & Business Media, 2001).
 - [40] V. E. Ostashev and D. K. Wilson, *Acoustics in moving inhomogeneous media* (CRC Press, 2015).
 - [41] M. Arntzen, S. Rizzi, D. Simons, and H. Visser, *A framework for simulation of aircraft flyover noise through a non-standard atmosphere*, in *18th AIAA/CEAS Aeroacoustics Conference (33rd AIAA Aeroacoustics Conference)* (2012) <https://arc.aiaa.org/doi/pdf/10.2514/6.2012-2079> .

2

SOUND PROPAGATION IN OUTDOOR ENVIRONMENTS

*The highest activity a human being can attain is learning for understanding,
because to understand is to be free.*

Baruch Spinoza

This chapter presents a comprehensive overview of sound propagation in outdoor environments, specifically short-range propagation within an urban area and long-range propagation around an airport. It surveys the current state of the art in noise propagation tools, with a particular focus on propagation modeling using ray acoustics and the consideration of atmospheric and ground effects on sound propagation. Additionally, a detailed theoretical framework for Gaussian beam tracing in inhomogeneous moving atmospheres is presented.

Parts of this chapter have been published in Yunus et al. [1]

2.1. SOUND PROPAGATION IN OUTDOOR ENVIRONMENTS

IN a typical outdoor environment, sound propagation is affected by atmospheric and ground conditions. The former is responsible for refraction, convection, and scattering by atmospheric turbulence, while the latter causes multiple reflections, diffractions, and sound absorption due to the finite impedance of the terrain surface.

Considering atmospheric effects, the refraction, i.e., the bending of the propagation paths by wind and temperature gradients, directs the sound energy into certain regions, as illustrated in Fig. 2.1. When wind speed increases with altitude, sound propagating downwind is refracted downward. Near the ground, this downward refraction can combine with ground reflections to create a duct, allowing acoustic waves to propagate in a waveguide instead of radiating in other directions. If the ground surface has a high reflection coefficient (i.e., it behaves like an acoustically rigid wall), sound can travel long distances with little loss. On the other hand, when sound propagates upwind, it refracts upward¹. A refractive shadow zone, characterized by very low sound levels, may appear, as indicated in Fig. 2.1. On the other hand, random fluctuations of wind velocity and temperature due to atmospheric turbulent motion result in scattering of acoustic energy into the shadow zones (insonification) and coherence loss of the propagated noise signals [2, 3]. Considering insonification and coherence loss of the noise signals due to atmospheric turbulence requires an additional level of sophistication in the prediction methods, which is not considered in this thesis.

When sound interacts with terrain boundaries, a portion of its energy is reflected, while the remaining energy is transmitted through the surface. The extent of transmission is contingent upon the impedance of the terrain's surface. Certain types of vegetation and grass absorb sound efficiently, while surfaces like rigid building walls or ice-covered ground act as nearly perfect reflectors [4]. In the present study, perfect reflectors are assumed for the terrain surfaces, so sound absorption by the terrain surface is not taken into consideration.

Obstacles such as buildings, hills, and mountains cause multiple reflections in the illuminated zone where sound reaches directly, depending on the complexity of the obstacle's topology. Meanwhile, a terrain shadow zone is formed on the opposite side of those obstacles with respect to the source location, as shown in Fig. 2.1. Depending on the wind velocity and temperature gradients, the terrain shadow zone may enlarge or contract [5]. If the acoustic wavelength is comparable to or larger than the characteristic length of the obstacle, sound waves diffract into the terrain shadow zone through the edges of the building and raise noise levels there.

Although atmospheric and ground conditions have a continuous effect on sound propagation, their cumulative impact increases with distance from the source. For large propagation distances, the atmospheric conditions become a dominant factor, while for short propagation distances over flat terrain, the effect of atmospheric condition can be neglected [6]. However, if the terrain is non-flat, its irregularity affects the wind and temperature distribution, eventually impacting sound propagation. For instance, the wind significantly affects noise propagation in an urban environment, although the propagation distance is not large [7, 8].

¹This condition results from a decrease in the phase velocity of sound waves. As the wavefronts bend towards the direction of lower phase velocity, the sound wave refracts upward.

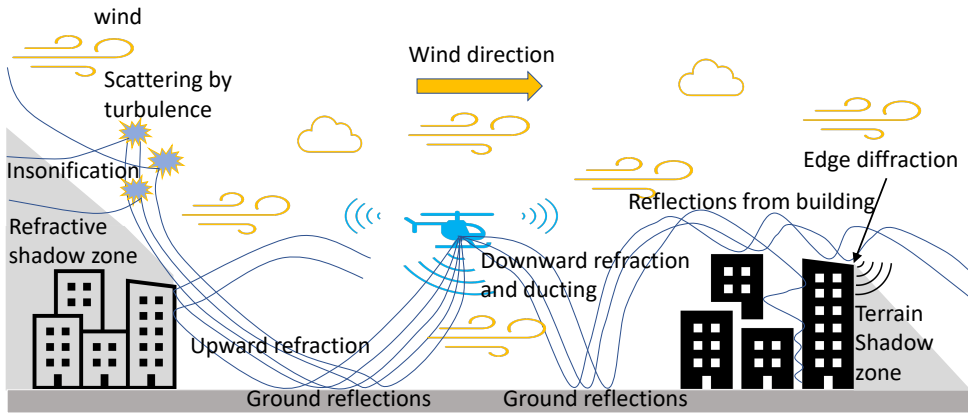


Figure 2.1: An illustration of outdoor sound propagation.

2.1.1. LONG-RANGE PROPAGATION AROUND AIRPORTS

Aircraft flyovers around airports are seen as a moving sound source with long-range propagation that is affected by range-dependent weather and ground conditions that significantly impact the received noise levels. In this case, the aircraft can be considered as a point source with all the acoustic sources concentrated on the airplane's center of gravity [9]. For approaching airplanes, in particular, the propagation from the sources to the receiver takes place over long distances (up to several km). During propagation over long distances, the acoustic waves travel through layers of the atmosphere and are affected by local changes in density, pressure, relative humidity, air temperature, and wind velocity. Consequently, the energy of sound waves is dispersed and absorbed by the atmosphere, reducing their magnitude. This reduction can be greater for higher-frequency sound waves, which are more susceptible to absorption and dispersion [3]. As a result, low-frequency noise can be more dominant in received noise levels after long-range propagation.

On the other hand, terrain topology plays a significant role in the propagation of aircraft noise as it reflects, absorbs or scatters the acoustic waves. For example, flat terrain allows noise to travel further, while mountainous terrain reflects and trap sound, leading to increased levels in nearby valleys. Additionally, the presence of buildings, trees, and other obstacles also affect aircraft noise propagation by scattering or absorbing the sound waves. Understanding the effects of terrain topology on aircraft noise propagation is essential in developing low-noise flight trajectories and reducing the impact of aircraft noise on communities.

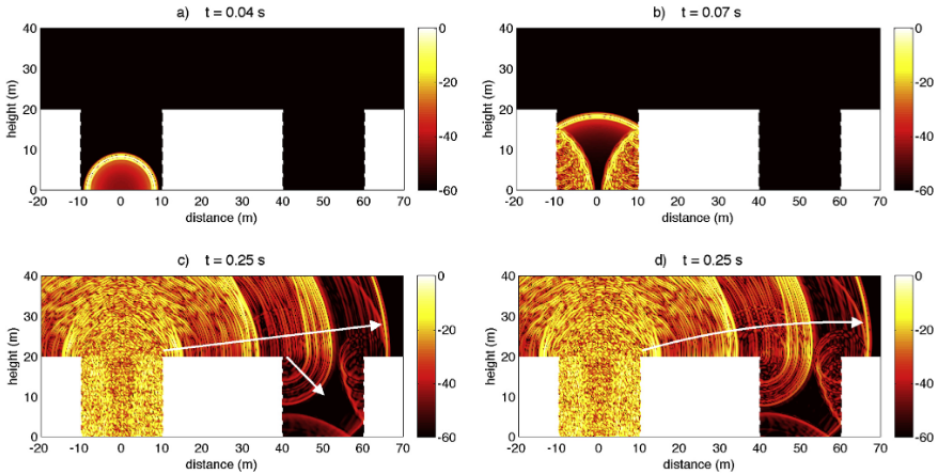


Figure 2.2: Snapshots of wave propagation in a city canyon, with levels expressed in dB relative to the maximum sound pressure level, adapted from [4].

2.1.2. SOUND PROPAGATION WITHIN AN URBAN SETTING

The propagation of sound in urban environments has been extensively studied in the context of road-based vehicles [4, 7, 8], where the source is in close proximity to the receivers. In an urban setting, the presence of buildings, trees, and other obstacles can have a significant impact on sound propagation [4], leading to various phenomena that occur when sound propagates within the urban area. For instance, multiple reflections between building blocks, diffraction at the edge of the buildings, refraction, and propagation scenarios, such as standing waves with large amplitude oscillations in narrow urban canyons, also known as the canyon effect, and scattering by building-induced turbulence, can be expected. These sound propagation phenomena are illustrated in Fig. 2.2 and briefly outlined in the following.

- Multiple reflections occur in an urban setting as acoustic waves encounter obstacles such as buildings, trees, and other surfaces and are reflected back into the environment (see Fig. 2.2(b)). As a result, sound waves can bounce multiple times between buildings and other obstacles before they reach the ground, leading to complex and dynamic patterns of sound propagation. Multiple reflections can have a significant impact on the magnitude and distribution of sound in urban areas, particularly in densely built-up areas where buildings are closely spaced [10]. This can result in increased noise levels in the illuminated zone, where direct sound rays can reach, and reduced levels in the building shadow zone where no direct sound ray is present [10]. The complex arrangement of buildings and other structures in an urban setting can cause sound waves to reflect and interfere with each other, leading to strong interference and even the formation of standing waves² between narrow urban canyons [11]. Various factors, including the frequency of the sound, the size, and shape of urban canyons, weather conditions,

²Standing waves are a type of wave that occurs when two waves of the same frequency and amplitude travel in

and the presence of other noise sources, influence the occurrence and impact of standing waves in urban settings.

The effects of multiple reflections on sound propagation in urban areas can be difficult to predict and model, as they are influenced by a variety of factors, including the shape and orientation of buildings, the presence of vegetation, and the frequency and direction of the noise source. However, in order to improve the evaluation of noise impact, it is essential to include multiple reflection effects when predicting the propagation of airborne noise in urban environments.

- Diffraction occurs when sound waves interact obstacle, such as a building or a wall, causing them to diffract or bend around the edge of the obstacle. Diffraction causes sound waves to reach areas that would otherwise be sheltered from the noise source as indicated by the lower arrow in Fig. 2.2(c), leading to complex patterns of sound propagation. Diffraction affects the magnitude and distribution of sound in urban areas, and the amount of diffraction that occurs depends on the size of the obstacle relative to the wavelength of the sound wave, as well as the position of the noise source [7]. Understanding the effects of diffraction on sound propagation in urban areas is crucial to developing effective noise abatement strategies, such as installing noise barriers and designing buildings to reduce residents' exposure to noise pollution from various sources.
- In urban areas, changes in wind velocity and air temperature cause sound to bend, i.e., refract, and reach areas that would typically be shielded from the noise source. The variations in wind velocity and temperature significantly affect the amount of refraction, which, in turn, increases the exposure of residents to aircraft noise. Wind also transports sound energy over long distances, further amplifying the noise exposure for residents. For UAM noise, where the noise source is situated above building rooftops, the refraction effects can be more substantial due to the large wind speed gradients above the roof level (See curved arrow indicated in Fig. 2.2(d)). Furthermore, buildings cause turbulence in airflow, resulting in eddies and disturbances that scatter and reflect sound waves in different directions, altering the received sound levels in various areas. Factors affecting building-induced turbulence on sound propagation include building size, shape, height relative to the sound source, and wind direction. Understanding how wind velocity and temperature variations impact sound propagation in urban areas is crucial for developing effective noise abatement strategies such as noise barriers, building design, and flight corridor planning for UAM operations to minimize aircraft noise exposure.

Simulating noise propagation in an outdoor environment is a complex task that requires consideration of many factors, including terrain geometry, and wind velocity, among others. To meet the diverse requirements of various applications, different numerical methods have been developed over the years, with varying levels of accuracy and computational efficiency. These methods can be broadly classified into two categories: wave-based methods and geometrical acoustics (GA) or ray acoustics (RA) methods. These

opposite directions and interfere with each other. The result of this interference is a wave pattern that appears to be stationary, hence the name "standing wave."

methods are briefly outlined, and their limitations and advantages are highlighted in the following section.

2.2. EXISTING NUMERICAL METHODS

2.2.1. WAVE-BASED METHODS

To simulate sound propagation in outdoor environments, wave-based methods solve the wave equation either in its full form, such as the finite element method (FEM), boundary element method (BEM), and finite-difference time-domain (FDTD) method, or a simplified form such as pseudo-spectral time domain (PSTD) method, transmission line matrix (TLM), the parabolic equation (PE) and the fast field program (FFP). By solving the wave equation, these methods provide a mathematical framework to describe wave behavior and predict phenomena such as interactions with objects and boundaries in the environment. This allows for a simulation of sound propagation in complex environments.

FINITE ELEMENT METHOD

FEM typically solves the discretized versions of the wave equation to determine the behavior of sound waves as they propagate through the environment, taking into account factors such as reflection, refraction, and diffraction. FEM can be used to model complex geometries and materials, making it a useful tool for predicting sound propagation in challenging outdoor environments. This method can provide detailed information about the behavior of sound waves, including the distribution of sound pressure and particle velocity, and can be used to study the effects of different environmental factors on sound propagation. The FEM has been used to include the effect of inhomogeneity of the media and flow effects [12–16] on the sound propagation and to estimate the insertion loss of a noise barrier in a city environment [17], and to simulate helicopter noise in a complex urban setting [18]. However, FEM requires extensive spatial grid resolution to resolve acoustic waves. Therefore, they are computationally demanding and could be unaffordable when the acoustic impact of high-frequency noise or large propagation distances are considered.

BOUNDARY ELEMENT METHOD

BEM is a well-known wave-based method that is applied mainly to surface scattering problems, whereas FEM is employed for volume scattering problems [19]. Compared to FEM, BEM is computationally more efficient for simulating sound propagation in outdoor environments because it only requires discretization of the surfaces. It can also handle complex geometrical configurations, but the computational cost is significant [20]. BEM is limited to homogeneous, quiescent media as it does not account for refraction. However, refraction effects can be included if it is coupled with a specialized Green function for the refractive media [21]. However, this method is restricted to media described by only a positive constant sound-speed gradient, thus, can not account for refraction due to more realistic profiles. In addition, the computational cost is still considerably large for 3D simulation [20].

FINITE-DIFFERENCE, TIME-DOMAIN METHOD

The FDTD method has been used for simulating outdoor sound propagation, accounting for atmospheric refraction due to wind variation [22, 23] and different ground conditions with varying terrain topology [24–27]. The algorithm uses a finite difference scheme to calculate the spatial derivatives and temporal evolution by time stepping, allowing for direct computation and visualization of the sound pressure field in discrete time steps [28]. This method solves coupled first-order partial differential equations, such as the complete set of linearized equations of fluid dynamics [2]. To improve computational efficiency and avoid redundant computation of ambient pressure and entropy, Ostashev et al. [29, 30] simplified the original set of linearized equations of fluid dynamics in a moving inhomogeneous medium. Blumrich et al. [22] investigated the influence of terrain topography with varying ground impedance and the state of the atmosphere on outdoor sound propagation using the FDTD method. However, the FDTD method has some limitations, such as the requirement for high spatial and temporal resolution to achieve accurate results for longer-range, high-frequency sound propagation problems [24].

PSEUDO SPECTRAL TIME DOMAIN METHOD

The PSTD method is an alternative to the Finite-Difference Time Domain (FDTD) method, which is computationally more efficient. It achieves this by using a pseudospectral technique to calculate spatial derivatives [31–35]. The PSTD method can use coarser spatial grids with only two points per wavelength, which reduces the computational cost and enables faster simulations using the Fast Fourier Transform (FFT) algorithm [35]. However, the Fourier PSTD method is not effective in handling discontinuities introduced by boundaries. An alternative, the Chebyshev PSTD method, can overcome this limitation but requires more than two points per wavelength and is more sensitive to instability [36]. In summary, the PSTD method can be an effective tool for simulating sound propagation in inhomogeneous media, but its assumption of homogeneity within each spatial subdivision limits its applicability in more complex and realistic environments [37].

TRANSMISSION LINE MATRIX

The TLM method relies on a discrete implementation of Huygens' principle³. In the TLM method, the computational region is discretized by a net of tubes connected by nodes. The scattering process at all nodes can be calculated with an initial pressure distribution. The TLM method has been widely applied in electromagnetics [38], room acoustics [39], active noise control in a duct [40], and outdoor sound propagation modeling [41, 42]. The TLM method can simulate sound propagation in an inhomogeneous atmosphere due to temperature variations [43], and moving atmosphere modeled by the effective sound speed approach [41] and single-direction mean flow [44]. Although the TLM method is more computationally efficient than the FDTD method, its application in outdoor sound propagation is still limited by the cost of discretizing a large domain [37].

³Huygens' principle states that every point on a wavefront is a source of secondary spherical wavelets that combine to produce the wavefront's propagation.

FAST FIELD PROGRAM

The FFP method, also known as the wavenumber integration method, is a well-established simulation model for long-range propagation that has been widely used in both ocean acoustics [45, 46] and atmospheric acoustics [47–50]. It models the medium as vertical profiles that are divided into several homogeneous layers with constant medium velocity and temperature. The sound field in each layer is then determined by solving the Helmholtz equation in the horizontal wavenumber domain [51]. While the FFP method is computationally efficient for long-range propagation [46], it has some limitations. The method is restricted to systems with a layered medium and a homogeneous ground surface due to the Fourier transformation in the horizontal wavenumber domain. Therefore, it cannot be used to simulate sound propagation in a medium with irregular terrain topology, range-dependent weather profiles, or ground impedance [51]. Additionally, FFP results show more deviations from the exact solutions at high frequencies, and the computational time increases with increasing frequencies [20, 51].

PARABOLIC EQUATION METHOD

The PE method is widely used in both ocean acoustics [45, 52, 53] and atmospheric acoustics [2, 51, 54–57]. In atmospheric acoustics, different versions of the PE method have been developed. Gilbert and White [54] introduced the Crank-Nicholson PE (CNPE) method, which employs the Crank-Nicholson scheme to model acoustic propagation in a non-turbulent atmosphere over a flat terrain. Gilbert and Di [55] developed the Green's function parabolic equation (GFPE) method. However, both PE methods are based on the axisymmetric approximation and are restricted to two-dimensional problems. The GFPE method is further extended for modeling wave propagation in a 3D environment [56]. The generalized terrain parabolic equation (GTPE) method is an extension of the CNPE method that includes wave propagation over irregular terrain profiles. However, the GTPE is limited to smooth terrains, and the local slope of the terrain topology should not exceed about 30° for accurate results [51, 57]. Compared to FFP, the PE method is not limited to a layered atmosphere and a homogeneous ground surface. In the PE method, the effects of range-dependent sound speed profile, atmospheric turbulence, and irregular terrain with varying terrain impedance can be accounted for [51]. The PE method employs the effective sound speed approximation⁴ to approximate the effect of a moving medium. However, the effective sound speed assumption is not valid for large elevation angles, which limits the applicability of PE methods to urban/rural environments with 3D varying wind profiles. To address these constraints, Ostashev et al. [2, 58] have developed wide-angle and extra-wide-angle PEs that eliminate the reliance on the effective sound speed approximation. Notably, the extra-wide-angle PEs are applicable to propagation angles up to 90 degrees in relation to the nominal direction [58]. Moreover, their work highlights that the use of the effective sound speed approximation is discouraged

⁴The effective sound speed assumption is used to approximate sound propagation in a moving atmosphere by a non-moving atmosphere with an effective sound speed $c_{\text{eff}} = c + u$, where c is the adiabatic sound speed, and u is the horizontal component of the wind velocity in the direction of sound propagation. In general, the effective sound speed approximation is valid in situations where sound waves travel with relatively small elevation angles, such as situations with the source and the receiver near the ground.

in wide-angle PEs. Furthermore, due to the one-way equation⁵ implemented in the PE method, back-scattering of sound waves, such as the scattering caused by sound speed gradients in the direction back to the source, is neglected [51].

2.2.2. GEOMETRICAL ACOUSTICS METHODS

The GA methods, also known as ray acoustics methods, are based on the high-frequency approximation of wave propagation. The GA methods hypothesize the existence of wavefronts (which are the loci of all points with the same phase) and the presence of rays that provide a spatial depiction of sound travel and energy flow [5]. The GA methods can efficiently compute the propagation paths intersecting with complex geometries [59] and can handle various reflections such as specular reflection, diffuse reflection [60, 61], and refraction due to medium inhomogeneity and [62] medium velocity [5]. Therefore, the GA methods have been applied to simulate the outdoor acoustic propagation to evaluate the noise impact of various noise sources [63, 64]. The most common geometrical acoustic methods include the image source (IS), ray tracing (RT), and beam tracing (BT) methods.

IMAGE SOURCE METHOD

The IS method is one of the most common methods to find the reflected paths in a homogeneous, quiescent medium [65] and is widely used to analyze the acoustic properties of enclosures [66]. The IS method calculates specular reflection paths by mirroring the location of the source over each polygonal surface of the environment. The IS method allows one to determine all the specular paths if the required order or the reverberation time is provided [67]. Borish [68] extended the IS method to arbitrary polyhedra with any number of sides. However, computation time increases exponentially when the number of polygonal surfaces rises. Hence the complexity of the shape of the obstacles is limited due to the computational cost.

RAY TRACING METHOD

The RT method is a popular approach for simulating wave propagation in complex environments, originally developed in geometrical optics. The method uses a finite number of rays to discretize the sound power emitted by a sound source, where rays are described as propagation paths perpendicular to the wavefronts and are governed by the eikonal equation. The eikonal equation is a partial differential equation that describes the wavefront of a wave as a surface of constant phase. The validity condition for the eikonal equation in the RT method requires that the gradient of the sound speed is sufficiently large relative to the wavelength of the wave. This condition, expressed as $|\nabla c \cdot \mathbf{n}|/c \geq 2\pi/\lambda$, means that the RT method is more suitable for simulating high-frequency wave propagation in slowly varying media without sharp discontinuities in the medium profile.

The eikonal equation provides analytical solutions for wave propagation in a quiescent medium with specific sound speed distributions [69]. In a homogeneous and quiescent environment, the eikonal equation yields a simple solution in which the ray path

⁵A parabolic equation is a one-way wave equation, taking into account only sound waves traveling in the direction from the source to the receiver.

is a straight line. If the sound speed gradient is constant (i.e., $\nabla c = \text{constant}$) [69], the ray path takes the form of a circular arc. A quadratic parabola ray curve can be formed if the gradient of the square of slowness⁶ is constant ($\nabla(c^{-2}) = \text{constant}$) [69].

When the medium has a complicated sound speed distribution or it is moving, the eikonal equation cannot be solved analytically. It is then solved using numerical integration techniques like the Runge-Kutta method or the Adams–Bashforth method to determine the ray paths [2, 5, 70–72]. These numerical integration methods are applicable to general media. However, the accuracy and computational cost of ray paths depend on the spatial or temporal step size. Yet, for atmospheric acoustic propagation, the computational cost can be reduced considerably if the atmosphere is assumed to be a vertically stratified medium [73]. In each layer, the sound speed is constant; thus, the ray segment is a straight line. At the same time, the media characteristics vary discretely at the boundaries of each layer. Consequently, the refraction appears only at the layer interface and can be calculated by Snell's law [74]. However, this method is limited to inhomogeneous medium due to temperature or density variation and can not account for acoustic refraction due to variations in medium velocity. Furthermore, the horizontally stratified atmosphere assumption may not be applicable if sound propagation within an urban or rural area is considered, where the temperature and wind profiles are distorted due to irregular terrain surfaces.

The RT method has been widely applied in outdoor sound propagation modeling [5, 75–77]. Nevertheless, the conventional RT method still suffers from the singularities at caustics and shadow boundaries [51, 59, 69, 78]. Ludwig [79] and Kravtsov [80] developed a theory representing the effect of caustics by caustic diffraction fields that smooth out the amplitude of the ray field⁷ in the vicinity of the caustics. Yet, this method increases the computational cost, makes the numerical implementation more complex, and causes the ray model less attractive for accurate prediction of sound propagation, particularly for irregular sound speed profiles [51]. As an alternative, caustics can be neglected if the source-receiver distance is large enough and a weak refracting atmosphere is considered such that there are only two contributing rays, i.e., one direct ray and one ground reflected ray, to the pressure field at the receiver location [51]. Arntzen et al. [81] developed a correction model to remove the singularity at the shadow boundaries and approximate sound levels in the shadow zone. The correction method was developed based on the FFP. Noise levels in the shadow zone were estimated with a linear loss parameter (dB per meter). The parameter depends on the strength of the sound speed gradients and the source frequency. This method estimates the sound levels at the transition from the illuminated zone to the shadow zone and predicts the additional propagation within the shadow zone.

To calculate the pressure field at receiver points, it's essential to determine the eigenrays connecting the source and receivers [2]. Various methods exist to trace eigenrays, such as the shooting method [2, 46, 82], bending method [83], Pseudo-bending method [84], Pseudo-bending coupling with genetic algorithms [85], and continuation method

⁶The slowness of acoustic waves in an inhomogeneous, quiescent medium is defined as the inverse of the sound speed $1/c$.

⁷A ray field refers to a mathematical representation of the path taken by light or sound waves in a medium. It is modeled as a collection of rays that describe the direction and intensity of the wave propagation at a particular point in space.

2 tracing [95, 96], since the entire space of directions leaving the source can be covered by beams exactly. The disadvantage is that the geometric operations required to trace beams through a 3D model, i.e., intersection detection, are relatively complex, as each beam may be reflected over several surfaces. Another limitation of geometric beam tracing is that the beamwidth vanishes at caustics, resulting in unrealistic pressure field prediction. Weinberg and Keenan [92] suggested limiting the ability of the beam to focus to a point by imposing a minimum beam width of $\pi\lambda$ where λ is the wavelength. That empirically-derived focal limit removes the singularities at caustics and generally improves the accuracy [46].

The Gaussian beam tracing (GBT) method is a more robust extension of geometric beam tracing. It is based on the paraxial approximation, which is a simplifying assumption commonly used in the analysis of optical and acoustic wave propagation. It states that the variation of the wavefront normal to the beam axis is much smaller than the variation along the axis⁸. This allows the wavefront to be described by a simple parabolic equation [91], which greatly simplifies the mathematical analysis. The parabolic wave equation is then solved in the vicinity of the ray path using a ray-centered coordinate system (see Fig. 2.4(a)) to obtain the wavefield [91]. As illustrated in Fig. 2.4, the amplitude profile along each cross-section of the beam is bell-shaped. Due to this property, the solutions of the parabolic wave equation may be called Gaussian beams [91].

The GBT method was originally designed for analyzing wave propagation in inhomogeneous motionless media that exhibit variations in density or other properties [91]. It has since been extended to inhomogeneous moving media, particularly in the field of seismology [97]. However, despite its potential, the use of the GBT method in atmospheric sound propagation has been limited to inhomogeneous media, and current tools do not account for the acoustic effects caused by the distribution of wind velocity. Gabillet *et al.* [88] presented a 2D version of the GBT method for sound propagation in the atmosphere, but they used slightly inconsistent equations for ray-path tracing (RPT) and GBT. While the RPT equations explicitly include wind velocity and its gradients, which are suitable for RPT in an inhomogeneous moving atmosphere, the GBT equations do not contain any terms related to wind velocity and its gradients and are only valid for inhomogeneous motionless media. Their work demonstrated that the 2D GBT model can handle weak refraction due to vertical variation in wind velocity, similar to the variation in air temperature. However, in the presence of strong refraction due to wind velocity variations, the GBT prediction deviates up to 10 dB from the experimentally measured results. In recent years, several GBT tools have been developed and applied to atmospheric acoustic propagation problems [37, 98–100]. While these tools are efficient in RPT, they do not consider atmospheric refraction resulting from horizontal or vertical variability in wind velocity in a 3D environment. This limitation stems from the fact that the RPT and GBT formulations used in these works are derived for GBT in a motionless inhomogeneous medium. As a result, there is a need to develop a GBT tool based on the GBT theory for inhomogeneous moving media that can account for the acoustic impact of wind velocity on sound propagation in typical outdoor environments.

Applying the GBT method to atmospheric sound propagation poses another intrinsic

⁸This statement implies the high-frequency nature of the paraxial approximation, as the high-frequency wave field propagates mainly along the central ray instead of being spread in its vicinity.

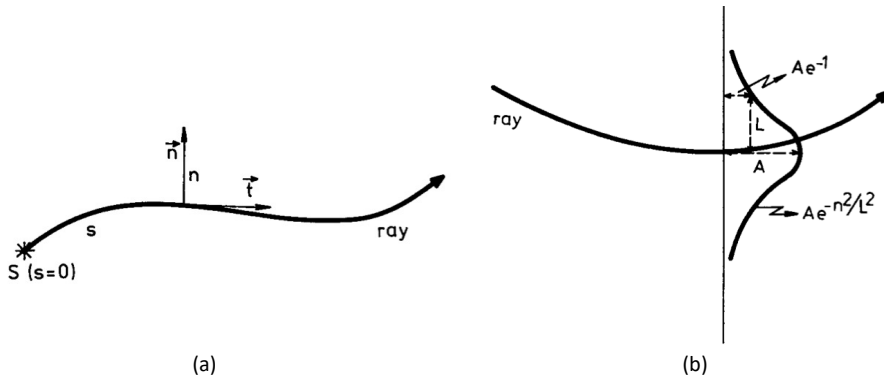


Figure 2.4: An example of ray-centred coordinate system (s, n) , where s is the ray path length, n is the length along the line perpendicular to the ray (a). Amplitude profile along the cross-section perpendicular to the axis of a Gaussian beam, where A , maximum amplitude; L , half-width of the beam (b). (adapted from [91]).

difficulty that arises when the wavefield is calculated on the terrain surface only. Namely, when the beams interact with the terrain boundary, the bottom end of the beam that grazes the terrain boundary passes below the boundary surface, causing spurious truncation error in the wavefield calculation [88, 98, 99]. To overcome this intrinsic limitation, Gabillet *et al.* [88] used large beams and introduced an *ad hoc* scale factor in the wavefield calculation that accounts for the reflected wavefield. Their model, however, failed to provide a more general approach to reduce the spurious truncation in the wavefield calculation. Despite the severity of this issue, recent publications did not address it. Those GBT models were validated either against some benchmark cases in ocean acoustics [37, 98] or on elevated surfaces in an outdoor environment where the receiver height is a few times larger than the acoustic wavelength [98]. Therefore, this thesis studies the impact of truncation error on the predicted wavefield and proposes an empirical formulation to reduce the truncation error. More details of this study are reported in Chapter 6.

Lastly, the GBT method is not able to accurately predict edge diffraction. This limitation arises from the reliance of the GBT on the paraxial approximation [88, 91]. Namely, when a Gaussian beam is tangent to a terrain boundary or interacts with a terrain discontinuity, a single beam cannot describe the diffracted field [88]. As such, GBT is limited in its ability to describe the diffraction that occurs at sharp edges. To overcome this limitation, more advanced models or numerical methods, such as the uniform geometrical theory of diffraction (UGTD) [88, 101] must be utilized. The inclusion of diffraction effects into the GBT approach requires another level of sophistication in the prediction models; hence, it is not considered in this work.

The studies mentioned above suggest that ray-based methods are well-suited for modeling outdoor sound propagation over long distances while considering a wide range of source frequencies, and accounting for 3D variations in terrain topology and weather profiles. However, existing ray-based prediction tools have limitations in their ability

to represent complex terrain and weather conditions accurately, and further improvements are needed. To address this, the following section introduces a complete theoretical framework for developing RT and GBT models to be applied for sound propagation in a generic 3D environment. These models aim to overcome the limitations of existing ray-based methods and provide more accurate predictions of sound propagation in complex outdoor environments.

2.3. PROPAGATION MODELLING USING RAY ACOUSTICS

In the study of sound propagation in an outdoor environment, the state of the medium generally changes little over a distance equal to the length of the sound wave λ [102]. The slow changes in the state of the medium determine the main features of the sound propagation. Under these circumstances, the application of the methods of ray acoustics is suitable. Namely, ray acoustics is a formal asymptotic method for computing an acoustic field which is valid when the non-uniformities of the medium vary gradually on the scale of the acoustic wavelength. The total field at a point is given by the sum of the contributions of rays passing through that point. In the upcoming section, fundamental descriptions of the theoretical background required to develop propagation models, detailed in Chapters 5-7, are presented. For further information on this topic, interested readers are referred to [2, 51, 74, 91, 97, 103].

2.3.1. RAY PATH TRACING

When the atmosphere has a steady temperature and no movement in velocity, an observer sees a wavefront $T(\mathbf{x}) = t$ (see Fig. 2.5(a)) as a surface that moves with speed $c\mathbf{n}$, where t is time and \mathbf{n} is normal to the wavefront, and c is the sound speed. However, when the air moves with velocity \mathbf{v} , the wavefront has a local speed equal to $d\mathbf{x}/dt = \mathbf{v} + c\mathbf{n} = \mathbf{u}$. Here both c and \mathbf{v} may vary with both position and time. The movement of $\mathbf{x}(t)$ over t forms a ray path. Consequently, the ray path vector \mathbf{x} follows the direction of \mathbf{u} instead of \mathbf{n} as indicated in Fig. 2.5(a). The propagation velocity \mathbf{u} is also known as group velocity, and the projection of \mathbf{u} in the direction of the normal \mathbf{n} equals the magnitude of phase velocity $\mathbf{v} = (c + \mathbf{n} \cdot \mathbf{v})\mathbf{n}$. Therefore, in an inhomogeneous moving atmosphere $|\mathbf{v}| \leq |\mathbf{u}|$ and, the direction of \mathbf{u} is not necessarily the same as that of \mathbf{v} .

The ray path can be obtained [70, 71] by employing the Hamiltonian formalism that solves the following eikonal equation derived by Pierce⁹ [104]

$$\frac{1}{c} - \frac{\mathbf{v} \cdot \nabla T}{c} = |\nabla T|. \quad (2.1)$$

Eq. 2.1 describes the propagation of the acoustic wavefront in an inhomogeneous moving atmosphere. Eq. 2.1 is a nonlinear first-order partial differential equation, also known as the Hamilton-Jacobi equation. Hence, the equation can be expressed in the form $\mathcal{H}(\mathbf{s}, \mathbf{x}) = |\nabla T| - 1/c + \mathbf{v} \cdot \nabla T/c = 0$, where $\mathcal{H}(\mathbf{s}, \mathbf{x})$ is the Hamiltonian and \mathbf{s} is the wave-slowness vector $\mathbf{s} = \nabla T$. The solution of $\mathcal{H}(\mathbf{s}, \mathbf{x})$ can be represented by a set of the ordinary differential equations

⁹This equation was first derived by Blokhintzev [102] with a slightly different form, in which a reference sound speed c_0 appears on the numerator of the first term.

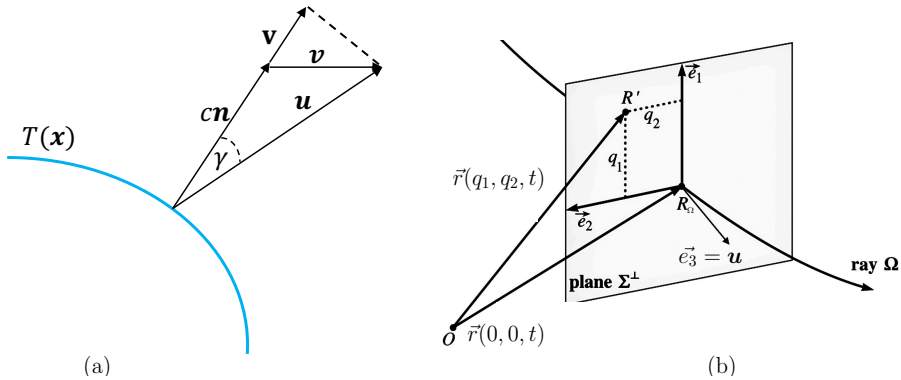


Figure 2.5: Wavefront normal vector \mathbf{n} , wind velocity \mathbf{v} , group velocity \mathbf{u} , and the phase velocity \mathbf{v} in a moving atmosphere, adapted from [2] (a). A field point R' located in the vicinity of a central ray (\mathbf{v}_{ray}) in the ray-centered coordinate system (b). The field point R' is located on a plane Σ^\perp tangent to the wavefront at point R_Ω on the central ray Ω .

$$\left. \begin{aligned} \frac{d\mathbf{x}}{d\tau} &= \frac{\partial \mathcal{H}}{\partial \mathbf{s}} \\ \frac{d\mathbf{s}}{d\tau} &= -\frac{\partial \mathcal{H}}{\partial \mathbf{x}} \\ \frac{dT}{d\tau} &= \mathbf{s} \cdot \frac{\partial \mathcal{H}}{\partial \mathbf{s}} \end{aligned} \right\}, \quad (2.2)$$

where τ is a monotonic independent variable, which may be related to the travel time. It is worth noting that there are various ways to choose the Hamiltonian \mathcal{H} , which consequently leads to different forms of the ray-path-tracing (RPT) equations. However, all these equations specify the same ray path because they must satisfy Fermat's principle. This principle states that the path of wave propagation between two points is the one that takes the shortest time, in other words, the wavefront will follow the path with the fastest arrival time from the source to the observer [104]. The same principle applies to RT in inhomogeneous moving media, where the final ray path is determined by the physical properties of the medium and the wavefront, which are not necessarily directly dependent on the choice of Hamiltonian.

One common approach is to use the eikonal equation as the Hamiltonian [2]. This provides a direct and intuitive method for deriving the equations of ray propagation in an inhomogeneous moving medium. In this dissertation, the Hamiltonian is selected as

$\mathcal{H} = |\mathbf{s}| - 1/c + \mathbf{s} \cdot \mathbf{v}/c$. Therefore, Eq. 2.2 becomes

$$\left. \begin{aligned} \frac{d\mathbf{x}}{d\tau} &= \frac{\mathbf{s}}{|\mathbf{s}|} + \frac{\mathbf{v}}{c} \\ \frac{d\mathbf{s}}{d\tau} &= -\frac{1}{c} \left[|\mathbf{s}| \nabla c + \mathbf{s} \times (\nabla \times \mathbf{v}) + (\mathbf{s} \cdot \nabla) \mathbf{v} \right] \\ \frac{dT}{d\tau} &= |\mathbf{s}| + \frac{\mathbf{s} \cdot \mathbf{v}}{c} \end{aligned} \right\}. \quad (2.3)$$

As $\mathbf{s}/|\mathbf{s}| = \mathbf{n}$, the right-hand side of the first equation in Eq. 2.3 is equal to \mathbf{u}/c and by substituting $\mathbf{s} = \mathbf{n}/(c + \mathbf{v} \cdot \mathbf{n})$ and $|\mathbf{s}| = 1/(c + \mathbf{v} \cdot \mathbf{n})$ the third equation in Eq. 2.3 takes the form $dT/d\tau = 1/c$. As $T = t$ for a single ray, hence, $dt/d\tau = 1/c$. This reveals the relation between the travel time t and the independent variable τ . This relation can also be achieved by relating the independent variable τ with the ray-path length l based on the first equation in Eq. 2.2 and Eq. 2.3 [2]. It should be noted that t represents the travel time T only along the ray-path \mathbf{x} , but not in its vicinity. If the travel time t is used instead of the independent variable τ , the Eq. 2.3 takes the form

$$\left. \begin{aligned} \frac{d\mathbf{x}}{dt} &= c \frac{\partial \mathcal{H}}{\partial \mathbf{s}} = \mathbf{u} = \frac{c\mathbf{s}}{|\mathbf{s}|} + \mathbf{v} \\ \frac{d\mathbf{s}}{dt} &= -c \frac{\partial \mathcal{H}}{\partial \mathbf{x}} = \boldsymbol{\eta} = -|\mathbf{s}| \nabla c - \mathbf{s} \times (\nabla \times \mathbf{v}) - (\mathbf{s} \cdot \nabla) \mathbf{v} \end{aligned} \right\}. \quad (2.4)$$

Eq. 2.4 is the final form of the RPT equation, which is equivalent to the one derived by Pierce [104, 105]. Eq. 2.4 is solved using a second-order Runge-Kutta scheme with the initial conditions $t = t_0$, $\mathbf{x}(t_0) = \mathbf{x}_0$, $\mathbf{s}(t_0) = \mathbf{s}_0$, where t_0 is an arbitrarily chosen initial time, and $\mathbf{s}_0 = [\mathbf{n}(t)/v(t)]_{t=t_0}$. A user defined number of time steps is used to march the solution forward in time. However, it should be noted that different factors, such as source-receiver distance, temperature, and wind velocity gradients, can influence the number of time steps needed in the simulation. For instance, the presence of large temperature and wind velocity gradients leads to a steeper wavefront and a greater bending of the sound rays, thus requiring more time steps to capture the propagation behavior accurately. In practice, a trade-off between accuracy and computational cost is often necessary, with a larger number of time steps providing improved accuracy at the cost of increased computational effort. The impact of the number of time steps on the prediction results is studied in Chapter 6.

The coordinates \mathbf{x} of the points on the ray trajectory and slowness vectors \mathbf{s} at these points are obtained by solving Eq. 2.4. As a by-product of ray path tracing, several other useful quantities can also be determined, which will be needed in the following: the ray-velocity vector $\mathbf{u} = d\mathbf{x}/dt$, the unit vector $\mathbf{t} = \mathbf{u}/|\mathbf{u}|$ tangent to the ray, the unit vector $\mathbf{n} = \mathbf{s}/|\mathbf{s}|$ perpendicular to the wavefront, the vector $\boldsymbol{\eta} = d\mathbf{s}/dt$, which represents the variations of the slowness vector along the ray, phase velocity $v = |\mathbf{v}| = |\mathbf{s}|^{-1}$. The RPT can be used to compute all the above-mentioned quantities only on the ray Ω , not in its vicinity, which is not sufficient to calculate the Gaussian beams. The reason is that the variation of the beam amplitude along the ray is determined by the paraxial ray field in the vicinity of the ray, not by a single ray. Furthermore, the calculation of the paraxial ray

field requires the resolution of the geometrical spreading and complex-valued paraxial travel time in the vicinity of the ray Ω . In order to compute the quantities related to the paraxial ray field, it is essential to augment the RPT with an additional procedure called dynamic ray tracing (DRT).

2.3.2. DYNAMIC RAY TRACING

DRT consists in a solution of a system of linear ordinary differential equations of the first order, which can be solved along a ray together with the RPT system or along an existing ray Ω . The solutions of DRT enable one to calculate the travel time in the vicinity of a ray. DRT system can be expressed in various coordinate systems (ray-centered, Cartesian, etc.). Following [97], this paper considers the ray-centered coordinate system q_i , $i = 1, 2, 3$. Many other details on ray-centered coordinates and DRT in ray-centered coordinates can be found in [74, 106].

One of the essential properties of the ray-centered coordinate system is that the central ray Ω represents its coordinate axis q_3 . Namely, the coordinate q_3 is defined as a quantity equal to the travel time t along the central ray Ω , $q_3 = t$. The q_1 and q_2 coordinate axes can be introduced as mutually perpendicular straight lines in the plane Σ^\perp tangent to the wavefront and intersecting at the central ray Ω as shown in Fig. 2.5(b). This property leads a simple relation between the Cartesian coordinates x_i and the ray-centered coordinates q_j

$$x_i(q_j) = x_i^\Omega(q_3) + H_{iM}(q_3)q_M, \quad (2.5)$$

where $i, j = 1, 2, 3$ and $M = 1, 2$. The central ray Ω is specified by $q_1 = q_2 = 0$, hence, $\mathbf{x}(q_1 = 0, q_2 = 0, q_3) = \mathbf{x}^\Omega(q_1 = 0, q_2 = 0, q_3)$, where \mathbf{x}^Ω denotes a point on the central ray Ω . The elements of the 3×3 transformation matrices \mathbf{H} and $\tilde{\mathbf{H}}$ from ray-centered to Cartesian coordinates and back, are defined as $H_{im} = \partial x_i / \partial q_m$ and $\tilde{H}_{im} = \partial q_i / \partial x_m$, respectively. As the ray-centered coordinate system is curvilinear and the medium is not stationary, it is necessary to introduce two systems of basis vectors: the contravariant basis vectors $\mathbf{e}_1, \mathbf{e}_2, \mathbf{e}_3$ (tangential to coordinate axes), and the covariant basis vectors $\mathbf{f}_1, \mathbf{f}_2, \mathbf{f}_3$ (perpendicular to coordinate surfaces). The basis vectors $\mathbf{e}_1, \mathbf{e}_2$ tangent to the wavefront and \mathbf{e}_3 tangent to the central ray Ω are shown in Fig. 2.5(b). These basis vectors are defined as columns of 3×3 transformation matrices $\mathbf{H} = (\mathbf{e}_1, \mathbf{e}_2, \mathbf{e}_3 = \mathbf{u})$ and $\tilde{\mathbf{H}}^T = (\mathbf{f}_1, \mathbf{f}_2, \mathbf{f}_3 = \mathbf{s})$. The relation between the transformation matrices $\tilde{H}_{ik}H_{kj} = \delta_{ij}$, where δ indicates the Kronecker delta function, can be expressed in terms of \mathbf{e}_i and \mathbf{f}_j as follows:

$$\mathbf{f}_i^T \mathbf{e}_j = \delta_{ij}. \quad (2.6)$$

Eq. 2.6 leads vectorial relations $\mathbf{s}^T \mathbf{u} = 1$, $\mathbf{s}^T \mathbf{e}_l = 0$, and $\mathbf{u}^T \mathbf{f}_l = 0$. Thus, vectors \mathbf{e}_l are perpendicular to the slowness vector \mathbf{s} , vectors \mathbf{f}_l are perpendicular to the group velocity \mathbf{u} , that is, to the ray. Eq. 2.6 also yields

$$\left. \begin{aligned} \mathbf{f}_1 &= \frac{\mathbf{e}_2 \times \mathbf{u}}{\mathbf{u}^T(\mathbf{e}_1 \times \mathbf{e}_2)} = \frac{\mathbf{e}_2 \times \mathbf{u}}{|\mathbf{v}|} \\ \mathbf{f}_2 &= \frac{\mathbf{u} \times \mathbf{e}_1}{\mathbf{u}^T(\mathbf{e}_1 \times \mathbf{e}_2)} = \frac{\mathbf{e}_1 \times \mathbf{u}}{|\mathbf{v}|} \end{aligned} \right\} \quad (2.7)$$

The contravariant basis vectors \mathbf{e}_1 and \mathbf{e}_2 can be determined by solving a simple ordinary differential equation of the first order along the central ray Ω :

$$\frac{d\mathbf{e}_I}{dt} = -\frac{(\mathbf{e}_I^T \boldsymbol{\eta})\mathbf{s}}{(\mathbf{s}^T \mathbf{s})}. \quad (2.8)$$

Here, \mathbf{s} and $\boldsymbol{\eta} = d\mathbf{s}/dt$ are known from the RPT. At a selected point t_0 of central ray Ω , initial values for \mathbf{e}_1 and \mathbf{e}_2 can be constructed such that they form a triplet of mutually perpendicular unit vectors with $\mathbf{n} = |\mathbf{v}|\mathbf{s}$. Based on this, one can ascertain that vectors \mathbf{e}_1 , \mathbf{e}_2 and \mathbf{n} are then right-handed, unit and mutually perpendicular along the whole central ray Ω . Hence, it is sufficient to calculate only $\mathbf{e}_1(t)$ using Eq. 2.8, as $\mathbf{e}_2 = \mathbf{n}(t) \times \mathbf{e}_1(t)$. Furthermore, the numerical solution of $\mathbf{e}_1(t)$ using Eq. 2.8 is adequate to calculate analytically all vectors \mathbf{e}_1 , \mathbf{e}_2 and \mathbf{f}_1 , \mathbf{f}_2 [97, 107]. Since, $\mathbf{e}_3 = \mathbf{u}$ and $\mathbf{f}_3 = \mathbf{s}$ are known from the RPT. Note that vectors \mathbf{f}_1 and \mathbf{f}_2 may not necessarily be unit and mutually perpendicular, but \mathbf{e}_1 and \mathbf{e}_2 are.

An orthonormal system of rays, specified by two ray parameters γ_1, γ_2 which represent the ray shooting angles at a point source, is now to be considered. Two 2×2 matrices, \mathbf{Q} and \mathbf{P} , with elements Q_{IJ} and P_{IJ} , are introduced along the central ray Ω by the following relation

$$Q_{IJ} = \partial q_I / \partial \gamma_J, \quad P_{IJ} = \partial p_I / \partial \gamma_J, \quad (2.9)$$

where $I, J = 1, 2$, p_I denotes the I th component of the slowness vector \mathbf{s} in the ray-centered coordinate system, $p_I = H_{kI} s_k$. The expressions for Q_{IJ} and P_{IJ} show, how q and p vary when parameters γ_1 and γ_2 change. Matrices \mathbf{Q} and \mathbf{P} can be computed by solving a system of ordinary differential equations of the first order along ray Ω , called the DRT system. In matrix form, the DRT system reads [97, 107]

$$\left. \begin{aligned} \frac{d\mathbf{Q}}{dt} &= \mathbf{A}\mathbf{Q} + \mathbf{B}\mathbf{P} \\ \frac{d\mathbf{P}}{dt} &= -\mathbf{C}\mathbf{Q} - \mathbf{D}\mathbf{P} \end{aligned} \right\} \quad (2.10)$$

All matrices in Eq. 2.10 are 2×2 . The matrices \mathbf{A} , \mathbf{B} , \mathbf{C} and \mathbf{D} are given by relations

$$\left. \begin{aligned} \mathbf{A} &= \mathbf{f}^T \mathbf{A}^{(x)} \mathbf{e} + \mathbf{d}, & \mathbf{B} &= \mathbf{f}^T \mathbf{B}^{(x)} \mathbf{f} \\ \mathbf{C} &= \mathbf{e}^T (\mathbf{C}^{(x)} - \boldsymbol{\eta} \boldsymbol{\eta}^T) \mathbf{e}, & \mathbf{D} &= \mathbf{e}^T \mathbf{D}^{(x)} \mathbf{f} + \mathbf{d}^T \end{aligned} \right\} \quad (2.11)$$

The 3×3 matrices $\mathbf{A}^{(x)}$, $\mathbf{B}^{(x)}$, $\mathbf{C}^{(x)}$ and $\mathbf{D}^{(x)}$ are defined in terms of Cartesian derivatives

of the Hamiltonian:

$$\left. \begin{aligned} A_{ij}^{(x)} &= \frac{\partial^2 \mathcal{H}}{\partial s_i \partial x_j}, & B_{ij}^{(x)} &= \frac{\partial^2 \mathcal{H}}{\partial s_i \partial s_j} \\ C_{ij}^{(x)} &= \frac{\partial^2 \mathcal{H}}{\partial x_i \partial x_j}, & D_{ij}^{(x)} &= \frac{\partial^2 \mathcal{H}}{\partial x_i \partial s_j} \end{aligned} \right\}. \quad (2.12)$$

Note that $D_{ij}^{(x)} = A_{ji}^{(x)}$. The 3×2 matrix \mathbf{e} is composed of two unit basis vectors, tangent to the wavefront: $\mathbf{e} = (\mathbf{e}_1, \mathbf{e}_2)$. The 3×2 matrix $\mathbf{f} = (\mathbf{f}_1, \mathbf{f}_2)$ composed of two covariant basis vectors \mathbf{f}_1 and \mathbf{f}_2 , perpendicular to the ray, can be computed using Eq. 2.7. The 2×2 matrix \mathbf{d} defined as $\mathbf{d} = \mathbf{f}^T d\mathbf{e}/dt$, where derivative $d\mathbf{e}/dt$ is given by Eq. 2.8. Numerically, the most time consuming procedure in DRT in ray-centered coordinates in an inhomogeneous moving medium is the determination of the 3×3 matrices $\mathbf{A}^{(x)} \equiv \mathbf{D}^{(x)T}$, $\mathbf{B}^{(x)}$, and $\mathbf{C}^{(x)}$ [97].

REFLECTION OVER TERRAIN SURFACES

Once a ray interacts with structural interfaces like irregular ground surfaces, it is essential to introduce the initial conditions for the DRT along central rays of reflected or transmitted waves at the point of incidence. At the point of incidence, this is achieved by the continuity property of \mathbf{Q} and \mathbf{P} that reads

$$\begin{pmatrix} \tilde{\mathbf{P}} \\ \tilde{\mathbf{Q}} \end{pmatrix} = \Pi(\tilde{t}_\Sigma, t_\Sigma) \begin{pmatrix} \mathbf{P} \\ \mathbf{Q} \end{pmatrix}, \quad (2.13)$$

where $\Pi(\tilde{t}_\Sigma, t_\Sigma)$ is 4×4 matrix known as the interface propagator matrix that is given by the relation

$$\Pi(\tilde{t}_\Sigma, t_\Sigma) = \begin{bmatrix} \tilde{\mathbf{K}}^T \mathbf{K}^{-T} & \mathbf{0} \\ \tilde{\mathbf{K}}^{-1} [\mathbf{E} - \tilde{\mathbf{E}} - (\sigma - \tilde{\sigma}) \mathbf{D}] \mathbf{K}^{-T} & \tilde{\mathbf{K}}^{-1} \mathbf{K} \end{bmatrix}. \quad (2.14)$$

Detailed derivation of Eq. 2.13 can be found in [103]. In Eq. 2.13 and 2.14, the symbols without a tilde correspond to the point of incidence, $t = t_\Sigma$, while the symbols with a tilde correspond to the point of reflection or transmission, $t = \tilde{t}_\Sigma$. As the explanation of symbols with and without tilde is analogous, here, only the symbols corresponding to the point of incidence t_Σ are presented.

Let Σ be a structural interface that separates the terrain surface from the air. The parametric description of the interface can be described by relations $\mathbf{x} = \mathbf{g}(w_1, w_2)$ and $w_I, I = 1, 2$, are the Gaussian coordinates of the surface. The Gaussian coordinates w_1 and w_2 , as a special case, can also be considered as the local Cartesian coordinates in a plane tangent to interface Σ at the point of incidence $t = t_\Sigma$ of the central ray Ω . In the vicinity of the point of incidence, the interface can be approximated to the second order in w_I by the relation

$$\mathbf{x}(w_I) = \mathbf{x}_{inc} + \mathbf{g}_I w_I + \frac{1}{2} \mathbf{g}_{IJ} w_I w_J. \quad (2.15)$$

Here, $\mathbf{g}_J = \partial \mathbf{g} / \partial w_J$ are vectors tangent to Σ at $\mathbf{x} = \mathbf{x}_{inc}$, and $\mathbf{g}_{IJ} = \partial^2 \mathbf{g} / \partial w_I \partial w_J$ are related to the curvature of the interface at $\mathbf{x} = \mathbf{x}_{inc}$. More details can be found in [103,

[108]. In general, vectors \mathbf{g}_J are neither unit nor mutually perpendicular. The unit normal vector to the interface \mathbf{N} is defined as $\mathbf{N} = \mathbf{g}_1 \times \mathbf{g}_2 / |\mathbf{g}_1 \times \mathbf{g}_2|$.

The 2×2 matrices in Eq. 2.14 \mathbf{K} and \mathbf{K}^{-1} are given by relations

$$\left. \begin{aligned} \mathbf{K} &= (\mathbf{g}_1, \mathbf{g}_2)^T (\mathbf{f}_1, \mathbf{f}_2), & \mathbf{K}^{-1} &= (\mathbf{e}_1, \mathbf{e}_2)^T (\mathbf{h}_1, \mathbf{h}_2) \\ \mathbf{h}_1 &= \frac{\mathbf{g}_2 \times \mathbf{u}}{\mathbf{u}^T (\mathbf{g}_1 \times \mathbf{g}_2)}, & \mathbf{h}_2 &= \frac{\mathbf{u} \times \mathbf{g}_1}{\mathbf{u}^T (\mathbf{g}_1 \times \mathbf{g}_2)} \end{aligned} \right\}. \quad (2.16)$$

Elements of the 2×2 inhomogeneity matrix \mathbf{E} are given by $E_{IJ} = (\mathbf{g}_I^T \mathbf{s})(\mathbf{e}_K^T \boldsymbol{\eta})(\mathbf{g}_J^T \mathbf{f}_K) + (\mathbf{g}_I^T \boldsymbol{\eta})(\mathbf{g}_J^T \mathbf{s})$, where \mathbf{s} and $\boldsymbol{\eta}$ are calculated from the RPT at the point of incidence. In a homogeneous media, $\mathbf{E} = \mathbf{0}$, as $\boldsymbol{\eta} = \mathbf{0}$. The 2×2 curvature matrix \mathbf{D} is defined as $D_{IJ} = \mathbf{g}_{IJ}^T \mathbf{N}$. For a plane interface, $\mathbf{D} = \mathbf{0}$. The scalars σ and $\tilde{\sigma}$ in Eq. 2.14 are given by relations $\sigma = \mathbf{N}^T \mathbf{s}$ and $\tilde{\sigma} = \mathbf{N}^T \tilde{\mathbf{s}}$. It should be noted that $\mathbf{g}_I = \tilde{\mathbf{g}}_I$, but $\mathbf{e}_I \neq \tilde{\mathbf{e}}_I$, $\mathbf{f}_I \neq \tilde{\mathbf{f}}_I$ and $\mathbf{h}_I \neq \tilde{\mathbf{h}}_I$. At t_Σ , vectors \mathbf{u} , \mathbf{s} and $\boldsymbol{\eta}$ are known from the RPT. At the reflection or transmission point of the selected reflected or transmitted wave, these quantities are denoted with a tilde, i.e., \tilde{t}_Σ , $\tilde{\mathbf{u}}$, $\tilde{\mathbf{s}}$ and $\tilde{\boldsymbol{\eta}}$, and can be calculated using Snell's law [103, 108]. The vectors $\tilde{\mathbf{e}}_I$ can be chosen as two arbitrary mutually perpendicular unit vectors in the plane perpendicular to $\tilde{\mathbf{s}}$. Once $\tilde{\mathbf{u}}$ and $\tilde{\mathbf{s}}$ are known, the determination of $\tilde{\mathbf{f}}_I$ and $\tilde{\mathbf{h}}_I$ is straightforward.

2.3.3. GAUSSIAN BEAMS AND WAVEFIELD CALCULATION

Once the RPT and DRT systems for a central ray Ω are resolved, the complex pressure contribution from point R_Ω along the Gaussian beam to the observer point R' situated in the vicinity of the central ray Ω (see Fig. 2.5) is given by [97]

$$p^b(R') = P^\Omega \exp \left[-\omega \operatorname{Im} T(R') \right] \times \exp \left\{ -i\omega \left[t - \operatorname{Re} T(R') \right] \right\}, \quad (2.17)$$

where \mathbf{U}^Ω is given by the relation

$$P^\Omega = A(t_0) \left[\frac{\rho(t_0)v(t_0) \det \mathbf{Q}(t_0)}{\rho(t)v(t) \det \mathbf{Q}(t)} \right]^{1/2} \mathcal{R}^C, \quad (2.18)$$

where ρ is the density, \mathcal{R}^C is the complete energy reflection/transmission coefficient along ray Ω from t_0 to t and $A(t_0)$ is a scalar amplitude at the source location. The complex-valued paraxial traveltime $T(R)$ is given by

$$T(R') = T(R_\Omega) + [\mathbf{x}(R') - \mathbf{x}(R_\Omega)]^T \mathbf{s}(R_\Omega) + \frac{1}{2} [\mathbf{x}(R') - \mathbf{x}(R_\Omega)]^T \mathbf{M}^{(x)}(R_\Omega) [\mathbf{x}(R') - \mathbf{x}(R_\Omega)]. \quad (2.19)$$

The elements of 3×3 matrix $\mathbf{M}^{(x)}$ are given by $\mathbf{M}^{(x)} = \mathbf{f} \mathbf{M} \mathbf{f}^T + \mathbf{s} \boldsymbol{\eta}^T + \boldsymbol{\eta} \mathbf{s}^T - \mathbf{s} \mathbf{s}^T (\mathbf{u}^T \boldsymbol{\eta})$. Here, \mathbf{M} is a 2×2 matrix of the second derivatives of traveltime field and defined as $\mathbf{M} = \mathbf{P} \mathbf{Q}^{-1}$. It should be noted that matrix \mathbf{M} is a complex-valued symmetric matrix that is determined by solving the DRT system with the initial conditions $\mathbf{Q}(t_0) = \mathbf{R}$, and $\mathbf{P}(t_0) = \mathbf{M}_0 \mathbf{R}$. Here, \mathbf{R} is an arbitrary constant real-valued finite 2×2 matrix and $\det \mathbf{R} \neq 0$. In this study, an identity matrix, i.e., $\mathbf{R} = \mathbf{I}$, is considered. The matrix $\mathbf{M}_0 = \mathbf{M}(t_0) = \mathbf{P}(t_0) \mathbf{Q}^{-1}(t_0)$ is complex-valued and $\operatorname{Re}(\mathbf{M}_0)$ and $\operatorname{Im}(\mathbf{M}_0)$ are real valued, symmetric and finite. Furthermore, $\operatorname{Im}(\mathbf{M}_0)$ is positive definite, and generally, $\operatorname{Re}(\mathbf{M}_0) = \mathbf{0}$ [97].

Finally, the total acoustic pressure at the receiver point R' is obtained by integrating the contributions of all individual Gaussian beams passing near the receiver point

$$U(R', \omega) = \iint_{\mathcal{D}} \Phi(\gamma_1, \gamma_2) p^b(R') d\gamma_1 d\gamma_2, \quad (2.20)$$

where \mathcal{D} is the region of integration over the initial ray parameters γ_1 and γ_2 , and $\Phi(\gamma_1, \gamma_2)$ is the weighting function. The weighting function is calculated by expanding the wave-field at the source and matching the high-frequency asymptotic behavior of the integral in Eq. (2.20) to the exact solution for a source in a homogeneous medium where the ray field is regular. The weighting function is given by [74]

$$\Phi(\gamma_1, \gamma_2) = \frac{\omega}{2\pi} [-\det(\mathbf{M} - \mathbf{M}^a)]^{1/2} |\det \mathbf{Q}^a|, \quad (2.21)$$

where the superscript $(.)^a$ indicates terms applied in the actual ray field, and $\mathbf{M} \neq \mathbf{M}^a$. In other words, matrix \mathbf{M} is affected by the choice of initial parameters of Gaussian beams used in the evaluation of Eq. (2.20). Whereas, matrices \mathbf{M}^a and \mathbf{Q}^a have similar meaning to \mathbf{M} and \mathbf{Q} and are again evaluated along the ray γ_1 and γ_2 . However, they are real-valued and characterize the paraxial ray approximation of the ray field under consideration, not a Gaussian beam. For a given ray field, corresponding to a point source, for instance, \mathbf{M}^a and \mathbf{Q}^a are fully specified at any point specified by the ray γ_1, γ_2 . They are not influenced by the choice of initial parameters of Gaussian beams used in Eq. (2.20) [109].

A necessary condition in the derivation of Eq. 2.21 is the regularity of the ray field. The ray field is regular on a surface if it covers continuously and uniquely the surface with rays, that is, if one and only one ray passes through any point of the surface [74]. Eq. 2.20 can give spurious truncation errors if performed on a receiver surface where the ray field is not regular. The terrain surfaces, for instance, are a typical example of such surfaces where the ray field is not regular. In this dissertation, this limitation is removed by deriving a semi-empirical formulation which will be outlined in Chapter 6

In this thesis, the propagation model outlined above has been adopted and implemented into two different computational frameworks: a point-to-point curved-ray tracer and a Gaussian beam tracer.

- The curved-ray tracer is developed based on the RPT equation (Eq. 2.4) and implemented within an optimization algorithm to determine eigenrays. It is designed to study the effects of weather on long-range acoustic propagation. In Chapter 5, this model will be thoroughly explained. While a detailed explanation of user input files of this tool can be found in Appendix B.
- The Gaussian beam tracer is a different computational framework that is developed based on the RPT (Eq. 2.4), DRT (Eq. 2.10), and Gaussian beam summation (Eq. 2.20) equations to study the impact of 3D varying terrain topology and weather conditions on noise propagation in both urban and rural environments. In Chapter 6, a rigorous validation of the Gaussian beam tracer is presented, whereas Chapter 7 presents its further extension to include complex source directivity in the presence of moving medium and application in short-range propagation within

an urban environment. While in Chapter 8, further extension to time-efficient calculation of broadband noise is presented along with its application in long-range propagation within a mountainous environment. More details of user input files of this tool can be found in Appendix C.

REFERENCES

- [1] F. Yunus, D. Casalino, F. Avallone, and D. Ragni, *Efficient prediction of airborne noise propagation in a non-turbulent urban environment using Gaussian beam tracing method*, *J. Acoust. Soc. Am.* **153**, 2362 (2023).
- [2] V. E. Ostashev and D. K. Wilson, *Acoustics in moving inhomogeneous media*, 2nd ed. (CRC Press, 2015).
- [3] E. M. Salomons, *Computational Atmospheric Acoustics* (Springer Science & Business Media, 2001).
- [4] M. Hornikx, *Ten questions concerning computational urban acoustics*, *Build Environ* **106**, 409 (2016).
- [5] J. S. Lamancusa and P. A. Daroux, *Ray tracing in a moving medium with two-dimensional sound speed variation and application to sound propagation over terrain discontinuities*. *J. Acoust. Soc. Am.* **93**, 1716 (1993).
- [6] T. Van Renterghem, K. V. Horoshenkov, J. A. Parry, and D. P. Williams, *Statistical analysis of sound level predictions in refracting and turbulent atmospheres*, *Appl. Acoust.* **185**, 108426 (2022).
- [7] M. Hornikx, M. Dohmen, K. Conen, T. van Hooff, and B. Blocken, *The wind effect on sound propagation over urban areas: Predictions for generic urban sections*, *Build Environ.* **144**, 519 (2018).
- [8] M. Hornikx and J. Forssén, *Noise abatement schemes for shielded canyons*, *Appl. Acoust.* **70**, 267 (2009).
- [9] A. Filippone, *Aircraft noise prediction*, *Progress in Aerospace Sciences* **68**, 27 (2014).
- [10] D. Oldham and M. Radwan, *Sound propagation in city streets*, *Building Acoustics* **1**, 65 (1994).
- [11] G. M. E. Sanchez, T. Van Renterghem, P. Thomas, and D. Botteldooren, *The effect of street canyon design on traffic noise exposure along roads*, *Build Environ* **97**, 96 (2016).
- [12] D. Casalino, *Reprint of: Benchmarking of different wave models for sound propagation in non-uniform flows*, *Procedia IUTAM* **1**, 163 (2010).
- [13] C. P. Vendhan, G. C. Diwan, and S. K. Bhattacharyya, *Finite-element modeling of depth and range dependent acoustic propagation in oceanic waveguides*, *J. Acoust. Soc. Am.* **127**, 3319 (2010).

- [14] D. Casalino, *Finite element solutions of a wave equation for sound propagation in sheared flows*, AIAA J. **50**, 37 (2012).
- [15] D. Casalino, S. Santini, M. Genito, and V. Ferrara, *Rocket noise sources localization through a tailored beam-forming technique*, AIAA J. **50**, 2146 (2012).
- [16] T. Nomura, K. Takagi, and S. Sato, *Finite element simulation of sound propagation concerning meteorological conditions*, International journal for numerical methods in fluids **64**, 1296 (2010).
- [17] N. M. Papadakis and G. E. Stavroulakis, *Finite element method for the estimation of insertion loss of noise barriers: comparison with various formulae (2D)*, Urban Sci. **4**, 77 (2020).
- [18] D. Casalino, M. Barbarino, and A. Visingardi, *Simulation of helicopter community noise in complex urban geometry*, AIAA journal **49**, 1614 (2011).
- [19] M. Kleiner, B.-I. Dalenbäck, and P. Svensson, *Auralization-an overview*, Journal of the Audio Engineering Society **41**, 861 (1993).
- [20] J. Defrance, E. Salomons, I. Noordhoek, D. Heimann, B. Plovsing, G. Watts, H. Jonasson, X. Zhang, E. Premat, I. Schmich, *et al.*, *Outdoor sound propagation reference model developed in the european harmonoise project*, Acta Acustica united with Acustica **93**, 213 (2007).
- [21] E. Premat and Y. Gabillet, *A new boundary-element method for predicting outdoor sound propagation and application to the case of a sound barrier in the presence of downward refraction*, J. Acoust. Soc. Am. **108**, 2775 (2000).
- [22] R. Blumrich and D. Heimann, *A linearized eulerian sound propagation model for studies of complex meteorological effects*, J. Acoust. Soc. Am. **112**, 446 (2002).
- [23] Z. C. Zheng and W. Li, *Numerical stabilities and boundary conditions in time-domain eulerian simulations of acoustic wave propagations with and without background flow*, Applied mathematics and computation **202**, 146 (2008).
- [24] D. Heimann and R. Karle, *A linearized euler finite-difference time-domain sound propagation model with terrain-following coordinates*, J. Acoust. Soc. Am. **119**, 3813 (2006).
- [25] B. Cotté and P. Blanc-Benon, *Time-domain simulations of sound propagation in a stratified atmosphere over an impedance ground*, J. Acoust. Soc. Am. **125**, EL202 (2009).
- [26] D. Dragna, P. Blanc-Benon, and F. Poisson, *Time-domain solver in curvilinear coordinates for outdoor sound propagation over complex terrain*, J. Acoust. Soc. Am. **133**, 3751 (2013).
- [27] T. Oshima, M. Imano, Y. Hiraguri, and Y. Kamoshida, *Linearized euler simulations of sound propagation with wind effects over a reconstructed urban terrain using digital geographic information*, Appl. Acoust. **74**, 1354 (2013).

- [28] S. Sakamoto, T. Seimiya, and H. Tachibana, *Visualization of sound reflection and diffraction using finite difference time domain method*, *Acoustical Science and Technology* **23**, 34 (2002).
- [29] V. E. Ostashev, D. K. Wilson, L. Liu, D. F. Aldridge, N. P. Symons, and D. Marlin, *Equations for finite-difference, time-domain simulation of sound propagation in moving inhomogeneous media and numerical implementation*, *J. Acoust. Soc. Am.* **117**, 503 (2005).
- [30] V. E. Ostashev and T. Van Renterghem, *Equations for finite-difference, time-domain simulation of sound propagation in moving media with arbitrary mach numbers*, *J. Acoust. Soc. Am.* **153**, 2203 (2023).
- [31] J. Gazdag, *Modeling of the acoustic wave equation with transform methods*, *Geophysics* **46**, 854 (1981).
- [32] X. Huang and X. Zhang, *A fourier pseudospectral method for some computational aeroacoustics problems*, *International Journal of Aeroacoustics* **5**, 279 (2006).
- [33] B. T. Cox, S. Kara, S. R. Arridge, and P. C. Beard, *k-space propagation models for acoustically heterogeneous media: Application to biomedical photoacoustics*, *J. Acoust. Soc. Am.* **121**, 3453 (2007).
- [34] C. E. Wasberg and Ø. Andreassen, *Pseudospectral methods with open boundary conditions for the study of atmospheric wave phenomena*, *Computer methods in applied mechanics and engineering* **80**, 459 (1990).
- [35] M. Hornikx, R. Waxler, and J. Forssén, *The extended fourier pseudospectral time-domain method for atmospheric sound propagation*, *J. Acoust. Soc. Am.* **128**, 1632 (2010).
- [36] J. S. Hesthaven, S. Gottlieb, and D. Gottlieb, *Spectral methods for time-dependent problems*, Vol. 21 (Cambridge University Press, 2007).
- [37] Q. Mo, H. Yeh, M. Lin, and D. Manocha, *Outdoor sound propagation with analytic ray curve tracer and Gaussian beam*, *J. Acoust. Soc. Am.* **141**, 2289 (2017).
- [38] P. B. Johns and R. L. Beurle, *Numerical solution of 2-dimensional scattering problems using a transmission-line matrix*, in *Proceedings of the Institution of Electrical Engineers*, Vol. 118 (IET, 1971) pp. 1203–1208.
- [39] M. Blau and A. Wilde, *Room acoustical simulation at low frequencies using the scattering element method*, *In other words* **2**, 6 (2004).
- [40] W. O'Connor and F. Cavanagh, *Transmission line matrix acoustic modelling on a pc*, *Appl. Acoust.* **50**, 247 (1997).
- [41] G. Guillaume, P. Aumond, B. Gauvreau, and G. Dutilleux, *Application of the transmission line matrix method for outdoor sound propagation modelling—part 1: Model presentation and evaluation*, *Appl. Acoust.* **76**, 113 (2014).

- [42] P. Aumond, G. Guillaume, B. Gauvreau, C. Lac, V. Masson, and M. Berengier, *Application of the transmission line matrix method for outdoor sound propagation modelling—part 2: Experimental validation using meteorological data derived from the meso-scale model meso-nh*, *Appl. Acoust.* **76**, 107 (2014).
- [43] J. Hofmann and K. Heutschi, *Simulation of outdoor sound propagation with a transmission line matrix method*, *Appl. Acoust.* **68**, 158 (2007).
- [44] Y. Kagawa, T. Tsuchiya, T. Hara, and T. Tsuji, *Discrete huygens' modelling simulation of sound wave propagation in velocity varying environments*, *Journal of Sound and Vibration* **246**, 419 (2001).
- [45] F. Dinapoli and R. Deavenport, *Ocean acoustics*, in *Topics in Current Physics Series* (Springer-Verlag, 1979).
- [46] F. B. Jensen, W. A. Kuperman, M. B. Porter, H. Schmidt, and A. Tolstoy, *Computational ocean acoustics*, Vol. 794 (Springer, 2011).
- [47] R. Raspet, S. Lee, E. Kuester, D. Chang, W. Richards, R. Gilbert, and N. Bong, *A fast-field program for sound propagation in a layered atmosphere above an impedance ground*, *J. Acoust. Soc. Am.* **77**, 345 (1985).
- [48] S. Lee, N. Bong, W. Richards, and R. Raspet, *Impedance formulation of the fast field program for acoustic wave propagation in the atmosphere*, *J. Acoust. Soc. Am.* **79**, 628 (1986).
- [49] L. Nijs and C. Wapenaar, *The influence of wind and temperature gradients on sound propagation, calculated with the two-way wave equation*, *J. Acoust. Soc. Am.* **87**, 1987 (1990).
- [50] D. K. Wilson, *Sound field computations in a stratified, moving medium*, *J. Acoust. Soc. Am.* **94**, 400 (1993).
- [51] E. M. Salomons, *Computational atmospheric acoustics* (Springer Science & Business Media, 2001).
- [52] F. D. Tappert, *Wave propagation and underwater acoustics*, *Lecture Notes in Physics* **70**, 224 (1977).
- [53] D. Lee, A. D. Pierce, and E.-C. Shang, *Parabolic equation development in the twentieth century*, *Journal of Computational Acoustics* **8**, 527 (2000).
- [54] K. E. Gilbert and M. J. White, *Application of the parabolic equation to sound propagation in a refracting atmosphere*, *J. Acoust. Soc. Am.* **85**, 630 (1989).
- [55] K. E. Gilbert and X. Di, *A fast green's function method for one-way sound propagation in the atmosphere*, *J. Acoust. Soc. Am.* **94**, 2343 (1993).
- [56] X. Di and K. E. Gilbert, *Wave propagation in a 3-d turbulent atmosphere: horizontal coherence*, in *Eighth International Symposium on Long Range Sound Propagation, University Park, PA, USA* (1998) pp. 169–180.

- [57] R. Sack and M. West, *A parabolic equation for sound propagation in two dimensions over any smooth terrain profile: the generalised terrain parabolic equation (gt-pe)*, *Appl. Acoust.* **45**, 113 (1995).
- [58] V. E. Ostashev, D. K. Wilson, and M. B. Muhlestein, *Wave and extra-wide-angle parabolic equations for sound propagation in a moving atmosphere*, *J. Acoust. Soc. Am.* **147**, 3969 (2020).
- [59] Q. Mo, H. Yeh, M. Lin, and D. Manocha, *Analytic ray curve tracing for outdoor sound propagation*, *Appl. Acoust.* **104**, 142 (2016).
- [60] M. Taylor, A. Chandak, Q. Mo, C. Lauterbach, C. Schissler, and D. Manocha, *Guided multiview ray tracing for fast auralization*, *IEEE Transactions on Visualization and Computer Graphics* **18**, 1797 (2012).
- [61] C. Schissler, R. Mehra, and D. Manocha, *High-order diffraction and diffuse reflections for interactive sound propagation in large environments*, *ACM Transactions on Graphics (TOG)* **33**, 1 (2014).
- [62] S. Siltanen, T. Lokki, S. Kiminki, and L. Savioja, *The room acoustic rendering equation*, *J. Acoust. Soc. Am.* **122**, 1624 (2007).
- [63] K. Heutschi, *A simple method to evaluate the increase of traffic noise emission level due to buildings, for a long straight street*, *Appl. Acoust.* **44**, 259 (1995).
- [64] J. Kang, *Sound propagation in interconnected urban streets: A parametric study*, *Environment and Planning B: Planning and Design* **28**, 281 (2001), <https://doi.org/10.1068/b2680>.
- [65] M. Dreher, G. Dutilleux, and F. Junker, *Optimized 3D ray tracing algorithm for environmental acoustic studies*, in *Acoustics 2012*, edited by S. F. d'Acoustique (Nantes, France, 2012).
- [66] J. B. Allen and D. A. Berkley, *Image method for efficiently simulating small-room acoustics*, *J. Acoust. Soc. Am.* **65**, 943 (1979).
- [67] T. Funkhouser, N. Tsingos, I. Carlbom, G. Elko, M. Sondhi, J. E. West, G. Pingali, P. Min, and A. Ngan, *A beam tracing method for interactive architectural acoustics*, *J. Acoust. Soc. Am.* **115**, 739 (2004).
- [68] J. Borish, *Extension of the image model to arbitrary polyhedra*, *J. Acoust. Soc. Am.* **75**, 1827 (1984).
- [69] Q. Mo, H. Yeh, and D. Manocha, *Tracing analytic ray curves for light and sound propagation in non-linear media*, *IEEE transactions on visualization and computer graphics* **22**, 2493 (2015).
- [70] C. Chessell, *Three-dimensional acoustic-ray tracing in an inhomogeneous anisotropic atmosphere using hamilton's equations*, *J. Acoust. Soc. Am.* **53**, 83 (1973).

- [71] P. Uginčius, *Ray acoustics and Fermat's principle in a moving inhomogeneous medium*, *J. Acoust. Soc. Am.* **51**, 1759 (1972).
- [72] S. M. Reilly, *WaveQ3D: Fast and accurate acoustic transmission loss (TL) eigenrays, in littoral environments*, Ph.D. thesis, University of Rhode Island (2016).
- [73] M. Arntzen, D. G. Simons, J. Shen, A. L. Varbanescu, and H. Sips, *Acoustic ray tracing parallelization*, Tech. Rep. (2015).
- [74] V. Cervený, *Seismic ray theory* (Cambridge university press Cambridge, 2001).
- [75] D. O. Elorza, *Room acoustics modeling using the raytracing method: implementation and evaluation*, Master thesis, Turku (Finland): University of Turku, Department of Physics (2005).
- [76] M. M. Boone and E. A. Vermaas, *A new ray-tracing algorithm for arbitrary inhomogeneous and moving media, including caustics*, *J. Acoust. Soc. Am.* **90**, 2109 (1991).
- [77] L. Yang and B. Shield, *Development of a ray tracing computer model for the prediction of the sound field in long enclosures*, *Journal of Sound and Vibration* **229**, 133 (2000).
- [78] R. N. Buchal and J. Keller, *Boundary layer problems in diffraction theory*, (1960), [10.1002/cpa.3160130109](https://doi.org/10.1002/cpa.3160130109).
- [79] D. Ludwig, *Uniform asymptotic expansions at a caustic*, *Communications on Pure and Applied Mathematics* **19**, 215 (1966).
- [80] I. KRAVTSOV, *Two new asymptotic methods in the theory of wave propagation in inhomogeneous media (asymptotic methods in wave propagation theory in inhomogeneous media, reviewing solutions in acoustics and radio physics)*, *Soviet Physics-Acoustics* **14**, 1 (1968).
- [81] M. Arntzen, S. Rizzi, D. Simons, and H. Visser, *A framework for simulation of aircraft flyover noise through a non-standard atmosphere*, in *18th AIAA/CEAS Aeroacoustics Conference (33rd AIAA Aeroacoustics Conference)* (2012) <https://arc.aiaa.org/doi/pdf/10.2514/6.2012-2079>.
- [82] R. de Moraes Calazan and O. C. Rodríguez, *Simplex based three-dimensional eigenray search for underwater predictions*, *J. Acoust. Soc. Am.* **143**, 2059 (2018).
- [83] B. Julian, D. Gubbins, *et al.*, *Three-dimensional seismic ray tracing*, *Journal of Geophysics* **43**, 95 (1977).
- [84] K. Koketsu and S. Sekine, *Pseudo-bending method for three-dimensional seismic ray tracing in a spherical earth with discontinuities*, *Geophysical Journal International* **132**, 339 (1998).
- [85] H. Sadeghi, S. Suzuki, and H. Takenaka, *A two-point, three-dimensional seismic ray tracing using genetic algorithms*, *Physics of the Earth and Planetary Interiors* **113**, 355 (1999).

- [86] H. Keller and D. Perozzi, *Fast seismic ray tracing*, [SIAM Journal on Applied Mathematics](#) **43**, 981 (1983).
- [87] M. B. Porter and H. P. Buckner, *Gaussian beam tracing for computing ocean acoustic fields*, [J. Acoust. Soc. Am.](#) **82**, 1349 (1987).
- [88] Y. Gabillet, H. Schroeder, G. A. Daigle, and A. L'Espérance, *Application of the Gaussian beam approach to sound propagation in the atmosphere: Theory and experiments*, [J. Acoust. Soc. Am.](#) **93**, 3105 (1993).
- [89] M. B. Porter, *Beam tracing for two- and three-dimensional problems in ocean acoustics*, [J. Acoust. Soc. Am.](#) **146**, 2016 (2019).
- [90] N. Dadoun, D. G. Kirkpatrick, and J. P. Walsh, *The geometry of beam tracing*, in [Proceedings of the first annual symposium on Computational geometry](#) (1985) pp. 55–61.
- [91] V. Červený, M. M. Popov, and I. Pšenčík, *Computation of wave fields in inhomogeneous media—Gaussian beam approach*, [Geophysical Journal International](#) **70**, 109 (1982).
- [92] H. Weinberg and R. E. Keenan, *Gaussian ray bundles for modeling high-frequency propagation loss under shallow-water conditions*, [J. Acoust. Soc. Am.](#) **100**, 1421 (1996).
- [93] S. M. Reilly, G. R. Potty, and M. Goodrich, *Computing acoustic transmission loss using 3d gaussian ray bundles in geodetic coordinates*, [Journal of Computational Acoustics](#) **24**, 1650007 (2016).
- [94] H. Lehnert, *Systematic errors of the ray-tracing algorithm*, [Appl. Acoust.](#) **38**, 207 (1993).
- [95] J. Amanatides, *Ray tracing with cones*, [ACM SIGGRAPH Computer Graphics](#) **18**, 129 (1984).
- [96] J. Vian and D. van Maercke, *Calculation of the room impulse response using a ray tracing method*, in [ICA Symposium at Vancouver, 1986](#) (1986).
- [97] V. Červený and I. Pšenčík, *Gaussian beams in inhomogeneous anisotropic layered structures*, [Geophys. J. Int.](#) **180**, 798 (2010).
- [98] H. Bian, R. Fattah, S. Zhong, and X. Zhang, *An efficient rectilinear Gaussian beam tracing method for sound propagation modelling in a non-turbulent medium*, [J. Acoust. Soc. Am.](#) **148**, 4037 (2020).
- [99] H. Bian, R. Fattah, S. Zhong, and X. Zhang, *On the efficient modeling of generic source directivity in Gaussian beam tracing*, [J. Acoust. Soc. Am.](#) **149**, 2743 (2021).
- [100] H. Bian, Q. Tan, S. Zhong, and X. Zhang, *Efficient computation of broadband noise propagation using Gaussian beam tracing method*, [J. Acoust. Soc. Am.](#) **151**, 3387 (2022).

- [101] R. G. Kouyoumjian and P. H. Pathak, *A uniform geometrical theory of diffraction for an edge in a perfectly conducting surface*, *Proceedings of the IEEE* **62**, 1448 (1974).
- [102] D. I. Blokhintsev, *Acoustics of a Nonhomogeneous Moving Medium*, Tech. Rep. (Physics Dept. Brown Univ., 1956).
- [103] V. Červený and T. Jan Moser, *Ray propagator matrices in three-dimensional anisotropic inhomogeneous layered media*, *Geophys. J. Int.* **168**, 593 (2007).
- [104] A. D. Pierce, *Acoustics: an introduction to its physical principles and applications*, 3rd ed. (Springer, 2019).
- [105] A. D. Pierce, *Wave equation for sound in fluids with unsteady inhomogeneous flow*, *J. Acoust. Soc. Am.* **87**, 2292 (1990).
- [106] L. Klimeš, *Transformations for dynamic ray tracing in anisotropic media*, *Wave Motion* **20**, 261 (1994).
- [107] V. Červený and L. Klimeš, *Transformation relations for second-order derivatives of travel time in anisotropic media*, *Studia Geophysica et Geodaetica* **54**, 257 (2010).
- [108] T. J. Moser and V. Červený, *Paraxial ray methods for anisotropic inhomogeneous media*, *Geophys. Prospect.* **55**, 21 (2007).
- [109] V. Červený *et al.*, *Gaussian beam synthetic seismograms*, *Journal of Geophysics* **58**, 44 (1985).

3

NOISE SOURCE PREDICTION

Normality is a paved road: It's comfortable to walk, but no flowers grow on it.

Vincent van Gogh

This chapter reports the numerical methods employed in this dissertation to predict noise source. Noise source prediction using the high-fidelity approach, based on the lattice-Boltzmann method (LBM), is described firstly. Then the low-order approach, based on the blade element momentum theory coupled with a time-domain compact dipole/monopole formulation and a frequency-domain analytical formulation, is presented.

3.1. HIGH-FIDELITY METHODS

3.1.1. COMPUTATIONAL FLUID DYNAMICS

THE CFD method adopted throughout this thesis is the lattice-Boltzmann method (LBM), which is implemented in the commercial software SIMULIA PowerFLOW® 6-2019.

The LBM is derived from Boltzmann's kinetic theory, which describes the advection of fluid particles on a microscopic scale and momentum exchange due to collisions between them. Fluid properties at the macroscopic level, such as momentum, pressure, and temperature, result from microscopic particle movements and momentum exchanges. Boltzmann's kinetic theory adopts a statistical approach to describe the particle motion at a position \mathbf{x} with discrete velocity \mathbf{V} at time t . The instantaneous state of the fluid is then determined using a probability density function $F(\mathbf{x}, t, \mathbf{V})$, which represents the probability of finding a particle with velocity \mathbf{V} at a spatial coordinate \mathbf{x} and time instance t . The Boltzmann transport equation (BTE), without the body force, reads

$$\frac{\partial F}{\partial t} + \mathbf{V} \cdot \nabla F = \boldsymbol{\kappa}. \quad (3.1)$$

The left-hand side of Eq. 3.1 describes the advection of fluid particles. On the right-hand side is the collision operator $\boldsymbol{\kappa}$, which describes the particle velocity distribution due to momentum exchanges between particles.

In the LBM, the BTE is discretized onto a Cartesian grid, i.e., lattice, and the discrete lattice-Boltzmann equation is given by:

$$F_q(\mathbf{x} + \mathbf{V}_q \Delta t, t + \Delta t) - F_q(\mathbf{x}, t) = \boldsymbol{\kappa}_q(\mathbf{x}, t), \quad (3.2)$$

where F_q is the particle distribution function in the q^{th} direction of the lattice, \mathbf{V}_q is the discrete particle velocity vector. The subscript represents a specific direction of the lattice, equal to the number of discrete velocity vectors. The left-hand side of Eq. 3.2 represents a time-explicit advection with the increment of in space $\Delta \mathbf{x} = \mathbf{V}_q \Delta t$ and in time Δt . On the right-hand side is a collision operator $\boldsymbol{\kappa}_q$.

The LBM considers the macroscopic flow quantities, such as density ρ , velocity \mathbf{u} , and total energy E , as a weighted average of the microscopic ones. The macroscopic flow quantities are obtained by computing the following moments of the distribution function F_q [1]:

$$\left. \begin{aligned} \rho(\mathbf{x}, t) &= \sum_q F_q(\mathbf{x}, t) \\ \rho \mathbf{u}(\mathbf{x}, t) &= \sum_q \mathbf{V}_q F_q(\mathbf{x}, t) \\ \rho E(\mathbf{x}, t) &= \sum_q \frac{1}{2} \mathbf{V}_q^2 F_q(\mathbf{x}, t) \end{aligned} \right\}. \quad (3.3)$$

The first step of LBM simulation is initialization. In this step, the simulation domain is discretized, and an initial state is imposed. The initial state can be a rest state, i.e., zero velocity, in the entire lattice or can also be directly imported from a different simulation

which is often referred to as "seeding". This is a typical case, for instance, for simulating a UAM vehicle operating in a windy urban area, where wind flow in the metropolitan area can be seeded from a previous simulation as an initial state. The second step involves the following two operations for each time step in the explicit time marching scheme: advection and collision. During advection, the particle distribution function in each lattice is shifted to the adjacent lattices according to discrete velocity directions, as described by Eq. 3.2, with the collision term assumed to be zero. In the collision step, macroscopic flow quantities are computed at each node based on the previously advected distribution functions. These quantities are then used to calculate the local equilibrium distribution function and collision term. Finally, the local distribution functions are updated (F_q^*) by incorporating the results of the collision process:

$$F_q^*(\mathbf{x} + \mathbf{V}_q \Delta t, t + \Delta t) = F_q(\mathbf{x} + \mathbf{V}_q \Delta t, t + \Delta t) + \kappa_q. \quad (3.4)$$

In the LBM, the most commonly used collision operator is the Bhatnagar-Gross-Krook (BGK) model [3], which is given by the relation

$$\kappa = -\frac{1}{\tau} [F_q(\mathbf{x}, t) - F_q^{eq}(\mathbf{x}, t)], \quad (3.5)$$

which expresses that the local distribution function F returns to the equilibrium one (F^{eq}) within a time scale τ , which is a function of F . The equilibrium distribution F_q^{eq} can take the form of the regular Maxwell-Boltzmann distribution [4].

$$F_q^{eq} = \frac{\rho}{(2\pi RT)^{D/2}} \exp\left(-\frac{|\mathbf{V}_q - \mathbf{u}|^2}{2RT}\right), \quad (3.6)$$

where R is the ideal gas constant, T is the gas temperature, and D is the number of spatial dimensions.

In this work, the simulations are conducted with an imposed ambient fluid temperature, and there are no significant thermal effects that require a highly accurate solution for the energy equation. Thus, a third-order expansion is used to approximate the equilibrium distribution function F_q^{eq} [2, 3]

$$F_q \approx \rho w_q \left[1 + \frac{(\mathbf{V}_q \cdot \mathbf{u})}{\Theta} + \frac{(\mathbf{V}_q \cdot \mathbf{u})^2}{2\Theta^2} - \frac{\mathbf{u}^2}{2\Theta} + \frac{(\mathbf{V}_q \cdot \mathbf{u})^3}{6\Theta^3} - \frac{(\mathbf{V}_q \cdot \mathbf{u})\mathbf{u}^2}{2\Theta^2} \right]. \quad (3.7)$$

The LBM solver employs the formulation Eq. 3.7 within a 3D lattice with 19 discrete velocity vectors, which are the abscissae of Gaussian-Hermite quadratures, also referred to as the D3Q19 model (see Fig. 3.1). For this model, the non-dimensional lattice temperature is $\Theta = 1/3$, while $w_q = 1/3$ for the rest velocity ($q = 0$), $1/18$ for the main axes, and $1/36$ for the diagonals. The relaxation time τ in the BGK model behaves as a kinematic viscosity ν . For a lattice with a grid spacing of Δx and time-step Δt , a relation between ν and τ can be established by using the Chapman-Enskog expansion [5] as

$$\nu = \frac{1}{3} \left(\frac{\Delta x}{\Delta t} \right)^2 \left(\tau - \frac{\Delta t}{2} \right). \quad (3.8)$$

The LBM scheme is performed on a lattice made of cubic elements known as voxels or volume elements [6]. The simulation domain is typically subdivided into regions with

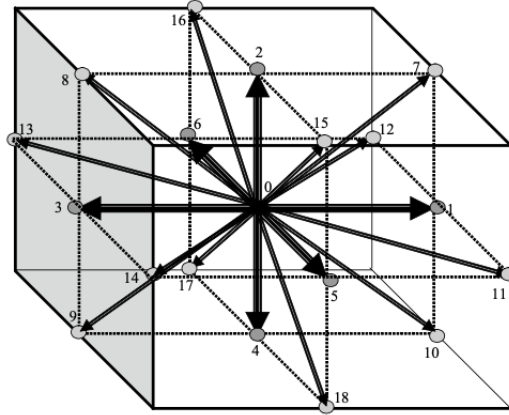


Figure 3.1: Lattice arrangements for 3-D problems with 19-velocity vectors [4].

varying voxel resolution (VR) levels, i.e., grid size. The resolution levels between adjacent regions vary by a factor of 2 [7]. The highest resolution or the finest voxel dimension is specified as a number of voxels along a prescribed characteristic length, e.g., an airfoil chord, with which a timestep is chosen such that the Courant number is equal to 1. The distribution function in each voxel is computed and updated at every time step for the finest resolution region, while the process is performed at different time steps according to the voxel resolution level. For instance, at coarser VRs, this process occurs at every 2^M time step, where M is the difference between the finest VR level and the respective one. To ensure the conservation of mass, momentum, and energy across regions with different resolution levels, a voxel-centered lattice scheme has been employed [7]. Solid walls are discretized using planar surfaces known as surfels or surface elements, which are tangential to the surface curvature.

Several boundary conditions are employed in the present study: periodic, inlet/outlet, and wall boundary conditions. The periodic boundary condition allows one to approximate an infinite domain in which geometry and flow features are expected to be repeated indefinitely. Implementing the periodic boundary condition is straightforward as distribution functions from one side of the domain need to be advected directly to the opposite side. Inlet and outlet boundary conditions are modeled by assuming that $F_q = F_q^{eq}$ at the boundaries. This enables one to specify certain values of macroscopic quantities, such as density, pressure, and velocity at the domain inlet and outlet. Wall boundary conditions are implemented using two techniques, depending on the selected surface characteristic. A bounce-back method is employed to model a no-slip wall. This is achieved by reflecting the particles in a direction opposite to the incident direction while maintaining the same velocities, i.e., $V_{q'} = -V_q$, where $V_{q'}$ is the reflected particle velocity. At the same time, a free-slip wall is modeled with a specular reflection process. In this technique, the incoming particles are deflected while their tangential velocity components are preserved. For the wall-normal velocity component $V_{q'} \cdot \mathbf{n} = -V_q \cdot \mathbf{n}$ and for the wall-parallel velocity component $V_{q'} - (V_{q'} \cdot \mathbf{n})\mathbf{n} = V_q - (V_q \cdot \mathbf{n})\mathbf{n}$, where \mathbf{n} is a

local unitary wall-normal vector.

VLES TURBULENCE MODEL

The LBM solver incorporates turbulence modeling into its scheme [8] by using a modified two-equation $\kappa - \epsilon$ model based on the renormalization group (RNG) formulation [9, 10]. This model operates on the unresolved scales [11], which are determined based on the local flow swirl [12]. In the LBM ecosystem, this methodology is referred to as LBM-very large eddy simulation (LBM-VLES). It is conceptually similar to non-zonal¹ hybrid RANS/LES, DES, or scale adaptive simulations (SAS) approaches [13]. The turbulence relaxation time τ_{turb} is calculated based on the modified two-equation RNG $\kappa - \epsilon$ model, which takes into account the contribution of all scales of turbulence on diffusion, unlike the regular $\kappa - \epsilon$ model. The effective relaxation time τ_{eff} takes the form

$$\tau_{eff} = \tau + \tau_{turb} = \tau + C_{\mu} \frac{\kappa^2 / \epsilon}{T(1 + \tilde{\eta}^2)^{1/2}}, \quad (3.9)$$

where $C_{\mu} = 0.09$, κ and ϵ are the turbulent kinetic energy and dissipation, respectively, and $\tilde{\eta}$ is a function of local strain parameter ($\kappa|S_{ij}|/\epsilon$), local vorticity parameter ($k|\Omega_{ij}|/\epsilon$), and local helicity parameters [10]. This approach allows for alleviating the sub-grid scale viscosity so that the resolved large-scale structures, which are responsible for most of the noise generation, are not numerically distorted or dampened.

The relaxation time in LBM is adjusted to match the characteristic time scales of turbulent flow motion. As a result, Reynolds stresses do not need to be explicitly included in the governing equations but rather emerge implicitly due to the chaotic exchange of momentum caused by turbulent flow. These stresses have a non-linear structure and are better able to represent turbulence in a non-equilibrium state, such as in the presence of distortion, shear, and rotation [14].

In LBM-VLES, unlike Navier-Stokes-based formulations, the Reynolds stresses are not solved simultaneously with the flow governing equations. Instead, the Reynolds stresses are considered as part of the solution [14] and can be obtained by computing the moment around the particle distribution function. This is because in Navier-Stokes-based formulations, the turbulence model is used as a closure of the flow governing equations as the Reynolds stresses are unknown, while in LBM-VLES, they are explicitly considered in the solution. The macroscopic flow properties, such as velocity and pressure, can also be computed using this method [15].

In order to improve the accuracy of the simulation without requiring an overly fine mesh near the wall, a wall function is applied to the first voxel adjacent to a surface with no slip. This is particularly important for high Reynolds number flows, where the thickness of the boundary layer (including the viscous sublayer) is small. By using a wall

¹"Non-zonal" refers to the absence of clear zones or regions in the simulation domain where only one type of turbulence modeling (either RANS or LES) is applied. In traditional hybrid RANS/LES methods, the simulation domain is divided into two regions: one where a RANS turbulence model is applied, and another where an LES turbulence model is applied. The boundary between these two regions is referred to as the "zonal" boundary. In non-zonal hybrid RANS/LES methods, this clear division into two regions is not present. Instead, a continuous transition is made between RANS and LES turbulence modeling, depending on the local flow conditions.

function, the mesh can be coarser near the wall while still capturing the important features of the flow. The wall function is based on the generalized law-of-the-wall model [16], extended to consider the effects of pressure gradient and surface roughness. The wall function is expressed as follows,

$$U^+ = \frac{1}{K} \ln \left(\frac{y^+}{A} \right) + B, \quad (3.10)$$

where

$$A = 1 + g \left(\frac{dp}{ds} \right), \quad B = 5.0, \quad K = 0.41, \quad y^+ = \frac{u_\tau y}{\nu}, \quad (3.11)$$

where $A = 1 + g(dp/ds)$ is a function of the pressure gradient dp/ds , $B = 5.0$, $K = 0.41$ and $y^+ = u_\tau y/\nu$.

The LBM-VLES used in this study offers a significant advantage over a Navier-Stokes formulation due to its inherent low dissipative and dispersive nature. This is particularly important for accurate prediction of acoustic perturbations, which are typically much lower than the characteristic pressure of a flow [17, 18]. Moreover, LBM's third-order scheme is less dissipative [18], making it effective in achieving accurate predictions of noise source propagation. The particle collision step in the solution process is carried out locally at each node and is independent of others, making it highly parallelizable using both CPUs and GPUs, reducing computational time and cost significantly [17].

3.1.2. AEROACOUSTIC PREDICTIONS

The aeroacoustic prediction in the high-fidelity approach is performed by employing computational aeroacoustics (CAA) methods. CAA methods refer to numerical techniques predicting the generation and propagation² of aerodynamically-generated sound. CAA methods can be divided into direct noise computation (DNC) and aeroacoustic analogies. The former refers to a numerical technique where acoustic information like acoustic pressure fluctuations, for instance, is obtained directly from within the simulation domain as part of the numerical simulation. In contrast to the approach discussed earlier, the noise computation and the flow simulation are separated in this method. The LBM-VLES is used for calculating noise sources, which include turbulence and other non-linearities in the flow field, for a relatively small domain that encompasses the source region where sound is generated. On the other hand, outside the source region, the noise propagation problem is solved using methods outlined in Chapter 2.

There are different hybrid CAA methods [19], such as the linearised Euler equations (LEE) [20], acoustic perturbation equations (APE) [21], and acoustic analogies, among others. The present dissertation considers only hybrid CAA methods based on the acoustic analogy.

FFOCWS-WILLIAMS & HAWKINGS ANALOGY AND THE ADVANCED TIME FORMULATION

To begin the FW-H acoustic analogy, a control surface \mathbb{S} is defined using a function $\mathbb{S}(\mathbf{x}, t) = 0$ that moves with velocity $\mathbf{u}_{\mathbb{S}}(\mathbf{x}, t)$, where \mathbf{x} and t represent the observer po-

²Due to computational complexity and expense in run-time, CAA-based propagation prediction is limited to a short range within a free space without obstacles.

sition and reception time, respectively. The function $\mathbb{S}(\mathbf{x}, t)$ is designed such that it has a negative value inside the flow region enclosed by the surface and a positive value outside of it, as shown in Fig. 3.2. In Fig. 3.2, the unit vector \mathbf{n} is normal to the surface \mathbb{S} , pointing in the outward direction, and satisfies $\nabla\mathbb{S} = \mathbf{n}$. In addition, \mathbf{u} denotes the flow velocity vector and \mathbf{y} represents the position of the source. The observer moves with velocity \mathbf{u}_0 . The inner volume of the control surface is assumed to be filled with fluid at rest, characterized by the density ρ_0 , pressure p_0 , and velocity $u_i = 0$. To maintain the conservative nature of the field, a distribution of mass and momentum sources is imposed on the control surface. This can be expressed in terms of generalized continuity and momentum equations using the Dirac $\delta(\mathbb{S})$ and Heaviside $H(\mathbb{S})$ functions [22]. The

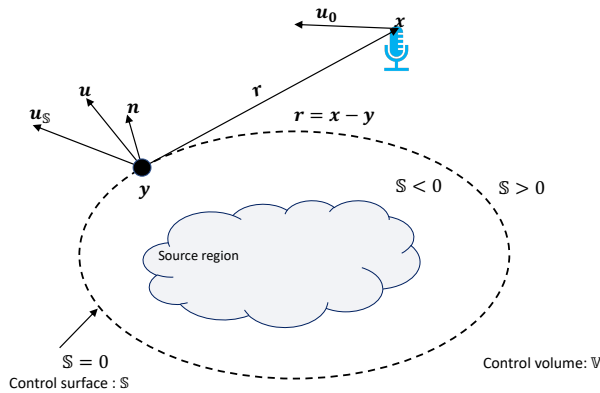


Figure 3.2: A sketch of the notations used in the formulation of the FW-H analogy, adapted from [23].

FW-H equation is given by [24, 25]

$$\square^2 \left[\rho' c_0^2 H(\mathbb{S}) \right] = \frac{\partial^2}{\partial x_i \partial x_j} [T_{ij} H(\mathbb{S})] - \frac{\partial}{\partial x_i} [L_i \delta(\mathbb{S})] + \frac{\partial}{\partial t} [Q_i \delta(\mathbb{S})] \quad (3.12)$$

with

$$Q = \rho_0 U_i n_i, \quad U_i = \left(1 - \frac{\rho}{\rho_0} \right) u_{\mathbb{S},i} + \frac{\rho u_i}{\rho_0}, \quad (3.13)$$

$$L_i = P_{ij} n_j + \rho u_i (u_n - u_{\mathbb{S},n}), \quad P_{ij} = (p - p_\infty) \delta_{ij} - \zeta_{ij}, \quad (3.14)$$

where $\square^2 = \frac{1}{c_0^2} \frac{\partial^2}{\partial t^2} - \frac{\partial^2}{\partial x_i^2}$ is the d'Alembert operator. The Heaviside function $H(\mathbb{S})$ by its definition (which is zero inside the control surface and one on and outside the control surface) restricts the validity of the equation to the surface boundary and the exterior. Eq. 3.12 is an exact equation, because it is a reformulation of the general fluidy dynamics equations. The left-hand side of equation Eq. 3.12 represents the acoustic wave propagation in free space, whereas the righ-hand side represents the noise sources. The first term on the right-hand side contains the Lighthill stress tensor contribution within the control volume. The second term is related to the unsteady forces exerted by the control surface onto the surrounding fluid, otherwise referred to as the loading source term.

The last one is the thickness source term, which accounts for the fluid displacement by the control surface. The Lighthill stress tensor is equivalent to a quadrupole source, while the loading source term corresponds to a dipole and the thickness source term to a monopole. An illustration of these sources is given in Fig. 3.3.

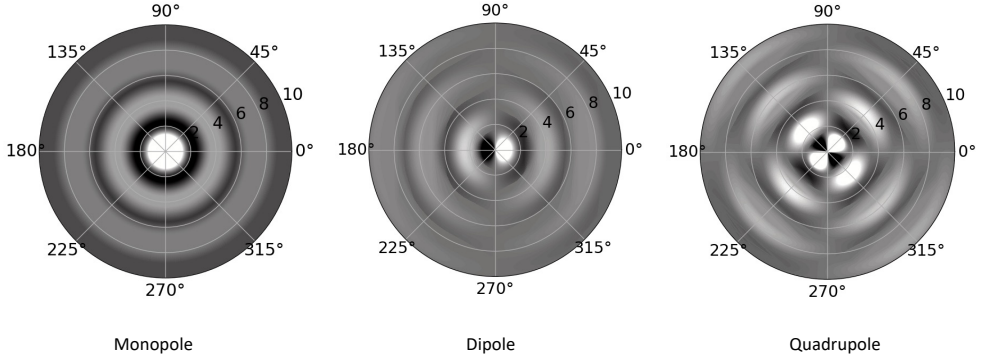


Figure 3.3: An illustration of various elementary acoustic sources in linear acoustic theory and their corresponding directivity patterns based on the wave propagation behavior. The plots are generated using analytical formulations [26].

The far-field solution of the FW-H equation can be obtained by employing the free-space Green's function [24].

$$\begin{aligned}
 4\pi p' = & \frac{\partial^2}{\partial x_i \partial x_j} \int_{\mathbb{S}>0} \left[\frac{T_{ij}}{\mathbf{r}(1-M_r)} \right]_{t'} dV \\
 & - \frac{\partial}{\partial x_i} \int_{\mathbb{S}=0} \left[\frac{L_i}{\mathbf{r}(1-M_r)} \right]_{t'} d\mathbb{S} \\
 & + \frac{\partial}{\partial t} \int_{\mathbb{S}=0} \left[\frac{Q}{\mathbf{r}(1-M_r)} \right]_{t'} d\mathbb{S},
 \end{aligned} \tag{3.15}$$

where subscript t' indicates that each source term is calculated at a retarded time $t' = t - (|\mathbf{x}_s(t) - \mathbf{x}_o(t')|/c_0)$, $\mathbf{r} = \mathbf{x}_o - \mathbf{x}_s$ and $M_r = M_{\mathbb{S},i} \mathbf{r}/|\mathbf{r}|$ is the projected source Mach number vector in the direction of the observer. $(1-M_r)$ is the Doppler amplification factor related to the projected motion on the line joining the source to the observer at \mathbf{x}_o .

The retarded time solution to the FW-H equation can be further simplified with some approximations. At low Mach numbers, for instance, the quadrupole source term can be neglected with respect to the others. For rotating machines, each blade section can be considered a compact dipole and monopole source, where the source terms take even simpler forms. The compact dipole/monopole formulation of the FW-H equation will be discussed in detail in the later part of the next section. Furthermore, if the control surface is considered to be solid, rigid, and non-vibrating, the monopole source term can also be discarded. As a result, only the dipole sources on the solid surface are relevant in this case. This simplification leads to the so-called solid FW-H formulation. Due to its

simplicity, the solid FW-H formulation has been widely used for aeroacoustics investigations [27]. However, it is not useful for cases where quadrupole sources are essential, such as helicopter high-speed impulsive noise.

This limitation has been removed by introducing a permeable control surface into the FW-H analogy [28]. The permeable surface encloses the entire source region, where flow non-linearities are present, thus including contributions of quadrupole sources. The contribution of quadrupole sources is incorporated by monopoles and dipoles that are distributed along the permeable surface as the Lighthill stress tensor is zero outside of the permeable surface. As a result, the permeable approach is more comprehensive compared to the solid FW-H method, with no substantial increase in computational expenses. However, the arrangement of the permeable surface in the simulation domain can become an issue in some applications [27]. For instance, the permeable FW-H surface can cut across regions containing vortical perturbations, such as turbulence in the wake of a propeller. Turbulent fluctuations passing through the permeable surface can be considered pseudo-sound sources³ that degrade the noise computation result. The present work adopts the multi-end-caps approach in calculating source noise in the high-fidelity approach, in which the noise computed using each end-cap is averaged to filter out spurious noise introduced by the larger vortical structures from the wake of the rotor.

To enhance the practicality of the FW-H solution for numerical implementation, Farassat derived formulation 1A [30]. In the 1A formulation, the spatial derivatives in Eq. 3.15 are converted into time derivatives and subsequently shifted inside the integrals using the retarded time formulation [31]. Thus, the temporal variation of the source's properties is used to calculate the thickness and loading noise components. In addition, the integral formulation is extended to account for a moving observer with a constant velocity $u_o = M_o c_0$ as illustrated in Fig. 3.2.

As an alternative to the retarded time solution of the FW-H equation, Casalino [23] proposed an advanced time approach where the sound contributions from each location in the source region are computed at the emission time. Accordingly, the time sound waves arrive at the observer is referred to as the advanced time. The advanced time formulation has been given by [23]

$$t_{adv} = t + \frac{|\mathbf{r}(t)|}{c_0} \left[\frac{M_{o,r}(t) + \sqrt{M_{o,r}^2(t) + (1 - M_o^2)}}{1 - M_o^2} \right], \quad (3.16)$$

where M_o is the observer Mach number and $M_{o,r} = M_o \mathbf{r}/|\mathbf{r}|$ is the projection of the observer Mach number vector towards the source direction. In this formulation, the Doppler shift factor in the denominator $(1 - M_o^2)$ may cause a mismatch between the discrete time-step at the source and the observer time domains. A linear interpolation procedure is employed to overcome this issue and to ensure the correspondence between both time series [23]. The advanced time formulation removes the iterative retarded time calculation. Furthermore, it allows for noise computation to be performed

³The pressure fluctuations that are associated with the reciprocal motion and do not propagate are called pseudo-sound. They do not contribute to the far field, but they can be heard or measured by a microphone close to the flow [29].

simultaneously for the CFD solution, reducing the overall computation time.

3.2. LOW-ORDER METHODS

3.2.1. BLADE ELEMENT MOMENTUM THEORY

Throughout this thesis, the blade element momentum theory (BEMT) is adopted as the low-order method for calculating aerodynamic forces. This method is implemented in *Opty∂B*-BEMT which is distributed by SIMULIA.

The BEMT is a hybrid method that combines the basic principles from both blade element and momentum approaches. In the momentum approach, the thrust generated by the propeller is defined by the time rate of change of momentum of the air that passes through the propeller. The momentum approach assumes that the flow passing through the propeller forms a well-defined streamtube, where the propeller is replaced by an actuator disk, as illustrated in Fig. 3.4. The momentum theory further assumes that the pressures and velocities are evenly distributed over the disk area and that the flow is incompressible and irrotational. Following the propeller's rotation, the freestream velocity $V_o = V_\infty$ is increased to the slipstream velocity ($V_\infty + V_{a3}$). Consequently, the airflow passing through the disk contracts further downstream [32], as illustrated in Fig. 3.4.

The actuator disk is divided into multiple annuli in the momentum approach, as depicted in Fig. 3.4. An annulus located at a distance R from the rotational axis and having a width of Δr has an area of $dA = 2\pi R\Delta r$. The conservation laws are applied to calculate the sectional thrust on each rotor annulus, assuming that successive annuli have no mutual effect on each other. The sectional thrust on an annulus is the product of the mass flow rate through the annulus and the total change in velocity between stations ① and ③, which is twice the induced velocity at that section ($V_{a3} = 2V_a = 2aV_\infty$). The axial velocity induction coefficient is denoted by a , and the axial velocity $V_x = V_\infty(1 + a)$. The mass flow rate over the annulus is $d\dot{m} = \rho_\infty dAV_x = 2\pi\rho_\infty V_x R\Delta r$, which leads to the sectional thrust on the annulus

$$\Delta T = d\dot{m}V_{a3} = 2\pi\rho_\infty V_x R\Delta r V_{a3} = 4\pi\rho_\infty V_\infty^2(1 + a)aR\Delta r. \quad (3.17)$$

On the other hand, the blade element approach evaluates the propeller characteristics, e.g., thrust and torque, either from existing experimental airfoil data or coupled panel/boundary-layer models like Xfoil [33]. To determine the forces at any blade radius, the blades are divided into radial elements of width Δr as illustrated in Fig. 3.4, where each blade element can be considered individually. Namely, the blade element theory considers that no forces act in the radial direction, so each element is subjected to two-dimensional flow. This approach has good validity except near the blade tips. Removing this two-dimensional restriction requires a considerably more advanced treatment of the problem using vortex wake theory [34]. Nevertheless, a good approximation to the tip-loss effect on the inflow distribution can be obtained by employing Prandtl's tip-loss correction model.

The *Opty∂B*-BEMT tool employed a uniform inflow and Prandtl tip-losses correction, and required blade sectional forces are computed using the boundary layer model by Drela & Giles [33, 35]. Aerodynamic polars are precomputed with an angular step of 1° in the angle of attack range from $[-16^\circ, 16^\circ]$, and at five values of the Reynolds number

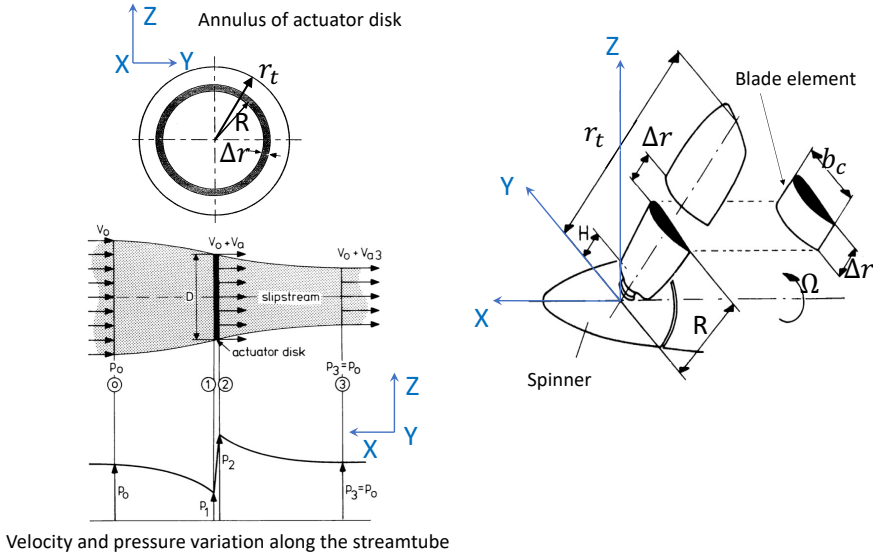


Figure 3.4: The annulus of the rotor disk (top left) and a streamtube created by the propeller motion (bottom left) and blade element of a rotor (right) (adapted from [32]).

encompassing the whole range of radial variation [36]. To enhance the practicality, numerical robustness, and efficiency, all quantities employed by the BEMT algorithm, i.e., sectional aerodynamic coefficients and stall angles, and by the broadband noise model (boundary layer properties at the trailing edge) are polynomially fitted with respect to the radial coordinate and the angle of attack. Post-stall lift and drag coefficients are determined by employing the Viterna & Corrigan approach [37].

In the BEMT procedure, the sectional thrust and torque on an annulus of width Δr can be determined by establishing an equilibrium that reads:

$$\Delta T = 4\pi R \rho_\infty V_\infty^2 (1+a) a \Delta r = \frac{1}{2} \rho_\infty V_1^2 b_c (c_l \cos \phi - c_d \sin \phi) B \Delta r, \quad (3.18)$$

$$\Delta Q = 4\pi r^3 \rho_\infty V_\infty \Omega (1+a) b \Delta r = \frac{1}{2} \rho_\infty V_1^2 b_c (c_d \cos \phi + c_l \sin \phi) B r \Delta r, \quad (3.19)$$

where b_c is the blade sectional chord, B is the number of blades, a is the axial velocity induction coefficient ($V_x = V_0(1+a)$), b is the azimuthal velocity induction coefficient ($V_t = \Omega R(1-b)$), $V_1 = \sqrt{V_x^2 + V_t^2}$ is the total velocity seen by every radial section and $\phi = \tan^{-1}(V_x/V_t)$ is the flow incidence angle. The local flow incidence as a consequence of the geometrical blade section pitch angle β and flow induction is $\alpha = \beta - \phi$, as illustrated in Fig. 3.5. The sectional lift and drag coefficients c_l and c_d are function of the local α , Reynolds, and Mach number and are determined using pre-computed look-up tables of polynomial fitting coefficients. More details of this approach can be found in [34, 36, 38].

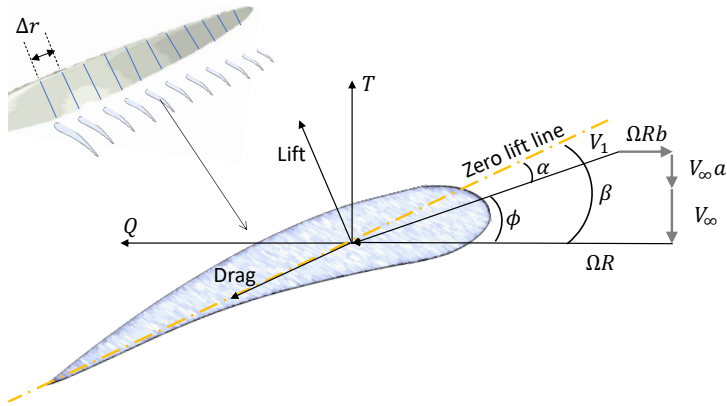


Figure 3.5: Blade element aerodynamic forces.

The overall thrust and torque generated by a single blade are then obtained by integrating the sectional thrust and torque along the blade's radial direction. The thrust and torque coefficients C_T and C_Q are acquired by multiplying the thrust and torque by $1/(\rho_\infty \Omega \pi R_T^4)$ and $1/(\rho_\infty \Omega^2 \pi R_T^5)$, respectively.

The radial distribution of the blade sectional force and the sectional airfoil surface are used to define the input of time-domain and frequency-domain propeller tonal noise computation methods. The time-domain approach is based on the compact dipole and monopole FW-H formulation [39], while the frequency-domain approach relies on frequency domain formulations derived by [40–42]. The broadband noise is computed using the trailing edge noise model by Roger & Moreau [43], extended to a rotating blade [44], and by using seven different semi-empirical Wall pressure spectrum (WPS) models based on boundary layer quantities extracted at 95% of the chord [36]. The following sections will outline the theoretical background of tonal noise computation approaches in the time and frequency domains, respectively.

3.2.2. TIME-DOMAIN COMPACT DIPOLE/MONOPOLE FW-H FORMULATION

As outlined earlier, at low Mach numbers, the quadrupole source term becomes negligible, and the dipole and monopole sources are responsible for the rotor noise. Realistic problems, however, would require the resolution of the FW-H at many receiver points, which may increase the computational cost dramatically. Casalino et al. [45] proposed a compact dipole/monopole FW-H formulation to reduce FW-H computational time while preserving an adequate level of accuracy. The compact dipole/monopole is based on the classical idea of replacing the rotor blade with an equivalent distribution of chordwise compact sources. According to the classical unsteady aerodynamic theories, a source region, e.g., blade chord at a radial distance, is said to be acoustically compact when retarded time variations over this region are negligible than a characteristic period T' of the source, considered in the moving frame of reference. This condition reads [29]

$$T' \gg \left[\frac{l}{c_0 \bar{\Delta}} \right], \quad (3.20)$$

where l is a characteristic length scale of the source region, e.g., blade chord length b_c , and $\bar{\Delta}$ an average value of the Doppler factor $\Delta = |1 - M\mathbf{r}/|\mathbf{r}||$.

When the source region is compact, it radiates in the same way as a point source, which implies negligible thickness noise contribution. However, the inclusion of the thickness noise contribution is shown to improve the near, far-field rotor noise prediction accuracy compared with the compact dipole model [45]. Hence, in the present approach, the thickness noise effect is incorporated with a compact monopole model.

Based on far-field and geometric compactness conditions, the chordwise pressure distribution p_r (See Fig. 3.6) can be approximated by a compact dipole through an equivalent constant pressure distribution p_{eq} that delivers the same aerodynamic load. Furthermore, to model the effect of flow displacement due to the blade motion (thickness noise), an equivalent monopole is introduced by considering a blade section of the equivalent area, i.e., $A_{eq} = A_r$. Thus, the blade is modeled as consecutive wedges distributed along the radial direction that experience the same rotational and pitching motion as the original blade [45].

The compact dipole/monopole approach, together with the forward-time solution

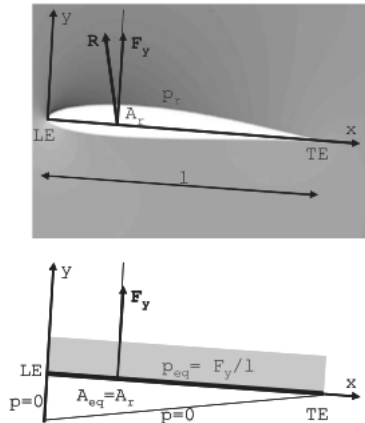


Figure 3.6: A sketch of the compact dipole/monopole model concept. The component of the total aerodynamic force R acting along the normal direction y obtained by integration of the real blade pressure p_r is employed to calculate an equivalent constant pressure p_{eq} applied to a flat plate. A triangular section of area A_{eq} equal to the real section area A_r is created by adding two unloaded edges ($p=0$), adapted from [39].

of formulation 1A of Farassat, is implemented in the tool *OptydB-PNOISE*. Namely, aerodynamic forces and blade sectional properties extracted from the BEMT calculation procedure are delivered as input for the noise calculation.

It is worth mentioning that the compact dipole/monopole FW-H model is a time-domain approach. Therefore, it may still be expensive if one considers tonal noise at receivers distributed over a vast area or if a low run-time is preferred. In contrast, the frequency-domain methods are generally inexpensive, particularly for tonal noise calculation, as it evaluates the noise only at the fundamental frequency and its harmonics. To this end, Hanson's frequency domain model, outlined in the following section, adopted in this work.

3.2.3. FREQUENCY-DOMAIN ANALYTICAL FORMULATION

The frequency-domain analytical formulation derived by Hanson [40–42] for steady loading and thickness noise extends the work of Garrick and Watkins [46], and Arnoldi [47] to incorporate the effects of non-compactness, sweep, and non-axial flow [40, 42, 48]. Hanson's model, however, was derived in a retarded reference frame, implying that a coordinate transformation is required before the method can be used. The coordinate transformations from a visual to a retarded reference frame needed to implement Hanson's model are included below for clarity and are explained in detail in Refs. [41, 49, 50]. Fig. 3.7 illustrates the orientation of the Cartesian coordinate system X , Y , and Z , with X being positive in front of the propeller plane. The axial direction points to the positive X -axis direction. Where $S = \sqrt{x^2 + y^2 + z^2}$ denotes the observer distance from the propeller hub and $\theta = \arccos x/S$ is the observer angle relative to the flight direction. α is the pitch angle of the propeller shaft axis relative to the flight direction, and $\phi = \tan^{-1}(z/y)$ is the receiver azimuthal angle, $H = \sqrt{y^2 + z^2}$ is the observer distance from the propeller shaft axis. Note that this formulation uses retarded coordinates, with variables referring to the retarded reference frame denoted by the subscript " r " and angles relative to the propeller shaft axis denoted by the superscript "'".

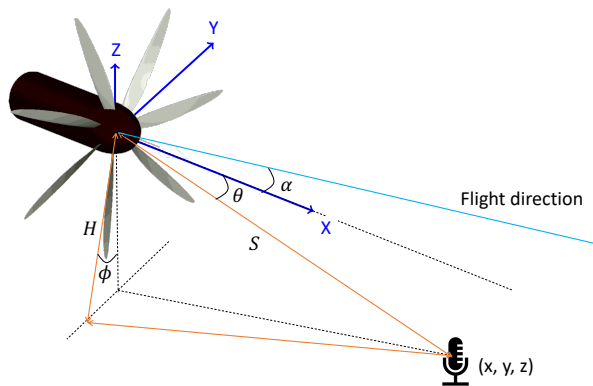


Figure 3.7: The coordinate system used in the derivation of Hanson's formulation.

The source-receiver geometry is illustrated in Fig. 3.7. The source-observer distance S and the observer angle θ in the retarded time are given by the relations

$$\left. \begin{aligned} \theta_r &= \arccos \left(\cos \theta \sqrt{1 - M^2 \sin^2 \theta} + M \sin^2 \theta \right) \\ S_r &= \frac{H}{\sin \theta_r} \end{aligned} \right\}. \quad (3.21)$$

The m^{th} harmonics of the steady loading noise P_{mL} and thickness noise P_{mT} terms are

given by the relations

$$P_{mL} = \frac{mB M_t \sin \theta_r \exp \left[i m B \left(\Omega \frac{S_t}{c} + (\phi' - (\pi/2)) \right) \right]}{2\sqrt{2}\pi H r_t (1 - M \cos \theta_r)} \times \int_{hub}^{tip} \left[\frac{\cos \theta'_r}{1 - M \cos \theta_r} \frac{dT}{dr} - \frac{1}{r^2 M_t r_t} \frac{dQ}{dr} \right] \exp(i\phi_s) J_{mB} \Psi_L dr, \quad (3.22)$$

$$P_{mT} = \frac{-\rho c^2 B \sin \theta_r \exp \left[i m B \left(\Omega \frac{S_t}{c} + (\phi' - (\pi/2)) \right) \right]}{4\sqrt{2}\pi (H/D) (1 - M \cos \theta_r)} \times \int_{hub}^{tip} M_s^2 (h/b_c) \exp(i\phi_s) J_{mB} k_x^2 \Psi_V dr, \quad (3.23)$$

$$J_{mB} = J_{mB} \left(\frac{mB r M_t \sin \theta'_r}{1 - M \cos \theta_r} \right), \quad (3.24)$$

where m indicates the harmonic number, B is the number of blades, r_t is the propeller tip radius, Ω is the angular frequency, $M_t = \Omega r_t / c$ is the tip Mach number, M is the freestream Mach number, b_c is the blade chord length, h is the maximum airfoil thickness and D is the propeller diameter. To clarify, c represents the speed of sound, and r denotes the non-dimensional radial distance along the propeller blade, specifically defined as $r = R/r_t$, where R is the radial distance along the blade. The blade sectional torque dQ , thrust dT , blade chord b_c , and blade thickness h at each radial distance R/r_t are directly obtained from the BEMT calculations (see Appendix A for further information). $J_{mB}(\zeta)$ is the Bessel function of order mB and argument ζ . The angles θ'_r and ϕ' are relate to α , which are defined as:

$$\left. \begin{aligned} \theta'_r &= \arccos \left(\cos \theta_r \cos \alpha + \sin \theta_r \sin \phi \sin \alpha \right) \\ \phi' &= \arccos \left(\frac{\sin \theta_r}{\sin \theta'_r} \cos \phi \right) \end{aligned} \right\} \quad (3.25)$$

and k_x is a wave number and ϕ_s represents phase lag due to sweep which are given by:

$$\left. \begin{aligned} k_x &= \frac{2mB b_c M_t}{M_s (1 - M \cos \theta_r)} \\ \phi_s &= \frac{2mB M_t}{M_s (1 - M \cos \theta_r)} \frac{MCA}{D} \end{aligned} \right\}, \quad (3.26)$$

where MCA is the mid-chord alignment. Furthermore, Ψ_V and Ψ_L are non-dimensional source transforms which represent the effect of chord-wise non-compactness. For Ψ_V and Ψ_L , a parabolic thickness distribution and uniform lift distribution, respectively, are employed.

$$\Psi_V(k_x) = \begin{cases} 2/3 & \text{if } k_x = 0, \\ \frac{8}{k_x^2} \left[\frac{2}{k_x} \sin\left(\frac{k_x}{2}\right) - \cos\left(\frac{k_x}{2}\right) \right] & \text{if } k_x \neq 0, \end{cases} \quad (3.27)$$

$$\Psi_L(k_x) = \begin{cases} 1 & \text{if } k_x = 0, \\ \frac{2}{k_x} \sin\left(\frac{k_x}{2}\right) & \text{if } k_x \neq 0. \end{cases} \quad (3.28)$$

Hanson's frequency-domain model is implemented in an in-house code in the present study. It employs the same aerodynamic forces distribution along the blade and sectional area extracted from the BEMT procedure to calculate the tonal noise at a receiver location. The following chapter examines the computational efficiency and accuracy of the frequency-domain model, while Appendix A provides more information on the input file and how to prepare run cases for this tool.

REFERENCES

- [1] S. Succi, *The lattice Boltzmann equation: for fluid dynamics and beyond* (Oxford university press, 2001).
- [2] H. Chen, S. Chen, and W. H. Matthaeus, *Recovery of the navier-stokes equations using a lattice-gas boltzmann method*, Physical review A **45**, R5339 (1992).
- [3] H. Chen, I. Goldhirsch, and S. A. Orszag, *Discrete rotational symmetry, moment isotropy, and higher order lattice boltzmann models*, Journal of Scientific Computing **34**, 87 (2008).
- [4] A. Mohamad, *Lattice boltzmann method*, 2nd ed. (Springer, 2019).
- [5] X. He and L.-S. Luo, *Theory of the lattice boltzmann method: From the boltzmann equation to the lattice boltzmann equation*, Physical review E **56**, 6811 (1997).
- [6] H. Chen, C. Teixeira, and K. Molvig, *Realization of fluid boundary conditions via discrete boltzmann dynamics*, International Journal of Modern Physics C **9**, 1281 (1998).
- [7] H. Chen, O. Filippova, J. Hoch, K. Molvig, R. Shock, C. Teixeira, and R. Zhang, *Grid refinement in lattice boltzmann methods based on volumetric formulation*, Physica A: Statistical Mechanics and its Applications **362**, 158 (2006).
- [8] H. Chen, S. Kandasamy, S. Orszag, R. Shock, S. Succi, and V. Yakhot, *Extended boltzmann kinetic equation for turbulent flows*, Science **301**, 633 (2003).
- [9] L. M. Smith and S. L. Woodruff, *Renormalization-group analysis of turbulence*, Annual review of fluid mechanics **30**, 275 (1998).
- [10] V. Yakhot, S. Orszag, S. Thangam, T. Gatski, and C. Speziale, *Development of turbulence models for shear flows by a double expansion technique*, Physics of Fluids A: Fluid Dynamics **4**, 1510 (1992).

- [11] C. M. Teixeira, *Incorporating turbulence models into the lattice-boltzmann method*, International Journal of Modern Physics C **9**, 1159 (1998).
- [12] C. G. Alexander, H. Chen, S. Kandasamy, R. Shock, and S. Govindappa, *Simulations of engineering thermal turbulent flows using a lattice boltzmann based algorithm*, ASME-PUBLICATIONS-PVP **424**, 115 (2001).
- [13] C. Mockett, W. Haase, and D. Schwamborn, *Go4Hybrid: Grey Area Mitigation for Hybrid RANS-LES Methods: Results of the 7th Framework Research Project Go4Hybrid, Funded by the European Union, 2013-2015*, Vol. 134 (Springer, 2017).
- [14] H. Chen, S. A. Orszag, I. Staroselsky, and S. Succi, *Expanded analogy between boltzmann kinetic theory of fluids and turbulence*, Journal of Fluid Mechanics **519**, 301 (2004).
- [15] P.-T. Lew, L. Mongeau, and A. Lyrintzis, *Noise prediction of a subsonic turbulent round jet using the lattice-boltzmann method*, J. Acoust. Soc. Am. **128**, 1118 (2010).
- [16] B. E. Launder and D. B. Spalding, *The numerical computation of turbulent flows*, in *Numerical prediction of flow, heat transfer, turbulence and combustion* (Elsevier, 1983) pp. 96–116.
- [17] G. Bres, F. Pérot, and D. Freed, *Properties of the lattice boltzmann method for acoustics*, in *15th AIAA/CEAS aeroacoustics conference (30th AIAA aeroacoustics conference)* (2009) p. 3395.
- [18] S. Marié, D. Ricot, and P. Sagaut, *Comparison between lattice boltzmann method and navier–stokes high order schemes for computational aeroacoustics*, Journal of Computational Physics **228**, 1056 (2009).
- [19] A. S. Lyrintzis, *Surface integral methods in computational aeroacoustics—from the (cfd) near-field to the (acoustic) far-field*, International journal of aeroacoustics **2**, 95 (2003).
- [20] C. Bailly and D. Juve, *Numerical solution of acoustic propagation problems using linearized euler equations*, AIAA journal **38**, 22 (2000).
- [21] J. W. Delfs, M. Bauer, R. Ewert, H. A. Grogger, M. Lummer, and T. G. Lauke, *Numerical simulation of aerodynamic noise with dlr's aeroacoustic code piano*, (2008).
- [22] F. Farassat, *Introduction to generalized functions with applications in aerodynamics and aeroacoustics*, Vol. 3428 (National Aeronautics and Space Administration, Langley Research Center, 1994).
- [23] D. Casalino, *An advanced time approach for acoustic analogy predictions*, Journal of Sound and Vibration **261**, 583 (2003).
- [24] J. E. Ffowcs Williams and D. L. Hawkings, *Sound generation by turbulence and surfaces in arbitrary motion*, Philosophical Transactions of the Royal Society of London. Series A, Mathematical and Physical Sciences **264**, 321 (1969).

- [25] G. Brès, F. Pérot, and D. Freed, *A fflowcs williams-hawkings solver for lattice-boltzmann based computational aeroacoustics*, in *16th AIAA/CEAS aeroacoustics conference* (2010) p. 3711.
- [26] D. A. Russell, J. P. Titlow, and Y.-J. Bemma, *Acoustic monopoles, dipoles, and quadrupoles: An experiment revisited*, *American Journal of Physics* **67**, 660 (1999).
- [27] P. R. Spalart, K. V. Belyaev, M. L. Shur, M. Kh Strelets, and A. K. Travin, *On the differences in noise predictions based on solid and permeable surface fflowcs williams-hawkings integral solutions*, *International Journal of Aeroacoustics* **18**, 621 (2019).
- [28] P. Di Francescantonio, *A new boundary integral formulation for the prediction of sound radiation*, *Journal of Sound and Vibration* **202**, 491 (1997).
- [29] M. Roger, *Applied aeroacoustics: prediction methods (von karman institute for fluid dynamics, lecture series 1996-04)*, (1996).
- [30] F. Farassat, *Derivation of Formulations 1 and 1A of Farassat*, Tech. Rep. (2007).
- [31] F. Farassat and G. P. Succi, *A review of propeller discrete frequency noise prediction technology with emphasis on two current methods for time domain calculations*, *Journal of Sound and Vibration* **71**, 399 (1980).
- [32] G. J. Ruijgrok, *Elements of airplane performance* (VSSD, 2009).
- [33] M. Drela, *Xfoil: An analysis and design system for low reynolds number airfoils*, in *Low Reynolds number aerodynamics* (Springer, 1989) pp. 1–12.
- [34] G. J. Leishman, *Principles of helicopter aerodynamics with CD extra* (Cambridge university press, 2006).
- [35] M. Drela and M. B. Giles, *Viscous-inviscid analysis of transonic and low reynolds number airfoils*, *AIAA journal* **25**, 1347 (1987).
- [36] D. Casalino, E. Grande, G. Romani, D. Ragni, and F. Avallone, *Definition of a benchmark for low reynolds number propeller aeroacoustics*, *Aerospace Science and Technology* **113**, 106707 (2021).
- [37] L. A. Viterna and R. D. Corrigan, *Fixed pitch rotor performance of large horizontal axis wind turbines*, *Large Horizontal-Axis Wind Turbines* (1982).
- [38] T. Burton, N. Jenkins, D. Sharpe, and E. Bossanyi, *Wind energy handbook* (John Wiley & Sons, 2011).
- [39] D. Casalino, M. Barbarino, and A. Visingardi, *Simulation of helicopter community noise in complex urban geometry*, *AIAA journal* **49**, 1614 (2011).
- [40] D. B. Hanson, *Helicoidal surface theory for harmonic noise of propellers in the far field*, *AIAA Journal* **18**, 1213 (1980).

- [41] D. B. Hanson and D. J. Parzych, *Theory for noise of propellers in angular inflow with parametric studies and experimental verification*, Tech. Rep. (1993).
- [42] D. Hanson, *Sound from a propeller at angle of attack: a new theoretical viewpoint*, Proceedings of the Royal Society of London. Series A: Mathematical and Physical Sciences **449**, 315 (1995).
- [43] M. Roger and S. Moreau, *Back-scattering correction and further extensions of amiet's trailing-edge noise model. part 1: theory*, Journal of Sound and vibration **286**, 477 (2005).
- [44] R. Amiet, *Frame of reference considerations for the forward flight noise problem*, United Technologies Research Center Report N212775 **1**, 76 (1974).
- [45] D. Casalino, M. Barbarino, and A. Visingardi, *Simulation of helicopter community noise in a realistic urban environment*, (2010).
- [46] I. Garrick and C. E. Watkins, *A theoretical study of the effect of forward speed on the free-space sound-pressure field around propellers*, Tech. Rep. (1953).
- [47] R. A. Arnoldi, *Propeller noise caused by blade thickness* (United Aircraft Corporation, Research Department, 1956).
- [48] B. Magliozzi, D. Hanson, and R. Amiet, *Propeller and propfan noise*, Aeroacoustics of flight vehicles: theory and practice **1**, 1 (1991).
- [49] D. B. Hanson, *Influence of propeller design parameters on far-field harmonic noise in forward flight*, AIAA Journal **18**, 1313 (1980).
- [50] J. Jacques, *Wind-tunnel simulation of the effects of flight on radiated sound*, (1976).

4

LOW-ORDER AEROACOUSTIC PERMANENCE CALCULATION OF PROPELLERS

When we are tired, we are attacked by ideas we conquered long ago.

Friedrich Nietzsche

This chapter reports a computationally efficient low-order methodology and its application for fast evaluation of the noise footprint of a propeller-driven aircraft considering various design and operating parameters. A homogeneous, quiescent atmosphere is considered, and the straight-ray propagator is employed to propagate noise signals from the source sphere to receivers distributed over flat terrain. In order to reduce the runtime, the frequency-domain acoustic formulation derived by Hanson (1980) is implemented and validated against high-fidelity results. It is found that, for a given thrust, a drop in advance ratio alters the source directivity dramatically, resulting in a variation of up to 30 dBA on the acoustic footprint. When the advance ratio is kept the same, and the number of blades increases from 5 to 7, the variation becomes 16 dBA due to the change in the source directivity, but the maximum noise level remains the same. The latter condition reduces the loading for each blade and, consequently, the associated noise. However, the total noise remains unchanged as a consequence of increasing thickness noise due to the lower advance ratio, high blade tip Mach number, and addition of extra blades.

Parts of this chapter have been published in Yunus et al. [1].

4.1. OBJECTIVES

LOW-order methods, such as blade element momentum theory (BEMT), have been widely used for the calculation of the steady loading of propellers, and they can also be coupled with an acoustic module to retrieve the tonal [2–6], and broadband [7] acoustic radiation. Nevertheless, the application of the low-order approach is limited to the radiated noise from stationary sources, and short propagation distances a few times larger than the rotor diameter [5–7]. Yet, considering an idealized operational environment with a homogeneous, quiescent atmosphere and flat terrain, the low-order approach could be applied for moving sources to explore the correlation between different design and operating parameters and acoustic footprint and identify trends to mitigate the noise impact on the community.

Therefore, this chapter aims to investigate the acoustic impact of design and operating parameters on the noise footprint of an isolated propeller in forward flight and identify trends to mitigate the noise impact using a computationally efficient and robust methodology. To this purpose, the low-order noise source prediction workflow outlined in Chapter 3 is coupled with a straight-ray propagator to compute the noise footprint of the propeller over flat terrain. In addition, the frequency-domain acoustic formulation described in Chapter 3 is also implemented and validated against high-fidelity results to reduce the runtime further.

The remainder of this chapter is structured as follows. An overview of the present low-order approach is given in Sec. 4.2, while the validation results of the low-order approach are presented in Sec. 4.3. A parametric study for evaluation of the acoustic effects of propeller advance ratio and blade number, which are the main driven factors that directly affect the noise footprint of an aerial vehicle, is presented in Sec. 4.4. Finally, trends to mitigate the noise impact are highlighted in Sec. 4.5.

4.2. OVERVIEW OF THE LOW-ORDER APPROACH

A standard hybrid approach is used to predict the source noise levels as well as the noise footprint of an isolated propeller. Once the propeller geometry is given in terms of blade and hub geometry, BEMT computations are carried out by means of the *Opty ∂ B*-BEMT tool to compute the radial distribution of aerodynamic loads and integral boundary layer parameters that represent the input for the tonal and broadband aeroacoustic predictions, respectively. Subsequently, the noise signals on microphones distributed on a hemisphere surrounding the propeller are computed using the *Opty ∂ B*-PNOISE tool. Finally, the propeller noise footprint is computed using the Noise Hemisphere Database (NHD) approach implemented in *Opty ∂ B*-FOOTPRINT with a straight-ray propagation model. A schematic illustration of the computational framework is displayed in Fig 4.1.

The *Opty ∂ B*-BEMT and *Opty ∂ B*-PNOISE tools outlined in Chapter 3 are employed to predict source noise spheres. Whereas the *Opty ∂ B*-FOOTPRINT is used to propagate the noise signals from the source sphere to the on-ground receivers. The user can input a series of waypoints defining the vehicle's planned trajectory that represents a portion of or a complete flight mission profile. The model subdivides this trajectory into a number of steady-state flight segments, each of which is then associated with a noise hemisphere representing the frequency and magnitude of noise radiated by the

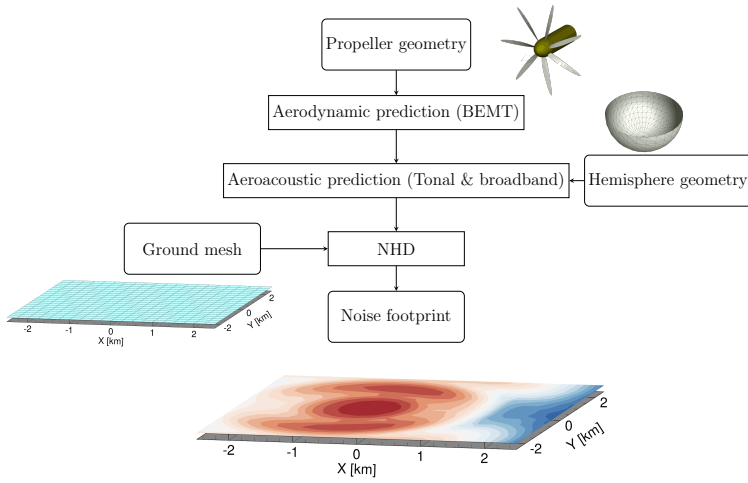


Figure 4.1: A schematic illustration of the computational framework.

propeller over a range of directions for that particular steady flight condition. For each noise hemisphere, *Opty δ B*-BEMT and *Opty δ B*-PNOISE are subsequently run to compute the noise signals on the microphones distributed on it. Finally, the noise footprint of the propeller is predicted using the straight-ray propagation model with the assumption of constant weather condition.

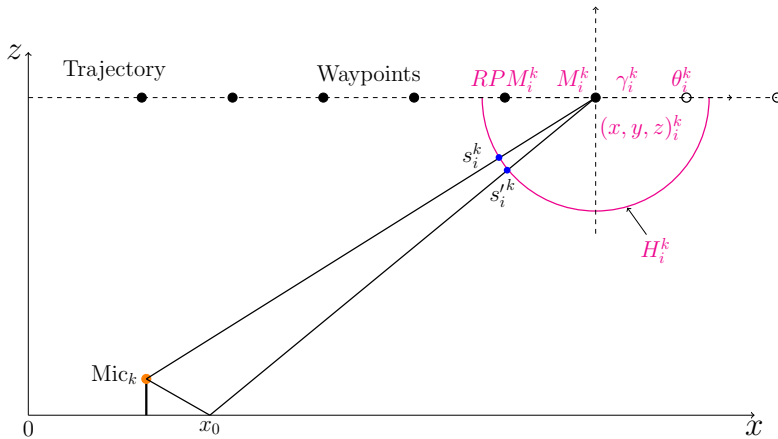


Figure 4.2: Illustration of the straight-ray NHD-based noise footprint calculation procedure.

In this study, a single flight condition that represents a constant speed level flight with constant flight direction is considered. As shown in Fig.4.2, for every microphone k on a ground surface and for every time window i of 0.5 s duration, the emission time position of the vehicle along its trajectory is determined. At this position, the glide an-

gle γ_i^k and the Mach number M_i^k are calculated from the coordinates of the trajectory waypoints, whereas the pitch angle θ_i^k , the rotor RPM_i^k are interpolated from the closest waypoints. Afterward, the angle of attack α is estimated by subtracting the pitch angle from the glide angle ($\alpha_i^k = \theta_i^k - \gamma_i^k$). Then, the narrow-band noise levels are interpolated at s_i^k and $s_i'^k$ from the closest points on the hemisphere. Finally, the ground noise levels are calculated using the direct and reflected ray paths, atmospheric absorption according to the standard procedure SAE ARP 866A, Doppler shift, and amplitude corrections.

4.3. LOW-ORDER APPROACH VALIDATION

The *OptydB*-BEMT and *OptydB*-PNOISE tools were assessed in the previous work from Casalino et al. [7] by comparing against experimental measurements and high-fidelity simulations from a small UAV propeller. In this study, the low-order approach is validated with high-fidelity simulations conducted using the high-fidelity CFD solver SIMULIA PowerFLOW® coupled with FW-H acoustic analogy [8] (referred to as high-fidelity approach hereafter) outlined in Chapter 3. Afterwards, the validity of the frequency-domain acoustic formulation [9] is verified by comparing it against the time-domain compact dipole/monopole formulation as well as high-fidelity simulation results. Finally, the validity of the outlined numerical approach is verified by comparing the noise footprints computed with the low-order approach and the high-fidelity approach.

The source noise in the high-fidelity approach is predicted by employing the FW-H solver of SIMULIA PowerACOUSTICS® on the scale-resolved flow data from PowerFLOW®. Broadband noise is also predicted, due to the scale-resolving property of the LB/VLES model.

Casalino et al. [7] performed a grid convergence study using the 3DS aeroacoustic workflow. A range of grid resolutions that spans from coarse to fine was used and the grid convergence was verified by monitoring the force and tonal noise with a medium resolution. In this work, the same medium resolution within the same workflow is employed to generate the high-fidelity simulation results, instead of repeating the grid convergence study.

4.3.1. CASE SETUP

The propeller geometry together with the employed reference system is shown in Fig. 4.3a. The chord and twist radial distribution are plotted in Fig. 4.3b. The propeller is cruising at a 2 km altitude. The propeller geometrical specifications and operating conditions of the reference case are listed in Table 4.1. The noise hemisphere is defined in the propeller reference system (zero pitch, yaw, and roll). The hemisphere radius R_h is set to 10 times the propeller diameter D to ensure the flow pressure is fully recovered and only acoustic pressure exists. The hemisphere is discretized in 17 parallels and 17 meridians. The hemisphere and propeller geometry along with the FW-H surfaces for the reference case are shown in Fig. 4.4a.

For the noise footprint, a straight-level flight trajectory is considered, as illustrated in Fig. 4.4b. The flight trajectory starts at the starting point S (-5, 0, 2) km and terminates at terminal point T (5, 0, 2) km. The flight direction points to the positive x-axis. An unperturbed atmosphere is used as the domain of the computation, where no wind

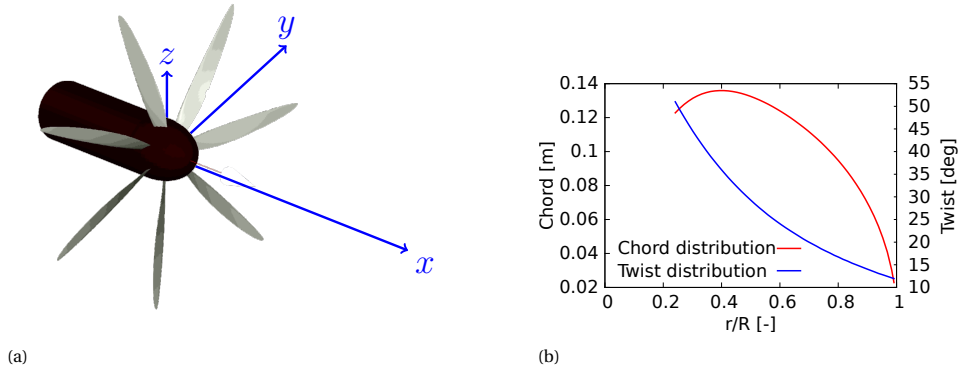


Figure 4.3: Propeller geometry and the reference system (a). Propeller chord and twist distributions (b).

Table 4.1: Specifications and operational conditions of the reference case.

Flight Mach Number (M)	0.2	-
Rotational Speed	1900	RPM
Total thrust (T_h)	1500	N
Advance Ratio (J)	0.84	-
Diameter (D)	2.5	m
Blade Number (NB)	7	-
Hub-to-Tip Ratio	0.1064	-
Flight Altitude	2000	m

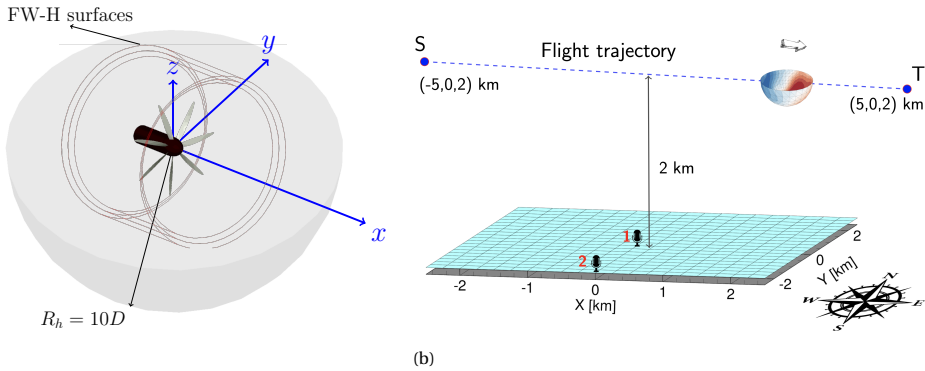


Figure 4.4: Propeller model of the reference case, including the permeable sampling surfaces for FW-H acoustic propagation and the noise hemisphere (a). The geometry of the problem (b).

and no temperature gradients are present. The model outputs the A-weighted OASPL for two prescribed microphones as well as microphones located in a 5 km square area discretized by 21 by 21 grid points on a hard ground plane. The first microphone (Mic 1) is located at the center of the ground plane (0, 0, 3) m and the second microphone (Mic 2) is located at (0, -2500, 3) m as indicated in Fig. 4.4b.

4.3.2. AERODYNAMIC VALIDATION

For the given rotational speed of 1900 RPM, the aerodynamic forces acting on the propeller blades are balanced iteratively through varying the collective pitch angle in order to generate the required target thrust of 1500 N. This is accomplished by means of an automatic trimming procedure integrated into the high-fidelity workflow. The reference collective pitch angle and the thrust obtained are -8.1° and 1520 N, respectively. The reference collective pitch angle is then given as an input along with the propeller geometry into *OptydB*-BEMT tool. The total thrust predicted with the *OptydB*-BEMT tool is 1517.06 N and it is in very good agreement with the reference one and the error between the two is 0.19 %.

Fig. 4.5 represents the sectional thrust dT/dr and thrust coefficient C_T distributions along the blade radial direction. The sectional thrust distribution from the low-order method (indicated as LF) is slightly underpredicted at $r/R \leq 0.43$ and $r/R \geq 0.78$ and overpredicted between $r/R = 0.45$ and $r/R = 0.74$ with respect to the high-fidelity prediction (indicated as HF). The underprediction is likely due to the limitations of the root and tip loss correction models that are implemented in the *OptydB*-BEMT tool. Overall, the low-order simulation results show a favorable agreement with the high-fidelity simulation results.

4.3.3. AEROACOUSTIC VALIDATION

In this section, the validity of the time-domain compact dipole/monopole formulation as well as the trailing edge noise model implemented in *OptydB*-PNOISE is checked

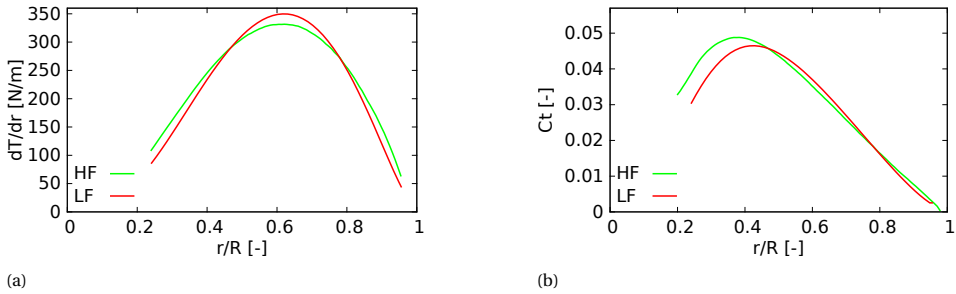


Figure 4.5: Sectional thrust distribution (a) and thrust coefficient (b) along the blade radial direction.

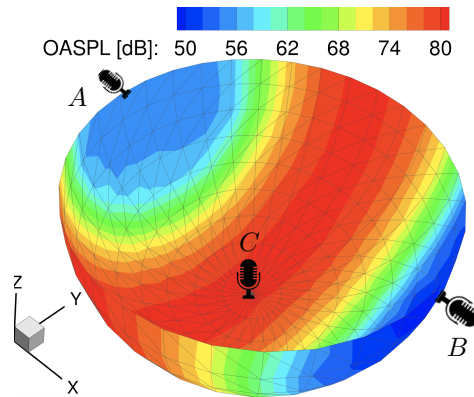


Figure 4.6: Overall Sound Pressure Levels (OASPL) over the noise hemisphere computed with the high-fidelity approach.

by comparing against the high-fidelity simulation results. Furthermore, the frequency-domain acoustic formulation derived by Hanson [9] (indicated as FD) is compared with both high-fidelity and *Opty∂B*-PNOISE results. The frequency-domain formulation is implemented in an in-house code based on the revised formulations given in [6]. It outputs only the tonal noise component based on the blade geometry and forces distribution along the blade span obtained with the *Opty∂B*-BEMT tool, while the low-order approach outputs both tonal and broadband noise. The OASPL on the hemisphere computed with the high-fidelity approach within a band from 200 Hz to 240 Hz that encompasses only the first Blade Passing Frequency (BPF) 221.67 Hz is shown in Fig. 4.6. Broadband contribution on the hemisphere is compared at microphone locations *A* ($-10D, 0, 0$) m, and *B* ($10D, 0, 0$) m, while the tonal contribution is compared at microphone location *C* ($0, 0, -10D$) m. The microphone *A* and *B* are located on the propeller axis, while microphone *C* is located at the propeller rotation plane as indicated in Fig. 4.6.

The comparisons of broadband contribution at microphone *A* and microphone *B* computed with the *Opty∂B*-PNOISE trailing edge noise module (indicated as LF) and high-fidelity predictions (indicated as HF) are displayed in Fig. 4.7a and Fig. 4.7b, respectively. As expected, the spectral content of microphone *A* and *B*, located in a plane

perpendicular to the propeller plane (see Fig. 4.6), is mainly broadband due to turbulent boundary layer trailing edge noise. At microphone *A*, the low-order approach overpredicts the high-fidelity result at all harmonics under consideration. It is noted that the difference between the two approaches is minimum at the first harmonic of BPF and it increases with the increasing number of harmonics. At microphone *B*, the low-order approach shows slightly better agreement than that of microphone *A* where the high-fidelity prediction decays faster at higher harmonics. A close agreement is observed at the first harmonic of BPF where the difference is 5.1 dB. These discrepancies are likely due to the limitations of the empirical trailing edge noise model that were used to compute the broadband noise.

The comparison of tonal contribution at microphone *C* computed with the frequency-domain formulation (indicated as FD), time-domain compact dipole/monopole formulation (indicated as TD), and high-fidelity approach is shown in Fig. 4.7c. The frequency-domain formulation is compared against both time-domain formulation and high-fidelity one. An excellent agreement is found between the frequency-domain and time-domain predictions at the first harmonic of BPF, while both models slightly underpredict the high-fidelity result. At higher harmonics of BPF, however, the noise levels predicted with the frequency-domain model decay faster compared to the time-domain and high-fidelity predictions. This is attributed to the general behavior of the Bessel function that decays rapidly and oscillates around zero when its argument increases considerably. Moreover, the thickness and loading noise components (indicated as T and L, respectively), due to the volume displacement in the propeller rotation plane and the steady loading on the propeller blades, respectively, are computed from the time-domain and frequency-domain models and compared against each other as shown in Fig. 4.7d. For the first harmonic of BPF, both loading and thickness noise components predicted with the two models are identical. From the second harmonics of BPF, the frequency domain model starts to underpredict both loading and thickness noise components, and the difference between these two models increases at higher harmonics. The difference is more noticeable in the loading noise prediction than the one in the thickness noise prediction. It is noted that, independently from the prediction model, the loading noise decays faster than the thickness noise at higher harmonics.

Fig. 4.8 compares the source directivity at the first harmonic of BPF at different microphone positions on the hemisphere with respect to the propeller reference system. On the *xy*-plane (Fig. 4.8a), the frequency-domain model correctly captures the trend of the time-domain prediction at the microphones around the propeller rotation plane. As noticed in Fig. 4.7c, both frequency-domain and time-domain models slightly underestimate the levels at the microphones on the propeller plane. The frequency-domain model predicts zero levels at the microphones close to the propeller axis, i.e. around 0° and 180° , as the broadband noise dominates at those microphone locations. A good agreement is observed between the prediction models at the propeller plane. On the *xz*-plane (Fig. 4.8b), the frequency-domain model is in good agreement with both low-order and high-fidelity approaches around the propeller plane. The low-order prediction is in better agreement with the high-fidelity prediction around 180° with a maximum difference of around 3 dB than that of around 0° with a maximum difference of around 9 dB. On the *yz*-plane (Fig. 4.8c), both frequency-domain and time-domain predictions are

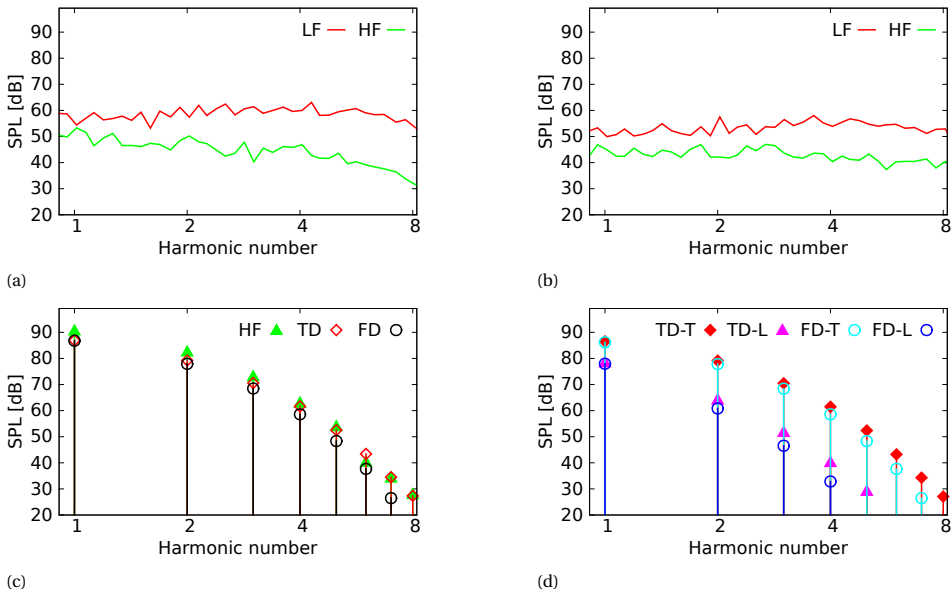


Figure 4.7: Comparison of the broadband contribution predicted with high-fidelity (HF) and low-order (LF) approaches at microphone *A* (a) and microphone *B* (b) on the hemisphere. Comparison of the tonal contribution predicted with high-fidelity, low-order time-domain (TD), and frequency-domain (FD) formulations at microphone *C* (c). Comparison of the thickness (T) and loading (L) noise contributions at microphone *C* (d).

identical. As noticed in Fig.4.7c, both models slightly underpredict the high-fidelity result with a maximum difference of around 2 dB.

As previously mentioned, the frequency-domain model is computationally less demanding than the time-domain model when a large number of microphones are considered. To better highlight this aspect, the CPU times required to compute a noise hemisphere with different number of microphones are obtained for each model and compared each other as illustrated in Fig. 4.9. The same hemisphere geometry is considered. The models run on an Intel(R) Xeon(R) Gold 6140 CPU @2.3 GHz processor with 36 cores, for a range of number of microphones on the hemisphere. The abscissa indicates the number of microphones on a noise hemisphere ($k = 1000$), and the ordinate represents the CPU time required to compute the noise hemisphere with a given number of microphones. The CPU time required to compute the noise hemisphere is roughly linear with the number of microphones on a hemisphere for both models. It is noted that independently of the number of microphones on the hemisphere, the frequency-domain model is approximately 430 times faster than the time-domain model. The results demonstrate that the frequency-domain model is in good agreement with both time-domain and high-fidelity models across all three planes being considered. This suggests that the model can be effectively used for predicting propeller tonal noise, particularly in design and optimization studies where computational efficiency is a priority.

The noise hemispheres computed with both high-fidelity and low-order approaches are projected onto the ground using the straight-ray propagation model along with the

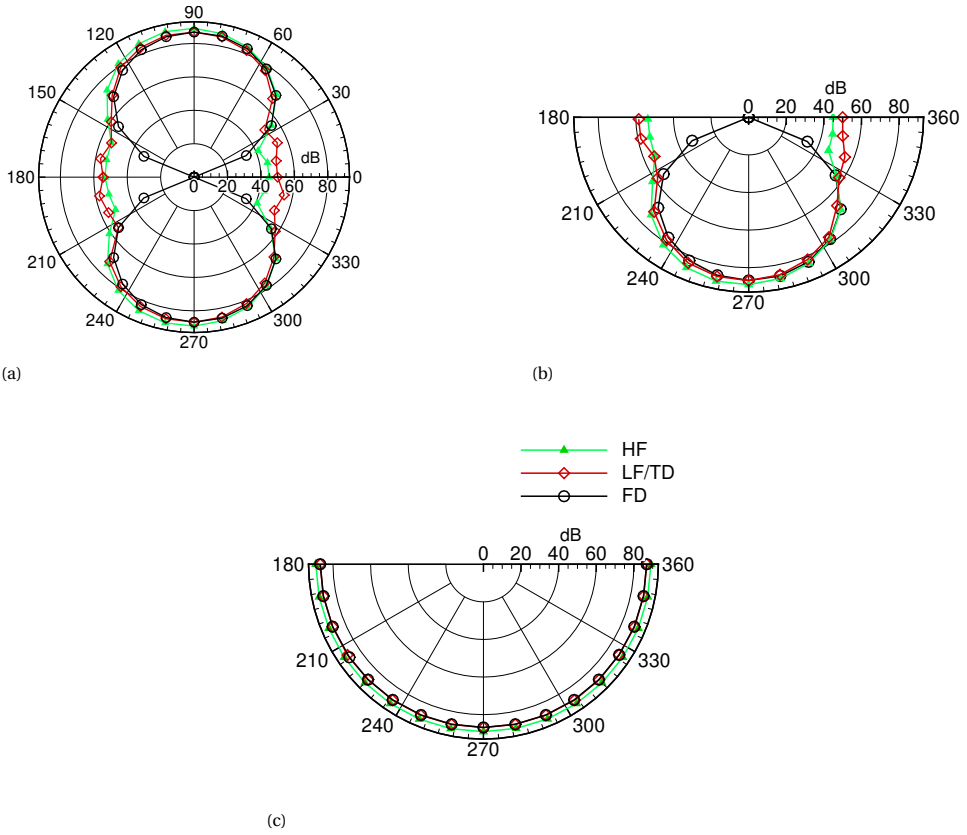


Figure 4.8: Source directivity at the first BPF at xy-plane (a), xz-plane (b), and yz-plane (c).

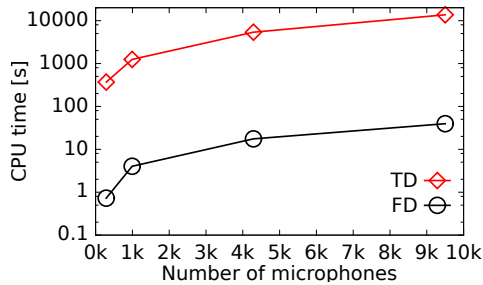


Figure 4.9: Comparison of time-domain and frequency-domain formulation executions CPU times as a function of number of microphones on a hemisphere.

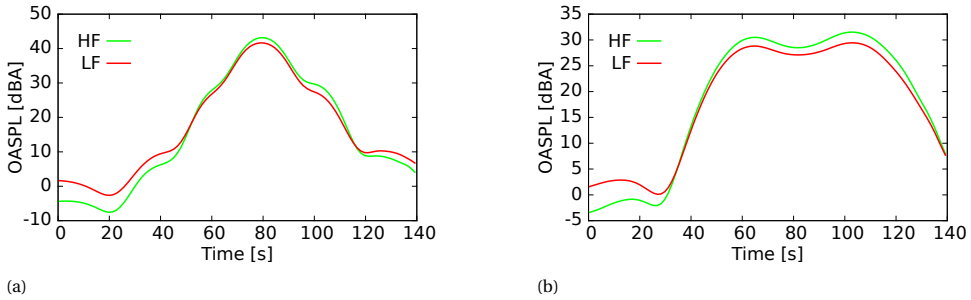


Figure 4.10: Noise signature at Mic 1 (a) and Mic 2 (b).

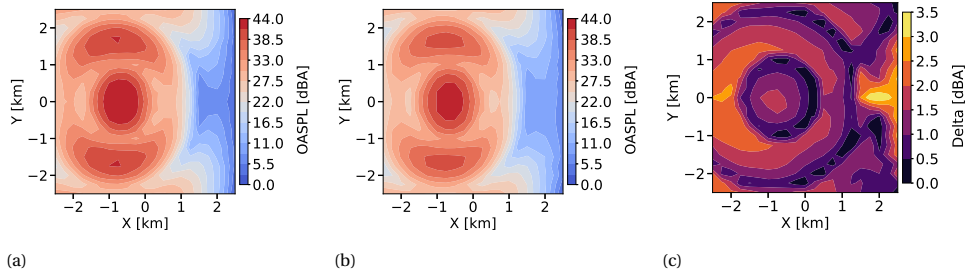


Figure 4.11: Noise footprint at flyover time 70 s. (a) High-fidelity result. (b) low-order result. (c) Field difference between these two results.

NHD-based footprint prediction methodology. It should be noted that the noise footprint is studied within a frequency band that encompasses only the first harmonic of BPF due to the dominance of low-frequency noise in most flight conditions and its efficient propagation in the atmosphere. The noise signatures at Mic 1 and Mic 2 are overlaid in Fig. 4.10. At both microphone locations, the low-order approach accurately predicts the trend of the high-fidelity results. Yet, there are discrepancies up to 5 dBA and 6 dBA at Mic 1 and Mic 2, respectively, that are observed in the first 30 s of the flyover time. These discrepancies are attributed to the mismatch between the two approaches that were observed at Mic A and Mic B at which the broadband noise dominates. It is noted that the noise signature at Mic 2 shows a completely different pattern and the maximum noise level drops by 10 dBA compared to the one at Mic 1. This can be interpreted by examining the source directivity on the hemisphere at the ray-hemisphere intersection points, i.e. source emission points. Fig. 4.11 displays the noise footprint of the propeller at reception time 70 s, computed with both high-fidelity and low-order approaches, together with the field difference between the two approaches. The interference pattern on the noise footprint is attributed to the source directivity and the emission points on the hemisphere at the emission time as well as the ground reflection. A good agreement is found between the two footprint results. The maximum difference observed is 3.5 dBA.

Overall, the close agreement between the low-order and high-fidelity approaches from the source noise hemisphere to the noise footprints suggests that the low-order approach is sufficient to model the tonal noise of a propeller in forward flight.

Table 4.2: Test matrix for the parametric analysis.

Case #	RPM	NB	J	Collective pitch angle	BPF [Hz]
1	1400	5	1.14	1.27°	116.67
2	1900	5	0.84	-7.55°	158.33
3	1900	7	0.84	-8.10°	221.67

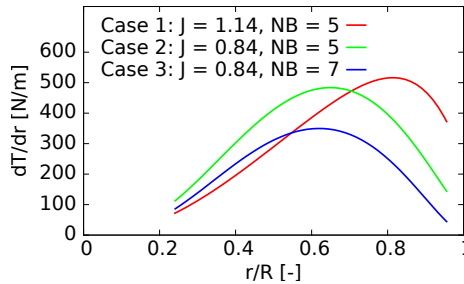


Figure 4.12: Sectional thrust distribution for a single blade.

4.4. ACOUSTIC EFFECTS OF VARYING ADVANCE RATIO AND NUMBER OF BLADES

In this section, the acoustic effects of varying advance ratio (J) and the number of blades (NB) on the noise footprints of the propeller are studied using the low-order approach. In total 3 cases that feature the acoustic effect of varying advance ratio and the number of blades are considered. The test matrix for this analysis is listed in Table 4.2. For all cases, the same blade and hub geometry as outlined in section 4.3 are considered; the flight altitude, Mach number, and the thrust are kept the same as 2 km, 0.2, and 1500 N, respectively. This implies that the blade is trimmed (varying the collective pitch angle) to generate the required thrust at different operating conditions. The sectional thrust distribution along a single blade span for all the test cases is displayed in Fig. 4.12. When the value of J decreases while the number of blades remains the same, the peak value of sectional thrust is reduced and shifted from a location around the blade tip, i.e., $r/R = 0.83$, towards the mid-span, i.e., $r/R = 0.63$. The peak value of sectional thrust decreases further when the number of blades increases and the value of J remains the same.

For all cases, the OASPL predicted over the hemisphere is calculated within a frequency range that encompasses only the first harmonic of BPF. Noise hemispheres are displayed in Fig. 4.13. Comparing the noise hemispheres in Case 1 and Case 2, a drop in the value of J raises the noise levels and alters the source directivity accordingly. The noise intensifies significantly around the propeller rotation plane and spreads towards the propeller axis. The maximum OASPL on the noise hemisphere in Case 2 is increased by 10 dB and there is up to 14 dB difference on the noise hemisphere as shown in Fig.

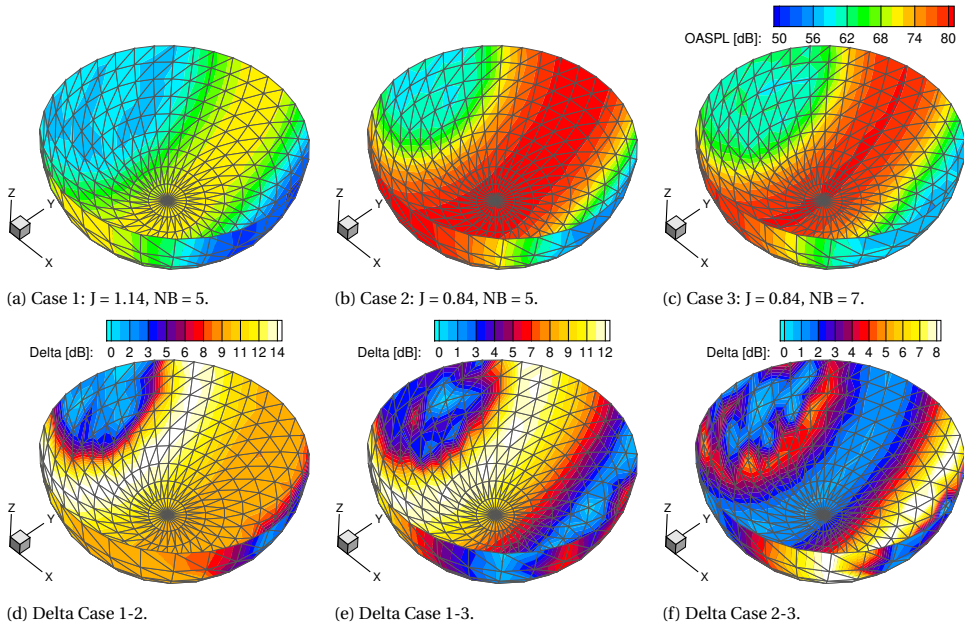


Figure 4.13: Noise hemispheres and the field difference between them for the test cases under consideration.

4.13d, due to the variation in the source directivity, which is mainly distributed on the left lower segment of the hemisphere. Comparing the noise hemisphere in Case 2 and Case 3, an increase in the blade count changes the source directivity considerably but does not affect the maximum OASPL on the hemisphere. The maximum difference on the noise hemisphere is 8 dB that is distributed on the right lower segment of the hemisphere. Noise footprints are then studied with the prescribed ground microphones and boundary conditions described in section 4.3.

4.4.1. THE CORRELATION BETWEEN J AND NOISE FOOTPRINT

The acoustic impact of varying J on the noise footprint is examined by comparing Case 1 and Case 2, in which the number of blades is the same while the value of J is decreased. The source spectra at microphone C on the hemisphere (see Fig. 4.6) are compared and displayed in Fig. 4.14. When the value of J decreases, the thickness noise increases significantly at all harmonics under consideration, while an increase in loading noise is visible only at the first three harmonics. As seen, thickness noise is more sensitive in the variation of advance ratio than the loading noise. Moreover, tonal peaks after the first harmonic of BPF diminish for Case 1, while an increase in the noise levels with more evident tonal peaks is observed in Case 2, as shown in Fig. 4.14c. As a consequence, the OASPL on the hemisphere raises (see Fig. 4.13).

The corresponding noise signatures at the prescribed ground microphone locations are shown in Fig. 4.15. As a result of decreasing J , the noise levels at Mic 1 and Mic 2 are increased up to 13.5 dBA and 15 dBA, respectively. The interference pattern be-

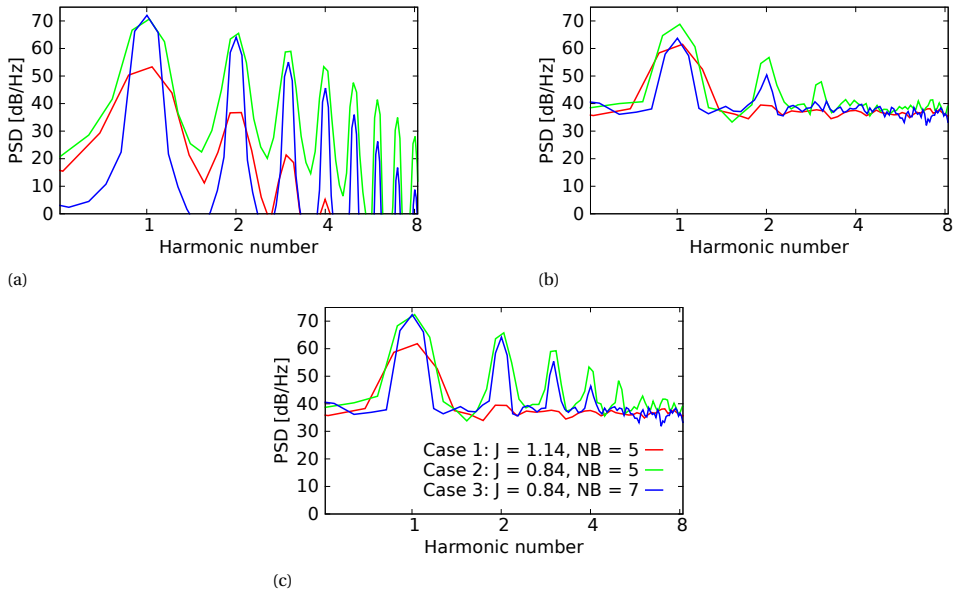


Figure 4.14: Comparison of the Source spectra at microphone C on the hemisphere for thickness noise (a), loading noise (b), and total noise (c).

comes more evident and the reception time of the maximum A-weighted OASPL is delayed about 10 s. The noise footprints at flyover time 70 s are compared and displayed in Fig. 4.16. The noise footprint in Case 2 shows totally different patterns and higher noise levels with respect to Case 1 due to the change in the source directivity and the corresponding frequency content on the hemisphere. The maximum noise level increased by 12.8 dBA and the difference between the footprints is 30 dBA that is mainly distributed at the left edge of the ground area.

The results presented above agree with similar studies [10, 11], where they found that the on-ground noise levels increase when flight speed increases.

4.4.2. THE CORRELATION BETWEEN NB AND NOISE FOOTPRINT

The acoustic effect of varying number of blades is investigated by comparing Case 2 with Case 3. The source spectra at the microphone C on the noise hemisphere are compared and displayed in Fig. 4.14. When NB increases, the thickness noise at the first BPF slightly increased, and then it drops gradually with increasing number of harmonics. As expected, a clear drop in the loading noise at all harmonics is seen. Furthermore, the tonal peak due to the loading noise diminishes after the second harmonics of BPF, while it is still visible at the third harmonic in Case 2. In general, both thickness and loading noise drop considerably at higher harmonics as a consequence of increasing blade count. However, in the total noise, the tonal peak at the first harmonics of BPF remains unchanged between the two cases. Hence, the OASPL on the hemisphere concentrates more around the propeller plane and the maximum noise level remains the

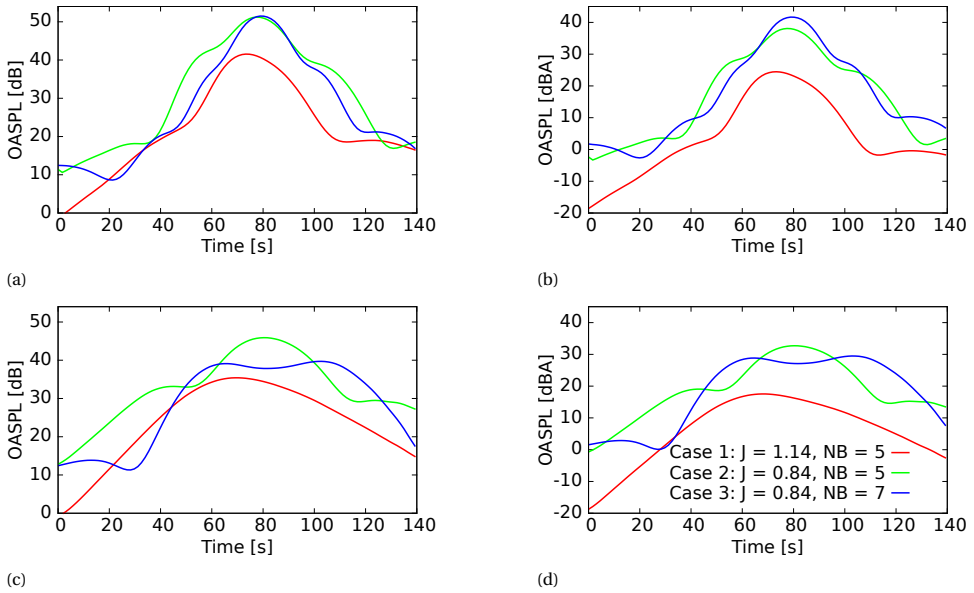


Figure 4.15: On-ground noise levels at microphone 1 in dB (a), dBA (b) and microphone 2 in dB (c), dBA (d) as a function of flight mission time.

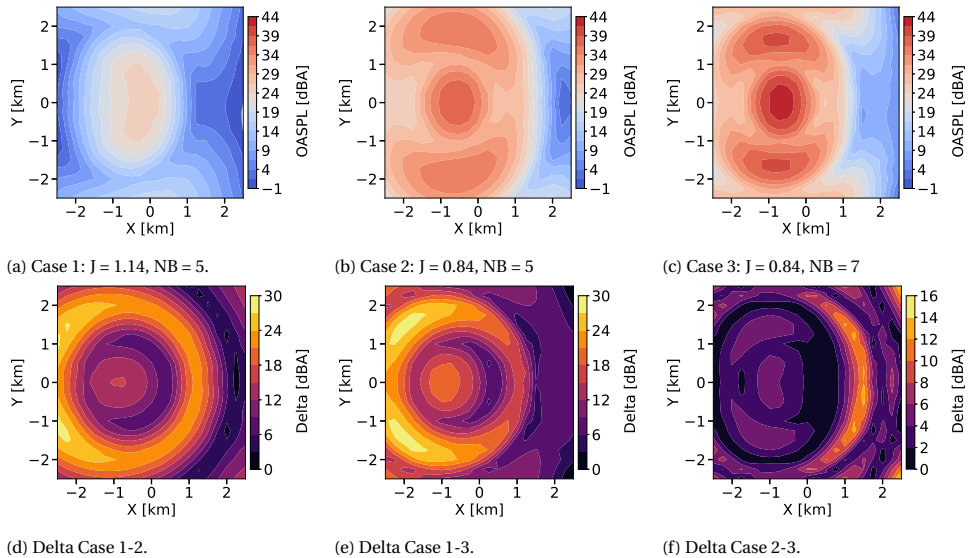


Figure 4.16: Noise footprints at flyover time 70 s and the field difference between them for the test cases under consideration.

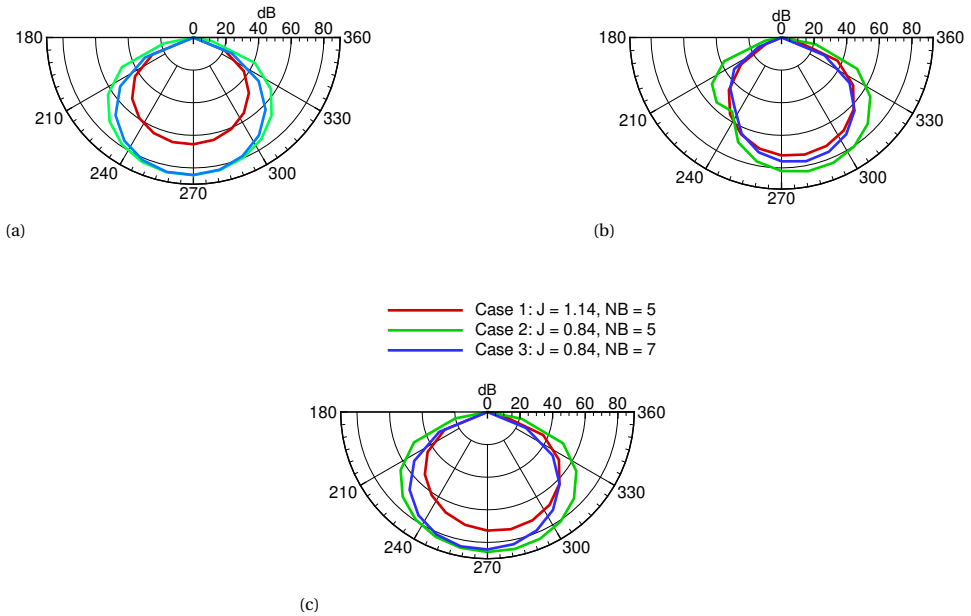


Figure 4.17: Comparison of the source noise levels at the first harmonic of BPF on the xz -plane for thickness noise (a), loading noise (b), and total noise (c).

same (see Fig.4.13c). Interestingly, one would expect a reduction in the tonal noise for Case 3 as a result of increasing number of blades that decrease the loading per blade and, as a consequence, the loading noise component. However, this is not observed in the total noise, in particular for the first two harmonics of BPF. In order to investigate this aspect, the development of thickness and loading noise contributions under varying J and blade counts are displayed in Fig. 4.17. When the value of J decreases both thickness and loading noise are increased, hence the total noise increases. It is noted that, compared to the loading noise, the thickness noise dominates when the value of J decreases. When comparing Case 2 against Case 3, the loading noise decreases as a result of increasing blade numbers. However, due to the lower J , and the addition of extra thickness noise source due to the addition of extra blades, the thickness noise still dominates the total noise radiated to the far-field. As a consequence, the reduction in the loading noise is overshadowed by the dominance of the thickness noise, thus, the total noise at the first harmonic of BPF remains unchanged. The results highlight the importance of thickness noise in the propeller noise predictions, in particular, for large propellers with many blades operating at relatively lower J .

The noise signatures at prescribed ground microphone locations are computed for Case 2 and Case 3. At Mic 1, the noise signature shows a similar trend for both cases.

Conversely, at Mic 2, the two cases display opposite interference patterns. This is attributed to the variation in the source directivity on the noise hemisphere and the ground reflection. As expected, at Mic 1, the maximum OASPL remains the same (see Fig. 4.15a). However, it is increased by 3.5 dBA in A-weighted OASPL (see Fig. 4.15b). This is due to the frequency dependence of the A-weighted noise metric. Magliozzi et al. [12] also highlighted this aspect and stated that adding blades raises the frequencies generated, so that metrics such as A-weighted OASPL commonly used in aircraft community noise (ACN) assessments may increase with increased blade count. At Mic 2, the maximum A-weighted OASPL is decreased by 4 dBA. The noise footprints at flyover time 70 s are computed for Case 2 and Case 3. The noise levels are relatively insensitive to the change in the number of blades except the interference pattern that narrows towards the center of the ground area. The increase in the blade count from 5 to 7 contributes to a mismatch up to 16 dBA on the acoustic footprint that is mainly distributed around the right edge of the ground area.

4.5. CONCLUDING REMARKS

A new computational framework that couples computationally efficient methods, which were initially validated against high-fidelity simulation results, is presented to predict the noise footprint of a propeller. The outlined approach showed good agreement with the reference data in terms of aerodynamic and aeroacoustic predictions from source noise prediction to noise footprint simulation. In addition, the tonal noise predicted with the frequency-domain formulation demonstrated fairly good agreement with both high-fidelity and time-domain compact dipole/monopole predictions that confirm the reliability and computational efficiency of the frequency-domain formulation for propeller tonal noise predictions. The computational framework is then applied to explore the correlation between propeller parameters, i.e., advance ratio and blade count, and the noise footprints. It is found that for a given thrust, a drop in advance ratio can alter the source directivity dramatically, resulting in a variation up to 30 dBA on the acoustic footprint. When the advance ratio is kept the same, and the number of blades increases from 5 to 7, the variation becomes 16 dBA due to the change in the source directivity, but the maximum noise level remains the same. The latter condition reduces each blade's loading and, consequently, the associated noise. However, the total noise remains unchanged as a consequence of increasing thickness noise due to the lower advance ratio, high blade tip Mach number, and addition of extra blades.

The results suggest that the on-ground noise levels are more sensitive to the variation in the advance ratio than the blade count. In general, on-ground noise levels can be reduced significantly by increasing the advance ratio without penalizing the propeller aerodynamic performance. The on-ground noise levels can also be reduced considerably by increasing the blade count only if the tonal noise at higher harmonics is targeted.

This chapter presents an initial exploration of the efficient prediction of propeller noise emission and footprint in an idealized environment with flat terrain and a homogeneous, quiescent atmosphere. It is important to note that the noise footprint pattern and signature at the prescribed ground microphones may vary if realistic atmospheric conditions with varying wind and air temperature gradients were considered. Therefore, the next chapter will investigate the impact of weather conditions on noise propagation

and received noise levels by replacing the straight-ray propagator with a two-point 3D curved-ray tracer.

REFERENCES

- [1] F. Yunus, E. Grande, D. Casalino, F. Avallone, and D. Ragni, *Efficient low-fidelity aeroacoustic permanence calculation of propellers*, [Aerospace Science and Technology](#) **123**, 107438 (2022).
- [2] C. Nana, J.-M. Moschetta, E. Bénard, S. Prothin, and T. Jardin, *Experimental and numerical analysis of quiet mav rotors*, in *50th 3AF international conference on applied aerodynamics* (2015).
- [3] N. S. Zawodny, D. D. Boyd Jr, and C. L. Burley, *Acoustic characterization and prediction of representative, small-scale rotary-wing unmanned aircraft system components*, in *Proceedings of 72nd American Helicopter Society International Annual Forum* (2016).
- [4] R. Serré, N. Gourdain, T. Jardin, A. Sabaté López, V. Sujjur Balaramraja, S. Belliot, M. C. Jacob, and J.-M. Moschetta, *Aerodynamic and acoustic analysis of an optimized low Reynolds number rotor*, in *International Symposium on Transport Phenomena and Dynamics of Rotating Machinery* (2017).
- [5] K. Pascioni and S. A. Rizzi, *Tonal noise prediction of a distributed propulsion unmanned aerial vehicle*, in *2018 AIAA/CEAS Aeroacoustics Conference* (2018) p. 2951.
- [6] M. T. Kotwicz Herniczek, D. Feszty, S.-A. Meslioui, J. Park, and F. Nitzsche, *Evaluation of acoustic frequency methods for the prediction of propeller noise*, [AIAA Journal](#) **57**, 2465 (2019).
- [7] D. Casalino, E. Grande, G. Romani, D. Ragni, and F. Avallone, *Definition of a benchmark for low reynolds number propeller aeroacoustics*, [Aerospace Science and Technology](#) **113**, 106707 (2021).
- [8] J. E. F. Williams and D. L. Hawkings, *Sound generation by turbulence and surfaces in arbitrary motion*, *Philosophical Transactions of the Royal Society of London* **264**, 321 (1969).
- [9] D. B. Hanson, *Helicoidal surface theory for harmonic noise of propellers in the far field*, [AIAA Journal](#) **18**, 1213 (1980).
- [10] T. Zhou, H. Jiang, Y. Sun, R. J. Fattah, X. Zhang, B. Huang, and L. Cheng, *Acoustic characteristics of a quad-copter under realistic flight conditions*, in *25th AIAA/CEAS Aeroacoustics Conference* (2019) p. 2587.
- [11] Y. Yang, Y. Liu, Y. Li, E. Arcondoulis, and Y. Wang, *Aerodynamic and aeroacoustic performance of an isolated multicopter rotor during forward flight*, [AIAA Journal](#) **58**, 1171 (2020).
- [12] B. Magliozzi, D. Hanson, and R. Amiet, *Propeller and propfan noise*, *Aeroacoustics of flight vehicles: theory and practice* **1**, 1 (1991).

5

ATMOSPHERIC EFFECTS IN AIRCRAFT-COMMUNITY-NOISE PREDICTIONS

All life is problem solving.

Karl Popper

This chapter presents an atmospheric propagation model, based on ray acoustics, that accounts for realistic weather conditions in the evaluation of the noise footprint of an aircraft. Noise sources, obtained using the Ffwocs Williams and Hawkings acoustic analogy applied to scale-resolved flow simulation data, are stored on a hemisphere surrounding the vehicle. These noise sources are propagated using a point-to-point 3D curved ray propagation model that takes into account the vertical variability of air temperature and wind velocity. The eVTOL aircraft, presented by Casalino et al. [2], is used as a case study; noise footprints, obtained considering various vertically varying temperature and wind velocity distributions, are compared. It is shown that weather conditions in the acoustic wave propagation can contribute to mismatch up to 4 dBA in the illuminated zone and a significant drop in the refractive shadow zone caused by the vertical air temperature and wind velocity gradients. This work constitutes the first accomplishment in including realistic atmospheric effects in aircraft-community-noise prediction based on scale-resolved flow simulations.

Parts of this chapter have been published in Yunus et al.[1].

5.1. OBJECTIVES

THE previous chapter investigated the impact of various design and operating parameters on acoustic footprints in a homogeneous, quiescent atmosphere using the noise-hemisphere-database (NHD) approach and a straight-ray propagator. However, in realistic atmospheric conditions, sound rays become curved over long distances, making the straight-ray propagation model invalid. Consequently, wind velocity and temperature gradients introduce two physical modifications to the NHD-based noise footprint prediction approach: the intersection point of the ray and hemisphere shifts as the ray becomes curved, and the path length of a ray between the source and receiver increases.

Therefore, this chapter aims to study these effects by coupling the NHD approach with a novel 3D curved ray-tracing propagation model that accounts for weather effects on the long-range propagation of aircraft noise. The study considers two typical summer weather conditions: clear day and clear night, each with different wind velocities.

The chapter is organized as follows: Section 5.2 describes the extension of the NHD approach to an inhomogeneous moving atmosphere. Section 5.3 studies the atmospheric refraction effects on the noise footprint through a case study. Finally, Section 5.4 provides a summary of the work.

5.2. EXTENSION OF THE NHD TO AN INHOMOGENEOUS MOVING ATMOSPHERE

This work utilizes the 3D ray-path-tracing equation 2.4, as discussed in Chapter 2. To determine the eigenray connecting the source to the receiver and calculate the source levels directed to the receiver, the optimal ray shooting angles are required, such that the ray lands at the target receiver location. The Nelder-Mead simplex-based function minimization algorithm [3] is utilized for this purpose. The algorithm employs a simplex, which is a geometrical figure that consists of N dimensions of $N + 1$ vertices and all their interconnecting line segments, polygonal faces, etc. A simplex is a triangle in two dimensions and a tetrahedron in three dimensions. The proposed propagation model aims to minimize the distance D between the endpoint of a ray and a receiver position, as illustrated in Fig. 5.1. This means that the elevation angle and azimuthal angle are the two variables to be optimized.

The eigenray computation procedure in the NHD-based noise footprint prediction framework is illustrated in Fig. 5.1. For each source and receiver position, the direct and ground reflected eigenrays are computed with the following steps. First, the procedure starts with the initial simplex. Unlike the eigenray search strategies outlined in [4], in this study, a rather simpler approach is used to create the initial simplex. Namely, the shooting angles from the straight rays in a constant atmosphere are used to construct the initial simplex. Next, the objective function D , which depends on the shooting angles, is evaluated at each vertex of the simplex. Based on the function values, one of the simplex operators known as reflection, expansion, contraction, and shrink is applied. If the function value at the new vertex is smaller, i.e. $D_{i+1} < D_i$, then a new simplex will be formed, and one of the simplex operators will be applied again. The whole process continues iteratively until the function satisfies the minimum termination criteria ϵ . An overview of the two-point 3D eigenray tracing algorithm is listed in Algorithm 1.

For a given vehicle configuration and a trajectory, computation of the on-ground noise footprint follows similar steps as NHD-based noise footprint prediction with straight-ray propagator as outlined in the previous chapter. For a typical eVTOL, the NHD is characterized by four parameters: flight Mach number, angle of attack, tilt angle of the rear rotors, and rotational speed of the four rotors. For fixed-wing aircraft and helicopters, the parameters would be less than four, e.g., for helicopters, advance ratio, rotor thrust, and tip-path-plane angle are sufficient to characterize the noise hemispheres for steady and unsteady maneuvers [5]. A flight envelope is treated by considering different combinations of those parameters. Each combination represents a noise hemisphere for which an unsteady flow solution is carried out to compute the noise signals on the microphones distributed on it. Narrow band noise (NBN) spectra are computed subsequently and stored in the NHD.

In this work, a single flight condition that represents a cruising flight is considered and the noise footprint calculation procedure is displayed in Fig. 5.1. For every microphone k on a ground surface and for every time window i of 0.5 s duration, the emission time position of the vehicle along its trajectory is found. At this position, the glide angle γ_i^k and the Mach number M_i^k are calculated from the coordinates of the waypoints, whereas the pitch angle θ_i^k , the rotor RPM_i^k and the rear rotor tilt angles ϕ_i^k are interpolated from the closest waypoints. Afterward, the angle of attack α is estimated by subtracting the pitch angle from the glide angle ($\alpha_i^k = \theta_i^k - \gamma_i^k$). The noise hemisphere corresponding to this point of the trajectory $(x, y, z)_i^k$ is used to interpolate the corresponding noise hemisphere H_i^k from the three closer conditions stored in the NHD. Finally, the propagation model with the two-point 3D eigenray tracing procedure is applied and the ray-hemisphere intersection point for direct ray c_i^k and for the reflected ray $c_i'^k$ are determined subsequently. The atmospheric refraction changes the ray-hemisphere intersection point, e.g. the point s_i^k is shifted to the point c_i^k on the hemisphere, and the straight eigenray paths (dashed blue lines) are replaced by the curved eigenray paths (continuous blue lines). After that, the NBN levels are interpolated at c_i^k and $c_i'^k$ from the closest points on the hemisphere. It is worth highlighting that in this work the ground reflection is performed by computing the curved-ray path and ground plane intersection point, e.g., x_0 in Fig. 5.1, and updating the wave-slowness vector based on the boundary conditions at x_0 .

The present propagation model has an advantage over the image source method to handle multiple reflections over terrain surfaces as the sound ray can be traced continuously for a given time period. Finally, the ground noise levels are calculated using the direct and reflected eigenray paths, atmospheric absorption according to the standard procedure SAE ARP 866A, Doppler shift, and amplitude corrections.

5.3. CASE STUDY

In the present study, the eVTOL vehicle described in Casalino *et al.* [2] is considered. The eVTOL vehicle is driven by eight, 1.17 m radius propellers, which contra-rotate to maintain balance and stability. The front propellers are activated during take-off and landing procedures. The rear propellers are shrouded and they feature a variable tilt-angle depending on the flight conditions. The total wingspan is 15 m long, while the full fuselage

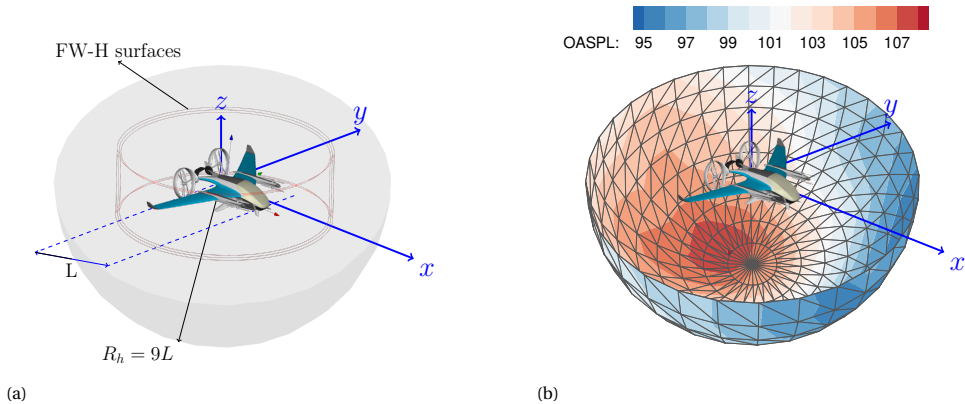


Figure 5.2: 3DS eVTOL model for forward flight, including the permeable sampling surfaces for FW-H acoustic propagation and the noise hemisphere (a). Overall Sound Pressure Levels (OASPL) over the noise hemisphere (b).

length L is approximately 7 m. This research considers only the cruising segment of the whole flight envelope. This indicates that only one operating condition is used to sample the source noise hemisphere, and it is used along the entire flight path. The operating conditions are: flight Mach number equal to 0.2 and rotor speed RPM equal to 1500. Noise hemisphere corresponding to these conditions is obtained from the NHD in Casalino *et al.* [2].

The noise hemisphere is defined in the vehicle reference system (zero pitch, yaw, and roll). The hemisphere radius R_h is set to 9 times the length of the fuselage to disregard the weather effects within the hemisphere. The hemisphere and the noise source distribution for the case under investigation are shown in Fig. 5.2.

The flight trajectory starts from point S (5, 0, 2) km and terminates at point T (-5, 0, 2) km. To investigate the weather effects on the noise footprint at different aircraft positions, two control points, A (4.5, 0, 2) km and B (3, 0, 2) km, are set on the trajectory. The model outputs the A-weighted OASPL for microphones located in a 6 km square area discretized by 21 by 21 grid points on a hard ground plane. Two different wind directions are considered: against the flight direction pointing to the positive x-axis, i.e. the East (E); and along the flight direction pointing to the negative x-axis, i.e. the West (W). An illustration of the computational scenario is shown in Fig. 5.3.

The vertical wind and temperature profiles are defined using the analytical formulas based on the Monin–Obukhov similarity theory (MOST) [6–8]. The vertical profiles are approximated by dimensional variables such as surface roughness, friction velocity (u_*), and sensible heat flux (Q_H). The surface roughness is set to 0.01 m that represents flat ground with short grass. For typical summer days, representative values of the friction velocity u_* for light, moderate, and strong wind conditions can be selected as 0.1, 0.3, and 0.6 m s^{-1} . For sunny conditions, during the daytime $Q_H = 200 \text{ Wm}^{-2}$. For clear sky at night with moderate or strong wind $Q_H = -20 \text{ Wm}^{-2}$. Based on these parameters, two different weather conditions are considered: clear day and clear night. To investigate if

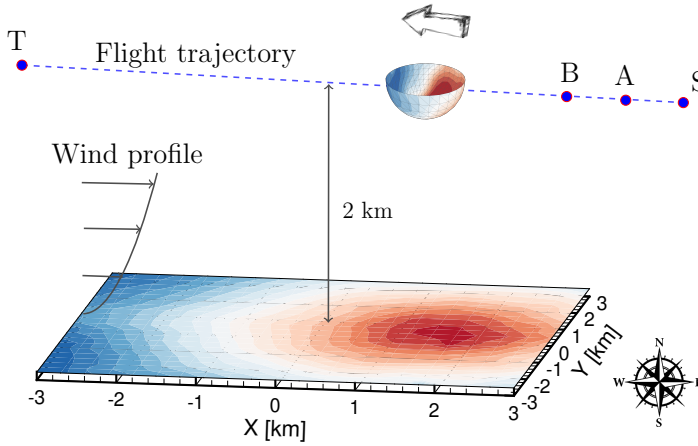


Figure 5.3: Geometry of the problem.

Table 5.1: Selected values of sensible heat flux and friction velocities for the weather conditions.

Weather conditions	Q_H [Wm^{-2}]	u_* [ms^{-1}]
Clear night	-20	0.5
Clear day	200	0.27

wind velocity or temperature is the dominant factor in the formation of the refraction for a specific weather condition, different friction velocities are selected for all two weather conditions. The selected values for these weather conditions are listed in table 5.1 and the weather profiles are illustrated in Fig. 5.4. It's important to note that the Monin-Obukhov temperature and wind velocity profiles are specifically designed for the Atmospheric Surface Layer (ASL), which constitutes approximately 10% of the Atmospheric Boundary Layer (ABL) height. This ABL height usually ranges from 0.5 km to 2 km. Consequently, the Monin-Obukhov Similarity Theory (MOST) cannot be effectively applied to temperature and wind velocity profiles extending up to 2 km. To put it differently, the profiles depicted in Fig. 5.4 serve as representative "model" profiles.

5.3.1. VALIDATION

In this section, the two-point 3D eigenray tracing implementation is validated. Then, a test case is used to demonstrate the accuracy of the curved-ray NHD approach in the footprint prediction.

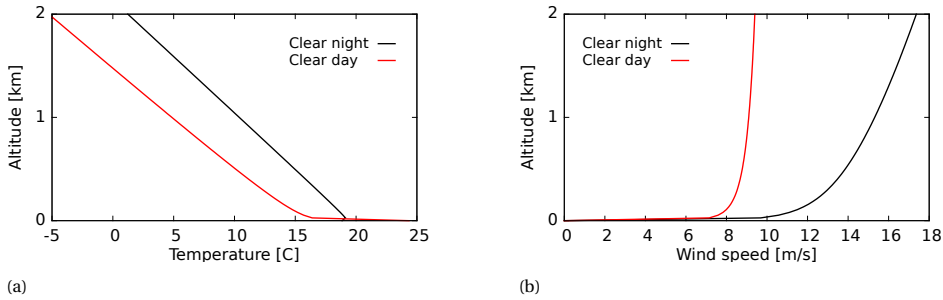


Figure 5.4: Weather profiles. Temperature profiles (a). Wind profiles (b). The wind direction points to the positive x-axis.

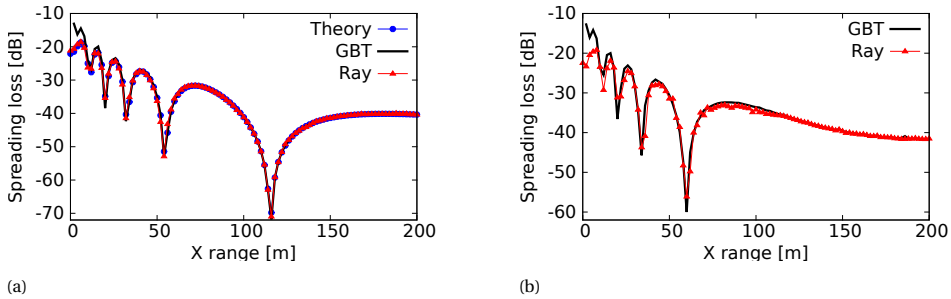


Figure 5.5: Comparison between the spreading loss calculated with different methods. Homogeneous atmosphere (a). Non-homogeneous atmosphere (b).

VALIDATION OF THE PROPAGATION MODEL

The ray-tracing propagation model is initially validated against an exact solution Salomons [9] that describes the elementary sound propagation problem in a homogeneous atmosphere where noise levels at the receiver locations are determined with the direct and ground reflected ray path lengths. Then, the model is validated against the Gaussian Beam Tracing (GBT) method outlined in Chapter 2 solution for the same problem in an inhomogeneous atmosphere. A monopole source is located at (0, 0, 20) m and all the receivers are distributed along with the horizontal range with a distance of 2 m. The receivers' height is 10 m. The horizontal range is set to 200 m to ensure that there are only two contributing rays i.e., direct and one reflected rays. The source frequency is 100 Hz. The non-homogeneous atmosphere is represented with a linearly increasing sound speed profile with a sound speed gradient of 0.5 s^{-1} .

The eigenray tracing model result, labeled "Ray" in Fig. 5.5a is compared with the exact solution for a point source above the rigid boundary and calculations from the GBT. The only difference is an over-prediction of GBT near the source. For the non-homogeneous atmosphere with a linear sound speed profile, Fig. 5.5b, the interference pattern is shifted. The ray-tracing result and GBT still show good agreement. On the basis of the results shown in Fig. 5.5a, it is likely that the ray-tracing approach is more accurate near the source and is able to capture the interference shift.

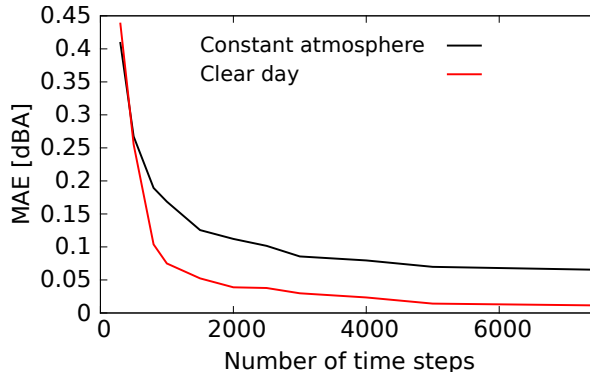


Figure 5.6: MAE as a function of the number of time steps for the cases with and without weather conditions.

ACCURACY OF THE CURVED-RAY NHD APPROACH

The accuracy of the ray-hemisphere intersection point and the travel time along an eigen-ray path is determined by the number of time steps that was used to march the ray-tracing system Eq. 2.4 solution forward in time. Namely, as outlined in section 5.2, a ray path with a larger number of time steps results in a smaller D as the ray path is characterized by many points. Once D is small enough, e.g., in a constant atmosphere, the ray-hemisphere intersection point and the travel time along the ray path will converge to the ray-hemisphere intersection point and travel time computed with the straight-ray NHD approach. In this subsection, the accuracy of the propagation model is investigated for cases with and without weather effects. For the case without weather effects, the straight-ray NHD is correct and used as a reference. Therefore, the flyover noise predicted with the curved-ray NHD for the different number of time steps is compared against the one predicted with the straight-ray NHD. The weather is characterized by stationary air with constant temperature of 287 K. For the case with weather effects, the curved-ray NHD with larger number of time steps is used as a reference. The flyover noise predicted with smaller number of time steps is compared against the one computed with subsequent larger number of time steps. The clear day condition with the wind blowing along the flight direction is considered.

The mean absolute error (MAE) at the microphone located at the center of the ground area is calculated for the different number of time steps and depicted in Fig. 5.6. It is seen that MAE is decreasing with the increasing number of time steps. It is found that independently on the conditions the curve start flattening for a total number of time steps larger than 1000. In the following, the number of time steps is set to 1200 to keep the MAE below 0.2 dBA.

5.3.2. RESULTS

CLEAR NIGHT

In order to investigate the effects of the wind velocity and temperature gradients on sound propagation path, sound rays are traced between vehicle emission time positions and the microphones located at the corners and the center of the ground area. The ve-

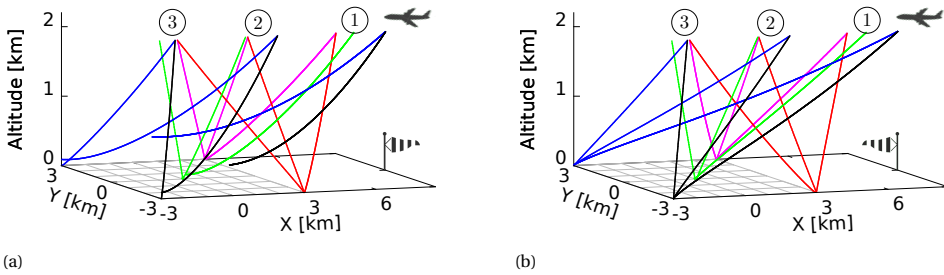


Figure 5.7: Direct eigenrays traced between vehicle emission time positions and the microphones located at the corners and the center of the ground area in the clear night condition for the wind blowing against the flight direction (a) and along the flight direction (b).

hicle emission time positions are sampled at three different waypoints, i.e. the starting point, middle point, and the terminal point of the trajectory. For convenience, those emission time positions are labeled as first, second, and third emission time position.

Fig. 5.7a illustrates how sound rays are refracted when the vehicle flies against the wind direction. For the microphones located at the farthest corners of the ground area, sound rays emitted from the first and second emission time positions (black and blue rays) are refracted upwards before they reach the microphones. This condition results in a refractive shadow zone. When the vehicle flies in the same direction as the wind, all sound rays tend to be straight despite the presence of the weather condition as shown in Fig. 5.7b. It is worth noting that, if the vehicle flies against the wind direction, sound rays curve more when the vehicle is farther away from the microphones and they become almost straight when the vehicle is closer to the microphones. This implies that weather has an effect on the refraction of the sound rays only if the vehicle is at a distant location.

In order to better illustrate this aspect, the on-ground noise footprints when the vehicle is located at control points A and B are displayed in Fig. 5.8. The loss in the refractive shadow zone is calculated by adding the loss estimated with the correction model Arntzen *et al.* [10] to the loss at the shadow zone boundary.

When the vehicle flies against the wind direction and is located at A, due to the refractive shadow zone, noise levels start to drop rapidly after $x = -0.7$ km along the flight direction. In contrast, when the vehicle flies along the wind direction, no significant refraction effect in the noise levels is observed. The field difference between these two conditions, shown in Fig. 5.8a, further highlights the relevant effect of the shadow zone; when the vehicle is at A, there is up to 24 dBA difference in the refractive shadow zone and up to 4 dBA in the illuminated zone between noise footprints computed for these two wind directions. When the vehicle flies against the wind and is positioned at B, the shadow zone boundary shifted from $x = -0.7$ km to $x = -2$ km. When the vehicle flies along the wind direction, no significant weather effects in the noise footprint is observed. The field difference between these two wind directions is plotted in Fig. 5.8b. It shows that there is still up to 12 dBA difference due to the strong wind.

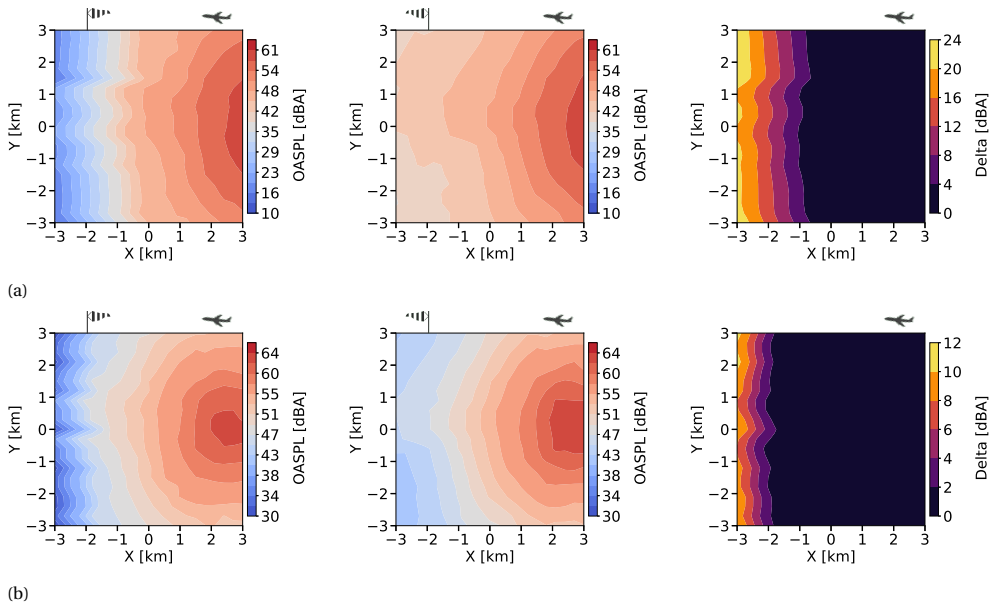


Figure 5.8: On-ground noise footprints at control point A (a) and B (b) in the clear night with wind directions against the flight direction, along the flight direction, and field difference between them.

CLEAR DAY

The effect of the clear day condition on the sound propagation with two different wind directions is shown in Fig. 5.9. When the vehicle flies against the wind direction, only the sound rays traced between the farthest microphones and the first emission time positions are refracted upwards, thus causing the refractive shadow zone. For the case where the vehicle flies along the wind direction, the longest eigenrays (black and blue rays emitted from the first emission time position) are refracted slightly upwards despite the wind velocity. This implies that the temperature gradient is the dominant variable that affects the refraction.

On-ground noise footprint at the control point A and B for the two wind directions are shown in Fig. 5.10. When the vehicle flies against the wind and is located at A, compared to the condition on the clear night, the shadow zone boundary is shifted from $x = -0.7$ km to $x = -1.8$ km along the flight direction. When the vehicle flies in the same direction as the wind, no significant weather effects on the noise footprint are seen. The difference between these two noise footprints is displayed in Fig. 5.10a. It indicates noise levels drop up to 15 dBA in the refractive shadow zone and up to 3 dBA in the illuminated zone. At B, the on-ground noise footprints computed for the two wind directions showed very similar trend. The field difference between these two conditions is shown in Fig. 5.10b. This shows the difference is minimal and the shadow zone is about to disappear completely.

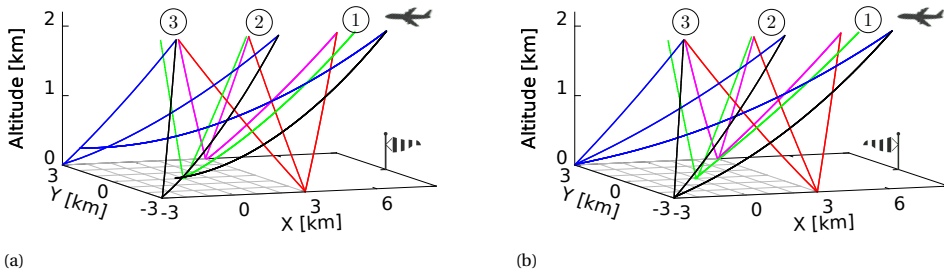


Figure 5.9: Direct eigenrays traced between vehicle emission time positions and the microphones located at the corners and the center of the ground area in the clear day condition for the wind blowing against the flight direction (a) and along the flight direction (b).

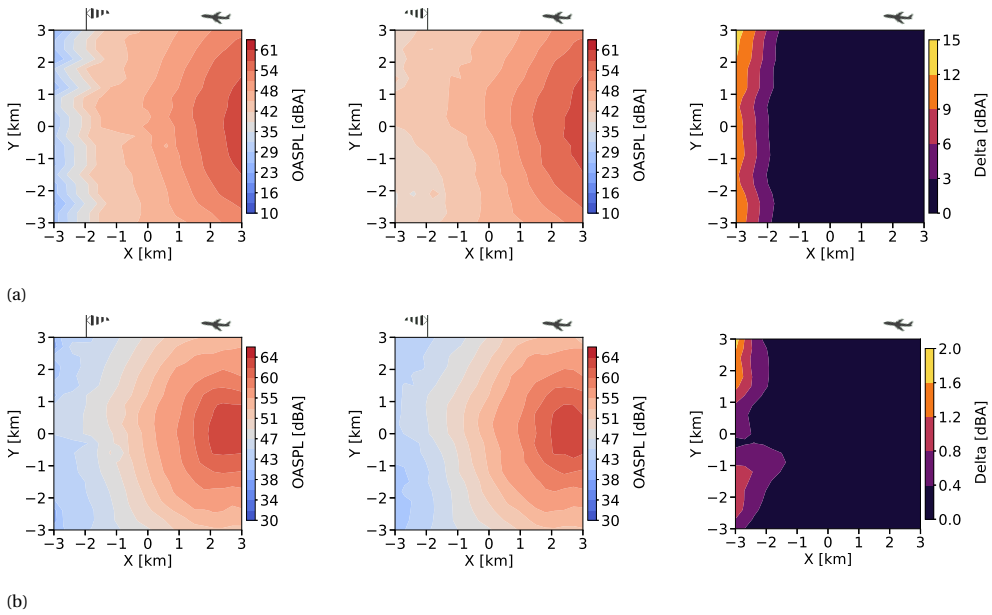


Figure 5.10: On-ground noise footprints at control point A (a) and B (b) in the clear day with wind directions against the flight direction, along the flight direction, and field difference between them.

5.4. CONCLUDING REMARKS

A new noise footprint prediction is proposed to simulate the noise footprint of an eV-TOL vehicle that is cruising over a flat terrain under realistic weather conditions. The meteorological effects on the on-ground noise footprint are studied with a propagation model based on the ray acoustics that is implemented in the NHD-based footprint prediction approach. For all weather conditions, on-ground noise footprints are computed. It is observed that the refractive shadow zone appears when the vehicle flies against the wind direction. The refractive shadow zone is stronger when the vehicle is farther away from the receivers and becomes weaker or disappears when the vehicle is closer to the receivers. When the vehicle flies along the wind direction, for all weather conditions, no significant weather effect on the noise footprint is observed. Comparing the influences of different meteorological conditions on the noise footprint, the effect of the refractive shadow zone is the most relevant for the clear night condition, i.e. the case with the higher temperature and wind velocity gradients compared to the other conditions.

The proposed methodology allows on-ground noise footprint computation under meteorological conditions in a reasonable time, but their need for input meteorological data remains a crucial point. For preliminary assessment, a flat terrain as a perfect reflector is considered, and the weather profiles obtained using MOST are used as a first approximation. However, in a realistic urban environment, temperature, and wind velocity gradients are highly affected by local urban geometries, and they become range dependent, therefore complex phenomena due to the combined effect of refraction, diffraction, multiple reflections, and their dependence on the propagation range would occur during the sound propagation. Besides, a simple linear model is applied to estimate the propagation loss in the refractive shadow zone. In the upcoming chapter, the limitations mentioned will be addressed by introducing a Gaussian beam tracer that eliminates the need for eigenray tracing and effectively handles the singularities at shadow zone boundaries and caustic points. Additionally, this new approach takes into consideration the impact of range-dependent terrain and weather profiles on acoustic propagation.

REFERENCES

- [1] F. Yunus, D. Casalino, F. Avallone, and D. Ragni, *Toward inclusion of atmospheric effects in the aircraft community noise predictions*, *J. Acoust. Soc. Am.* **150**, 759 (2021).
- [2] D. Casalino, W. C. van der Velden, and G. Romani, *Community noise of urban air transportation vehicles*, in *AIAA Scitech 2019 Forum* (2019) p. 1834.
- [3] J. A. Nelder and R. Mead, *A simplex method for function minimization*, *The computer journal* **7**, 308 (1965).
- [4] R. de Moraes Calazan and O. C. Rodríguez, *Simplex based three-dimensional eigenray search for underwater predictions*, *J. Acoust. Soc. Am.* **143**, 2059 (2018).
- [5] M. Gennaretti, J. Serafini, G. Bernardini, A. Castorrini, G. De Matteis, and G. Avanzini, *Numerical characterization of helicopter noise hemispheres*, *Aerospace Science and Technology* **52**, 18 (2016).

- [6] V. E. Ostashev and D. K. Wilson, *Acoustics in moving inhomogeneous media*, 2nd ed. (CRC Press, 2015).
- [7] R. B. Stull, *An Introduction to Boundary Layer Meteorology* (Springer Science & Business Media, 1988) Chap. 9.
- [8] H. Panofsky and J. Dutton, *Atmospheric turbulence: Models and methods for engineering applications*, 1st ed. (John Wiley, 1984) Chap. 6.
- [9] E. M. Salomons, *Computational Atmospheric Acoustics* (Springer Science & Business Media, 2001).
- [10] M. Arntzen, S. A. Rizzi, and H. G. Visser, *A framework for simulation of aircraft flyover noise through a non-standard atmosphere*, in *Proceedings of the 18th AIAA/CEAS aeroacoustics conference*, Vol. 2079 (American Institute of Aeronautics and Astronautics, Colorado Springs, CO, USA, 2012).

6

AIRBORNE NOISE PROPAGATION IN A NON-TURBULENT URBAN ENVIRONMENT

Knowledge is the conformity of the object and the intellect.

Averroes (Ibn Rushd)

This chapter presents a noise propagation approach based on the Gaussian beam tracing (GBT) method that accounts for multiple reflections over three-dimensional (3D) terrain topology and atmospheric refraction due to horizontal and vertical variability in wind velocity. A semi-empirical formulation is derived to reduce truncation error in the beam summation for receivers on the terrain surfaces. The reliability of the present GBT approach is assessed with an acoustic solver based on the finite element method (FEM) solutions of the convected wave equation. The predicted wavefields with the two methods are compared for different source-receiver geometries, urban settings, and wind conditions. When the beam summation is performed without the empirical formulation, the maximum difference is more than 40 dB; it drops below 8 dB with the empirical formulation. In the presence of wind, the direct and reflected waves can have different ray paths than those in a quiescent atmosphere, which results in less apparent diffraction patterns. A 17-fold reduction in computation time is achieved compared to the FEM solver. The results suggest that the present GBT acoustic propagation model can be applied to high-frequency noise propagation in urban environments with acceptable accuracy and better computational efficiency than full-wave solutions.

Parts of this chapter have been published in Yunus et al. [1–3]

6.1. OBJECTIVES

THE previous chapter investigated the impact of atmospheric conditions on noise propagation over flat terrain using the curved-ray tracing method. However, in urban settings, the local urban geometry can result in varying wind velocity and temperature gradients, leading to range-dependent propagation phenomena. Thus, weather becomes an important factor in noise propagation, even over shorter distances between the source and receivers.

Compared to the curved-ray tracing method, the Gaussian beam tracing (GBT) method is computationally efficient, as it does not require calculating eigenrays connecting the source to receivers distributed over a fast area. Additionally, the GBT method smooths out singularities at the shadow zone boundary and caustic regions, making it a more accurate solution than the ray tracing method. However, the GBT method is not well-suited to calculate reflected wavefields on terrain surfaces, which can cause truncation errors [6–8].

To investigate the effects of urban topology and weather conditions on airborne noise propagation in a non-turbulent urban environment, two modifications are required in the state-of-the-art GBT tools. Firstly, the GBT formulations must account for the impact of wind on acoustic propagation in an inhomogeneous moving medium. Secondly, an approach is necessary to consider the reflected wavefields on terrain surfaces, which can reduce truncation errors in the beam summation on the terrain boundary.

This chapter aims to address these issues by developing a propagation model based on the GBT formulations outlined in Chapter 2. To reduce the truncation error in the beam summation, a semi-empirical formulation is derived.

The rest of this chapter is organized as follows. Section 6.2 presents an overview of the computational approach, including the derivation of the semi-empirical formulation. Section 6.3 evaluates the GBT-based atmospheric acoustic propagation approach using a validation case study. Finally, Section 6.4 provides a summary of the work.

6.2. AN OVERVIEW OF THE COMPUTATIONAL APPROACH

A standard hybrid methodology is used to predict airborne noise propagation in a 3D urban environment. An in-house solver acoustic ray and Gaussian beam tracer (UYGUR) is developed based on the 3D ray-path-tracing (RPT) method [4], and the GBT method [5] outlined in Chapter 2. A schematic illustration of the computational procedure is shown in Fig. 6.1. The input for the computational framework includes the terrain geometry, as well as the 3D wind and temperature profiles. For more information on the file structure of the input, please refer to Appendix C. After reading the environmental profiles, UYGUR calculates the noise propagation in an urban environment in the following steps. In the first step, RPT [4] is carried out to determine the central ray Ω associated with each Gaussian beam (see Fig. 2.5(b)). In the second step, dynamic ray tracing (DRT) [5] is performed to calculate the geometrical spreading and wavefront variation of the sound wave in the vicinity of each ray. Finally, the acoustic field at receiver points is calculated by summing the contribution of each Gaussian beam passing nearby the receiver location. To calculate the wavefield at the receivers located on the terrain surface, a combination of beam summation and a new semi-empirical formulation is used. This

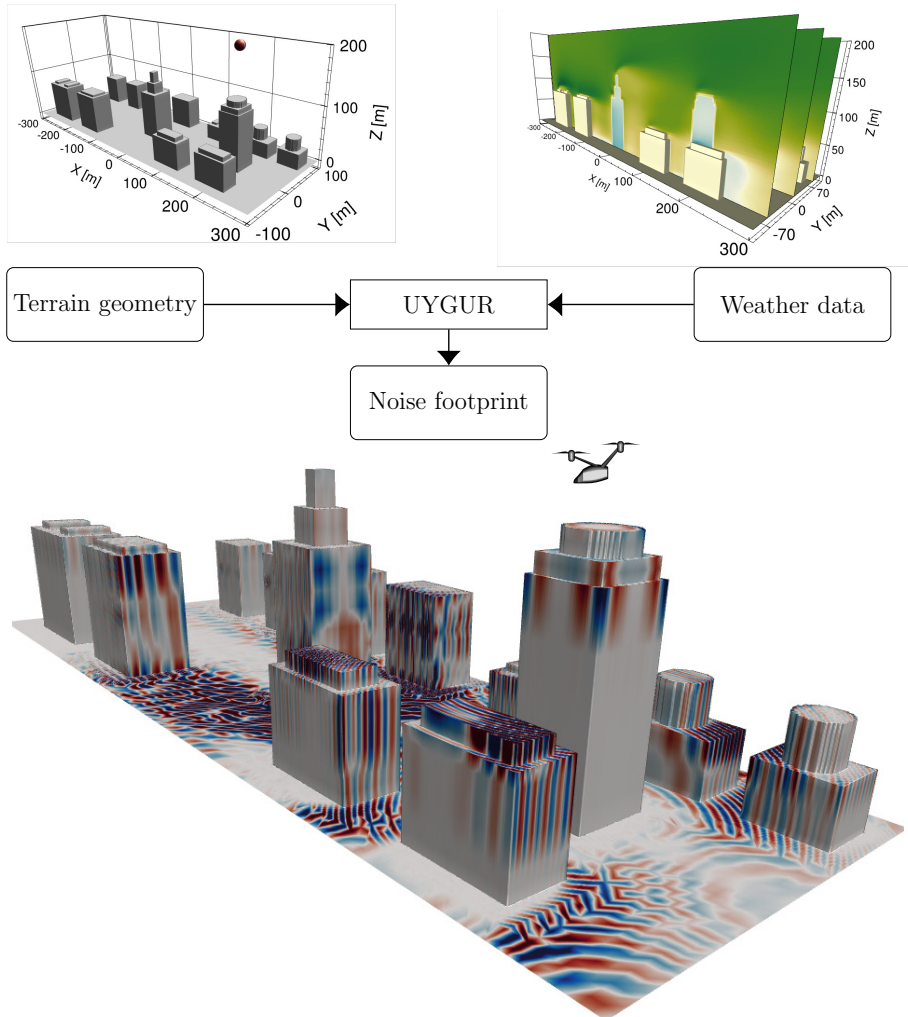


Figure 6.1: Schematic illustration of the computational procedure.

approach reduces the truncation error and considers the reflected wavefields. The next section will outline the details of this novel approach.

6.2.1. WAVEFIELD ON THE TERRAIN SURFACES

If the wavefield on the terrain surface is calculated using Eq. 2.20, a truncation error will arise as the regularity condition is violated [6–8]. This error is related to the beamwidth and becomes more significant when the source frequency ω decreases. The half-width of a beam reads

$$L(R', \omega) = \left[\frac{2}{\omega} \text{Im}(\mathbf{M}^{-1}) \right]^{1/2} \quad (6.1)$$

At lower frequency, for instance, the beamwidth becomes large; therefore, the bottom end of the beam that grazes the terrain boundary pass below the boundary surface (see Fig. 6.2). To eliminate the truncation error, one must perform the beam summation in a way that does not violate the regularity condition. To this end, this work proposes to lift the receivers \mathbf{x}_0 on the terrain surface Z_r with an offset d and to carry out beam summation on a virtual surface or line $Z_v = Z_r + d$ instead of on the terrain surface (see Fig. 6.2). In this case, one can not only satisfy the regularity condition of the ray field around the receivers but also account for the reflected wavefields as d will be defined in the vicinity of \mathbf{x}_0 . Based on this observation, an expression of d can be sought in the form of $d = d(L(\mathbf{x}_0, \omega))$. As the beamwidth is a function of \mathbf{M} , it can not be determined analytically without solving the DRT system. Furthermore, considering many receiver points at which the beamwidth can be different, it is not feasible to obtain a closed-form expression for d . Therefore, this study attempts to obtain a semi-empirical formulation through curve fitting.

In order to determine d , the impact of the wind and the inhomogeneity of the atmosphere on the wavefield on the terrain surfaces is assumed to be negligible. Hence, a 2D case with a homogeneous, quiescent atmosphere and a flat terrain is considered. For convenience, the acoustic wavelength $\lambda = c/f$ instead of the source frequency $f = \omega/2\pi$ is employed. The sound speed is $c = 340.3$ m/s and $f = [100, 3500]$ Hz. A time-harmonic monopole source is located at $(0, 5.28\lambda_0)$, here λ_0 is the wavelength corresponding to $f = 100$ Hz. Receivers \mathbf{x}_0 are distributed along the positive X-axis in a range $\bar{x} = [0, 14\lambda_0]$ with $0.14\lambda_0$ interval.

The beamwidth at \mathbf{x}_0 are calculated and the dependence of $L(\mathbf{x}_0, \omega)$ on ω and the range is illustrated in Fig. 6.3(a). As seen, $L(\mathbf{x}_0, \omega)$ increases considerably with increasing propagation range at lower frequencies. The increase in $L(\mathbf{x}_0, \omega)$ at a higher frequency is not so significant compared to the one at a lower frequency. To further analyze the dependence of $L(\mathbf{x}_0, \omega)$ on the frequency and the range, obtained $L(\mathbf{x}_0, \omega)$ values are normalized with their peak value of $L_{max} = 8.43$ m. Fig. 6.3(b) depicts normalized beamwidth $L(\mathbf{x}_0, \omega)/L_{max}$ variation along the range at some frequencies. As seen, the variation along the range is almost linear; it is larger at the lower frequency and starts flattening when the frequency increases. Hence, one can state the relation as follows:

$$d = \mathcal{B}SD \quad (6.2)$$

where \mathcal{B} is the amplitude factor and here $\mathcal{B} = 1$ as normalized beamwidth of unit amplitude is considered, S is a dimensionless factor that describes the variation of the nor-

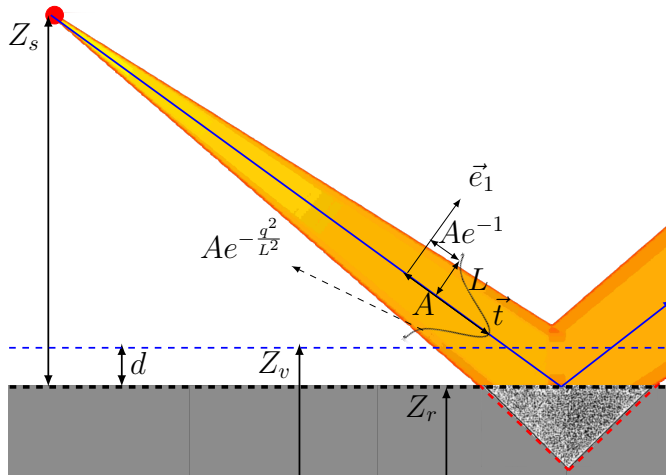


Figure 6.2: A sketch of a beam interacting with the terrain surface. The amplitude profile of the Gaussian beam along the trajectory of a straight ray and the ray-centered coordinates specified by the unit vector \vec{t} tangent to the ray and the unit vector \vec{e}_1 normal to the ray. A indicates the beam amplitude on the central ray (blue line), and Ae^{-1} denotes the beam amplitude at the edge of the beam. The top boundary of the shaded area (black dashed line) represents the actual receiver line, while the dashed blue curve indicates the virtual line. The area inside the dashed triangle denotes the part of the beam that passes below the terrain surface.

malized beamwidth with respect to the frequency and the source-receiver distance D ; hence, $S = S(D, \omega)$. The frequency dependence of the normalized beamwidth is illustrated in Fig. 6.3(c). At the receiver closer to the source location, the variation with the frequency is negligible, while the variation exhibits an exponential behavior at longer ranges. By performing a curve fitting, an expression for S is obtained as

$$S = 1 - \exp\left(-\frac{0.1D/\lambda + 4\pi}{D/\lambda}\right) \quad (6.3)$$

A much better fit is obtained if D in 6.2 is replaced by $D - Z_s$. The fitted curves of d based on these expressions are depicted with the solid lines in Fig. 6.3(b) and (c). As seen, the curves fit well with the data points. In conclusion, since the parameter S in Eq. 6.2 has been determined by fitting the normalized beamwidth obtained with the GBT method, d can be interpreted as an offset that equals the beamwidth multiplied by the constant \mathcal{B} ($\mathcal{B} < 1$).

The above expression of d is obtained based on the normalized beamwidth of unit amplitude. Furthermore, the GBT solutions do not provide any information about \mathcal{B} except $d < L(\mathbf{x}_0, \omega)$ and $d \rightarrow 0$ if $L(\mathbf{x}_0, \omega) \rightarrow 0$. Moreover, an essential criterion determining \mathcal{B} is that the GBT results obtained with d should account for the reflected wavefields from buildings/obstacles on the terrain surface. Hence, the amplitude factor \mathcal{B} must be determined by fitting the GBT solutions calculated using the expression of d with corresponding reference solutions. To this end, reference solutions are generated with a FEM-based reference solver considering the single-building urban configuration, which will be outlined in the following section. The amplitude factor \mathcal{B} is found to be

$\mathcal{B} = \pi/19$, which is obtained as the value that minimizes the error between the reference and GBT solutions for 45 GBT cases. These cases are generated considering sources in the frequency range [100 Hz, 150 Hz, 200 Hz] and locations [(50, 0, 5) m, (50, 5, 15) m, (50, 0, 18) m] and five values of B in the range [0, 1]. The final expression of d reads:

$$d = \frac{\pi}{19} \left[1 - \exp \left(-\frac{0.1\zeta + 4\pi}{\zeta} \right) \right] (D - Z_s) \quad (6.4)$$

where $\zeta = D/\lambda$.

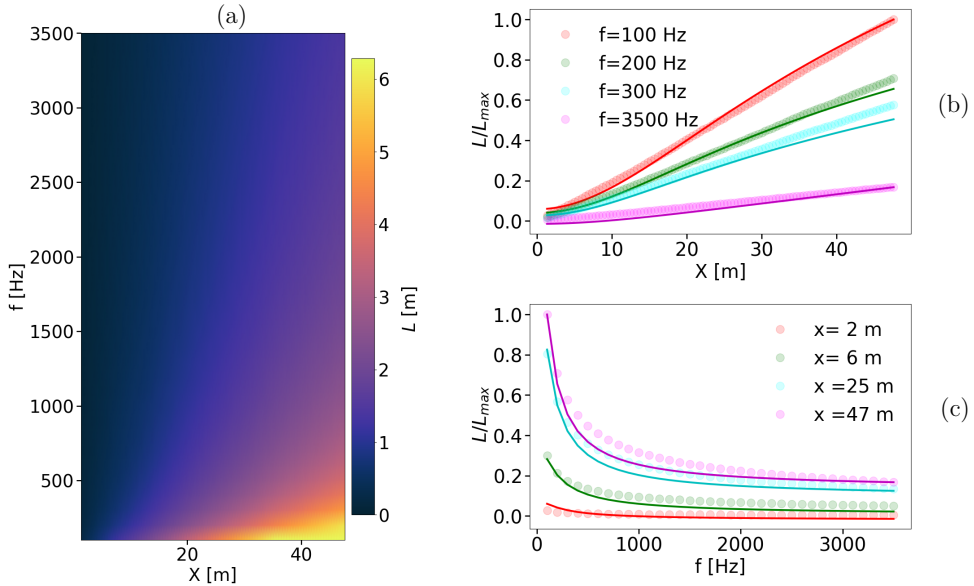


Figure 6.3: Beamwidth, L , as a function of source frequency and propagation range (a). Variation of the normalized beamwidth along the propagation range at some frequencies (b) and along the frequency at some receiver points (c). Filled circles indicate the data generated by the GBT tool, and solid lines represent the fitted curves.

6.3. VALIDATION CASE STUDY

The GBT model was assessed in the previous work from Yunus *et al.* [9] by comparing it against an exact solution that describes the elementary sound propagation problem in a homogeneous atmosphere over flat terrain. In this work, the proposed semi-empirical formulation is validated against the FEM-based reference solution for different source frequencies and source position. Then, the effect of 3D wind flow on acoustic propagation is investigated.

6.3.1. REFERENCE SOLUTION

The reference solution is obtained using the frequency-domain FEM acoustic solver *OptydB-GFD* [10] and solving a second-order wave equation derived by Pierce [11]. The wave

equation describes the propagation of potential fluctuations superimposed to a rotation mean flow that varies slowly over the length and time scales of the sound waves (high-frequency limit). *Opty∂B*-GFD uses an immersed boundary technique for automatic mesh generation. The immersed boundary method relies on the intrinsic capabilities of a finite-element scheme of decoupling the nodes at which the solution is calculated from the points where an equation is satisfied. Therefore, the zero-normal derivative equation of the perturbation velocity potential¹ (slip condition) is satisfied at the exact points of the imported immersed geometry, using the exact value of the surface normal. In order to improve the capability of the method to take into account the diffraction of an edge, when one mesh volume element is crossed by a wedge, one or more mutually unconnected virtual nodes are added to the volume mesh by duplication, and an equal number of new equations are added to the system. Every additional equation corresponds to the slip condition with a local value of the surface normal. The FEM code *Opty∂B*-GFD has been validated for a variety of canonical problems [13–15] involving acoustic propagation in uniform and non-uniform flows, and its complete description is outside the scope of the present work.

6.3.2. CASE SETUP

Two different urban settings are considered. The urban setting with a single building block is used to validate the proposed semi-empirical formulation. At the same time, a three-building configuration is considered to study the acoustic effects of wind flow. All three building blocks have the same dimensions. The building length L_B is set to 4 m to keep the computational cost reasonable for the reference solution. The first two building blocks create the first urban canyon A, whose width is $4L_B$, and the second and third building blocks create the second urban canyon B, whose width is L_B . The urban boundary is considered to be a perfect reflector; hence no acoustic energy is absorbed by the boundaries. The dimensions of the computational domain and the building blocks are listed in Table. 6.1.

A time-harmonic monopole source with two different source frequencies, i.e., 100 Hz, 200 Hz, and two different source locations, is considered. The source is stationary, and the source amplitude at a radial distance of 1 m from the source position is 0.2 Pa. The acoustic wavefield is studied on two different receiver planes: XZ-plane at $Y = 0$ m and XY-plane at $Z = 2.5L_B$. The building 1 is used to represent the single building configuration. Examples of source-receiver geometry for the three building configurations are displayed in Fig. 6.4.

For the given source frequencies, the perfectly matched layer (PML) thickness in the reference solution is set to $0.5L_B$ to prevent any contamination due to possible reflected waves from the domain boundaries and ensure the PML absorbs acoustic energy properly. Moreover, the domain is discretized by considering 9 points per wavelength to ensure an acceptable numerical accuracy.

In total, 5 cases that feature acoustic impacts of varying source frequencies, source-receiver geometries, urban settings, and weather conditions are considered to validate

¹Pierce does not use this terminology. Ostashev *et al.* [12] clarify that Φ in Pierce [11] is the auxiliary function which is "a scaled acoustic velocity potential to order α^0 ". See the text above and below Eq.(7) in Ostashev *et al.* [12].

Table 6.1: Dimensions of the computational domain and building blocks.

Domain	x [m]	length [m]	y [m]	width [m]	z [m]	height [m]
Domain	[0, 60]	$15L_B$	[-10, 10]	$5L_B$	[0, 20]	$5L_B$
building 1	[8, 12]	L_B	[-4, 4]	$2L_B$	[0, 12]	$3L_B$
building 2	[28, 32]	L_B	[-4, 4]	$2L_B$	[0, 12]	$3L_B$
building 3	[36, 40]	L_B	[-4, 4]	$2L_B$	[0, 12]	$3L_B$

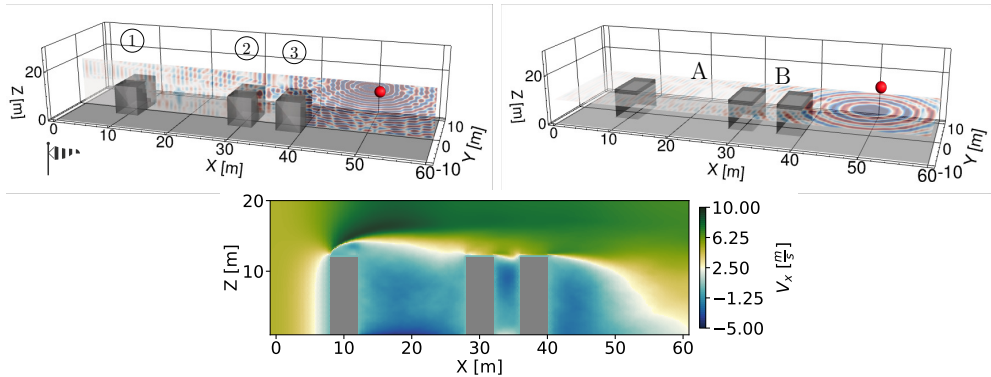


Figure 6.4: Source receiver geometry in a three-building environment. Vertical receiver plane at $Y = 0$ m (left). Horizontal receiver plane at $Z = 2.5L_B$ (right). Snapshot of the mean flow field on the vertical receiver plane (bottom). Wind direction points to the positive X-axis.

the present GBT model. The test matrix for this validation is listed in Table 6.2. The GBT and the reference tools run on an Intel(R) Xeon(R) Gold 6140 CPU @2.3 GHz processor with 36 cores.

WEATHER CONDITIONS

Two weather conditions, a windy daytime and a quiescent daytime with a constant temperature of 15 °C ($c = 340.3$ m/s) are considered. The flow field in the computational domain is resolved using the high-fidelity CFD solver SIMULIA PowerFLOW® outlined in Chapter 3. In this work, three VRs are used, with the smallest voxel size of $0.0167L_B$. This results in a total voxel count of 72 million within 70 million fine-equivalent voxels. The VRs are placed onto regions of interest, e.g., around the building edges. The initial velocity is set to 5 m/s at the inlet, and the wind direction points to the positive X-axis direction. The mean flow required by the GBT and reference calculations is then acquired by time-averaging flow data sampled at multiple time frames. A snapshot of the mean flowfield on the vertical receiver plane for the three-building configuration is displayed in Fig. 6.4. It should be noted that the mean flow profile may not fully represent the realistic wind profile as it is imposed only 8 m away from the first building.

Table 6.2: Test matrix for the case study.

Case #	f [Hz]	urban setting	source location [m]	receiver height [m]	atmosphere
1	100	single building	$(12.5, 1.25, 1.25)L_B$	0	quiescent
2	200	single building	$(12.5, 1.25, 1.25)L_B$	0	quiescent
3	100	single building	$(12.5, 0, 4.5)L_B$	0	quiescent
4	200	three buildings	$(12.5, 0, 4.5)L_B$	receiver planes	quiescent
5	200	three buildings	$(12.5, 0, 4.5)L_B$	receiver planes	windy

6.3.3. VALIDATION

ACCURACY OF THE PROPOSED SEMI-EMPIRICAL FORMULATION FOR THE BEAM SUMMATION

The validity of the semi-empirical formulation, for varying source frequency, is evaluated by comparing the GBT predictions to the reference solutions in Case 1 and Case 2. Real values of the complex pressure and corresponding sound pressure levels (SPL), calculated with and without the proposed empirical formulation, are compared to the reference results, as shown in Fig. 6.5 and Fig. 6.6.

When the beam summation is performed without the proposed empirical formulation, i.e., on the terrain surface Z_r , the GBT predicts a very low-pressure magnitude due to the truncation error, as displayed in the second row of Fig. 6.5. A dramatic reduction of up to 40 dB is seen in the noise levels (see fourth row of Fig. 6.5). A remarkable improvement is achieved when the beam summation is performed with the proposed empirical formulation on the corresponding virtual surface at Z_v that captures well the general trend of the interference pattern of the reference result. The slight difference in the interference pattern is ascribed to the presence of diffraction in the reference solution, which is not included in the GBT model. To further highlight the improvement, mean absolute error (MAE) in pressure magnitude and phase and absolute error (AE) in the noise levels are calculated. The MAEs are evaluated at receiver points distributed along the X-axis with a $0.25L_B$ interval. At each point, an MAE is recorded by taking the mean value of the AEs sampled along Y-axis with a $0.25L_B$ interval. The MAEs calculated with and without the empirical formulation are compared to each other. In Case 1, the maximum MAE of the pressure magnitude occurs around the source location and is reduced by an order of 2 with the proposed empirical formulation. The AE in the noise levels can reach up to 40 dB when the beam summation is performed on Z_r . While the beam summation is calculated on Z_v , the AE reduces greatly and is below 8 dB in the illuminated zone where direct rays can reach. Furthermore, the AE drops under 5 dB around the top and bottom sides of the building. This is attributed to the larger beamwidth of the limiting beam that separates the shadow and illuminated zones. Higher values of the AE behind the building are due to the lack of diffraction effects in the GBT model. The MAE of the phase calculated with the empirical formulation increases slightly in front of the building and reduces gradually at the receivers farther away from the building. A similar trend is observed in Case 2. However, the AE around the top and bottom sides and the top left corner of the building increases noticeably more than in Case 1. This is

due to the smaller beamwidth in Case 2 as a consequence of higher frequency; hence, the limiting beam can not contribute more to the shadow zone behind the building.

The validity of the semi-empirical formulation under varying source locations is further examined by comparing the GBT predictions to the reference solutions in Case 1 and Case 3. The results are displayed in Fig. 6.5 and Fig. 6.7, respectively. As seen from the field plots of the pressure magnitude and corresponding noise levels, for Case 3, the beam summation calculated on Z_r failed to approximate the reference solution. In contrast, the beam summation performed on Z_v can capture the general trend of the interference of the reference solution. The MAEs of the pressure magnitude calculated on both Z_r and Z_v get smaller than in Case 1. This is due to the higher source altitude, which improves the GBT prediction. For relatively lower frequency problems, the GBT method can give very satisfactory results if $Z_s - Z_r \gg \lambda$ so the beams can reflect properly [16]. This has been discussed in ocean acoustics, and a validity condition is proposed as $Z_s - Z_r > 10\lambda$ [17]. However, this has never been addressed in outdoor sound propagation problems. It remains unknown how small the wavelength should be with respect to the source altitude to ensure a satisfactory result. Further research is needed to investigate this aspect of the GBT method for outdoor sound propagation problems.

In general, the field predictions with the proposed semi-empirical formulation showed good agreement with the reference results. The proposed method can account for the reflected wavefields in the beam summation performed on the terrain surfaces for various source frequencies and locations and can be readily applied for outdoor sound propagation problems. However, it should also be noted that a smooth terrain surface is assumed in the derivation of the empirical formulation; therefore, it may fail when applied for receivers around the building corners. Moreover, it is noticed that the inclusion of the empirical formulation in the GBT calculations does not affect the CPU time. For the lower frequency (Case 1 and Case 3), the CPU time of the reference and the GBT solver are comparable. However, for the higher frequency (Case 2), a 17-fold reduction in computation time is achieved with the GBT tool with respect to the reference solver.

IMPACT OF 3D MEAN FLOW ON THE ACOUSTIC PROPAGATION

The present GBT model is validated against the reference solution for the three-building urban setting with and without the mean flow. The acoustic wavefields predicted with the GBT and the reference for Case 4 and Case 5 are studied. The real values of the pressure field computed with the two approaches are compared at the vertical receiver plane and displayed in Fig. 6.8. In both Cases, the GBT is able to capture the general trend of the reference result except inside the narrow canyon B, where the GBT predicts a smaller pressure amplitude than the reference solution. Nevertheless, a strong pressure oscillation is visible in the reference result due to the diffraction and multiple reflections. A remarkable improvement in the GBT prediction is observed when comparing the line plots in Case 4 and Case 5. In the presence of mean flow, the direct and reflected waves can have different ray paths than those in a quiescent medium. The phase increments along each path can change considerably, resulting in less apparent diffraction patterns and oscillations in the pressure amplitude. Furthermore, compared to Case 4, acoustic pressure amplitude in Case 5 drops in canyon A and rises in canyon B, highlighting the significant impact of different flow regimes inside urban canyons on acoustic propagation.

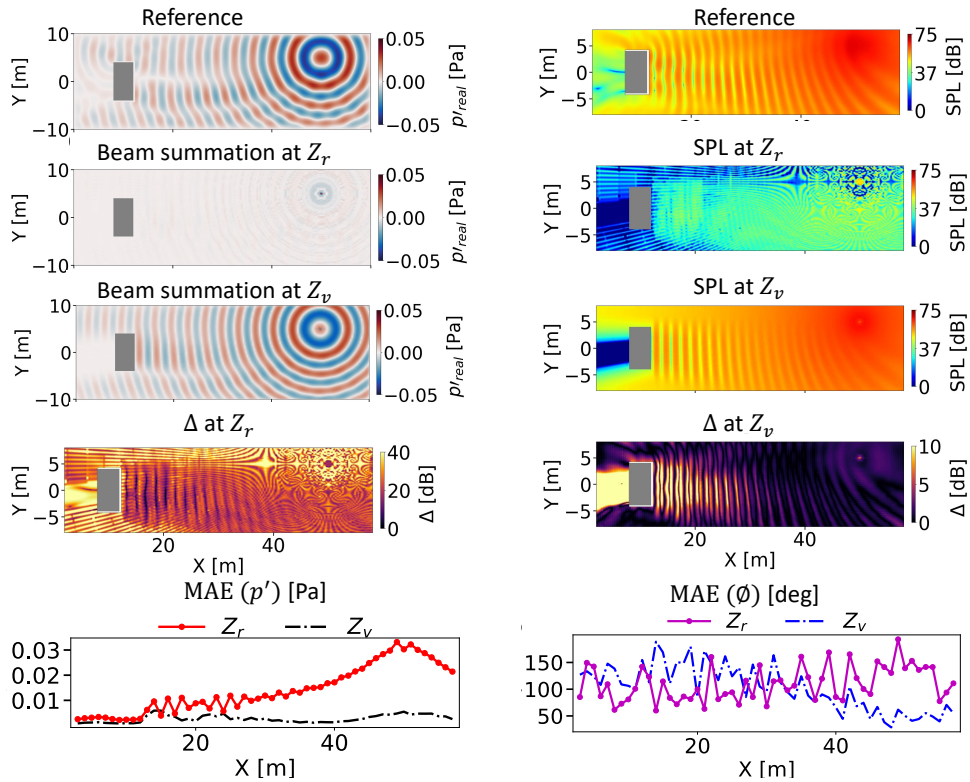


Figure 6.5: Comparison of the GBT with and without the semi-empirical formulation and the reference predictions on the terrain surface for Case 1: $f = 100$ Hz, source location = $(12.5, 1.25, 1.25)L_B$. The reference results are placed on the first row. The GBT results without the empirical formulation are presented in the second row and with the empirical formulation in the third row. AE in SPL without the empirical formulation is overlaid in the fourth row left and with the empirical formulation on the right. The MAE in pressure magnitude and phase are presented in the last row. This layout of results is maintained in the next two figures.

Fig. 6.9 compares the predicted wavefields on the horizontal receiver plane. In the presence of the mean flow, the GBT approach can capture the general trend of the interference pattern of the reference solution. However, the GBT predictions decay considerably at receivers located farther away from the source in the upstream direction and rise noticeably in the downstream direction. The line plot in Case 5 further highlights the impact of the mean flow on the diffraction pattern, particularly in terms of the phase of the complex pressure, as an excellent agreement is obtained.

6.4. CONCLUDING REMARKS

A new noise propagation approach is proposed to simulate airborne noise propagation in a non-turbulent urban environment with 3D varying terrain topology and weather conditions. The present GBT approach corrects the inconsistency between the RPT and the GBT equations presented in Gabillet *et al.* [6] and establishes a complete framework

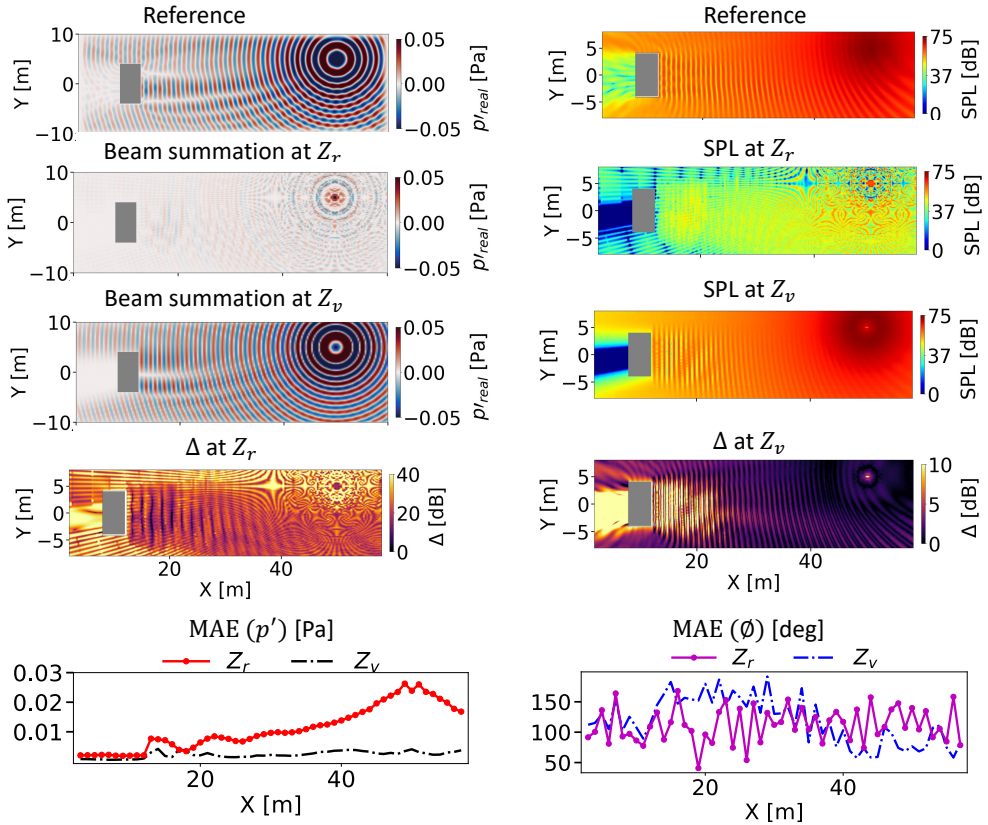


Figure 6.6: Comparison of the GBT with and without the semi-empirical formulation and the reference predictions on the terrain surface for Case 2: $f = 200$ Hz, source location = $(12.5, 1.25, 1.25)L_B$.

for the GBT in an inhomogeneous moving atmosphere that accounts for the refraction due to vertical and horizontal variation in wind velocity and air temperature. A semi-empirical formulation is derived to reduce the truncation error in the beam summation and account for the reflected wavefields on the terrain surfaces. When the beam summation is performed without the empirical formulation, the maximum error is more than 40 dB due to the truncation error. In contrast, the agreement is improved significantly with the semi-empirical formulation, and the maximum error drops below 8 dB in the illuminated zone. The reflected wavefields on the terrain surface is also captured with a slight difference in the interference that is attributed to a lack of diffraction in the GBT model. The phase of the complex pressure showed excellent agreement with the reference data in the presence of wind flow, revealing the significant effect of the wind on the diffraction pattern. For the lower frequency, i.e., $f = 100$ Hz, the CPU time of both approaches are comparable. However, for the higher frequency, i.e., $f = 200$ Hz, a 17-fold reduction in computation time is achieved with the GBT tool with respect to the FEM

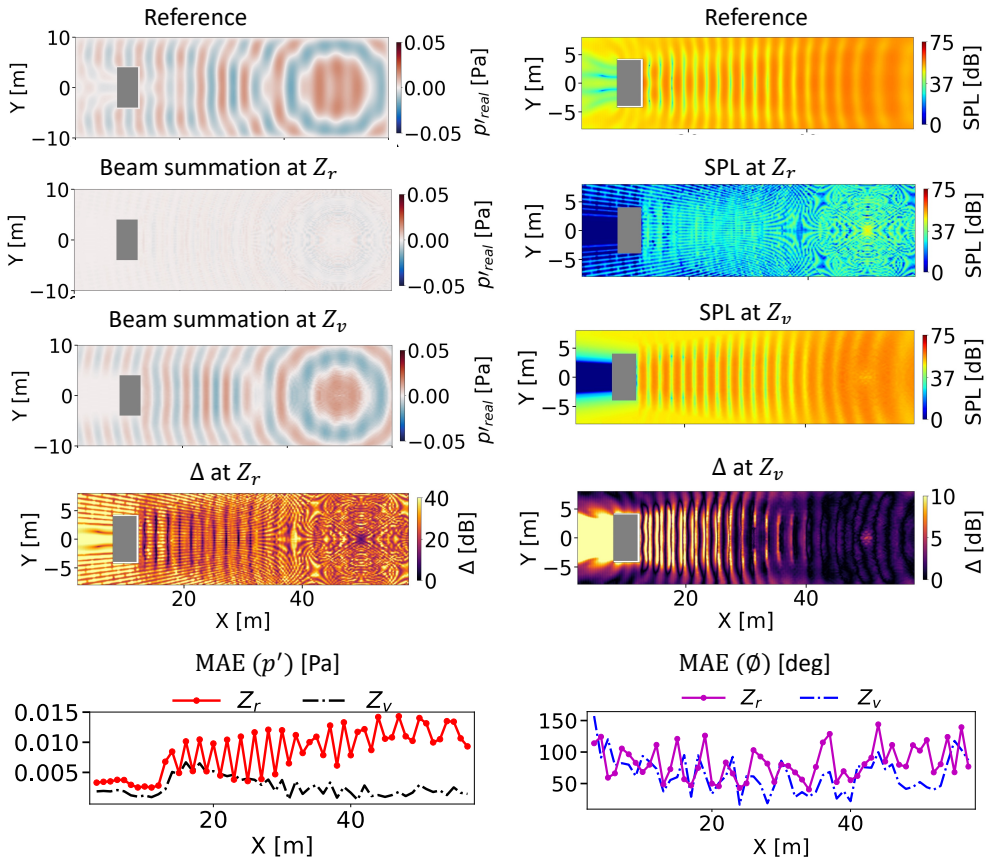


Figure 6.7: Comparison of the GBT with and without the semi-empirical formulation and the reference predictions on the terrain surface for Case 3: $f = 100$ Hz, source location = $(12.5, 0, 4.5)L_B$.

solver.

The results suggest that the 3D wind flow should be accounted for when simulating airborne noise propagation in an urban environment. In the presence of mean flow, the direct and reflected waves can have different ray paths than those in a quiescent atmosphere. The phase increments along each path can change considerably, resulting in less apparent diffraction patterns and oscillations in the pressure amplitude. Furthermore, flow regimes inside urban canyons significantly impact acoustic propagation.

The comparison with FEM provides a semi-quantitative validation, and any attempt to quantify the acoustic impact of various conditions is avoided. Because the GBT approach presents an approximate solution of the wave equation. Furthermore, its accuracy threshold depends on the application [16, 18, 19]. Furthermore, not even the FEM is an exact solution to the problems for two main reasons: First, it is a numerical solution affected by discretization error. Second, it is based on the solution of a second-

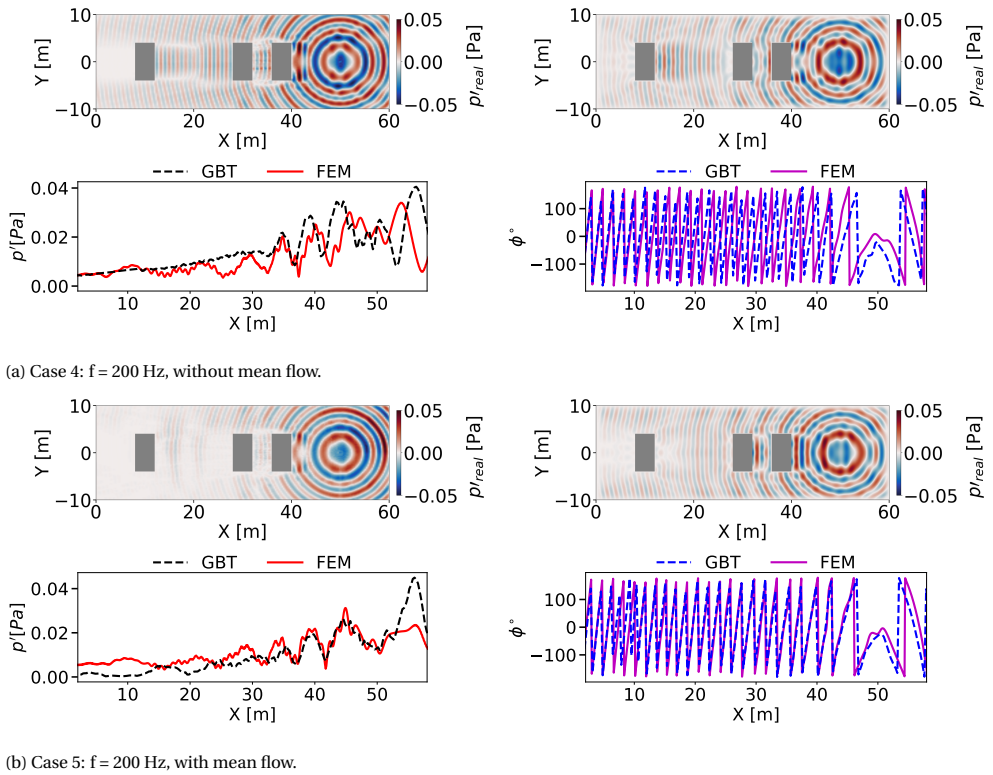


Figure 6.8: Comparison of the GBT and the reference solutions on the vertical receiver plane for Case 4 (a) and Case 5 (b). The first and third rows present the pressure field calculated with the GBT (left) and the reference (right) solvers. The second and fourth rows compare the pressure magnitude and the phase on a line $Z = 2.5L_B$ (10 m).

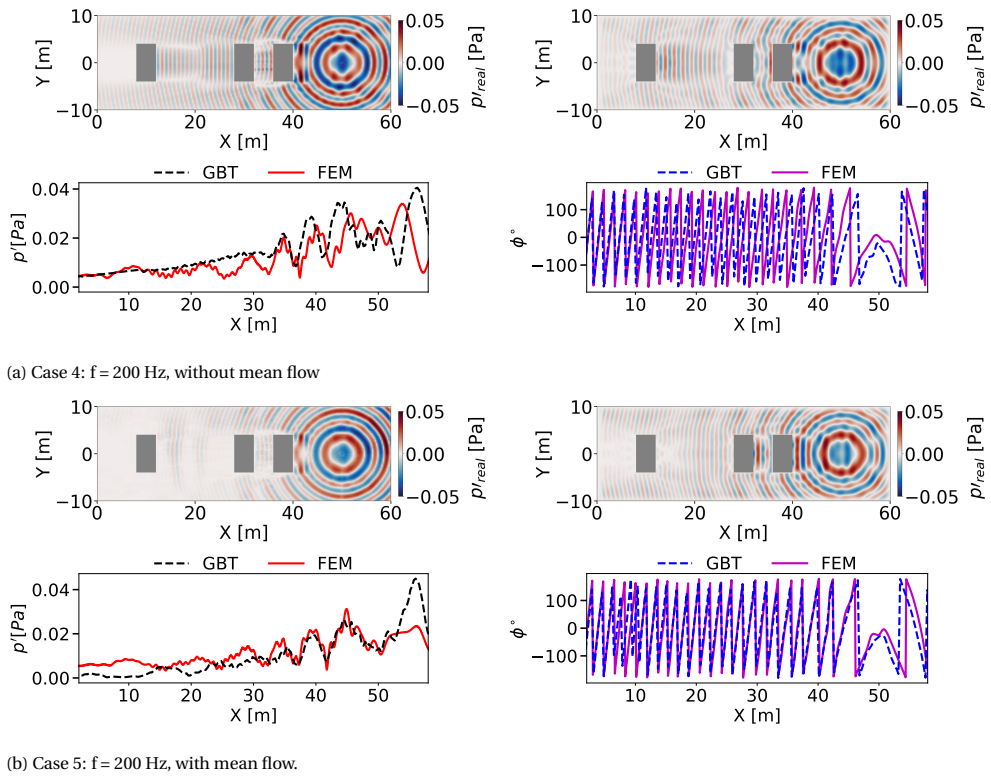


Figure 6.9: Comparison of the GBT and the reference solutions on the horizontal receiver plane for Case 4 (a) and Case 5 (b). The first and third rows present the pressure field calculated with the GBT (left) and the reference (right) solvers. The second and fourth rows compare the pressure magnitude and the phase on a line $Y = 1.75L_B$ (7 m).

order wave model for the acoustic velocity potential [11], which may not describe the correct acoustic propagation in a highly sheared mean flow that would require the solution of the linearized Euler equation. In addition, the GBT approach proposed in this study assumes an omnidirectional monopole source, which does not take into account the complex source directivity in the propagation medium required for accurate calculation of the aircraft's noise footprint. To address this limitation, the subsequent chapter introduces a straightforward numerical approach that incorporates source directivity.

REFERENCES

- [1] F. Yunus, D. Casalino, F. Avallone, and D. Ragni, *Efficient prediction of airborne noise propagation in a non-turbulent urban environment using Gaussian beam tracing method*, *J. Acoust. Soc. Am.* **153**, 2362 (2023).
- [2] F. Yunus, D. Casalino, F. Avallone, and D. Ragni, *Aircraft community noise prediction in 3d environment using Gaussian beam tracing*, in *28th AIAA/CEAS Aeroacoustics 2022 Conference* (2022) p. 3079.
- [3] F. Yunus, D. Casalino, F. Avallone, and D. Ragni, *Urban air mobility noise prediction in a 3d environment using Gaussian beam tracing*, in *DICUAM 2022 Conference* (2022).
- [4] V. E. Ostashev and D. K. Wilson, *Acoustics in moving inhomogeneous media*, 2nd ed. (CRC Press, 2015).
- [5] V. Červený and I. Pšenčík, *Gaussian beams in inhomogeneous anisotropic layered structures*, *Geophys. J. Int.* **180**, 798 (2010).
- [6] Y. Gabillet, H. Schroeder, G. A. Daigle, and A. L'Espérance, *Application of the Gaussian beam approach to sound propagation in the atmosphere: Theory and experiments*, *J. Acoust. Soc. Am.* **93**, 3105 (1993).
- [7] H. Bian, R. Fattah, S. Zhong, and X. Zhang, *An efficient rectilinear Gaussian beam tracing method for sound propagation modelling in a non-turbulent medium*, *J. Acoust. Soc. Am.* **148**, 4037 (2020).
- [8] H. Bian, R. Fattah, S. Zhong, and X. Zhang, *On the efficient modeling of generic source directivity in Gaussian beam tracing*, *J. Acoust. Soc. Am.* **149**, 2743 (2021).
- [9] F. Yunus, D. Casalino, F. Avallone, and D. Ragni, *Toward inclusion of atmospheric effects in the aircraft community noise predictions*, *J. Acoust. Soc. Am.* **150**, 759 (2021).
- [10] D. Casalino, M. Barbarino, M. Genito, and V. Ferrara, *Hybrid empirical/computational aeroacoustics methodology for rocket noise modeling*, *AIAA J.* **47**, 1445 (2009).
- [11] A. D. Pierce, *Wave equation for sound in fluids with unsteady inhomogeneous flow*, *J. Acoust. Soc. Am.* **87**, 2292 (1990).

- [12] V. E. Ostashev, D. K. Wilson, and M. B. Muhlestein, *Wave and extra-wide-angle parabolic equations for sound propagation in a moving atmosphere*, *J. Acoust. Soc. Am.* **147**, 3969 (2020).
- [13] D. Casalino, *Reprint of: Benchmarking of different wave models for sound propagation in non-uniform flows*, *Procedia IUTAM* **1**, 163 (2010).
- [14] D. Casalino, *Finite element solutions of a wave equation for sound propagation in sheared flows*, *AIAA J.* **50**, 37 (2012).
- [15] D. Casalino, S. Santini, M. Genito, and V. Ferrara, *Rocket noise sources localization through a tailored beam-forming technique*, *AIAA J.* **50**, 2146 (2012).
- [16] M. B. Porter, *Beam tracing for two-and three-dimensional problems in ocean acoustics*, *J. Acoust. Soc. Am.* **146**, 2016 (2019).
- [17] F. B. Jensen, W. A. Kuperman, M. B. Porter, H. Schmidt, and A. Tolstoy, *Computational ocean acoustics*, Vol. 794 (Springer, 2011).
- [18] V. Cervený, *Seismic ray theory* (Cambridge university press Cambridge, 2001).
- [19] W. B. Beydoun and A. Ben-Menahem, *Range of validity of seismic ray and beam methods in general inhomogeneous media-ii. a canonical problem*, *Geophysical Journal International* **82**, 235 (1985).

7

URBAN AIR MOBILITY NOISE IN A VERTIPORT ENVIRONMENT

*Great minds do not think alike.
They challenge each other to think again.*

Adam Grant

This Chapter presents a computationally efficient low-order approach for calculating the noise footprint of a propeller-driven aircraft in a generic 3D environment. The Gaussian beam tracer is extended to include complex source directivity with a novel approach without modifying the beam summation equation. Noise sources, predicted using the low-order noise source prediction toolchain, are stored on a sphere surrounding the aircraft and propagated through an urban environment. The noise footprints predicted for different terrain topologies, source directivities, and wind flow conditions are compared. It is shown that building blocks increase on-ground noise levels by 5 dB in the illuminated zone due to multiple reflections and create shadow zones behind the buildings. The change between source directivities corresponding to the first and second harmonics of the blade passing frequency results in a difference of up to 40 dB in the noise footprint. Wind flow contributes a significant variation in the acoustic footprint, intensifying the noise levels and changing the lobes of the footprint pattern, with the variation increasing with frequency. The present approach reduces the prediction error by 5 dB in the illuminated zones and 35 dB in the terrain shadow zones, compared to the straight-ray propagator.

Parts of this chapter have been published in Yunus et al. [1, 2]

7.1. OBJECTIVES

COMputationally efficient and reliable evaluation of UAM noise impact is crucial in developing vertiports that consider the acoustic impacts of design, operational, and environmental factors. This chapter presents a methodology that efficiently investigates the acoustic impacts of various parameters on the noise footprint of an eVTOL vehicle in a non-turbulent 3D environment.

The proposed approach combines the computationally efficient, low-order noise source prediction method [3, 4] with the GBT model presented in the previous chapter. In this work, the GBT model is extended to account for complex source directivity in the presence of atmospheric refraction due to variations in wind velocity distribution. This approach aims to predict the noise footprints of an eVTOL vehicle in a vertiport environment with two objectives: (i) to compare the performance of the current GBT propagation model with the traditional straight-ray-tracing (SRT) method in predicting noise footprints and (ii) to evaluate the impact of terrain topology, source directivity, and wind flow distribution on the acoustic signature of an eVTOL aircraft during hover operations in a vertiport. To simulate the vertiport environment, 3D wind profiles are directly imported from a high-fidelity CFD simulation. For this case study, it is assumed that the flow field does not affect the source noise sphere, and the distance between the eVTOL and surrounding buildings is larger than 40 times the rotor diameter.

The rest of this chapter is structured as follows: Section 7.2 gives an overview of the computational methodology, while Section 7.3 presents the verification results. In Section 7.4, the study results are discussed, including the improvements in the noise footprint predictions, the impact of various terrain topologies, source directivity, and wind flow profiles. Finally, concluding remarks are given in Section 7.5.

7.2. AN OVERVIEW OF THE COMPUTATIONAL APPROACH

This study predicts the source noise levels and noise footprint of an eVTOL in a vertiport environment using a hybrid approach that focuses on propeller-generated noise. Aerodynamic calculations are performed using the *OptydB*-BEMT tool [4] to determine the radial distribution of aerodynamic loads and integral boundary layer parameters. These outputs are then used as inputs for the tonal and broadband aeroacoustic prediction tool *OptydB*-PNOISE, which calculates noise signals on microphones distributed on a sphere surrounding the eVTOL vehicle. The resulting noise sphere and environmental profiles are analyzed, and a GBT-based propagation model [5] is used to compute the eVTOL noise footprint. This approach considers complex source directivity, 3D varying terrain geometry, and wind velocity profiles to provide an accurate evaluation of noise impact. The 3D temperature and wind velocity profiles are modeled as a combination of 2D slices (Fig. 7.1). Combining the low-order noise source prediction method with the GBT-based propagation model provides an efficient and effective evaluation of the noise footprint of eVTOL aircraft in a vertiport environment. The computational procedure can be divided into three steps, which are depicted in Fig. 7.1: noise sphere calculation, reading environmental profiles, and noise footprint calculation. While the second step has been described in the previous chapter, the first and third steps will be outlined in detail in the following section.

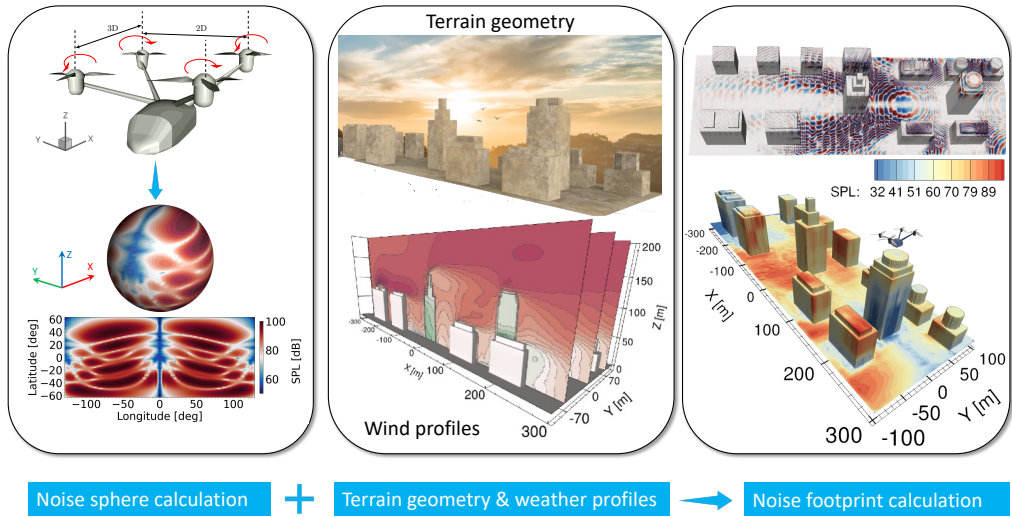


Figure 7.1: Schematic illustration of the computational procedure.

7.2.1. NOISE SPHERE CALCULATION

The noise sphere calculation is carried out by employing the *Opty∂B*-BEMT and *Opty∂B*-PNOISE tools. *Opty∂B*-BEMT adopts a conventional BEMT formulation with uniform inflow and Prandtl tip-loss correction for loads computation. The aerodynamic module implemented inside the tool is based on the coupled panel/boundary layer model by Drela & Giles [6]. More details of the formulation can be found in the work of Casalino et al. [4]. The *Opty∂B*-PNOISE tool is used to calculate the noise signals on microphones distributed on a sphere surrounding the eVTOL. The tonal noise contribution is computed using either the time-domain FW-H formulation based on the compact dipole/monopole formulation by Casalino et al. [7] or the frequency-domain formulation derived by Hanson [8–10]. The frequency-domain formulation provides similar accuracy as the time-domain formulation while reducing the computational cost significantly [3]. The broadband noise contribution is computed using Roger and Moreau's trailing edge noise model extended to a rotating blade and by using the Schinkler and Amiet wall pressure spectrum model [11].

7.2.2. GBT-BASED NOISE FOOTPRINT PREDICTION

The GBT solver UYGUR (acoustic ray and Gaussian beam tracer)[5] is developed based on the 3D ray path tracing (RPT) method [12], and the GBT method [13] that accounts for multiple reflections over irregular terrain topology and atmospheric refraction due to vertical and horizontal variations in air temperature and wind velocity gradients. After reading as input the noise sphere and the environmental profiles, the noise levels at a receiver point are calculated in the following three steps. In the first step, rays are traced from the aircraft center position toward the ground, and ray-path trajectories are

obtained by performing RPT. Next, the geometrical spreading and wavefront variation along each ray-path trajectory are determined by solving the dynamic ray tracing (DRT) equations [13]. The DRT equations allow for computing the travel time on the ray-path trajectories and their vicinity. The Gaussian beams are constructed along each ray-path trajectory based on the solution of RPT and DRT systems. Finally, the acoustic field at a receiver point is calculated by summing the contribution of each Gaussian beam passing nearby the receiver location.

The present work extends UYGUR to include complex source directivity in the acoustic footprint, which is achieved in the following three steps:

- The first step determines ray-sphere intersection points within the RPT procedure.
- Afterward, each Gaussian beam's initial phase and magnitude are updated with the ones stored on the ray-sphere intersection point and propagated towards the terrain with the DRT procedure.
- If no values are available at the intersection point, an interpolation based on the inverse-distance interpolation scheme is performed to determine the corresponding values using the data points available on the sphere.

Compared to earlier works [14–17], the present approach has two remarkable advantages:

- It does not require modifying the beam summation equation, which removes extra computational time.
- As both RPT and DRT equations explicitly incorporate the effect of medium velocity, the present GBT propagator can accurately propagate the noise signals even in the presence of strong refraction due to horizontal and vertical variations in wind velocity profiles. In this case, sound rays curve more with increasing propagation distances resulting in the shift of the ray-sphere intersection points, as illustrated in Fig. 7.2. For instance, the ray-sphere intersection points corresponding to direct and ground reflected rays passing nearby the receiver location are shifted from D and R to D' and R' , respectively, in the presence of wind.
- The present approach does not need to trace eigenrays connecting the source to the receivers by optimizing the shooting angles as presented in [14]. Instead, on-ground noise levels are calculated by weighted summation of contributions of each beam passing nearby the receiver location.

The shift in the ray-sphere intersection point will be evident on the noise footprint only if the source directivity pattern is well captured on the sphere with proper spatial resolution. In other words, the footprint accuracy highly depends on the spatial resolution of the noise sphere; a higher number of sampling points on the sphere usually gives much better accuracy but increases computational cost. This aspect will be investigated in the following section.

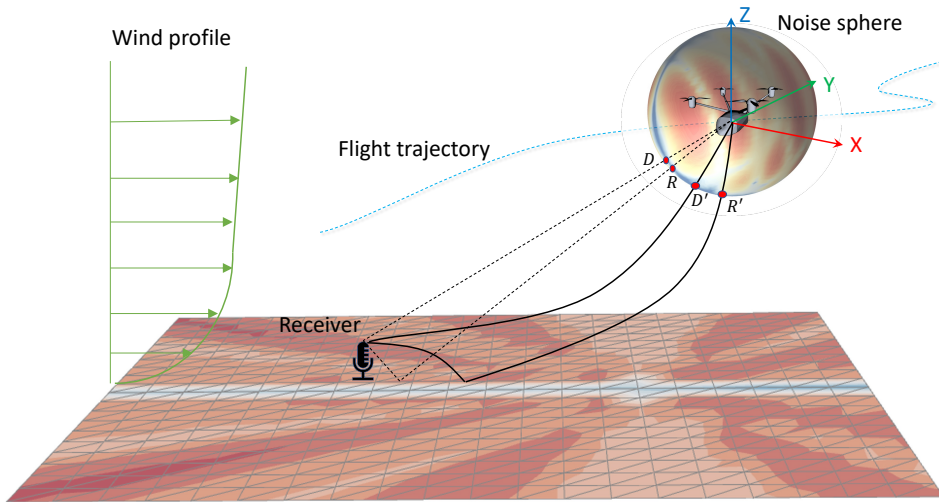


Figure 7.2: A sketch of the source noise sphere and sound rays passing nearby a ground receiver. Dashed lines represent sound rays in a quiescent, homogeneous atmosphere, while curved solid lines represent the sound rays in a windy atmosphere.

7.3. VALIDATION AND VERIFICATION

The low-order noise-sphere calculation toolchain composed of the *Opty∂B*-BEMT and *Opty∂B*-PNOISE tools was validated for a variety of propellers by comparing against experimental measurements [4] and high-fidelity simulations [3, 4]. In addition, the GBT model was also verified by comparing it against an exact solution that describes the propagation of sound from a monopole source in a homogeneous isotropic atmosphere over flat terrain [14] and finite element solutions of the convected wave equation in the presence of multiple building blocks and 3D wind flow profiles [5].

This section first evaluates the accuracy of the noise sphere for a range of spatial resolutions. Then, the reliability of the present GBT tool to include complex source directivity into the acoustic footprint is assessed by comparing the noise footprints over flat terrain calculated with the GBT tool against a reference solution. The *Opty∂B*-FOOTPRINT [3] tool, based on the SRT model, is used as a reference solver. *Opty∂B*-FOOTPRINT evaluates the noise levels at a receiver point by calculating the Euclidean distance between the source and the receiver and applying spherical spreading, atmospheric absorption according to SAE ARP866A, Doppler shift, and amplitude corrections related to the sphere radius and ground reflection. The SRT model allows only for a single reflection by mirroring the source with respect to the ground plane [3, 14, 18]. All tools run on an Intel(R) Xeon(R) Gold 6140 CPU @2.3 GHz processor with 36 cores.

7.3.1. THE SPATIAL RESOLUTION OF THE NOISE SPHERE

The same propeller but with five blades and the same validation case as described in [3] is considered. Two propellers instead of a single propeller are employed to highlight bet-

ter the interference pattern on the source sphere caused by the acoustic interaction. The two propellers were designed to be symmetrical with respect to the XZ-plane. To minimize the impact of aerodynamic interaction on the acoustics, the tip-to-tip distance between them was set to $2D$ [19, 20], where D is the diameter of the propellers ($D = 2.5$ m). The configuration of the twin propellers is illustrated in Figure 7.3a. Both propellers rotate at 1900 RPM at an altitude of 2000 m and each generates 1500 N thrust. The phase angle between the propellers is 0° . The advance ratio is $J = 0.84$. The blade passing frequency (BPF) is 158.33 Hz. The radius of the noise sphere is set to $R_h = 10D$. The atmosphere is homogeneous and quiescent and has a constant temperature of 22°C . As illustrated in Fig. 7.3b, a straight-level flight trajectory is considered that spans from a starting point S ($-5, 0, 2$) km to a terminal point T ($5, 0, 2$) km and has a length of 10 km. The flight trajectory is oriented along the X-axis of the ground reference system. The flight direction points to the positive X-axis. Two on-ground microphones are considered to investigate the noise signature. The first microphone (Mic 1) is located at the center of the ground plane ($0, 0, 3$) m and the second microphone (Mic 2) is located at ($0, -2500, 3$) m as shown in Fig. 7.3b.

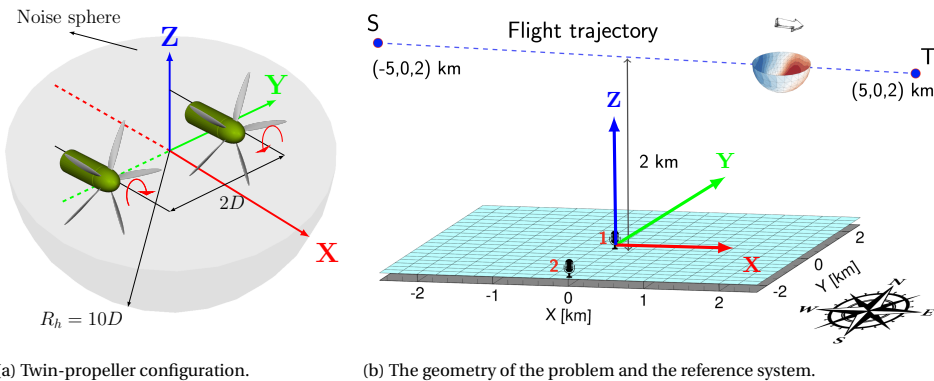


Figure 7.3: A sketch of the twin-propeller configuration, the noise sphere and the reference system (a). The geometry of the problem (b), adapted from [3].

The spatial resolution of a sphere can be represented by the number of vertices on its surface. This can be determined by the number of points along the sphere's radius. Given μ points along the sphere's radius, the number of vertices on the sphere can be calculated as $(\mu + 1)^2$. This simple relationship allows for a precise representation of the sphere's surface and the grid representation of its geometry. Six noise spheres corresponding to $\mu = [8, 18, 22, 32, 47, 60]$ are considered, where $\mu = 8$ represents the coarsest sphere and $\mu = 60$ indicates the finest one. The noise spheres for each value of μ are calculated using the *Opty∂B*-BEMT and *Opty∂B*-PNOISE tools, and three of the noise spheres are displayed in Fig. 7.4. Due to the lower resolution of the noise sphere for $\mu = 8$, the interference dips and peaks are not well captured. However, a significant improvement is observed in the noise sphere for $\mu = 32$ as the separation between interference dips and peaks becomes more evident. At the same time, the noise spheres for $\mu = 32$ and $\mu = 60$ appear almost identical.

On-ground noise signatures of the six noise spheres at Mic 1 and Mic 2 are calculated using the reference solver and displayed in Fig. 7.4d and 7.4e, respectively. At Mic 1, the difference between the noise signatures is not significant. The maximum difference between the noise signature for $\mu = 8$ and $\mu = 60$ is around 3 dB that appeared at flyover time $t = 7$ s. This slight difference is due to Mic 1 and the flight trajectory lying on the XZ plane. Hence, the ray-sphere intersection point on the noise sphere traverses within the same interference peak at the center of the bottom half of the noise sphere during the total flight time (see Fig. 7.4). At Mic 2, a significant change up to 8 dB is seen between the noise signature for $\mu = 8$ and $\mu = 60$. While the noise signatures for $\mu = 32$ and $\mu = 60$ remain nearly identical. This is attributed to the relative position of Mic 2 and the corresponding ray-sphere intersection point that crosses consecutive interference dips and peaks during the flyover time. To better highlight the accuracy of the noise sphere with respect to the different spatial resolutions, the mean absolute error (MAE) at Mic 1 and 2 are calculated for the five values of μ and plotted in Fig. 7.4f. Here, the noise signature calculated with the larger μ is used as a reference. The noise signature calculated with a smaller μ is compared against the one computed with a subsequent larger μ . It is seen that for both microphones, the maximum MAE occurs for $\mu = 8$. The MAE is nearly identical at both microphone locations for $\mu \geq 32$ and is below 0.35 dB. Moreover, a two-fold reduction in the computation time is achieved for $\mu = 32$ with respect to $\mu = 47$. In the following, the spatial resolution of the noise sphere is set to $\mu = 32$.

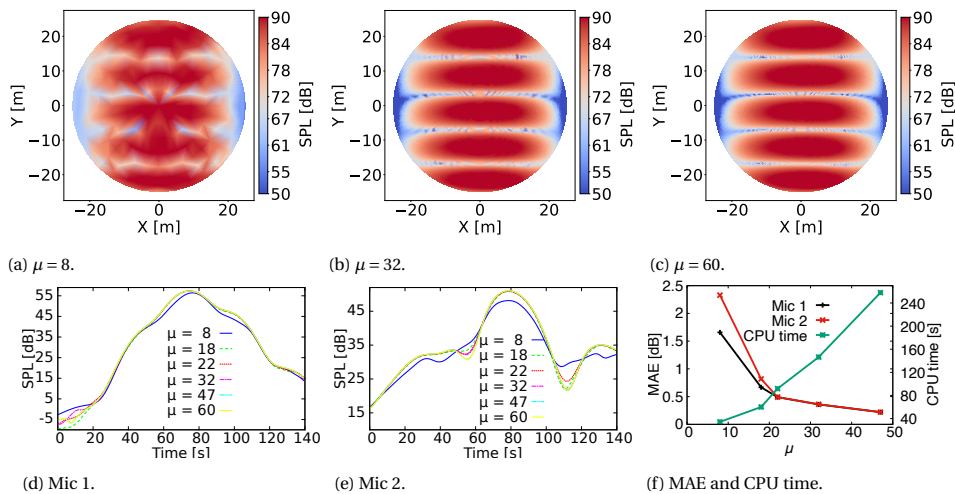


Figure 7.4: Bottom view of the noise spheres of the twin-propeller configuration corresponding to $\mu = 8$ (a), $\mu = 32$ (b), and $\mu = 60$ (c). Noise signature at Mic 1(d) and Mic 2(e) and the MAE at Mic 1 and Mic 2 and CPU time as a function of μ (f).

7.3.2. INCLUSION OF COMPLEX SOURCE DIRECTIVITY INTO THE ACOUSTIC FOOTPRINT

The same validation case and the noise sphere calculated for $\mu = 32$ (see Fig. 7.4b), as outlined in the previous section, are considered. The source is stationary and lo-

cated at (0,0,2000) m and the receivers are distributed over a 5 km square area at ground level. The noise footprints calculated with the GBT tool and the reference solver over the square area and on a line along the X-axis at $Y = -2.4$ km are compared and displayed in Fig. 7.5. In both results, the interference patterns on the source sphere are well captured on the noise footprints. A favorable agreement is observed between the two results that verifies the reliability of the present GBT-based propagation model for including complex source directivity into the acoustic footprint.

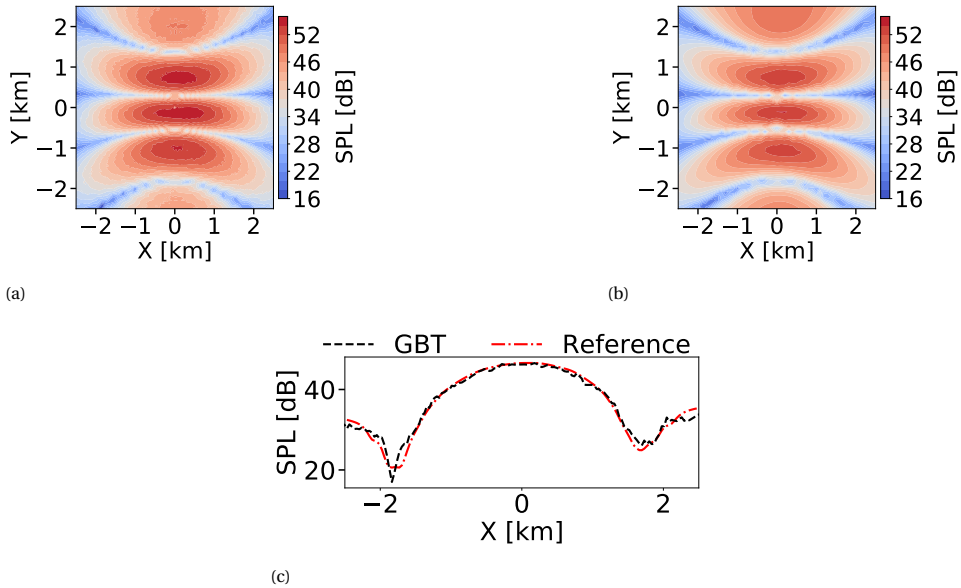


Figure 7.5: Noise footprint computed with the GBT solver (a) and the reference (b) and comparison between them at a line along the X-axis at $Y = -2.4$ km (c).

7.4. CASE STUDY

7.4.1. CASE SETUP

A quadrotor-like eVTOL vehicle is considered. The vehicle's gross weight is assumed to be 629 kg, which can carry a max of two people. The eVTOL is powered by four rotors, as shown in Fig. 7.6a. The vehicle body is designed by the author based on the single-passenger quadrotor concept proposed by NASA [21], and delivered as part of a high-fidelity CFD simulation workflow for UAM noise research purposes [22]. For this case study, the vehicle body is for illustrative purposes only and is not used for the noise sphere calculation. Each rotor has three blades, and the blade has the same radial distribution of twist angle and chord length as the one described in [4]. The rotor diameter D is 1.8 m. In the local reference system of the vehicle, the relative distance between the two rotors along the Y-axis is set to $2D$ to avoid aerodynamic interference. At the same time, the distance between the rotors along the X-axis is set to $3D$. The rear rotors are elevated by $0.8D$ with respect to the front rotors to decrease the aerodynamic interaction

between front, and rear rotors [23]. It is assumed that all four rotors rotate at the same rotational speed. Moreover, the total required thrust is distributed evenly at all rotors. Each rotor generates 1/4 of the target thrust, i.e., 1540 N, which is achieved by trimming the rotor blade pitch angle for a given rotor speed of 3000 RPM. In this study, the source sphere radius has been chosen to be equal to $13D$. This radius has been selected such that it satisfies the acoustic far-field condition, ensuring independence between source directivity and environmental effects. For this specific vehicle geometry, the distribution of rotors and eVTOL fuselage are designed in a way that does not significantly affect acoustics, as shown in [23]. As the rotors are the primary noise source, noise scattered by the airframes is not considered in the present study. It's important to note that such effects could still be included in the GBT solver if needed. The noise spheres, corresponding to the first and second harmonics of the blade passing frequency (BPF) of 150 Hz, are computed using the *OptydB*-BEMT and *OptydB*-PNOISE tools. The acoustic pressure fluctuations at each microphone on the noise sphere are obtained by uncorrelated summation of the contribution of each rotor. The resulting acoustic spheres are plotted using the equidistant cylindrical projection [24] and displayed in Fig. 7.6b and Fig. 7.6c, respectively.

The geometry of the vertiport and surrounding environment is modeled based on the recently released report by the Federal Aviation Administration (FAA) that provides guidance for vertiport design [25]. The report recommended the touchdown and lift-off area (TLOF) and final approach and takeoff area (FATO) to be elevated at least 0.8 m above the surrounding surface. The size of the TLOF, FATO, and safety area are characterized by square areas as illustrated in Fig. 7.7a, which are measured based on an aircraft's controlling dimension (CD). The CD indicates the longest distance between the two farthest opposite points on the aircraft, e.g., rotor tip to rotor tip, measured on a level horizontal plane that includes all adjustable components extended to their maximum outboard deflection [25]. The width of TLOF is advised to be at least 1CD and the width of FATO to be 2CD, while the width of the safety area is recommended to be 3CD.

Based on the geometry of the eVTOL, whose CD equals $6D$, the safety area of the vertiport considered in this study is set to 3CD. Two different vertiport configurations are considered. The first one is an elevated vertiport installed on the rooftop of a high-rise building, and the building height is 12CD. This vertiport environment represents a typical city center connected with many transportation hubs. The eVTOL vehicle is hovering at an altitude of 19CD over the vertiport, as shown in Fig. 7.7b. As the present GBT propagator does not account for diffracted wavefields behind the building blocks, the characteristic length of the smallest building is set to be 1.75 times larger than the wavelength of the fundamental frequency (first BPF) to minimize the diffraction effects. The second one is a ground-based vertiport installed on flat terrain, which shares the same ground area, and dimensions as the first vertiport environment, except for the vertiport location.

Two different atmospheric conditions are considered: a windy atmosphere and a quiescent atmosphere with a constant temperature of 22 C°. The mean flow in the metropolitan area is resolved using the high-fidelity CFD solver SIMULIA PowerFLOW® for an initial wind velocity of 5 m/s along the positive X-axis direction. Snapshots of the mean flow on the XY-plane at $Z = 55$ m and on the XZ-plane at $Y = 0$ m are displayed in

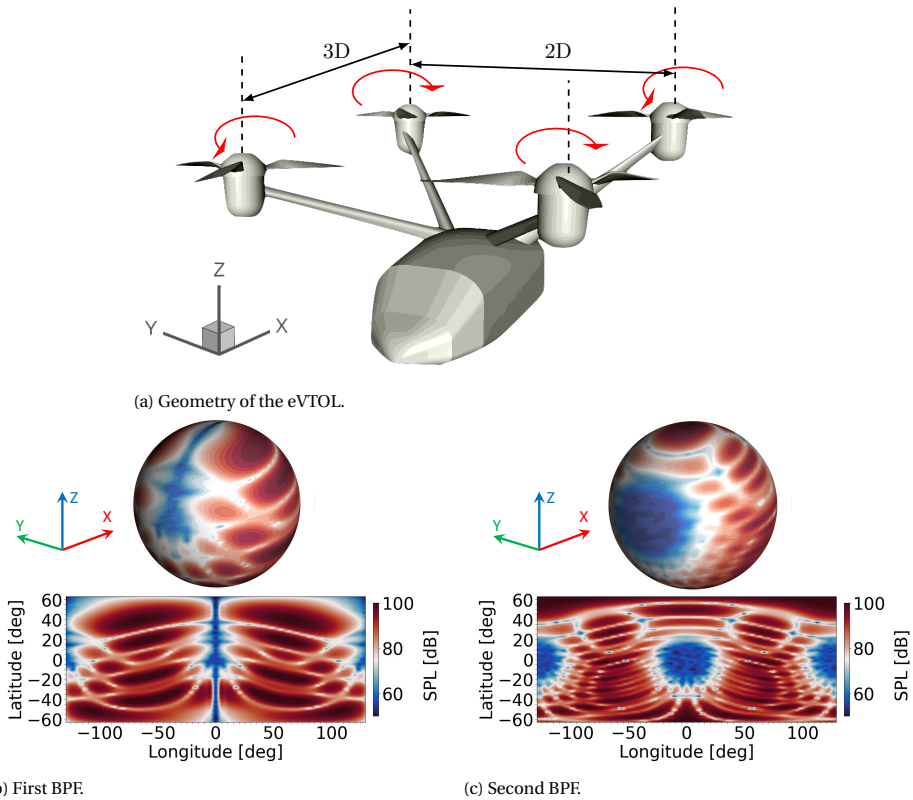


Figure 7.6: The geometry of the eVTOL vehicle's four propellers, and the reference system (a). SPL computed over the noise sphere for the first BPF (150 Hz) (b) and the second BPF (300 Hz) (c).

Fig. 7.7c and Fig. 7.7(d), respectively. They show how the building geometries affect the wind field.

Altogether, 6 cases are considered to investigate differences in the footprint predictions with the GBT and SRT models, acoustic effects of varying terrain geometry, complex source directivity, and wind flow. The test matrix for this analysis is listed in Table 7.1. To further highlight the difference between cases, noise levels at four particular regions, i.e., A, B, C, D, as indicated in Fig. 7.7b, are considered.

The following sections analyze the improvements in footprint prediction using the current approach. The study then investigates the impact of varying terrain geometry on noise footprint distribution, followed by an examination of the effects of changes in source directivity on acoustic footprint. Lastly, the study examines how changes in wind flow affect the distribution of noise footprint.

7.4.2. RESULTS

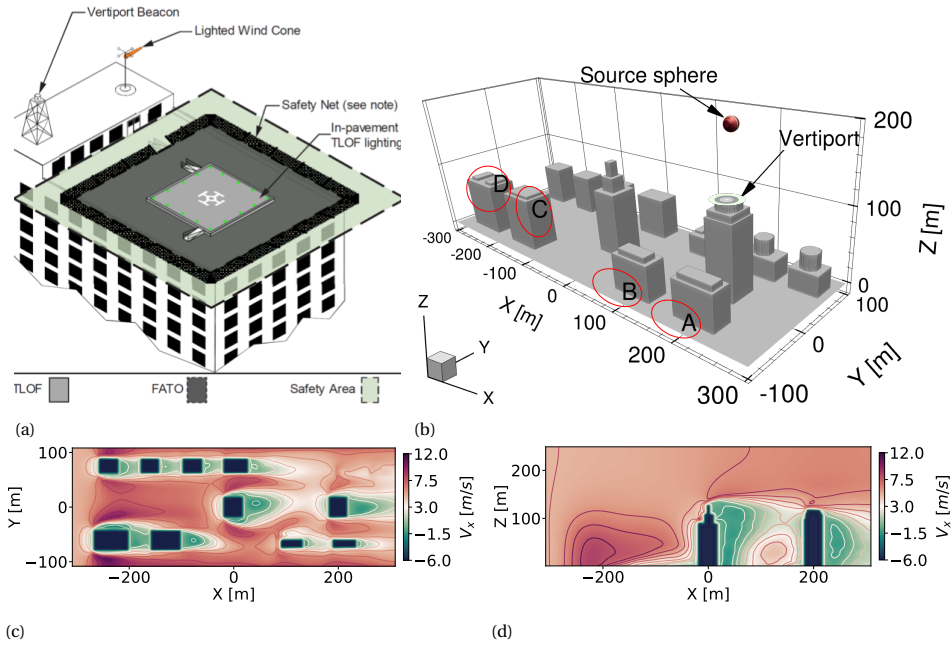


Figure 7.7: An example of an elevated vertiport configuration [25] (a). An illustration of the urban environment includes an elevated vertiport (b). Snapshots of wind field on the XY-plane at $Z = 55$ m (c) and on the XZ-plane at $Y = 0$ m (d). The wind direction points to the positive X-axis.

Table 7.1: Test matrix for the case study.

Case #	Solution method	f [Hz]	atmosphere	terrain
1	GBT	1 th BPF	quiescent	non-flat
2	SRT	1 th BPF	quiescent	non-flat
3	GBT	1 th BPF	quiescent	flat
4	GBT	1 th BPF	windy	non-flat
5	GBT	2 nd BPF	quiescent	non-flat
6	GBT	2 nd BPF	windy	non-flat

IMPROVEMENTS IN THE FOOTPRINT PREDICTION

The improvement in the footprint predictions is investigated by comparing the noise footprints calculated for Case 1 and Case 2. As shown in Fig. 7.8, in Case 2, the noise levels in the illuminated zones are predicted to be slightly lower than in Case 1, and the difference between the two cases varies in a range of 0-5 dB. This is attributed to the limitation of the SRT to include multiple reflections. The SRT model allows only for a single reflection, whereas the GBT can account for multiple reflections. A significant improvement noticed in the GBT solutions is the detection of irregular terrain surfaces and the proper prediction of terrain shadow zones. As seen, the SRT failed to predict the terrain shadow zones where the difference between the two solutions exceeds 35 dB. This is one of the main limitations of the SRT, which does not account for reflecting rays bouncing from the surfaces of obstacles. Additionally, it has been noted that the SRT model is significantly faster, with a computation time that is 15 times faster than the GBT approach.

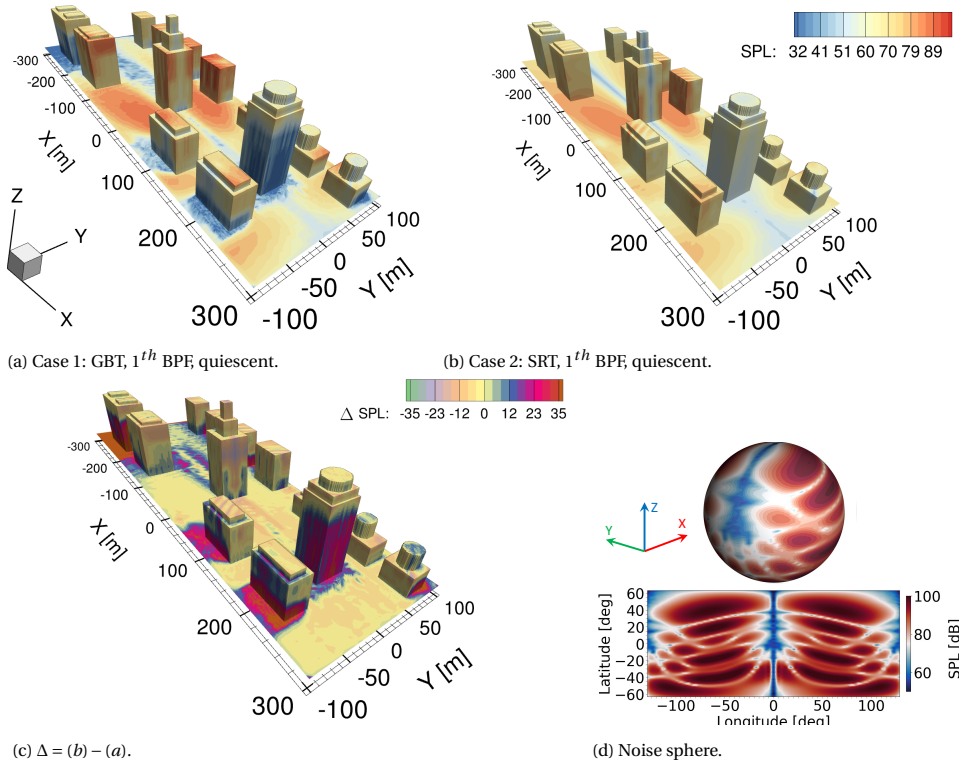


Figure 7.8: Noise footprint of the eVTOL calculated with the GBT method (a) and the SRT method (b) and the field difference between them (c) for the 1th BPF.

THE IMPACT OF VARYING TERRAIN GEOMETRY ON THE NOISE FOOTPRINT DISTRIBUTION

The impact of varying terrain topology on the noise footprint is analyzed by comparing the results from Case 1 and Case 3. As shown in Figure 7.9, the presence of building

blocks leads to the creation of shadow zones due to the shielding of noise. Additionally, the building blocks result in multiple reflections that enhance noise levels in illuminated zones. In the illuminated zones of the urban area, the difference between the noise footprints varies between 0 dB and 5 dB due to the contribution of multiple reflecting rays. The maximum difference between the noise footprints is mainly distributed on the terrain shadow zones, where the difference is more than 20 dB. The current GBT method lacks consideration for the insonification of the shadow zone, caused by both edge diffraction and scattering due to atmospheric turbulence. In practical terms, if the insonification of terrain shadow zones were taken into account, the discrepancy would likely be smaller than 20 dB. It is worth mentioning that an increase of 19% in computation time is observed for Case 1 due to the tracing of multiple reflected rays between the building blocks.

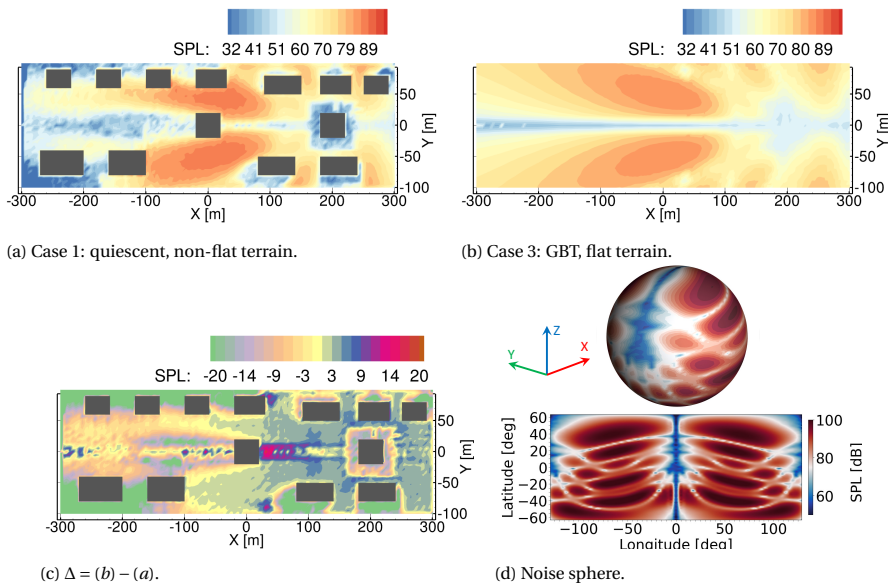


Figure 7.9: Noise footprint of the eVTOL in the urban area (a) and in flat terrain (b), the field difference between them (c) and the corresponding noise sphere (d) for 1st BPF.

THE IMPACT OF CHANGES IN SOURCE DIRECTIVITY ON THE NOISE FOOTPRINT DISTRIBUTION

The acoustic impact of varying source directivity on the noise footprint is examined by comparing the noise footprint calculated for Case 1 and Case 5. As shown in Fig. 7.10, the noise footprint on the illuminated zone shows a totally different pattern, and the varying source directivity contributes to a mismatch of up to 40 dB. Notably, the noise levels on the vertiport are increased up to 30 dB in Case 5 with respect to Case 1. Furthermore, in Case 5, the noise levels in the terrain shadow zones, particularly at regions A and B, are further decreased due to higher source frequency. This is expected physically and agrees with the results presented by several authors [26, 27]; they reported that the diffraction

shielding by the urban geometry is higher for the higher frequencies. Although the GBT method presented in this work does not account for the diffracted wavefield behind a building, the limiting ray, separating the illuminate and shadow zones, contributes to the shadow zone due to a finite beamwidth. This contribution is usually more substantial for lower frequencies than the higher ones as the beamwidth L is inversely proportional to the source frequency $L \propto \omega^{-1/2}$ [28]. As a consequence, a difference of up to 10 dB is seen in the terrain shadow regions A and B. Furthermore, it has been noted that the computational time remains constant for both cases as the same spatial resolution is used for both noise spheres.

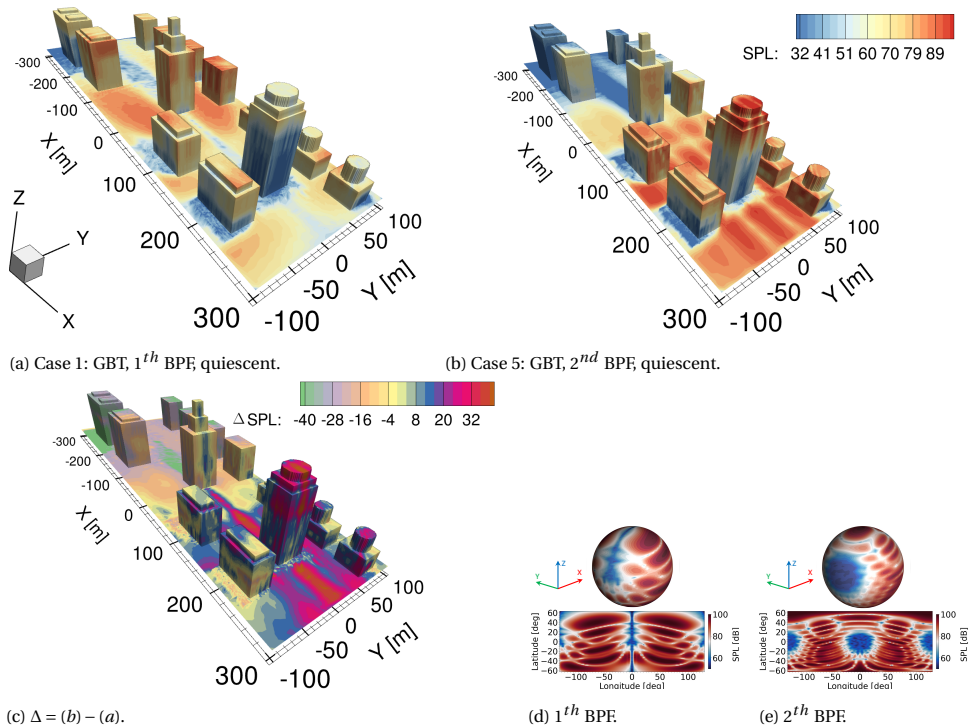


Figure 7.10: Noise footprint of the eVTOL in the first BPF (a) and in the second BPF (b) and the field difference between them (c). The noise spheres for the first BPF (d) and the second BPF (e).

THE IMPACT OF VARIATIONS IN WIND FLOW ON THE NOISE FOOTPRINT DISTRIBUTION

The effects of varying wind conditions are evaluated for the first and second BPFs. For the first BPF, the noise footprints calculated for Case 1 and Case 4 are compared. As seen in Fig. 7.11, compared to Case 1, the on-ground noise levels in Case 4 increased considerably in the region enclosed by $x = [-100, 300]$ m and $y = [-100, -25]$ m, particularly behind the building at the center of the domain and region A and B. As outlined in the previous sections, those regions are seen as terrain shadow zones, and due to the presence of the wind flow, sound rays are refracted into those regions, eventually raising

the noise levels. As highlighted in [14], the weather significantly impacts the predicted noise footprint at longer distances due to the refractive shadow zone that occurs when the source-receiver distance is a few times larger than the source height, and the local sound speed decreases towards the receiver. This is also observed in Fig. 7.11b, where the noise levels drop significantly at the rooftop of the farthest buildings, particularly at region D. As shown in Fig. 7.11c, the presence of the wind can contribute up to 23 dB difference in the predicted noise footprint, changing the lobes of the footprint pattern and intensifying the noise levels.

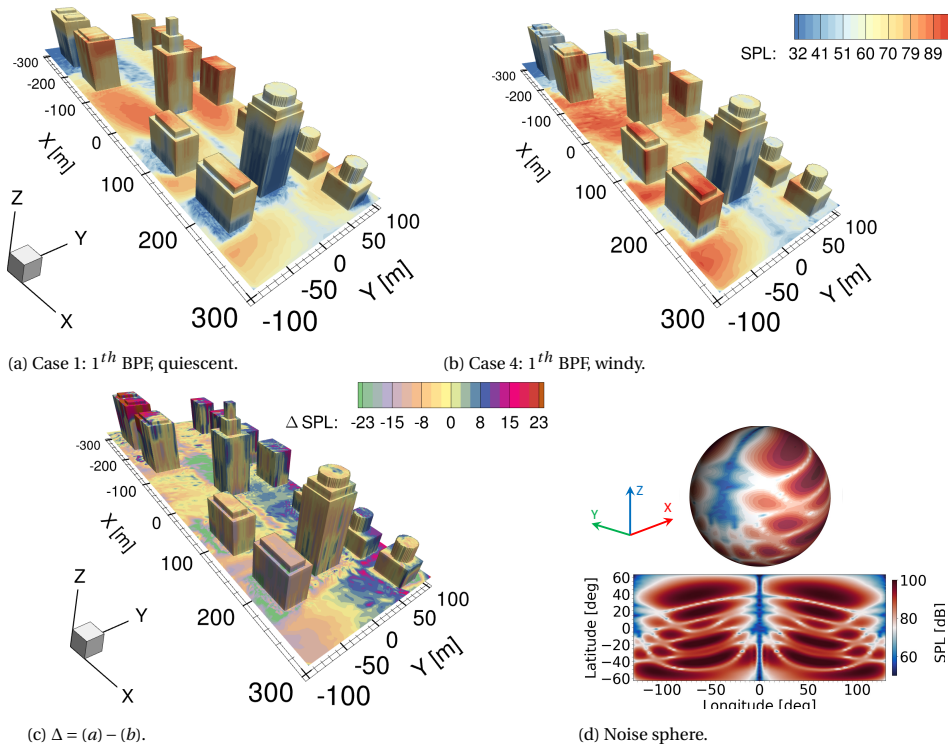


Figure 7.11: Noise footprint of the eVTOL in a quiescent atmosphere (a) and in a moving inhomogeneous atmosphere (b), the field difference between them (c) and the corresponding noise sphere (d) for 1th BPF.

For the second BPF, the acoustic footprint calculated for Case 5 and Case 6 are compared. The wind effect becomes even more substantial than the one at the first BPF, as seen in Fig. 7.12. This is attributed to an increase in the source frequency. As outlined in the previous section, high-frequency noise is shielded by the urban topology, while lower-frequency noise diffracts into the building shadow region. In the presence of the wind field, the shielding is reduced due to atmospheric refraction, which mainly influences the higher frequencies [26]. Moreover, in the presence of the wind flow, the sound rays connecting the source to the receiver become more curved, particularly for distant receivers. Thus, the ray-sphere intersection points shift. Consequently, the noise signals propagated from the noise sphere toward distant receivers change accordingly. This can

be seen from the sudden change of the noise levels predicted on the illuminated surface of the building in region C.

Significant differences in the predicted noise footprints can be expected when including wind flow, especially in terrain shadow regions (regions A and B) and refractive shadow regions (regions C and D). These regions are areas where the presence of obstacles and changes in air temperature and wind velocity can cause sound waves to bend and refract, leading to complex noise propagation patterns. By considering wind flow in the simulations, the GBT solver can better capture these effects and provide more accurate noise predictions. The present results are in close agreement with the findings of a previous work [26], which showed that the wind effect might reach over 30 dB for a single 1/3 octave band and ranges from 15 to 23 dB(A) for road traffic noise propagating across multiple urban canyons. Nevertheless, in a more realistic scenario considering the effects of diffraction and atmospheric turbulence, the difference would be smaller than 23 dB. Moreover, it is observed that the computation time increases by twofold when wind flow is considered. This is attributed to the additional computation required for interpolating weather data at each step of the ray propagation.

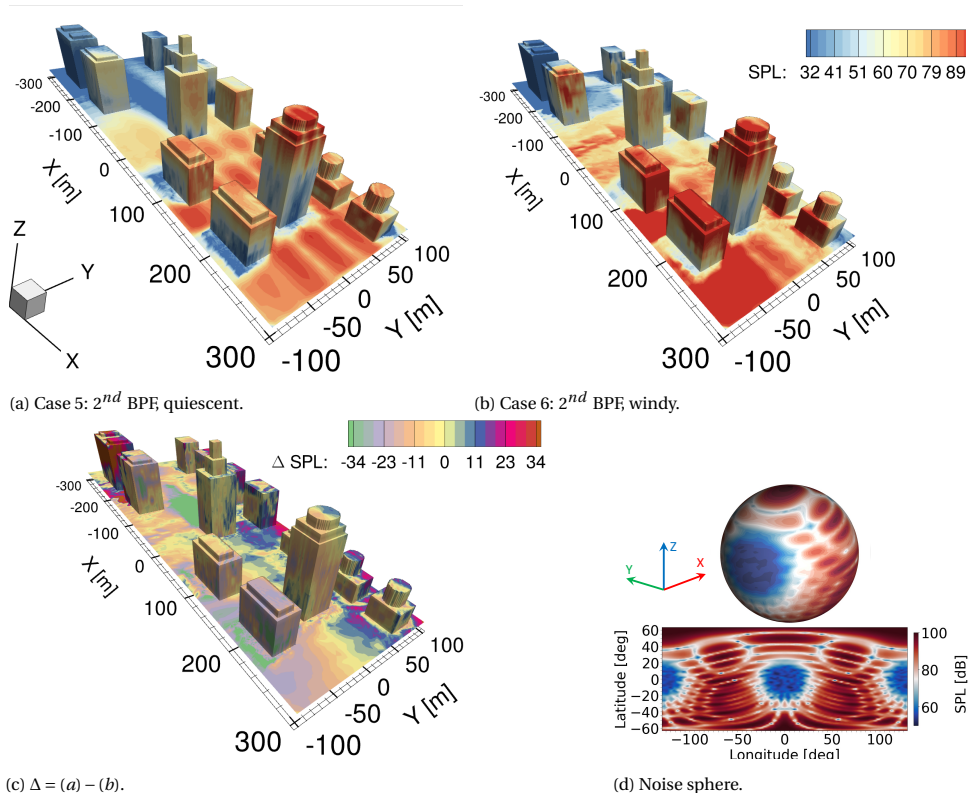


Figure 7.12: Noise footprint of the eVTOL in a quiescent atmosphere (a) and in a moving inhomogeneous atmosphere (b), the field difference between them (c) and the corresponding noise sphere (d) for 2nd BPE.

7.5. CONCLUDING REMARKS

A new computational framework that couples computationally efficient methods, which were initially validated against high-fidelity simulation results, is presented to predict the noise footprint of an eVTOL vehicle hovering in a vertiport environment. The SRT model is replaced with the more advanced propagation model, based on the GBT method, that accounts for sound wave refraction, and multiple reflections due to 3D variations in the weather conditions and terrain topology. The GBT model is further extended to include complex source directivity with a novel numerical approach without modifying the beam summation equation and without tracing eigenrays. The reliability of the outline approach to include the complex source directivity is verified. The computational framework is then applied to investigate the acoustic effects of 3D wind flow distribution and terrain topology on the noise footprint of an eVTOL aircraft hovering in a vertiport environment. For the case under investigation, it is found that the building blocks increase on-ground noise levels by 5 dB in the illuminated zone due to multiple reflections and shield the incoming sound field by creating shadow zones behind the building. The effectiveness of noise shielding increases with increasing frequency in a quiescent atmosphere. The variation in the source directivity results in a difference of up to 40 dB in the noise footprint. The presence of the wind flow can contribute a significant variation in the acoustic footprint by changing the lobes of the footprint pattern and intensifying the noise levels; the variation increases with increasing frequency. The presented approach shows differences up to 35 dB in the terrain shadow zones and 5 dB in the illuminated zones with respect to the SRT-based noise footprint prediction approach. It is noticed that the computation time increases as the complexity of the propagation environment increases.

The results suggest that in the presence of irregular terrain surfaces, methods like GBT must be employed to account for multiple reflections over terrain surfaces and terrain shadow zones. Due to the low-operational altitude, the high-frequency noise from the UAM vehicles may not be masked by the background noise [29, 30], cannot be properly shielded by the building blocks due to wind flow effects, and could impact the community. Thus, high-frequency noise should be among the main targets to mitigate UAM noise in a vertiport environment.

The findings of this study offer new insights into the potential of the GBT propagation model for predicting eVTOL noise footprints and examining the effect of environmental factors on the acoustic signature of eVTOL aircraft. However, it is important to acknowledge the limitations of this study. In the case study, it was assumed that the flow field does not impact the source noise sphere. However, this is not always the case in real-world scenarios, particularly when operating near tall buildings. Variations in wind conditions can have a significant impact on both the performance of the eVTOL and its acoustic emissions [22]. As a result, the noise signals sampled on the noise sphere could be strongly influenced by the flow field, potentially altering the source directivity and strength of the noise signals. To address this issue, wave-based solvers using BEM [31, 32] or FEM [7] discretization should be utilized. Moreover, the GBT method presented in this study does not consider the insonification of shadow zones. Nonetheless, it is essential to incorporate the insonification of shadow zones when investigating noise propagation within urban canyons.

The present chapter provides valuable information on the acoustic impacts of varying source directivity, vertiport geometry, and wind flow conditions on the noise footprint of an eVTOL vehicle hovering in a short-range propagation environment. However, it is important to note that atmospheric and ground conditions could have a more pronounced impact on long-range propagation if terrain and atmospheric conditions vary on the propagation range. The following chapter will explore the impact of range-dependent terrain and weather profiles on long-range propagation.

REFERENCES

- [1] F. Yunus, D. Casalino, F. Avallone, and D. Ragni, *Efficient prediction of urban air mobility noise in a vertiport environment*, [Aerospace Science and Technology](#) **139**, 108410 (2023).
- [2] F. Yunus, D. Casalino, F. Avallone, and D. Ragni, *Urban air mobility noise prediction in a 3d environment using Gaussian beam tracing*, in *DICUAM 2022 Conference* (2022).
- [3] F. Yunus, E. Grande, D. Casalino, F. Avallone, and D. Ragni, *Efficient low-fidelity aeroacoustic permanence calculation of propellers*, [Aerospace Science and Technology](#) **123**, 107438 (2022).
- [4] D. Casalino, E. Grande, G. Romani, D. Ragni, and F. Avallone, *Definition of a benchmark for low reynolds number propeller aeroacoustics*, [Aerospace Science and Technology](#) **113**, 106707 (2021).
- [5] F. Yunus, D. Casalino, F. Avallone, and D. Ragni, *Efficient prediction of airborne noise propagation in a non-turbulent urban environment using Gaussian beam tracing method*, [J. Acoust. Soc. Am.](#) **153**, 2362 (2023).
- [6] M. Drela and M. GILES, *Viscous-inviscid analysis of transonic and low reynolds number airfoils*, [Aiaa Journal - AIAA J](#) **25**, 1347 (1987).
- [7] D. Casalino, M. Barbarino, and A. Visingardi, *Simulation of helicopter community noise in complex urban geometry*, [AIAA journal](#) **49**, 1614 (2011).
- [8] D. B. Hanson, *Helicoidal surface theory for harmonic noise of propellers in the far field*, [AIAA Journal](#) **18**, 1213 (1980).
- [9] D. B. Hanson and D. J. Parzych, *Theory for noise of propellers in angular inflow with parametric studies and experimental verification*, Tech. Rep. (1993).
- [10] D. Hanson, *Sound from a propeller at angle of attack: a new theoretical viewpoint*, *Proceedings of the Royal Society of London. Series A: Mathematical and Physical Sciences* **449**, 315 (1995).
- [11] R. Schlinker and R. Amiet, *Helicopter rotor trailing edge noise*, in *7th Aeroacoustics Conference* (1981) p. 2001.

- [12] V. E. Ostashev and D. K. Wilson, *Acoustics in moving inhomogeneous media*, 2nd ed. (CRC Press, 2015).
- [13] V. Červený and I. Pšenčík, *Gaussian beams in inhomogeneous anisotropic layered structures*, *Geophys. J. Int.* **180**, 798 (2010).
- [14] F. Yunus, D. Casalino, F. Avallone, and D. Ragni, *Toward inclusion of atmospheric effects in the aircraft community noise predictions*, *J. Acoust. Soc. Am.* **150**, 759 (2021).
- [15] H. Bian, R. Fattah, S. Zhong, and X. Zhang, *An efficient rectilinear Gaussian beam tracing method for sound propagation modelling in a non-turbulent medium*, *J. Acoust. Soc. Am.* **148**, 4037 (2020).
- [16] H. Bian, R. Fattah, S. Zhong, and X. Zhang, *On the efficient modeling of generic source directivity in Gaussian beam tracing*, *J. Acoust. Soc. Am.* **149**, 2743 (2021).
- [17] H. Bian, Q. Tan, S. Zhong, and X. Zhang, *Efficient computation of broadband noise propagation using Gaussian beam tracing method*, *J. Acoust. Soc. Am.* **151**, 3387 (2022).
- [18] D. Casalino, W. C. van der Velden, and G. Romani, *Community noise of urban air transportation vehicles*, in *AIAA Scitech 2019 Forum* (2019) p. 1834.
- [19] T. Zhou and R. Fattah, *Tonal noise acoustic interaction characteristics of multi-rotor vehicles*, in *23rd AIAA/CEAS Aeroacoustics Conference* (2017) p. 4054.
- [20] R. de Vries, N. van Arnhem, T. Sinnige, R. Vos, and L. L. Veldhuis, *Aerodynamic interaction between propellers of a distributed-propulsion system in forward flight*, *Aerospace Science and Technology* **118**, 107009 (2021).
- [21] W. Johnson, C. Silva, and E. Solis, *Concept vehicles for VTOL air taxi operations*, in *AHS Specialists' Conference on Aeromechanics Design for Transformative Vertical Flight*, ARC-E-DAA-TN50731 (2018).
- [22] R. Atasi, I. Paden, F. Yunus, I. Gonzalez-Martino, D. Casalino, and C. Garcia-Sanchez, *Numerical aerodynamics and aeroacoustics predictions of a drone under real urban environments*, in *Quiet Drones Symposium 2022* (2022).
- [23] Z. Jia and S. Lee, *Acoustic analysis of a quadrotor eVTOL design via high-fidelity simulations*, in *25th AIAA/CEAS Aeroacoustics Conference* (2019) p. 2631.
- [24] J. P. Snyder, *Map projections—A working manual*, Vol. 1395 (US Government Printing Office, 1987).
- [25] *Federal Aviation Administration (FAA). Memorandum subject to Engineering Brief No. 105, vertiport design*, https://www.faa.gov/airports/engineering/engineering_briefs/drafts/media/eb-105-vertiport-design-industry-draft.pdf, accessed: 2022-10-17.

- [26] M. Hornikx, M. Dohmen, K. Conen, T. van Hooff, and B. Blocken, *The wind effect on sound propagation over urban areas: Predictions for generic urban sections*, *Build Environ.* **144**, 519 (2018).
- [27] M. Hornikx and J. Forssén, *Noise abatement schemes for shielded canyons*, *Appl. Acoust.* **70**, 267 (2009).
- [28] Y. Gabillet, H. Schroeder, G. A. Daigle, and A. L'Espérance, *Application of the Gaussian beam approach to sound propagation in the atmosphere: Theory and experiments*, *J. Acoust. Soc. Am.* **93**, 3105 (1993).
- [29] Z. H. Jia and S. Lee, *Computational study on noise of urban air mobility quadrotor aircraft*, *J. Am. Helicopter Soc.* **67**, 1 (2022).
- [30] S. Lee *et al.*, *Prediction of urban air mobility multirotor VTOL broadband noise using ucd-quietfly*, *J. Am. Helicopter Soc.* **66**, 1 (2021).
- [31] M. Barbarino, F. Petrosino, and A. Visingardi, *A high-fidelity aeroacoustic simulation of a VTOL aircraft in an urban air mobility scenario*, *Aerosp. Sci. Technol.* **125**, 107104 (2022).
- [32] M. Barbarino and D. Bianco, *A BEM-FMM approach applied to the combined connected helmholtz integral formulation for the solution of aeroacoustic problems*, *Comput. Methods Appl. Mech. Eng.* **342**, 585 (2018).

8

AIRCRAFT-COMMUNITY-NOISE PREDICTION IN OUTDOOR ENVIRONMENTS

The greatest obstacle to discovery is not ignorance; it is the illusion of knowledge.

Daniel J. Boorstin

This chapter investigates the impact of range-dependent terrain and weather conditions on long-range acoustic propagation using a case study of a Dassault Systemes helicopter. The noise sources are obtained using Ffwocs Williams and Hawking's acoustic analogy, and the propagation of noise signals is modeled using the Gaussian beam tracing approach. The Gaussian beam tracing solver has been extended to efficiently calculate broadband noise propagation. Terrain geometry is obtained from a GIS database, and 3D wind flow distribution is simulated using CFD. Acoustic footprints are compared for different source noise spheres and wind flow conditions. It is shown that variations in source directivity can cause differences up to 15 dB in a quiescent atmosphere, while in the presence of mean flow, the terrain shadow zone is further enlarged by the refractive shadow zone, leading to a significant difference in the acoustic footprint of up to 35 dB. This study highlights the importance of incorporating range-dependent terrain and weather profiles in assessing aircraft-community-noise impact and represents a significant achievement in accounting for realistic atmospheric and terrain effects in aircraft-community-noise prediction using scale-resolved flow simulations.

Parts of this chapter have been published in Yunus et al. [1].

8.1. OBJECTIVES

OUTDOOR sound propagation problems often treat the atmosphere as a horizontally stratified medium and assume flat ground. However, in reality, the terrain and weather profiles change over the propagation range, significantly affecting noise propagation over long distances. Although range-dependent weather profiles and ground effects are crucial factors that should be considered in community noise predictions, especially for long-range sound propagation, the literature has paid relatively little attention to them.

In addition, accurately evaluating aircraft-community-noise (ACN) over large areas requires high-resolution source directivity accounting for the contributions of various noise sources and the acoustic interaction between propulsors and airframes. The low-fidelity noise source prediction approach, presented in the previous chapter, is insufficient in this case, and high-fidelity noise spheres obtained through scale-resolved flow simulations are necessary. Realistic terrain and flow data are also required to improve the prediction accuracy. Additionally, broadband noise is a commonly encountered issue in outdoor sound propagation scenarios, such as transportation noise [2] and drone noise [3]. Therefore, it is crucial to efficiently compute the amount of broadband noise present in outdoor sound calculations.

This chapter examines the impact of range-dependent terrain and weather conditions on long-range acoustic propagation using a new computational framework that consists of the high-fidelity noise source prediction approach outlined in Chapter 2 and the Gaussian beam tracing (GBT) propagation model outlined in the previous chapters. In this work, the GBT approach is further extended to include broadband noise contributions in a very time efficient approach, thanks to the GBT algorithm, in which the time-consuming ray tracing part is decoupled from the wavefield calculation. In addition, terrain geometry is extracted from a geographical information system (GIS) database for a given longitudinal and latitude coordinates on Earth, and the 3D wind flow distribution is obtained using high-fidelity CFD simulation.

The organization of this chapter is as follows. An overview of the computational approach is provided in Section 8.2. Validation results are presented in Section 8.3. The noise footprint simulation application of a helicopter flying over a mountain is presented in Section 8.4. The concluding remarks of this work is given in Section 8.5.

8.2. AN OVERVIEW OF THE COMPUTATIONAL APPROACH

A hybrid approach is used to predict the noise sources and noise footprint of a helicopter hovering in a mountainous environment. The computational approach comprises three steps, as illustrated in Figure 8.1. The first step involves calculating the noise sphere by utilizing the 3DS aeroacoustic workflow [4]. This workflow requires the user to provide one blade in the form of standard triangle language (STL) file, a hub STL file, and an airframe STL file. The workflow enables user-friendly access to a multi-fidelity approach in the 3DS model-based system engineering framework for multicopter flight mechanics and acoustic emission assessment. To set up the simulation, the user specifies ambient and flight conditions, rotor settings (center, axis, RPM), and, if necessary, a reference thrust value for an automatic collective/cyclic pitch trim of the rotor. The 3DS workflow

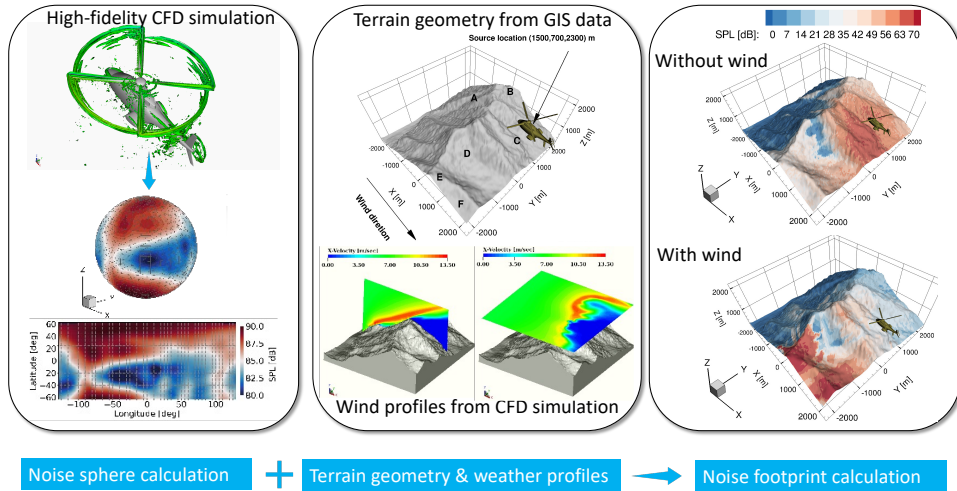


Figure 8.1: An illustration of the computational procedure.

creates a simulation setup from scratch, following established best practices in terms of mesh resolution and solution sampling properties. Casalino *et al.* [4] performed a grid convergence study using the 3DS aeroacoustic workflow. A range of grid resolutions that spans from coarse to fine was used, and the grid convergence was verified by monitoring the force and tonal noise with a medium resolution. In this work, the same medium resolution within the same workflow is employed to generate the high-fidelity simulation results instead of repeating the grid convergence study. For additional details about the workflow, please consult [4]. The second step is the preparation of the 3D terrain geometry and flow data. The terrain geometry is extracted by running a python script developed by 3DS Dassault systems that outputs the terrain geometry in STL file format for a given longitudinal and latitude coordinate of any location on Earth. At the same time, the wind flow is obtained by means of the high-fidelity CFD simulation. It is worth mentioning that, in this work, the first and second steps do not depend on each other; thus, they can be run simultaneously. In the last step, the noise signals are propagated from the source sphere toward receivers on the terrain surface using the GBT propagation model.

8.2.1. BROADBAND NOISE CALCULATION

Broadband noise propagation can be efficiently computed by discretizing the frequency range into N frequencies, denoted by $\omega = 2\pi f_i$ where $i = 1, 2, \dots, N$ (see Fig. 8.2). This approach was first introduced in the underwater acoustic solver Bellhop by Porter [5] and later adopted by Bian *et al.* [6] in their acoustic solver EnvARC. The goal of this section is to incorporate this approach into the GBT solver UYGUR.

The work by Bian *et al.* [6] has shown that the solutions of the DRT equations for an

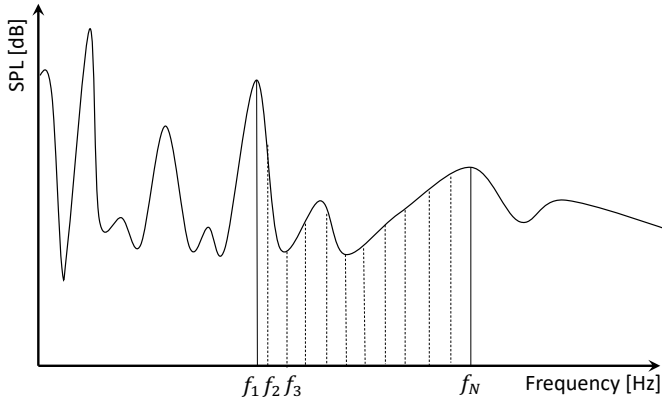


Figure 8.2: Discretized source spectrum illustrating N source frequencies within a target frequency range.

inhomogeneous quiescent medium, represented by \mathbf{P} , \mathbf{Q} and \mathbf{M} , are not influenced by ω under the geometrical acoustics assumptions. This also holds true for the solutions of the DRT equations for inhomogeneous moving media presented in Chapter 2. Therefore, the solution of Eq. 2.10 and \mathbf{M}^x in Eq. 2.19 are not affected by ω . This implies that the RPT equation Eq. 2.4 and DRT equation Eq. 2.10 need only be calculated once for all frequencies of interest. At each frequency ω_i , the source amplitude and phase, reflection coefficient \mathcal{R}^C in Eq. 2.18, and ω in Eq. 2.17 and Eq. 2.21 can be included in the wavefield calculation using the Gaussian beam summation Eq. 2.20. This approach results in a significant computational reduction in the wavefield calculation for broadband noise, as the repeated computation of propagation paths for each frequency component is not necessary for the broadband noise calculation. Furthermore, calculating frequency-dependent coefficients and summing Gaussian beams require minimal extra computational time, which makes it easier to efficiently compute the propagation of sound over a wide frequency range in vast and intricate environments.

This work assumes that source components at different frequencies are uncorrelated, so the OASPL is determined by conducting an incoherent summation of the acoustic energy from all source frequencies:

$$OASPL = 10 \log_{10} \left(\frac{1}{2N} \sum_{i=1}^{i=N} \frac{p^2(\omega_i)}{p_{ref}^2} \right) \quad (8.1)$$

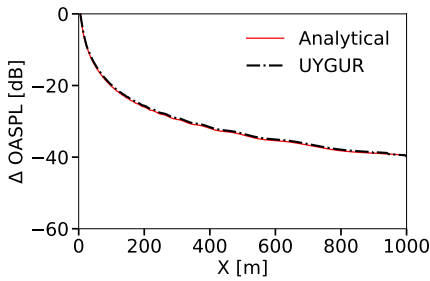
where $p_{ref} = 2 \times 10^{-5}$ Pa.

8.3. VALIDATION

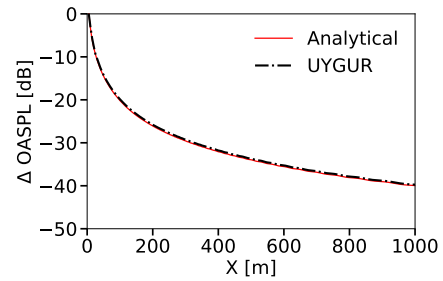
In this section, the computational efficiency and accuracy of UYGUR's broadband noise calculation are assessed by comparing its solutions against analytical solutions of the homogeneous wave equation. The analytical solutions are obtained by performing the incoherent summation of the results at each individual frequency using the analytical

Table 8.1: Test matrix for the case study.

Case #	Spectrum type	frequency range [Hz]	N_{freq}	μ_0	σ_0
1	flat	100-2000	200	-	-
2	flat	100-10000	1000	-	-
3	Gaussian	100-2000	100	1500	100
4	Gaussian	100-5000	500	2500	100
5	Gaussian	100-10000	1000	5000	100



(a)



(b)

Figure 8.3: Δ OASPL for Case 1 (a) and Case 2 (b).

formulation given in [7]. The source is located at (0, 0, 15) m above a rigid flat terrain and receivers distributed with 0.2 m spacing along the positive X-axis within a range of [0, 1000] m and at a height of 10 m. To evaluate computational efficiency and accuracy of UYGUR, five test cases with different source spectra, frequency ranges, and numbers are considered. The test matrix is listed in Table 8.1. For all cases, the discretized tonal components are uniformly spaced within the given frequency band, and the comparison with analytical solutions of Δ OASPL = OASPL - SPL₀ is conducted, where SPL₀ is the SPL at the observer with a range of 0 m. UYGUR runs on a single core of an Intel(R) Xeon(R) Gold 6140 CPU @2.3 GHz processor.

To investigate the impact of discretizing the frequency range into a predetermined number of frequencies (N_{freq}), the results for Case 1 and Case 2 with a flat source spectrum are compared in Fig. 8.3. For both cases an excellent agreement is obtained between UYGUR and analytical solutions. When comparing Case 1 and Case 2, it is seen that with more frequency components, changes become smaller in the OASPL.

Cases 3-5 analyze a sound source with a Gaussian spectrum, where the amplitude varies with frequency according to $A(f) = (1/\sigma_0\sqrt{2\pi}) \exp(-(f - \mu_0)^2/2\sigma_0)$. Case 3 uses a Gaussian spectrum with $\mu_0 = 1500$ Hz and $\sigma_0 = 100$ Hz, which is displayed in Fig. 8.4a. Cases 4-5 follow similar shapes but have different center frequencies and frequency ranges. The corresponding OASPL for Cases 3-5 is shown in Fig. 8.4b-8.4d, and for all Cases, excellent agreements are obtained between UYGUR and analytical solutions. Furthermore, compared to the previous two cases with a flat spectrum, an interference pat-

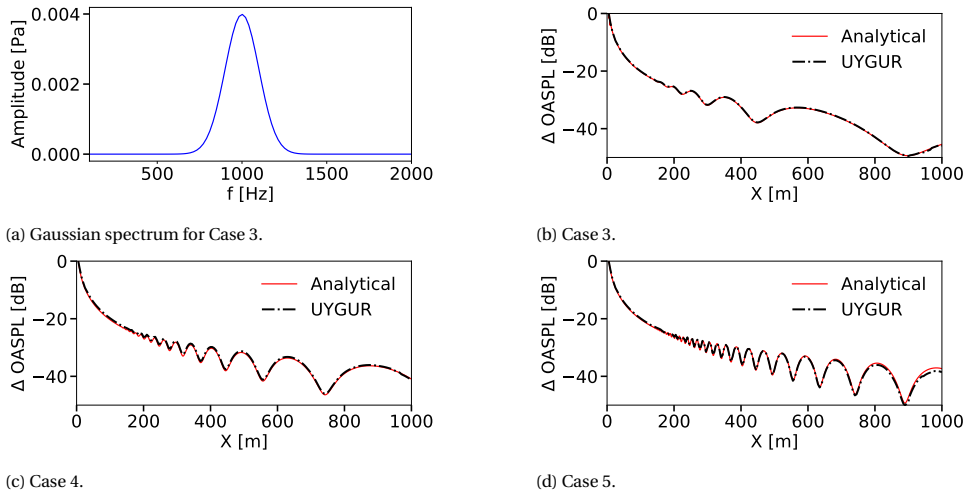


Figure 8.4: Gaussian spectrum profile for Case 3 (a). Δ OASPL for Case 3 (b), Case 4(c) and Case 5(d).

Table 8.2: The CPU time of broadband cases.

Case #	1	2	3	4	5
CPU Time [s]	1.37	5.13	1.54	3.59	6.31

tern is observed due to the Gaussian profile of the source spectrum. It is seen that the interference becomes stronger when the increasing frequency increases.

The computational efficiency of UYGUR for broadband noise calculation is highlighted in Table 8.2, which shows the CPU time for all cases. Notably, even with a significant increase in the number of frequencies (N_{freq}), the increase in CPU time is only moderate. For instance, a tenfold increase in N_{freq} results in only a fourfold increase in CPU time. This indicates that UYGUR is a highly efficient solver for broadband noise calculations, as it requires only a fraction of the CPU time compared to other methods.

8.4. CASE STUDY

The high-fidelity noise source approach and the GBT propagation model have been validated in previous works and beyond the scope of the present study. In this section, the proposed approach is applied to study the effects of range-dependent weather and terrain profiles on the long-range noise propagation of an helicopter hovering over a mountainous terrain.

8.4.1. NOISE SOURCE PREDICTION

The helicopter geometry considered in this study was designed by Dassault Systemes and delivered as part of the helicopter automatic simulation workflow of SIMULIA PowerFLOW®. The helicopter is driven by a main rotor and a tail rotor; the tail rotor is mounted on the starboard side, as shown in Fig. 8.5a. The geometrical specification of the vehicle and operational conditions for the case under consideration are listed in Table 8.3. The noise sphere is defined in the vehicle reference system (zero pitch, yaw, and roll), as shown in Fig. 8.5b. The noise sphere radius R_h is set to 6 times the length of the fuselage to ensure the flow pressure is fully recovered, and only the acoustic pressure exists on the surface of the sphere. 32 meridians and 32 parallels are used to discretize the sphere to capture the complex source directivity on the sphere. The source noise spheres are calculated by employing the high-fidelity noise source prediction approach outlined in Chapter 3.

Here, the source noise spheres corresponding to the fifth and tenth harmonics of the main rotor Blade Passing Frequency (BPF) 20 Hz are considered. The resulting acoustic spheres are plotted using the equidistant cylindrical projection [8] and displayed in Fig. 8.5c and Fig. 8.5d, respectively. The tail rotor's contribution to noise levels on the source sphere is clearly visible for the 5th BPF, while it is not apparent for the 10th BPF.

Table 8.3: Specifications and operational conditions of the case under investigation.

Main rotor blade tip Mach number (M)	0.51	-
Main rotor rotational speed	300	RPM
Tail rotor rotational speed	1500	RPM
Estimated gross weight	3567.0	kg
Fuselage length (L)	10.6	m
Main rotor diameter (D_m)	10.7	m
Tail rotor diameter (D_t)	2.12	m
Main rotor blade number (NB)	4	-
Tail rotor blade number (NB)	2	-
Main rotor hub-to-tip ratio	0.0561	-
Tail rotor hub-to-tip ratio	0.2682	-
Flight Altitude	2300	m

8.4.2. TERRAIN GEOMETRY AND WIND FLOW

The mountain geometry is obtained by running a python script developed in 3DS Dassault Systems that can extract the earth's elevation using the shuttle radar topography mission (SRTM) database for given coordinates. SRTM database provides detailed elevation information of the Earth's surface, which is a key component in many GIS applications. The Python script exports the terrain geometry in STL format, which UYGUR can directly read. Appendix C provides more details on the structure of the terrain input

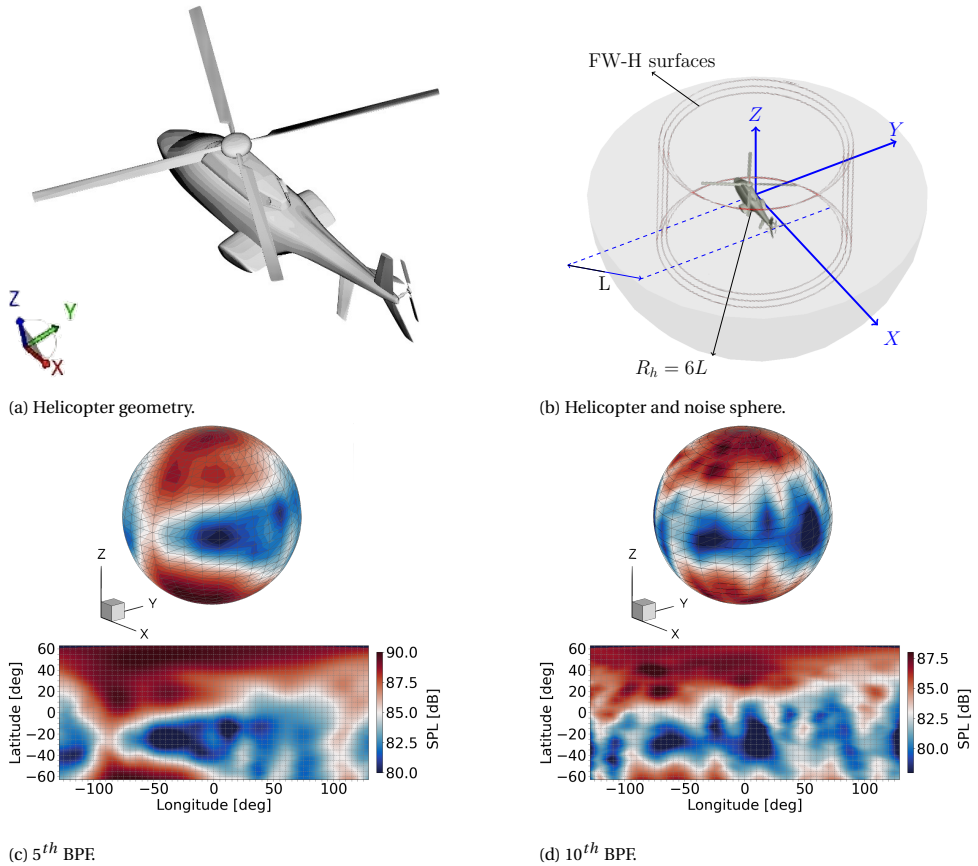


Figure 8.5: 3DS helicopter model for hover (a), including the measurable sampling surfaces for FW-H acoustic propagation and noise sphere (b). Source noise spheres calculated for the 5th BPF (c) and 10th BPF (d) of the main rotor.

file. The mountain geometry is exported in a square area of 2500 m by 2500 m and is shown in Fig. 8.6. The highest point of the mountain is 2153 m. Receivers are distributed on the mountain's surface with 30 m spacing in X and Y directions. To investigate the acoustic impact of variations in the source directivity, wind flow, and the mountain geometry, noise levels at six particular locations, as indicated in Fig. 8.6, are considered. The helicopter hovers at (1500, 700, 2300) m, where the impact of the mean flow on the noise signals sampled on the surface of the sphere is assumed to be negligible. The wind field in the computational domain is resolved using the high-fidelity CFD solver SIMULIA PowerFLOW® for an initial wind velocity of 6 m/s that points to the positive X-axis direction. Snapshots of the wind field on the XZ-plane at $Y = 700$ m and the XY-plane at $Z = 2300$ m are displayed in Fig. 8.6b and Fig. 8.6c, respectively, that show how the mountain geometry distort the wind field.

Three cases that feature the acoustic effects of varying source directivity and wind

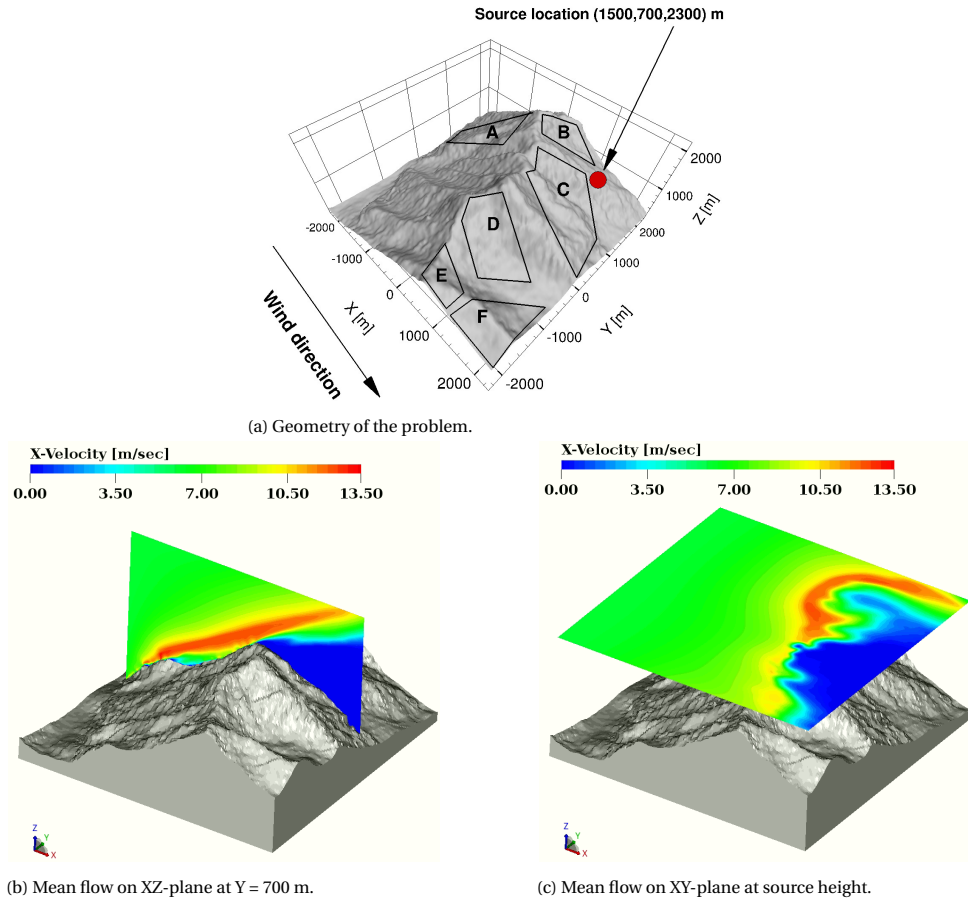


Figure 8.6: Geometry of the problem (a). Snapshots of the mean flow on XZ plane at Y = 700 m (b) and on XY-plane at the source height (c).

flow on the noise footprint are considered. All cases share the same total thrust of 35000 N. The test matrix for this analysis is listed in Table 8.4.

Table 8.4: Test matrix for the case study.

Case #	main rotor BPF [Hz]	atmosphere
1	100	quiescent
2	200	quiescent
3	100	windy

8.4.3. RESULTS

ACOUSTIC IMPACT OF VARYING SOURCE DIRECTIVITY ON THE LONG-RANGE PROPAGATION

The acoustic impact of varying source directivity on the long-range propagation is evaluated by comparing the noise footprints calculated for Case 1 and Case 2. As seen in Fig. 8.7a, in Case 1, the other side of the mountain is predicted as a terrain shadow except for region A. This is due to region A being relatively elevated with respect to its neighborhood; hence, it is still in the illuminated zone with respect to the source location. However, noise levels dropped considerably in region A in Case 2, as shown in Fig. 8.7b, even if it is in the illuminated zone. This is attributed to the variation in the source directivity; the lower noise levels on the sphere are projected into region A. The field difference between the two cases is calculated and displayed in Fig. 8.7c. As seen, the noise levels in region A reduced up to 15 dB when the BPF increased. Similar trends are observed for regions B and C. Furthermore, in Case 2, the terrain shadow zone predicted in region D appeared to be expended. In fact, the lower noise levels on the noise sphere are projected on region D; thus, the shadow zone seems to be expanded in region D. Moreover, the noise levels in region F, particularly in the area around the edge of the domain, dropped significantly, which is again attributed to the variation in the source directivity. The results suggest that receivers in the illuminated zone and around the terrain shadow zone can experience totally different noise levels when source directivity changes.

ACOUSTIC IMPACT OF THE WIND FLOW ON THE LONG-RANGE PROPAGATION

The acoustic impact of mean flow on the long-range propagation is studied with Case 2 and Case 3. The noise footprint for Case 3 is calculated and displayed together with the field difference in Fig. 8.8. As seen in Case 3, noise levels in regions A, B, and C are decreased considerably due to the upward refraction, which forms the refractive shadow zone. In a non-turbulent medium, the effectiveness of the refractive shadow zone increases with increasing propagation range [9]. As highlighted in [10], in the presence of wind flow over the mountain, the terrain shadow zone can be enlarged with upward refraction or contracted with downward refraction, depending on the wind direction. In Case 3, for instance, the terrain shadow zone is enlarged due to upward refraction; hence, noise levels in regions A and B dropped about 30 and 23 dB, respectively. A significant reduction in the noise levels at region C is also observed. This is attributed to the following two reasons: First, there is still substantial upward refraction due to the large wind speed gradients (see Fig. 8.6) even though region C is closer to the source location. Second, noise levels on the source sphere are shifted to the negative y-axis and positive x-axis directions as ray-sphere intersection points are changed due to the atmospheric refraction effects [9]. The terrain shadow zone in region D is slightly contracted due to downward refraction and shifted to the negative y-axis direction. Higher noise levels are observed in regions E and F for two reasons: First, downward refraction increases noise levels as multiple reflections can occur due to sound rays with lower grazing angles (sound waves refracted towards the ground and reflected off the ground). Second, due to the atmospheric refraction, sound rays become more curved with increasing propagation range [9]. Thus, the ray-sphere intersection points are shifted to another point with a different phase and magnitude, which eventually alters the projected noise levels on the ground.

In reality, the field differences could be lower than those estimated in this work. In

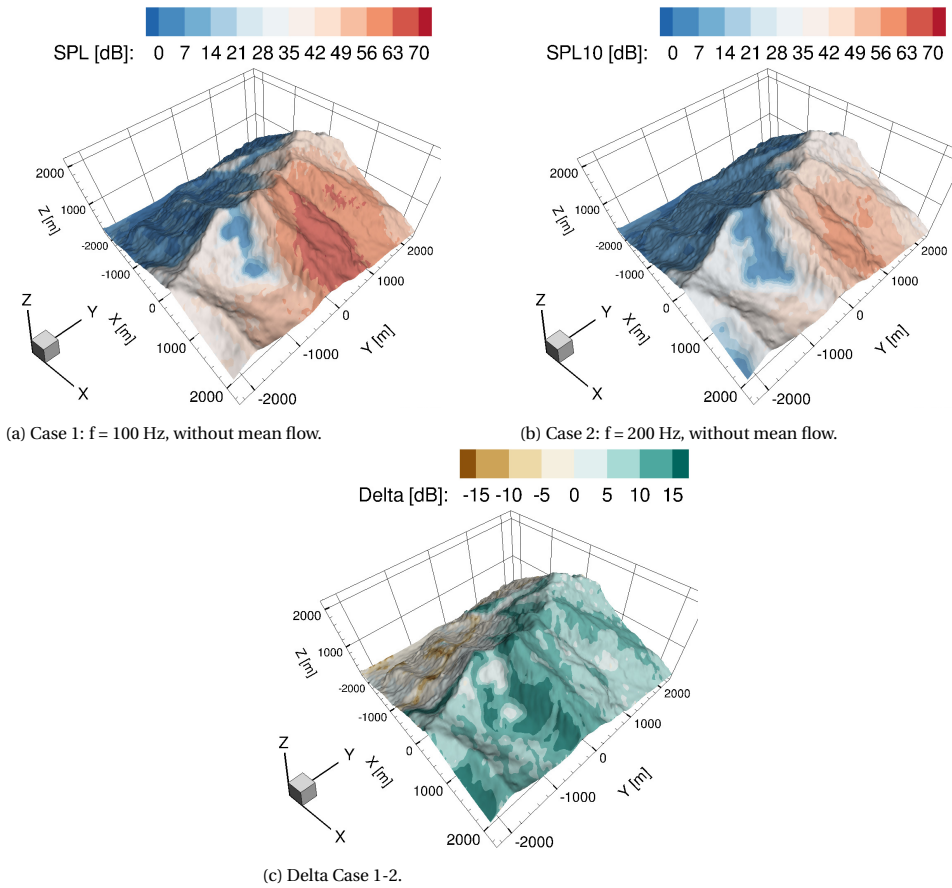


Figure 8.7: Noise footprint calculated for Case 1 (a) and Case 2 (b). The field difference is calculated by subtracting the noise levels in Case 2 from Case 1. The negative values indicate higher noise levels in Case 2.

the present study, for instance, the terrain surface is assumed to be a perfect reflector which is another factor that increases noise levels in a downward refracting medium [11, 12]; however, as pointed out in [12] the soil composition plays a significant role like the ground topology in sound propagation, altering the noise levels and its spatial distribution.

8.5. CONCLUDING REMARKS

This chapter presents a new approach to incorporate range-dependent terrain and weather effects in ACN predictions. The approach constructed in a way to improve the practicality and prediction accuracy through providing high-fidelity input data. To expand the capabilities of UYGUR, modifications have been made to incorporate broadband noise calculation. The accuracy and computational efficiency of UYGUR in calculating broadband noise have been verified by comparing with analytical solutions. Solutions were

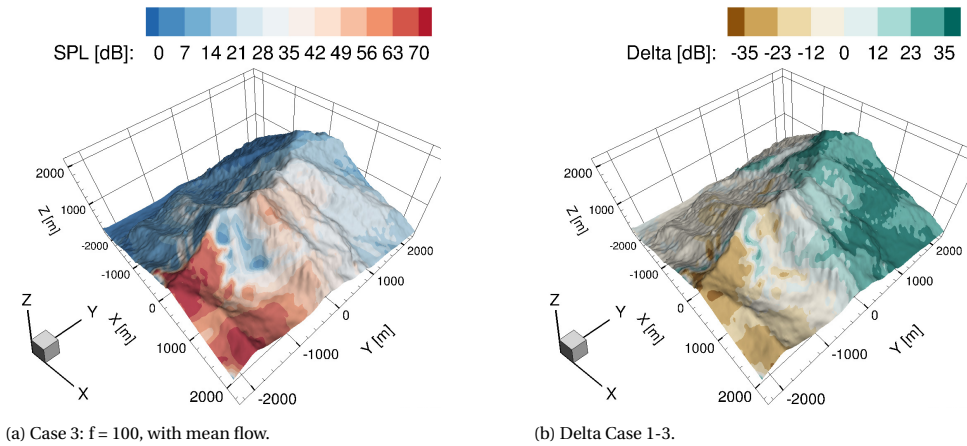


Figure 8.8: Noise footprint calculated for Case 3 (a) and the field difference between Case 1 and Case 3 (b). The negative values indicate higher noise levels in Case 3.

obtained for various source spectra, source frequency ranges, and frequency resolutions. The findings demonstrate that UYGUR can accurately and efficiently compute broadband noise.

The approach is used to analyze the effects of varying source directivity and wind flows on the noise footprint of a helicopter hovering over mountainous terrain. It is shown that changing source directivity in a quiescent atmosphere can alter the acoustic footprint by up to 15 dB. In the presence of mean flow, the terrain shadow zone is further enlarged by the refractive shadow zone, resulting in a significant difference in the acoustic footprint of up to 35 dB. Furthermore, the presence of wind can also cause quieter locations in a quiescent atmosphere to experience increased noise levels. This is due to the shift of directed source levels away from the source sphere, which occurs as a result of refraction caused by the mean flow.

The findings suggest that the range-dependent weather and terrain profiles in an outdoor environment can significantly affect the noise levels received by the community, particularly around the terrain shadow zone boundary. It is crucial to use reliable weather and terrain data to evaluate low-noise flight trajectories to minimize noise impact on the community. Future research could explore trends and patterns to further enhance noise reduction strategies.

REFERENCES

- [1] F. Yunus, D. Casalino, F. Avallone, and D. Ragni, *Aircraft community noise prediction in 3d environment using Gaussian beam tracing*, in *28th AIAA/CEAS Aeroacoustics 2022 Conference* (2022) p. 3079.
- [2] D. Dragna, B. Cotté, P. Blanc-Benon, and F. Poisson, *Time-domain simulations of outdoor sound propagation with suitable impedance boundary conditions*, *AIAA J.* **49**, 1420 (2011).

- [3] A. Torija Martinez *et al.*, *Drone noise, a new public health challenge?* in *Quiet Drones International e-Symposium on UAV/UAS Noise 2020* (International Institute of Noise Control Engineering, 2020) pp. 448–454.
- [4] D. Casalino, E. Grande, G. Romani, D. Ragni, and F. Avallone, *Definition of a benchmark for low reynolds number propeller aeroacoustics*, *Aerospace Science and Technology* **113**, 106707 (2021).
- [5] M. B. Porter, *Beam tracing for two-and three-dimensional problems in ocean acoustics*, *J. Acoust. Soc. Am.* **146**, 2016 (2019).
- [6] H. Bian, Q. Tan, S. Zhong, and X. Zhang, *Efficient computation of broadband noise propagation using Gaussian beam tracing method*, *J. Acoust. Soc. Am.* **151**, 3387 (2022).
- [7] E. M. Salomons, *Computational Atmospheric Acoustics* (Springer Science & Business Media, 2001).
- [8] J. P. Snyder, *Map projections—A working manual*, Vol. 1395 (US Government Printing Office, 1987).
- [9] F. Yunus, D. Casalino, F. Avallone, and D. Ragni, *Toward inclusion of atmospheric effects in the aircraft community noise predictions*, *J. Acoust. Soc. Am.* **150**, 759 (2021).
- [10] J. S. Lamancusa and P. A. Daroux, *Ray tracing in a moving medium with two-dimensional sound speed variation and application to sound propagation over terrain discontinuities*. *J. Acoust. Soc. Am.* **93**, 1716 (1993).
- [11] D. Wilson, E. Nykaza, M. White, M. Swearingen, L. Pater, and G. Luz, *Sound outdoors and noise pollution*, *Handbook of Environmental Fluid Dynamics, Volume Two: Systems, Pollution, Modeling, and Measurements*, 203 (2012).
- [12] J. Serafini, G. Bernardini, G. Grignaffini, S. Modini, and M. Gennaretti, *Acoustic wave three-dimensional ground reflection and bouncing*, *Appl. Acoust.* **180**, 108110 (2021).

9

CONCLUSIONS AND RECOMMENDATIONS

*No book can ever be finished. While working on it we learn just enough to find it
immature the moment we turn away from it.*

Karl Popper

*The game of science is, in principle, without end. He who decides one day that scientific
statements do not call for any further test, and that they can be regarded as finally
verified, retires from the game.*

Karl Popper

9.1. SUMMARY AND CONCLUSIONS

THE thesis presents a study on sound propagation in complex environments and the impact of various design, operational, and environmental factors on noise propagation. In this final chapter, the research goals defined in Chapter 1 are evaluated based on the work presented in the previous chapters.

1. To study the correlation between various design and operating parameters and acoustic footprint and identify trends to mitigate the noise impact.

The study utilized a novel computational framework that combined a low-fidelity noise source prediction method with a straight-ray propagator, assuming a homogeneous propagation medium (as described in Chapter 4). The framework's reliability and computational efficiency are verified by comparing it against high-fidelity simulations. The study included a parametric investigation to assess the correlation between propeller parameters (such as advance ratio and blade count) and the noise footprints. The findings showed that decreasing the advance ratio could alter the source directivity, leading to a significant variation of up to 30 dBA in the acoustic footprint. Similarly, increasing the blade count from 5 to 7 while keeping the advance ratio constant resulted in a variation of 16 dBA due to the change in the source directivity.

Based on the study, two key trends were identified: i) on-ground noise levels were more sensitive to the variation in the advance ratio than blade count, and increasing the advance ratio without affecting propeller aerodynamic performance could substantially reduce on-ground noise levels; ii) increasing the blade count could reduce on-ground noise levels if the goal is to target tonal noise at higher harmonics.

Overall, the proposed computational framework presents a practical and computationally efficient approach for quickly evaluating noise footprints. The study's findings could have significant implications for propeller design aimed at reducing on-ground noise levels.

2. To explore the link between vertical variation in air temperature and wind velocity profiles and noise footprint of a moving source with respect to the propagation range.

To achieve this research goal, a new 3D point-to-point curved-ray-tracer has been developed (Chapter 5). This solver calculates the directed source levels to a specific ground observer throughout the mission time while accounting for atmospheric refraction due to changes in air temperature and wind velocity gradients.

The study found that for receivers distributed over flat terrain, a refractive shadow zone appears when the vehicle flies upwind. This refractive shadow zone is stronger when the vehicle is further away from the receivers and becomes weaker or disappears when the vehicle is closer to the receivers. This suggests that weather has a significant impact when the source is at a distant location, but its impact decreases as the source approaches the receivers. No significant weather effect on

the noise footprint was observed when the vehicle flies downwind for all weather conditions.

The results demonstrate that weather conditions can significantly affect noise propagation, particularly for distant sources. The findings of this study highlight the importance of considering weather conditions when designing low-noise flight trajectories for long-range noise sources.

3. To develop a propagation model based on ray acoustics to be applied to sound propagation in urban areas and study the correlation between variations in terrain geometry, wind flow, and acoustic propagation.

The study is carried out by developing a novel Gaussian beam tracing (GBT) solver that accounts for vertical and horizontal variations in terrain topology and wind flow distribution in a 3D environment (Chapter 6).

The developed GBT approach extends the state-of-the-art of GBT tools in atmospheric acoustic propagation by including refraction due to 3D variation in wind velocity and establishing a complete theoretical framework for the GBT in an inhomogeneous moving atmosphere. A semi-empirical formulation is also derived to improve the accuracy of the GBT solutions at the terrain surface. The results show that the semi-empirical formulation significantly improves the agreement between the GBT solutions and the reference data, reducing the maximum error below 8 dB in the illuminated zone, compared to more than 40 dB without the empirical formulation. In terms of computational efficiency, it is demonstrated that for the higher frequency ($f = 200$ Hz), the GBT tool achieves a 17-fold reduction in computation time with respect to the FEM solver.

It is also shown that in the presence of a moving medium, the direct and reflected waves can have different ray paths than those in a quiescent atmosphere, and the phase increments along each path can change considerably, resulting in less apparent diffraction patterns and oscillations in the pressure amplitude. Furthermore, flow regimes inside urban canyons significantly impact acoustic propagation, suggesting the importance of including wind flow effects in evaluating airborne noise propagation in an urban environment.

It is demonstrated that the present GBT acoustic propagation model can be applied to high-frequency noise propagation in urban environments with acceptable accuracy and better computational efficiency than full-wave solutions.

4. To evaluate the noise distribution in a vertiport environment by exploring the correlation between variations in source directivity, vertiport geometry, wind flow, and the noise footprint distribution.

In order to investigate the impact of environmental factors on the acoustic signature of eVTOL vehicle, the GBT approach developed in Chapter 6 is extended to include complex source directivity. This is necessary to consider the source directivity of complex noise sources, such as eVTOL vehicle. The extended GBT approach is then coupled with the low-fidelity noise source prediction approach outlined in Chapter 2. This coupling reduced the computational resources required for noise

source calculation and enabled faster noise footprint predictions. The resulting approach is applied to calculate noise footprints of an eVTOL vehicle in a vertiport environment, taking into account variations in source directivity, terrain topology, and wind flow conditions, as described in Chapter 7 .

It is shown that building blocks increased on-ground noise levels by 5 dB in the illuminated zone, due to multiple reflections, and shielded the incoming sound field by creating shadow zones behind the building. Noise shielding effectiveness increased with increasing frequency in a quiescent atmosphere. Variation in source directivity resulted in differences of up to 40 dB in the noise footprint. Wind flow presence contributed a significant variation in the acoustic footprint by changing the lobes of the footprint pattern and intensifying the noise levels. The presented approach improved the prediction error up to 35 dB in terrain shadow zones and 5 dB in illuminated zones, with respect to the straight-ray propagation model. It is also noted that the computation time increased as the complexity of the propagation environment increased.

The findings of this study indicate that when irregular terrain surfaces are present, methods such as GBT must be used to account for multiple reflections over terrain surfaces and terrain shadow zones, rather than relying on a straight-ray propagator. Additionally, due to the low operational altitude of UAM vehicles, their high-frequency noise may not be masked by background noise, and building blocks may not properly shield the noise due to wind flow effects. Therefore, reducing high-frequency noise should be a primary target for mitigating UAM noise in a vertiport environment.

Overall, this study provides valuable insights into the potential of the GBT propagation model for efficiently and reliably evaluating the noise footprints of eVTOL vehicles and assessing the impact of environmental factors on their acoustic signature.

5. To study the impact of range-dependence of weather and terrain profiles on long-range noise propagation, and investigate the resulting changes in the noise footprint distribution.

The impact of range-dependent weather and terrain profiles on long-range propagation may be more significant than on short-range propagation in an urban environment. To study this, the developed GBT propagator is coupled with a high-fidelity noise source prediction approach to calculate the noise footprint of a helicopter hovering over a 5 km by 5 km mountainous terrain. To improve the accuracy of the predictions and the practicality of the proposed approach, the terrain geometry is directly extracted from a GIS database, while high-fidelity CFD simulation is used to obtain the wind flow data.

The results show that variation in terrain topology along the range significantly affects noise signal propagation in a quiescent atmosphere, particularly around the terrain shadow zone boundary. Furthermore, a change in source directivity can cause up to a 15 dB variation in the acoustic footprint in the illuminated zone. However, in the presence of wind velocity, the variation in the noise footprint

can increase up to 35 dB due to upward refraction, forming a refractive shadow zone around the terrain shadow zone boundary and further extending the overall shadow zones. As a result, noise levels are significantly decreased compared to a quiescent atmosphere.

The findings of this study suggest that in outdoor environments, the range-dependent variations in weather and terrain profiles can have a substantial impact on the noise levels received by communities, especially around the boundary of the terrain shadow zone. It is crucial to utilize accurate and reliable weather and terrain data for assessing the noise impact of low-flight trajectories. Providing such data can facilitate the evaluation of noise-reducing trends and help minimize noise pollution in the community.

The research objectives outlined in Chapter 1 have been achieved through the studies presented in this work. Valuable insights into improving aircraft-community-noise predictions, while considering the acoustic effects of atmospheric and ground conditions, have been gained. Multiple methods have been developed and proposed, each with its strengths and weaknesses, and thoroughly investigated for their ability to improve prediction accuracy.

Despite the progress made in this work, there are still opportunities for further expansion. These opportunities are outlined in the next section and provide a clear path for future research on this topic.

9.2. RECOMMENDATIONS FOR FUTURE WORK

To improve the prediction capability and extend the range of applicability of the developed methodologies, several recommendations are proposed. Firstly, the low-fidelity approach presented in Chapter 4, which is limited to hover and forward flight conditions with a fixed angle of attack, should be extended to include unsteady loading contributions and coupled with the frequency domain formulation that accounts for the inflow angle of attack. This coupling will enable the approach to be applied to other flight conditions, such as conversions from hover to forward flight, and explore correlations between various source parameters and noise footprint during conversion flight phases.

Secondly, the 3D point-to-point curved ray tracer should be extended to account for multiple reflections over irregular terrain and calculate the signal amplitude at any ray step using the dynamic ray tracing approach instead of spherical spreading. This will allow the tool to be applied for sound propagation in an urban environment where strong refraction is expected and a few receiver is is targeted. This extension could improve the UAM noise auralization.

Thirdly, the Gaussian beam tracer should be extended with a proper diffraction model, such as the uniform geometrical theory of diffraction, to account for diffraction effects when evaluating noise propagation in an urban area where the wavelength is comparable to the characteristic length of obstacles in the propagation medium. Varying terrain impedance should also be included to improve prediction accuracy.

Furthermore, the Gaussian beam tracer should also be extended to account for turbulence effects on acoustic propagation. Considering atmospheric turbulence is essential for improving the accuracy of sound propagation prediction models, especially in

urban environments where its impact is significant.

Moreover, it's noteworthy that both the GBT and curved-ray tracer algorithms possess a remarkable level of parallelism. This arises from the fact that each calculation involving a ray or beam is inherently self-contained and doesn't rely on the outcomes of other calculations. Moreover, these algorithms feature data-level parallelism, as identical operations are applied consistently throughout the ray or beam tracing process. Therefore, a prudent approach would involve implementing the GBT and curved-ray tracer algorithms within an environment leveraging GPUs and multicore CPUs. This strategic choice has the potential to significantly accelerate computation speed, yielding efficient results.

To gain further insight into the impact of the urban flow-field on noise source prediction of eVTOL vehicles, it is recommended to investigate the effect of building-induced turbulence on source directivity when the eVTOL operates near buildings. A quantitative study is necessary to determine the minimum distance between buildings and vehicles at which flow impact on source directivity can be disregarded. This study should highlight the source and building distances at which the GBT approach developed in this study can be applied to simulate eVTOL noise propagation in an urban environment.

A

FREQUENCY DOMAIN TONAL NOISE SOLVER INPUT FILE DESCRIPTION

This appendix provides information on the user input file for the frequency-domain tonal noise solver outlined in Chapters 3 and 4. This tool is developed by implementing the frequency-domain formulation presented in Chapter 3 using C programming language with C99 standard. Based on the propeller geometry and blade aerodynamic data obtained from the BEMT calculation, this tool outputs the tonal noise at a set of prescribed microphones/receivers distributed over a sphere.

```
1 ADScase8 ..... Case name
2 [#===== PROPELLER AERO DATA=====]
3 2.5 ..... Propeller blade diameter (m)
4 7 ..... Number of blades
5 1900.0 ..... RPM
6 0.2 ..... Free stream Mach number
7 0.0 ..... pitch angle of propeller shaft axis relat
8 0.0 ..... Propeller hub coordinate along x axis
9 0.0 ..... Propeller hub coordinate along y axis
10 0.0 ..... Propeller hub coordinate along z axis
11 10 ..... Acoustic harmonic numbers
12 FD_analytical_blade_in_NE7RPM1900.txt ..... Input file for aerodynamic sources
13 [#===== ATMOSPHERE SECTION =====]
14 2000.0 ..... Flight altitude (m)
15 275.15 ..... Temperature (K)
16 79500.0 ..... Pressure (Pa)
17 1.007 ..... Density (Kg/m^3)
18 332.65 ..... Sound speed at this altitu (m/s)
19 [#===== RECEIVER SECTION =====]
20 1 ..... Logic for observer mics [0: automatically]
21 hemisphere_ads.txt ..... Receiver geometry file
22 51 ..... Polar angle num
23 101 ..... Azimuthal angle num
```

Figure A.1: An overview of the input file of the frequency domain tonal noise solver. Where the case name is used to generate output file name string.

The input file for this tool uses a menu-style format and is divided into three sections: propeller aero-data, atmosphere data, and receiver data. The layout of the input file is illustrated in Figure A.1. While the input file has been designed to be self-explanatory,

a brief outline of each section of the input file will be provided in the following section, along with necessary information about additional input files. Moreover, the structure of the output files will be explained for clarity.

A.1. INPUT FILE

A.1.1. PROPELLER DATA

Lines 3-10 specify the propeller data in terms of blade and hub geometry, along with the corresponding operational conditions. The inflow angle between the propeller shaft axis and the relative wind is specified in line 7. The harmonic number m is specified in line 11, while line 12 contains the name of the input file. This file is an ASCII-text file containing essential aerodynamic data for a single blade, calculated using the Blade Element Momentum Theory (BEMT). Figure A.2 provides an overview of the file, where β indicates the blade angle, and $area$ represents the equivalent sectional area of a blade element. The area is calculated as $A = 0.6863b_ch$ [1], where b_c denotes the chord length and h denotes the maximum thickness of the airfoil. The values for dT/dr and dQ/dr represent sectional thrust and torque, respectively. All of this information is extracted by directly reading the output file from the BEMT calculation performed by the *OptydB*-BEMT tool, as outlined in Chapter 3-4.

1	#	r/R [-]	chord [m]	beta [deg]	Area [m ²]	dT/dr [N/m]	dQ/dr [N*m/m]
2		0.2411800000	0.1254125000	51.0100000000	0.0016173406	86.2178396602	115.3998252258
3		0.2556300000	0.1282375000	49.3590000000	0.0016906957	98.3128062984	123.5646597695
4		0.2700600000	0.1306875000	47.7710000000	0.0017555733	110.9362955506	131.4732132906
5		0.2845000000	0.1327625000	46.2430000000	0.0018112356	123.9960709684	139.0682832464
6		0.2989300000	0.1345250000	44.7740000000	0.0018591023	137.4250591360	146.3275923436
7		0.3133500000	0.1359625000	43.3610000000	0.0018984918	151.1091206000	153.1853662137
8		0.3277800000	0.1371250000	42.0020000000	0.0019305313	164.9807488105	159.6416445845
9		0.3422000000	0.1380250000	40.6940000000	0.0019445254	178.9241666893	165.6455874070
10		0.3566200000	0.1386875000	39.4360000000	0.0019449646	192.8664336850	171.1864433333
11		0.3710400000	0.1391125000	38.2270000000	0.0019371640	206.6787874306	176.2191912972
12		0.3854500000	0.1393375000	37.0630000000	0.0019238845	220.2882148052	180.7491806074
13		0.3998700000	0.1393750000	35.9430000000	0.0019053006	233.6293639327	184.7754244122

Figure A.2: An overview the data file specified in line 12 of the input file.

A.1.2. ATMOSPHERE DATA

Lines 14-18 specify information regarding flight altitude, as well as corresponding ambient temperature, atmospheric pressure, density, and sound speed. This section is complete and no further data is required, as the noise calculation performed at receivers distributed over a sphere at which a homogeneous, uniform atmosphere is assumed.

A.1.3. RECEIVER DATA

Two options are available for generating receiver coordinates: direct reading from a hemisphere geometry or generation based on a given number of elevation and azimuthal angles. The logic to activate either option is specified in line 20. When the logic is set to 1, the receiver geometry is read from the provided file, the name of which is specified in line 21. This file is prepared in ASCII-text file format, and an overview is shown in Fig. A.3.

1 #	Mic	x [m]	y [m]	z [m]
2	0.0000000000000000E+00	0.2451963200000000E+02	-0.4877255000000000E+01	
3	-0.4783534000000000E+01	0.2404847100000000E+02	-0.4877255000000000E+01	
4	0.4783545000000000E+01	0.2404849400000000E+02	-0.4877255000000000E+01	
5	0.0000000000000000E+00	0.2500000000000000E+02	0.2000000000000000E-05	
6	0.2000000000000000E-05	0.2309697500000000E+02	-0.9567081000000000E+01	
7	0.4506001000000000E+01	0.2265318700000000E+02	-0.9567081000000000E+01	
8	-0.4505997000000000E+01	0.2265317500000000E+02	-0.9567081000000000E+01	
9	-0.4877250000000000E+01	0.2451961300000000E+02	0.2000000000000000E-05	

Figure A.3: Receiver geometry file.

A.2. OUTPUT FILES

Two types of output files are generated: one contains sound pressure levels in terms of thickness and loading noise contributions at each receiver location. This file is generated for each microphone separately, resulting in a number of files equal to the number of microphones on the hemisphere. The second file contains microphone locations and their corresponding overall sound pressure level (OASPL), and is a single file. An example of the first type of output file can be seen in Fig. A.4.

1 #	BPF [hz]	SPL_Th [dB]	SPL_L [dB]	SPL [dB]
2	221.666667	86.181222	77.966001	86.791321
3	443.333333	77.824184	60.837541	77.910246
4	665.000000	68.437684	46.529344	68.465581
5	886.666667	58.580787	32.829557	58.592324
6	1108.333333	48.332249	18.712899	48.336987
7	1330.000000	37.659527	2.872412	37.660969
8	1551.666667	26.463706	-21.362327	26.463777
9	1773.333333	14.548215	-23.646328	14.548873
10	1995.000000	1.480990	-27.222169	1.486840
11	2216.666667	-14.038614	-34.583063	-14.000470

Figure A.4: An overview of an output file at a single microphone location.

The SPLs for thickness noise (indicated by SPL_{Th}) and loading noise (indicated by SPL_L) are calculated for each Blade Passage Frequency (BPF). The total SPL is indicated by SPL . The OASPL at each microphone is calculated and output in an ASCII-file format in the OASPL output file, as illustrated in Fig. A.5.

1 #	Mic	x [m]	y [m]	z [m]	OASPL [dB]
2	0.0000	24.5196	-4.8773		89.4843
3	-4.7835	24.0485	-4.8773		88.6972
4	4.7835	24.0485	-4.8773		88.1438
5	0.0000	25.0000	0.0000		89.4843
6	0.0000	23.0970	-9.5671		89.4843
7	4.5060	22.6532	-9.5671		88.2818
8	-4.5060	22.6532	-9.5671		88.8019
9	-4.8773	24.5196	0.0000		88.6601
10	4.8773	24.5196	0.0000		88.0954
11	-9.3832	22.6532	-4.8773		85.7627

Figure A.5: An overview of an OASPL output file.

REFERENCES

- [1] M. T. Kotwicz Herniczek, D. Feszty, S.-A. Meslioui, and J. Park, *Applicability of early acoustic theory for modern propeller design*, in *23rd aiaa/ceas aeroacoustics conference* (2017) p. 3865.

B

3D CURVED-RAY TRACER INPUT FILE DESCRIPTION

This appendix provides information on the user input file for the 3D point-to-point curved ray tracer. The ray tracer is developed based on the 3D eigenray tracing algorithm described in Chapter 5, which is implemented using FORTRAN 90 and integrated into the *Opty∂B*-FOOTPRINT tool. In the atmosphere section of the *Opty∂B*-FOOTPRINT tool input file, three options are provided, as shown in Fig. B.1. To activate the curved ray tracer, the user should select either the 2000 or 3000 atmospheric profile option. The following sections briefly outline each option and provide details on the necessary input files.

```
69 # ATMOSPHERE SECTION =====  
70 1000 ..... Atmosphere kind [1000]:  
71 atmosphere_profile.txt ..... Atmosphere profile file
```

Figure B.1: An overview of the *Opty∂B*-FOOTPRINT tool input file in which the curved ray tracing is implemented.

B.1. ATMOSPHERE MODEL

B.1.1. OPTION 1000

This is the default option in the *Opty∂B*-FOOTPRINT tool and uses straight-ray propagation to determine the distance between the source and receiver, and applies spherical spreading based on this distance. This method is highly time-efficient as it does not require ray tracing. However, it can only be used when the atmosphere is constant and homogeneous. If the atmosphere is not constant and homogeneous, curved ray tracing must be used instead.

B.1.2. OPTION 2000

Enabling this option requires an additional file, the atmosphere file specified at line 71 of the *Opty∂B*-FOOTPRINT input file. The atmosphere file, provided in an ASCII text

file format, contains information about the number of time steps used in the integration of the curved-ray tracing equation in 2.4, along with temperature and the three components of wind speed at each vertical station. An example of the atmosphere file content is shown in Figure B.3. Specifying the number of time steps in the user input file is crucial since it affects the accuracy of the results and the computational time needed for the simulation, as detailed in Chapter 5. By enabling the user to control this parameter, the tool can be fine-tuned to strike a balance between computational efficiency and accuracy for a particular problem, resulting in satisfactory results while saving computational time.

1	800					
2	#	altitude [m]	temperature [K]	vx [m/s]	vy [m/s]	vz [m/s]
3		0.0100	297.5000	0.0000	0.0000	0.0000
4		26.5922	286.6884	12.4640	0.0000	0.0000
5		53.1743	285.8026	13.2726	0.0000	0.0000
6		79.7565	285.1998	13.7141	0.0000	0.0000
7		106.3386	284.7058	14.0141	0.0000	0.0000
8		132.9208	284.2692	14.2395	0.0000	0.0000
9		159.5029	283.8678	14.4191	0.0000	0.0000

Figure B.2: An overview of the atmosphere file for option 2000. The first row represents the number of time-steps to integrate the curved ray tracing equation. The columns represents altitude, air temperature, and the three components of the wind velocity.

B.1.3. OPTION 3000

When enabled, this option uses an analytical formulation that assumes a constant wind speed and temperature gradient to determine the weather profiles. The atmosphere file specified at line 71 of the *OptydB-FOOTPRINT* input file contains the required information. An example of the atmosphere file is shown in Figure B.3. The file begins with the number of time steps used to integrate the curved ray tracing equation. The second and third lines specify the wind speed gradient and temperature gradient. The wind speed v at a given altitude z is determined using the gradient dv/dz , which is read from the input file, and the expression $v = zdv/dz$. The sound speed is calculated using the expression $c = \sqrt{\gamma R z dT/dz}$, where γ is the specific heat ratio of air, R is the gas constant, and their values are $\gamma = 1.4$ and $R = 287.0$, respectively.

1	800	Number of time steps
2	-0.015	wind speed gradient
3	0.001	Temperature gradient

Figure B.3: An overview of the atmosphere file for option 3000. The first line represents the number of time-steps to integrate the curved ray tracing equation, while the second and third lines represents the wind speed gradient and air temperature gradient.

C

UYGUR INPUT FILE DESCRIPTION

C.1. INPUT FILE

This appendix explains the structure of the input file for the Universal Ray and Gaussian Beam Tracer (UYGUR), which is implemented in FORTRAN 90. The input file is presented in a menu-style format and is divided into four sections: the atmosphere section, source section, terrain/receiver section, and output section. Figure C.1 provides an overview of the input file.

Although the input file is designed to be self-explanatory, there are still a few important points that need to be emphasized. These points are explained in further detail below.

C.1.1. ATMOSPHERE SECTION

Line 7 of the input file determines how weather profiles are represented in the simulation - either as analytical formulas or data files. When set to true, analytical profiles are used, with constant sound speed and wind velocity gradient that can be specified in lines 12-15. Otherwise, weather data is read from files listed between lines 8-11. In this case, the 3D wind and sound speed profiles are imported directly from CFD simulations. However, it's important to note that the weather data must be preprocessed and organized as an ordered combination of 2D slices, as illustrated in Fig. C.2. For reference, an overview of the 3D field of the X component of the wind velocity is provided in Fig. C.3.

C.1.2. SOURCE SECTION

UYGUR is set by default to run for a monopole source whose amplitude and frequency are specified in lines 18-19 of the input file. However, it can also include complex source directivity by reading a directivity file. This feature can be activated by setting the logic in line 20 to true. If left as false, UYGUR assumes a monopole. The name of the directivity file is specified in line 21, and it contains the Cartesian coordinates of vertices on a sphere and the corresponding noise level at each vertex, as shown in Fig. C.4. It's important to note that the directivity file corresponds to a single source frequency, which should be

```

1 'JASA2Fig9a' ..... case title
2 #===== ATMOSPHERE SECTION =====
3 283.15 ..... Ambient Temperature
4 101325.0 ..... Ambient Pressure
5 1.225 ..... Ambient density
6 80 ..... Relative humidity in percentage [%]
7 T ..... Logic to approximate the weather profiles [F : read fr
8 sspField_cnst.txt ..... temperature/sound speed data file name
9 windField_vx.txt ..... wind velocity data file name
10 windField_vy.txt ..... wind velocity data file name
11 windField_vz.txt ..... wind velocity data file name
12 0.0 0.0 0.0 ..... sound speed/temperature gradients [dc/dx,dc/dy,dc/dz]
13 0.0 0.0 0.0 ..... wind gradients along x [dvx/dx,dvx/dy,dvx/dz]
14 0.0 0.0 0.0 ..... wind gradients along y [dvy/dx,dvy/dy,dvy/dz]
15 0.0 0.0 0.0 ..... wind gradients along z [dvz/dx,dvz/dy,dvz/dz]
16 0 20.0 ..... Ground level and actual height of the computational do
17 #===== SOURCE SECTION =====
18 0.15125 ..... Source amplitude in [Pa]
19 200.0 ..... Source frequency [Hz]
20 F ..... Logic to read the source hemisphere data
21 dummy.txt ..... Source hemi/sphere directivity file name
22 1 ..... Nsx number of source coordinates in x
23 50.0 / ..... x coordinate of the source [m]
24 1 ..... Nsy number of source coordinates in y
25 0.0 / ..... y coordinate of the source [m]
26 1 ..... Nsz number of source coordinates in z
27 18.0 / ..... z coordinate of the source [m]
28 1801 ..... Number of source elevation angles
29 -90.0 90.0 / ..... Range of elevation angle
30 2 ..... Number of source azimuthal angles
31 0 180 / ..... Range of azimuthal angle
32 #===== TERRAIN/RECEIVER SECTION =====
33 T ..... Reading terrain mesh from a STL file [T: true; F: Fals
34 optydb_gfd_val_3block_building.stl ..... ground mesh stl file name
35 501 ..... Number of vertical receiver points
36 0.0 20.0 / ..... Range of vertical receiver points [m]
37 501 ..... Number of horizontal receiver points
38 0.0 100.0 / ..... Range of horizontal receiver points [m]
39 3 ..... Number of receiver azimuthal angles
40 0.0 360.0 / ..... Range of receiver azimuthal angles [m]
41 T ..... Logic for ground reflection [True for reflection on, a
42 115 115 25.0 ..... Max x,y,z ranges of the computational domain [-x,x; -y
43 #===== OUTPUT SECTION =====
44 1000 ..... Run type [1000: Beam tracing; 2000: Ray path tracing ]

```

Figure C.1: An overview of UYGUR input file.

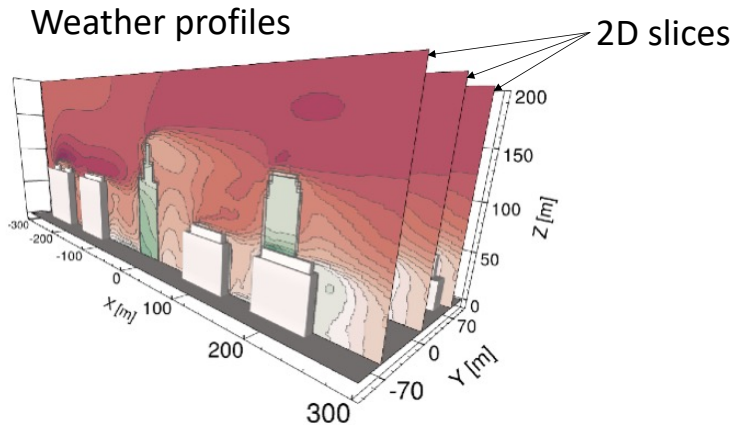


Figure C.2: An illustration of 3D weather profiles as a combination of 2D slices.

```

1 # Number of horizontal stations along x
2 # Number of horizontal stations along y
3 # Number of vertical stations
4 # Values of horizontal stations along x
5 # Values of horizontal stations along y
6 # Values of vertical stations
7 # Wind speed field matrix XZ stacked along y direction
8 344
9 15
10 122
11 -0.8700000 -0.6900000 -0.5100000 -0.3300000 -0.1500000 0.0300000 0.2100000 0.39
12 -10.0000000 -8.0000000 -6.0000000 -5.0000000 -4.0000000 -3.0000000 -2.0000000 0
13 0.0100000 0.182562 0.355124 0.527686 0.700248 0.872810 1.045372 1.217934
14 4.955614 4.955793 4.957642 4.958461 4.960555 4.968087 4.969657 4.977478
15 4.955614 4.955793 4.957642 4.958461 4.960555 4.968087 4.969657 4.977478
16 4.955614 4.955793 4.957642 4.958461 4.960555 4.968087 4.969657 4.977478
17 4.955614 4.955793 4.957642 4.958461 4.960555 4.968087 4.969657 4.977478
18 4.955614 4.955793 4.957642 4.958461 4.960555 4.968087 4.969657 4.977478
19 4.955614 4.955793 4.957642 4.958461 4.960555 4.968087 4.969657 4.977478
20 4.955614 4.955646 4.957906 4.958521 4.959544 4.968779 4.969145 4.976911

```

Figure C.3: An overview of x component of the 3D wind field.

1 #	Mic. x [m]	Mic. y [m]	Mic. z [m]	SPL [dB]
2	0.25000E+02	-0.00000E+00	0.00000E+00	0.56539E+02
3	0.24971E+02	0.12078E+01	-0.00000E+00	0.58334E+02
4	0.24971E+02	-0.12078E+01	-0.00000E+00	0.57326E+02
5	0.24971E+02	0.00000E+00	-0.12078E+01	0.55002E+02
6	0.24942E+02	0.12064E+01	-0.12078E+01	0.57725E+02
7	0.24942E+02	-0.12064E+01	-0.12078E+01	0.57464E+02
8	0.24883E+02	-0.24128E+01	0.00000E+00	0.55518E+02
9	0.24883E+02	0.24128E+01	0.00000E+00	0.58946E+02
10	0.24883E+02	0.00000E+00	-0.24128E+01	0.57185E+02
11	0.24854E+02	-0.24100E+01	-0.12078E+01	0.59068E+02
12	0.24854E+02	0.24100E+01	-0.12078E+01	0.58477E+02
13	0.24854E+02	0.12022E+01	-0.24128E+01	0.56965E+02
14	0.24854E+02	-0.12022E+01	-0.24128E+01	0.56911E+02
15	0.24767E+02	0.24016E+01	-0.24128E+01	0.56119E+02
16	0.24767E+02	-0.24016E+01	-0.24128E+01	0.58117E+02
17	0.24738E+02	-0.00000E+00	-0.36122E+01	0.60080E+02
18	0.24738E+02	0.36122E+01	-0.00000E+00	0.58870E+02
19	0.24738E+02	-0.36122E+01	-0.00000E+00	0.56475E+02
20	0.24709E+02	0.11952E+01	-0.36122E+01	0.58412E+02

Figure C.4: An overview of source sphere directivity file.

specified in line 19 of the input file when this option is activated.

The number of source positions and corresponding coordinates are specified in lines 22-27, while the number of beam shooting angles along elevation and azimuthal angles and their range are specified in lines 28-31. The definition of the elevation and azimuthal angles is illustrated in Fig. C.5.

C.1.3. TERRAIN/RECEIVER SECTION

By default, UYGUR is designed to run for flat terrain at ground level ($z = 0$ m). However, if an irregular terrain geometry is provided, it can be imported by setting the logic at line 33 to true and specifying the name of the geometry file. The terrain geometry file must be in the STL (stereolithography) file format, and the x and y coordinates of all vertices must be equally spaced. The z coordinate of each vertex must be uniquely defined by a single pair of x and y coordinates, i.e., $z = f(x, y)$. To illustrate, examples of the STL file used in this work is shown in Fig. C.6.

C

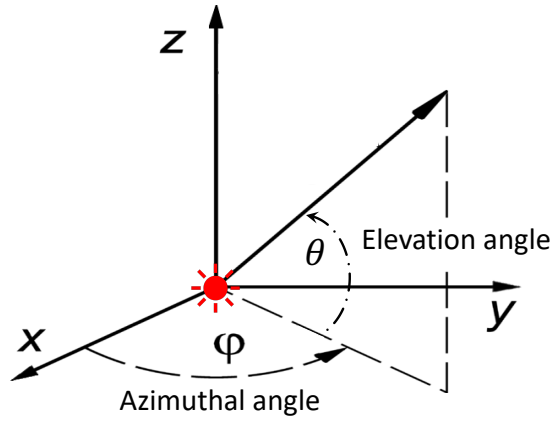


Figure C.5: The definition of elevation and azimuthal angles.

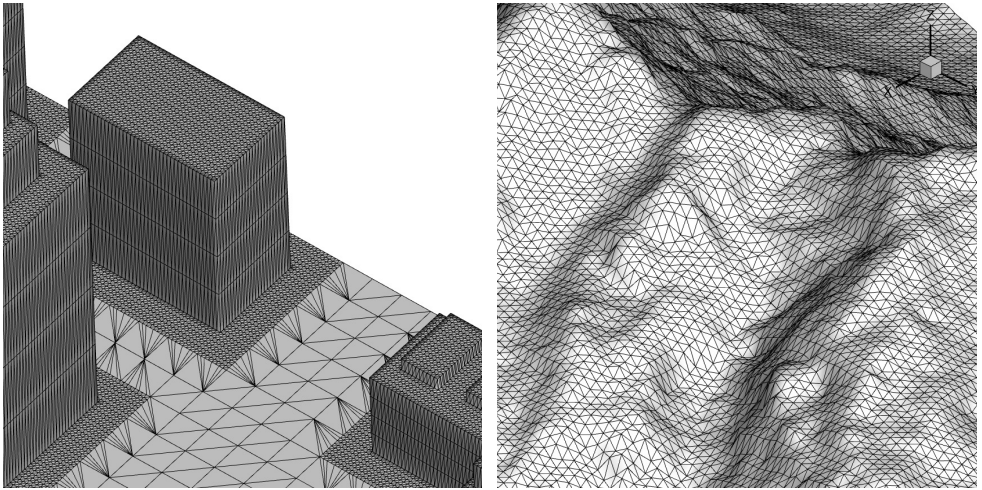


Figure C.6: Close-up view of STL geometries used in this work. Urban geometry used in Chapter 7 (left) and mountain geometry used in Chapter 8 (right).

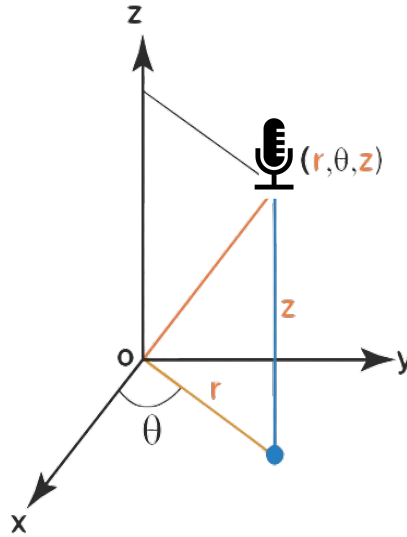


Figure C.7: The receivers are defined using the cylindrical coordinate system.

To simplify implementation and reduce computational time in the beam summation, receivers are defined using a cylindrical coordinate system, as illustrated in Fig. C.7. For example, the number of receiver points along the z -axis is specified in line 35 of the UYGUR input file, while the minimum and maximum values of the receivers along the z -axis are specified in line 36. Similarly, the number of receivers and their ranges along the r -axis are specified in lines 37 and 38, respectively. Finally, the number of azimuthal angles (θ) and their minimum and maximum values are specified in lines 39-40.

C.2. OUTPUT FILES

In the user input file, line 44 specifies the type of output data. The default option is beam tracing, which outputs the wavefield on the selected receiver surface as a binary file with a '.ugr' extension. If the user only wants to visualize ray-path trajectories, they should select the output data type 2000. This generates an ASCII text file with a '.raypath' extension, allowing visualization of the ray-path trajectories in the computational domain.

To visualize the acoustic wavefields, a Python library called *UYGUR.py* has been developed. This library includes several classes and functions that can read the binary file and generate 2D field plots or line plots on vertical or horizontal planes. The Python library also generates data for 3D visualization. Further details on the library can be found in the following section.

C.2.1. UYGUR.PY

The UYGUR.py file contains three classes: VizXZfields, VizXYfields, and Viz3Dfields. Each class has six arguments:

- **srcPos**: a list representing the position of the source
- **fnUGR**: the name of the binary file that contains the pressure field data
- **fnRef**: the name of the reference file in an ASCII-text format (optional)
- **plot**: a string specifying the type of plot to generate; if "preal", then the real part of the pressure field is plotted; if "spl", then the sound pressure level (SPL) is plotted.
- **vmin**: the minimum value of the color scale used in the plot
- **vmax**: the maximum value of the color scale used in the plot
- **station**: the value of the receiver station used in the line plot

The classes in this module provide several methods for reading and visualizing pressure fields, including **readUGR**, **calcPressure**, and **plot2Dfield**. To output and visualize 2D field data and color plots on the XZ and XY planes, respectively, the classes **VizXZfields** and **VizXYfields** are used.

It's important to note that the receivers are defined in a cylindrical coordinate system. Therefore, when a user visualizes a 2D field plot on the XY plane, the polar field needs to be converted to a 2D Cartesian field. This conversion is accomplished using the static method **polar_to_cart**, which is specified in the class **VizXYfields**.

If the user wants to visualize the acoustic field on building surfaces, the **Viz3Dfields** class must be used. This class extracts horizontal field data at different vertical receiver stations specified in lines 35-36 of the UYGUR input file and outputs the 3D field. The resulting 3D field data can then be imported into **TECPLOT** or **PARAVIEW**, along with the terrain STL file. The acoustic field on the terrain surface can be visualized by interpolating the field data onto the terrain surface.

LIST OF PUBLICATIONS

JOURNAL PAPERS

5. **F. Yunus**, D. Casalino, F. Avallone, D. Ragni, *Toward inclusion of atmospheric and ground effects in the aircraft community noise predictions*, to be submitted to the AIAA Journal, (2023).
4. **F. Yunus**, D. Casalino, F. Avallone, D. Ragni, *Efficient prediction of urban air mobility noise in a vertiport environment*, [Aerospace Science and Technology Volume 139, 108410 \(2023\)](#).
3. **F. Yunus**, D. Casalino, F. Avallone, D. Ragni, *Efficient prediction of airborne noise propagation in a non-turbulent urban environment using Gaussian beam tracing method*, [The Journal of the Acoustical Society of America 153, 2362 \(2023\)](#).
2. **F. Yunus**, D. Casalino, F. Avallone, D. Ragni, *Efficient low-fidelity aeroacoustic permanence calculation of propellers*, [Aerospace Science and Technology Volume 123, 107438 \(2022\)](#).
1. **F. Yunus**, D. Casalino, F. Avallone, D. Ragni, *Toward inclusion of atmospheric effects in the aircraft community noise predictions*, [The Journal of the Acoustical Society of America 150, 759 \(2021\)](#).

CONFERENCE PROCEEDINGS

4. D. Casalino, G. Romani, **F. Yunus**, *Electric vertical and take-off landing vehicle community noise prediction: from flow simulation to flight mission analysis*, In 10th Convention of the European Acoustics Association, Forum Acusticum 2023, (2023).
3. **F. Yunus**, D. Casalino, F. Avallone, D. Ragni, *Aircraft community noise prediction in 3D environments using Gaussian beam tracing*, In [28th AIAA/CEAS Aeroacoustics 2022 Conference](#), p. 3079, (2022).
2. R. Atassi, I. Paden, **F. Yunus**, I. Gonzalez-Martino, D. Casalino, C. Garcia-Sanchez, *Numerical aerodynamics and aeroacoustics predictions of a drone under real urban environments*, in [QUIET DRONES Second International e-Symposium on UAV/UAS Noise](#), (2022).
1. **F. Yunus**, D. Casalino, F. Avallone, D. Ragni, *Urban air mobility noise prediction in a 3D environment using Gaussian beam tracing*, In [Delft International Conference of Urban Air Mobility](#), (2022).